EVOLUTION OF THE LUCKY STRIKE VENT FIELD, MID-ATLANTIC RIDGE

by

© Dennis Sánchez Mora

A Thesis submitted to the School of Graduate Studies in partial fulfillment of the requirements for the degree of

Doctor of Philosophy

Department of Earth Sciences, Faculty of Science

Memorial University of Newfoundland

July 2022

St. John's, Newfoundland and Labrador, Canada

Abstract

Seafloor hydrothermal discharge results in accumulations of sulfide minerals that can be rich in base, precious, and critical metals. An increasing demand in these metals in order to transition to a low-carbon economy has resulted in an interest to evaluate the potential of seafloor resources. This dissertation focuses on fundamental geological processes that lead to the formation of these hydrothermal metal-rich deposits. To achieve this, the age, rate of accumulation, composition, and efficiency of metal deposition of the hydrothermal deposits was determined at the Lucky Strike vent field, which is located on the Mid-Atlantic Ridge, ~400 km southwest of the Azores archipelago. Using the ^{226}Ra/Ba dating technique, hydrothermal barite is dated from these hydrothermal deposits to determine that the hydrothermal field at Lucky Strike has been active at least for ~6,600 years. The tonnage of hydrothermal material that accumulated above the seafloor at Lucky Strike was estimated to be ~1.3 Mt, this was estimated using ~1 m resolution bathymetry at this site. This means that the hydrothermal deposits are accumulation at a minimum rate of ~194 tons/year. The hydrothermal deposits are dominated by barite, anhydrite, marcasite, pyrite, sphalerite, and chalcopyrite, and supergene alteration that consists of goethite and minor atacamite, covellite, and bornite. The bulk composition of these deposits is similar to other Mid-Atlantic ridge hydrothermal deposits but show elevated concentrations of Ba, Sr, and Mo, which reflects the E-MORB substrate geochemistry associated with the nearby Azores hotspot. Furthermore, the average deposit Ba/Co is useful to discriminate between different substrate compositions, such as E-MORB, N-MORB, and ultramafic-hosted sites. The sulfur isotopic composition of marcasite and chalcopyrite ranges from -2.5 to 8.7‰. The Capelinhos vent site, located 1.4 km east of the main Lucky Strike field is enriched in ^{34}S, which reflects differences in sub-seafloor fluid/rock interactions and fluid pathways at these two sites. Sub-seafloor precipitation at the main Lucky Strike field results in <20% of the reduced sulfur of the upwelling hydrothermal fluid reaching the seafloor. Moreover, data on the rate of accumulation and

geochemical composition of the hydrothermal deposits and compared to available fluid flux and fluid chemistry was used to determine how much of the metals were lost to seawater and how much of this was precipitated as hydrothermal deposits. This efficiency of metal precipitation is estimated for two of the sites at Lucky Strike, Sintra and tour Eiffel. The metal precipitation efficiency was determined to be 38-99% for Cu, 64-78% for Zn, 14-76% for Fe, and <1% for Mn and Si and seems to be element specific and temperature dependent. In addition, these efficiencies vary at the different scales when this study is compared to the recalculated depositional efficiencies at other hydrothermal sites such as TAG and Endeavour. Furthermore, the efficiencies of precipitation vary at the vent field scale, with the Sintra site showing overall higher efficiencies for Cu, Zn, and Fe, when compared to Tour Eiffel. These estimated metal depositional efficiencies have implications for metal fluxes to the oceans as well as ore forming processes. Finally, fault geometry analysis indicates that hydrothermal venting and associated hydrothermal deposits are largely controlled by enhanced permeability that results from local scale offsets in stress field orientations that form relay ramps and fault linkages.

Acknowledgements

First, I would like to thank my family for keeping me sane and happy for these five years. What a wild ride! Yohanna, coming to Canada was a huge challenge for you and we have struggled at times but you always had our backs when we most needed you and I have learned a lot from your resilience. Yohanna, I love you and I am proud of how you have evolved here. Emely, I had the privilege to watch you grow and I am so proud of the genuinely kind person that you have become. I also really enjoyed taking you to soccer, swimming, and gymnastics. Thanks, Emely, for always being so loving and having a great sense of humor, I love you so much. Ximena, you fill me with joy and I will never forget riding a bike to take you to daycare. Mami and papi, thanks for your ongoing support and for always having encouraging words for me. Thanks for being excellent role models, everyday I think I am more like you two.

To my brothers, Ariel, Javi, and Mau, thanks for always being in touch and sharing memes. I love you guys! A shout-out to my soccer team Bachata FC for great games and post-games throughout these years that have really helped for my mental and physical health.

To the early JJ crew, Ben Peterkin and Euri Papanicolaou thanks for the #songoftheday and for being always available to chat about SMS deposits! To the rest of the JJ lab, thanks Andrew Martin, Caroline Gini, Chris Galley, Sarah Moriarty, and Natalie McNeil thanks for #memeoftheday and so many great discussions of diverse topics of SMS/VMS deposits and marine geology! Special thanks to Andrew for providing insight in some of the chapters in this thesis.

Thanks to my committee Steve Piercey and Luke Beranek for your very helpful comments, suggestions, and discussions during this whole process and for genuinely showing interest in my research. Thank to Glenn Piercey for your disposition during SIMS analyses.

Thanks to Michelle Miskell, Keir Hiscock, Jane O'Neill, Danyelle Drodge and all the admin people, thanks for being so efficient in your work and and most importantly, kind.

Thanks to Carlos Arbiol for helping with comps and proposal edits and for those gym days. Matt Manor, Nikola Denisová, and Kei Quinn for great SMS/VMS discussions either during Beers N Peers or at any other occasion, what a great SEG crew!

Thanks to all the mentors that I have encountered throughout the years that have in different ways inspired me and encouraged me to get to where I am today, this includes; Dave Lentz, Jim Walker, and Sergio Gelcich.

Thanks to my supervisor John Jamieson for the ongoing support. Thanks for your patience and understanding especially with family related issues, during Ximena's birth, and during COVID times. Thanks for always being available to talk. I really feel that we did good science with all our discussions, and this has made me a better scientist. Thanks for giving me freedom to explore ideas and also for helping me keep focus.

Table of Contents

List of Tables

List of Figures

List of Appendices

1. Introduction

1.1. Background

1.1.1. Global distribution of seafloor massive sulfide deposits and global resources

Seafloor massive sulfide (SMS) deposits are accumulations of dominantly sulfide minerals that precipitate at or below the seafloor, and are associated with sites of focused seawater-derived hydrothermal fluid discharge (Figure 1.1) (Lydon, 1988; Hannington et al., 1995; Hannington, 2014). These deposits commonly occur at submarine tectonic plate boundaries (e.g., mid-ocean ridges, arc-related environments), where there is a correlation between magmatism, seismicity, faulting, and high temperature hydrothermal venting (Figure 1.2) (Hannington, 2014; Hannington et al., 2005; Lydon, 1988).

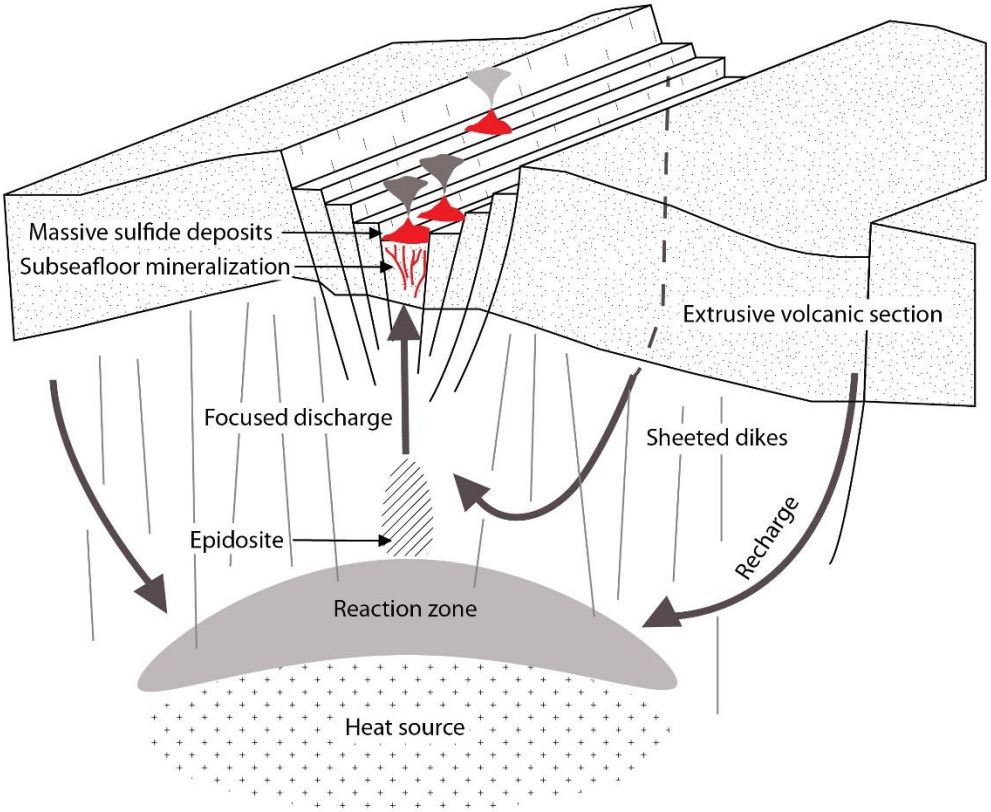

Figure 1.1. Schematic cross-section of a typical mid-ocean ridge hydrothermal system. Seawater percolates through faults and fractures (recharge), where it is heated to ~400˚C. The hot fluid leaches metals from the reaction zone and rises buoyantly to the seafloor where sulfide and sulfate minerals precipitate upon mixing with cold seawater. Modified from Alt (1995).

More than 700 sites of seafloor hydrothermal activity and associated mineralization are presently known (Figure 1.2; Beaulieu and Szanfrański, 2020). In recent years, considerable interest has arisen surrounding the economic potential and mining of SMS deposits. For example, the Solwara 1 project, located in the Bismarck Sea, within the exclusive economic zone of Papua New Guinea, has been explored and drilled in order to establish a metal resource for this deposit (Golder Associates Pty. Ltd., 2012). Furthermore, because the ocean covers 70% of the Earth's surface it has been proposed that oceanic crust likely contains a proportionally large number of these deposits (Rona, 2003; Cathles, 2011). Therefore, SMS deposits can potentially be an important source of metals. However, the topic on whether these metallic resources are worth developing for commercial use has been an ongoing debate (Van Dover et al., 2018; Hannington et al., 2011; Petersen et al., 2016; Rona, 2003). A recent resource estimate of the neovolcanic zones of the global oceans was 600 Mt of massive sulfide material (~30 Mt of copper and zinc) and suggests that these deposits are not sufficient to satisfy a growing global demand for metals (Hannington et al., 2010, 2011). For comparison, the on land Windy Craggy deposit in British Columbia alone has a tonnage of 300 Mt (Galley et al., 2007). On the other hand, only a very small percentage of the ocean floor has been mapped in resolutions necessary to produce detailed geological maps, and therefore better resource estimates. Bathymetric mapping of the seafloor also cannot discern mineralization that occurs below the seafloor.

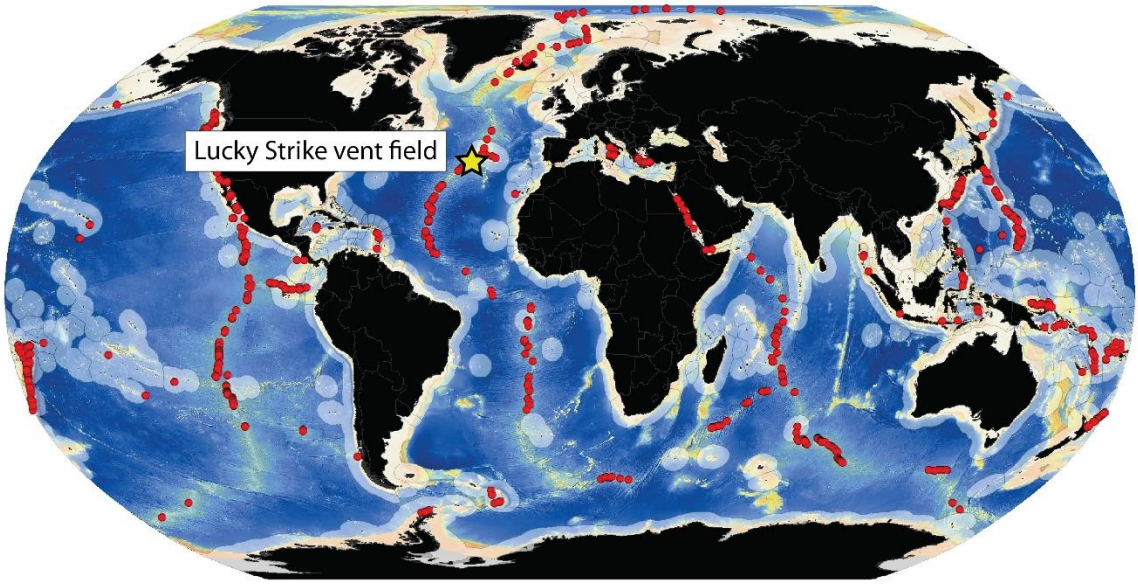

Figure 1.2. Map of the global distribution of vent fields and associated SMS deposits. The yellow star shows the location of the Lucky Strike vent field, which is the study site of this dissertation. The red dots indicate known locations of hydrothermal vent fields. White areas delineate exclusive economic zones.

Recent advances in underwater vehicle navigation and sonar technology have allowed the generation of bathymetric maps with sub-meter resolution (Ferrini et al., 2007; Wölfl et al., 2019). High-resolution bathymetry has been demonstrated to be an important tool to distinguish volcanic features in detail (Chadwick et al., 2013). Similarly, inactive seafloor massive sulfide deposits have been identified using high-resolution bathymetry, allowing the definition of significantly greater amounts of hydrothermal material than previous estimates based on visual surveys using underwater vehicles (Jamieson et al., 2014).

1.1.2. Age and rate of formation of seafloor massive sulfide deposits

Dating of SMS deposits using U-series disequilibrium methods has been undertaken at different sites on volcanic arcs (e.g., Ditchburn et al., 2012; de Ronde et al., 2005), and on mid-ocean ridges (e.g., Cherkashov et al., 2017; Jamieson et al., 2013; Lalou et al., 1990; Münch et al., 2001; Wang et al., 2012). Dating of these deposits has revealed that hydrothermal activity can be cyclic and controlled by the local tectonic/structural environment. For example, in general the lower the spreading rate of a ridge, the longer the lifespan of the hydrothermal system (Hannington, 2009). Dating of sulfide deposits coupled with tonnage estimates derived from high-resolution bathymetry, which provides a volume estimate of hydrothermal precipitates at the seafloor, has been demonstrated to be necessary for determining sulfide accumulation rates, i.e. how fast these hydrothermal deposits form (Graber et al., 2020; Jamieson et al., 2014). The study of actively forming SMS deposits provide a unique opportunity to study these accumulation rates because ages and tonnages can be determined at sites where samples and high-resolution bathymetric data have been collected. However, these accumulation rates should be considered minimum accumulation rates as sub-seafloor tonnage cannot be accounted for with high-resolution bathymetry. The estimate of accumulation rates provides a fundamental constraint for the genetic model of formation of both SMS deposits and volcanogenic massive sulfide (VMS) deposits, which represent ancient analogues of SMS deposits that are now exposed on land. Recent advances in the precision of zircon U-Pb geochronology allow for accumulation rates to be evaluated in VMS deposits (Bleeker and van Breemen, 2011; Ross et al., 2020; Manor et al., 2022).

1.1.3. Composition seafloor massive sulfide deposits

Understanding of the mineralogy and geochemical composition of SMS deposits is becoming increasingly important due to the economic potential that these deposits represent for metals like Cu, Zn, Au, and Ag (Rona, 2003; Hannington et al., 2011; Petersen et al., 2016). In addition to Cu and Zn, SMS deposits can also contain minor to trace amounts of Bi, Co, Ga, Ge, In, Mo, Sb, and Te, which have been deemed as critical metals for a transition to a low-carbon economy (Monecke et al., 2016; Natural Resources Canada, 2021). However, environmentally deleterious metals such as As, Cd, Se, and Sb can also occur as minor or trace elements within sulfide minerals (Hannington et al., 1999; Layton-Matthews et al., 2008; Martin et al., 2019; Fallon et al., 2019). Therefore, the study of the mineralogy and geochemistry of seafloor massive sulfide deposits can result in better understanding of the economic potential and environmental risks associated with the exploitation of SMS deposits. The distribution of these metals in hydrothermal deposits vary with tectonic setting and substrate and can be used to assess economic and environmental risks (Hannington et al., 2005; Monecke et al., 2016). In addition, the bulk composition of SMS deposits is one of the key variables to estimate the total metals that have been trapped as mineral precipitates within a hydrothermal system.

1.1.4. Metal fluxes and efficiency of metal precipitation of seafloor massive sulfide deposits

The study of seafloor hydrothermal systems provides an opportunity to study hydrothermal metal fluxes to the ocean, which can be significant enough to modify the chemistry of

seawater and has direct implications for biological communities that live in the proximity of hydrothermal vents (Elderfield and Schultz, 1996; Van Dover et al., 2002). Metal flux studies commonly rely on measuring vent fluid elemental or isotopic composition, temperature, and fluid flux (Elderfield and Schultz, 1996; German and Seyfried, 2014). However, to establish the chemical mass balance, a quantification of how much metal is retained at the seafloor as well as how much is ejected to the overlying water column is required. The mass of metals that is retained or trapped in the hydrothermal system is represented by the mass of the associated SMS deposit. The mass that exits the system is represented by the vent fluid composition and flux over the period in which the system has been active. The comparison of these mass fluxes are used to calculate the efficiency of metal precipitation within the hydrothermal system (Humphris and Cann, 2000; Jamieson et al., 2014). Other approaches addressing metal fluxes have been done using the geochemistry of altered epidosites and unaltered sheeted dikes, which have been recognized as being the main source of leached metals (not considering magmatic volatiles) for VMS deposits, and also probabilistic approaches (Jowitt et al., 2012; Coogan and Dosso, 2012; Patten et al., 2016a, 2017).

1.1.5. The Lucky Strike vent field

This dissertation focuses on the study of the Lucky Strike vent field as it is currently one of the most well-studied vent fields (Cannat et al., 1999; Humphris et al., 2002; Escartín et al., 2014). Seismic reflection studies have revealed the depth (~3.4 km) and extent (~7 km along axis) of the current axial magma chamber as well as major faults in the segment (Singh et al., 2006; Combier et al., 2015). Seismological work indicates that hydrothermal

circulation at Lucky Strike occurs along-axis (Crawford et al., 2013). The analysis of vent fluid composition from active vents indicate a deep and common source for all of the vent field (Charlou et al., 2000; Pester et al., 2012; Chavagnac et al., 2018). The extent of the hydrothermal deposits has been mapped using high-resolution (1 m) multibeam surveys, a near-seafloor photographic survey, and remotely operated vehicle (ROV) video footage. A limited number of rock samples have been collected to determine the elemental composition and mineralogy of the deposits (Langmuir et al., 1997; Bogdanov et al., 2006; Ondréas et al., 2009; Barreyre et al., 2012; Escartín et al., 2015, 2021). There are, however, a lack of constraints on the age, size (mass), and metal flux into and out of this system. The data collected so far at Lucky Strike can be used to constrain the evolution of the vent field and associated hydrothermal deposits. The Lucky Strike segment is located approximately 400 km southwest from the Azores archipelago and the Lucky Strike vent field is associated with a central volcano at the center of the segment (Figure 1.3A) (Escartín et al., 2015). The Lucky Strike vent field is composed of several massive sulfide mound and chimney complexes (Figure 1.3B-C).

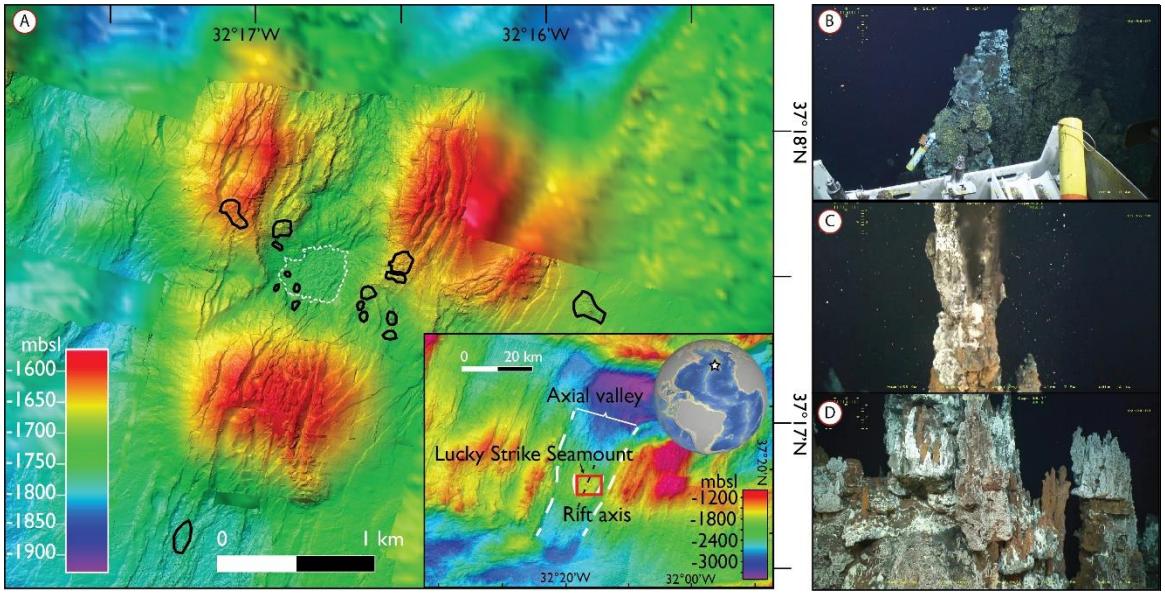

Figure 1.3. A) Bathymetric map of the center of the Lucky Strike segment that hosts the Lucky Strike vent field. Black outlines are hydrothermal vent complexes, and the dashed white outline is a fossil lava lake. The inset globe map (N. Augustin - GEOMAR) shows the location of the Lucky Strike segment with a white star. B) Massive sulfide chimney structures venting clear to gray vent fluid from the Sintra site at the Lucky Strike vent field. C) Massive sulfide chimney structure venting black fluid from the Capelinhos site. D) Chimney complex at the Capelinhos site. Bathymetry sources: Ondréas et al. (2009), Escartín et al. (2015), and Escartín et al., (2021).

1.2. Objectives

The main goal of this dissertation was to investigate the evolution and metal flux of hydrothermal venting and formation of SMS deposits within the Lucky Strike vent field. This goal was achieved by addressing the following specific questions:

- What is the age of the Lucky Strike vent field and how does it compare to other vent field in mid-ocean ridges?
- What is the mass of the hydrothermal deposits and at what rate did this material accumulate on the seafloor? Can we extrapolate calculated rates to ancient volcanogenic massive sulfide deposits?

- What are the variations in mineralogy and chemical composition of the hydrothermal deposits at Lucky Strike? Are there variations that can be linked to specific geological settings or processes? What is the influence of enriched mid-ocean basalt (E-MORB) substrate on the composition of Lucky Strike?
- What is the efficiency of metal precipitation at Lucky Strike? How does it compare to other sites, and what controls variability in precipitation efficiency?
- What are the optimal conditions for trapping metals in a seafloor hydrothermal system?
- Are certain fault interactions more favourable to focus fluid flow and therefore the formation of hydrothermal deposits?

These questions will be addressed through the following objectives:

- Determine the age of the seafloor massive sulfide deposits to understand the duration of hydrothermal venting.
- Calculate the mass of hydrothermal precipitates that have accumulated at the seafloor using high-resolution bathymetric data.
- Determine the rate of accumulation of seafloor massive sulfide deposits and compare with other seafloor sites as well as with volcanogenic massive sulfide deposits.
- Characterize the mineralogy and composition of hydrothermal deposits at Lucky Strike.
- Evaluate the effect that substrate composition has on the geochemistry and mineralogy of associated massive sulfide deposits on the Mid-Atlantic Ridge.

- Determine the controls on the sulfur isotope composition of sulfide minerals at the Lucky Strike vent field.
- Calculate the efficiency of metal precipitation for Cu, Zn, Fe, Mn, and Si by integrating all available datasets at Lucky Strike and test if solubility is a major control on efficiency.
- Determine the structural controls on the location of the hydrothermal deposits and venting.

The integration of geochronology, vent fluid chemistry, sulfide mineralogy and high-resolution bathymetry has resulted in a more detailed understanding of the evolution and metal flux of the hydrothermal system and associated massive sulfide deposits at the Lucky Strike vent field.

1.3. Importance of research

The integration of high-resolution bathymetry, vent fluid chemistry, geochronology, mineralogy, geochemical analyses, and sulfur isotope data has advanced our understanding of SMS deposit formation, and in particular how metals are concentrated over the life cycle of an SMS deposit and how long deposits remain hydrothermally active. With the use of high-resolution bathymetry, estimates of the tonnage of hydrothermal precipitates on the seafloor can be performed. This provides an assessment technique to calculate SMS deposit tonnage at a time when the economic feasibility of extracting metals from SMS deposits is being considered. When deposit tonnage estimates are combined with vent fluid chemistry and fluid flux estimates, geochronology, and geochemical analysis, it allows for the efficiency of metal deposition to be calculated. Previous estimates on the depositional

efficiency of metals in SMS deposits have been highly variable and generally thought to be low, especially in sediment-free oceanic ridges (Converse et al., 1984; Humphris and Cann, 2000; Cathles, 2011; Hannington, 2011; Jowitt et al., 2012; Jamieson et al., 2014; Patten et al., 2016b, 2017). Moreover, evaluating the flux of metals and fluid provides insights into the flux of metals to the wider ocean. The application of geochronology in SMS deposits is also important for testing if fluid flux is continuous or if it occurs in discrete pulsed events, if enough samples are collected. Finally, data obtained in this study have direct implications when applied to on land VMS deposits, providing information on the duration of deposit formation and the processes that are critical for the concentration of metals in economic quantities.

1.4. Organization of dissertation

The remainder of this dissertation is subdivided into four Chapters, each addressing a different aspect of hydrothermal processes at the Lucky Strike vent site.

Chapter 2: **"Age and rate of accumulation of metal-rich hydrothermal deposits on the seafloor: the Lucky Strike vent field, Mid-Atlantic Ridge".** This Chapter assesses the age and size of the hydrothermal deposits at Lucky Strike. Using these data, the rate at which deposits on the surface of the Lucky Strike vent field are estimated. Data in this study are compared to other well-characterized deposits on the seafloor.

Chapter 3: "Effects of substrate composition and subsurface fluid pathways on the geochemistry of seafloor hydrothermal deposits at the Lucky Strike vent field, Mid-Atlantic Ridge". The mineralogy, bulk composition, and the *in situ* sulfur isotopic

compositions of hydrothermal deposits at Lucky Strike are presented. The differences in bulk composition and sulfur isotopic compositions within the vent field are investigated by comparing the Capelinhos vent site, located 1.4 km from the main ridge axis, with the hydrothermal deposits located at the ridge axis. The main on axis field and Capelinhos have slightly different geological settings (and fluid pathways), which makes it the ideal location to ascertain if spatial variations exist in fluid flow regimes, metal enrichment signatures and sulfur isotope systematics with distance from the ridge axis. The temporal differences in composition, using ages of the deposits from Chapter 2, are also investigated. The bulk composition of hydrothermal deposits from Lucky Strike and the nearby Menez Gwen hydrothermal vent field, which are both in close proximity to the Azores hot spot and hosted in enriched mid-ocean ridge basalts (E-MORB), are compared to hydrothermal sites that are distal to the hot spot and are hosted in different substrates. These comparisons are used to investigate the influence of the Azores hotspot and composition of substrate on the geochemistry of hydrothermal precipitates at Lucky Strike.

Chapter 4: "Efficiency of metal precipitation at seafloor hydrothermal vents". In this chapter, the chemical mass balance of the Lucky Strike vent field is estimated. The tonnage estimates calculated in chapter 2 are used to estimate the amount of metal that is trapped in the deposit relative to the amount that is lost in the hydrothermal plume. With the determined mass balances, the efficiency of precipitation from metals in the hydrothermal system can be determined, which is a measure of how much metal is being retained as an SMS deposit versus how much is "lost" to the hydrothermal plume. These data provide new insights into the flux of metals into the ocean, which has direct implications for ore forming processes at the seafloor and the flux of metals into the ocean.

Chapter 5: "Investigating brittle deformation and rifting processes at the Lucky Strike hydrothermal field, Mid-Atlantic Ridge, from quantitative fault analysis derived from high-resolution bathymetry". In this chapter, a methodology is presented to extract geological information (strike, dip, fault displacement) from high-resolution bathymetric datasets by using the 3D modelling and visualization software *Leapfrog Geo*. The use of bathymetric data has also been applied to gain information on the link between faulting, hydrothermal venting, and SMS deposit formation (Rona and Clague, 1989; Kleinrock and Humphris, 1996; Graber et al., 2020; Dyriw et al., 2021), as well as to define controls on the location of volcanic eruptions (Anderson et al., 2016). These previous studies have used lineaments to interpret faulting without considering the amount of dip of these faults, which is key to understand the true geometry of faulting

Chapter 6: Synthesis and Conclusions. The main findings of this dissertation are summarized, and suggestions are recommended for future work, and the implications for the exploration of seafloor massive sulfide deposits and for on land volcanogenic massive sulfide deposits are stated.

1.5. Co-authorship statement

This dissertation is presented in manuscript format. The manuscripts are in various stages of the publication process for peer-reviewed journals. The manuscripts are chapters 2, 3, and 4, for all of these the author of this thesis is the main researcher.

Chapter 2: "Age and rate of accumulation of metal-rich hydrothermal deposits on the seafloor: the Lucky Strike vent field, Mid-Atlantic Ridge". This research has been published in the *Journal of Geophysical Research: Solid Earth*. The author of this

dissertation is the main contributor of this manuscript in conceptualization, methodology, data curation, and writing of the original draft. Dr. John Jamieson was the supervisor for this manuscript, provided funding, aided in the conceptualization of the study, and reviewed and edited the manuscript. Dr. Mathilde Cannat contributed with sampling, data curation, and reviewed and edited the manuscript. Dr. Javier Escartín contributed with data curation and reviewed and edited the manuscript. Dr. Thibaut Barreyre contributed with data curation and reviewed and edited the manuscript.

Chapter 3: "Effects of substrate composition and subsurface fluid pathways on the geochemistry of seafloor hydrothermal deposits at the Lucky Strike vent field, Mid-Atlantic Ridge". This manuscript has been published in the journal *Geochemistry, Geophysics, Geosystems*. The author of this dissertation is the principal contributor of this manuscript in conceptualization, methodology, data curation, and writing of the original draft. Dr. John Jamieson supervised, provided funding, aided in the conceptualization of the study, and reviewed and edited the manuscript. Dr. Mathilde Cannat contributed with sampling, data curation, and reviewed and edited the manuscript. Dr. Javier Escartín contributed with data curation and reviewed and edited the manuscript. Dr. Thibaut Barreyre contributed with data curation and reviewed and edited the manuscript.

Chapter 4, "Efficiency of metal precipitation at seafloor hydrothermal vents". This research will be submitted to *Geology*. The author of this dissertation is the principal contributor of this manuscript in conceptualization, methodology, data curation, and writing of the original draft. Dr. John Jamieson supervised, provided funding, aided in the conceptualization of the study, and reviewed and edited the manuscript. Dr. Thibaut Barreyre contributed by determining heat flux estimates at Lucky Strike, as well as aided

in data curation, and reviewed and edited the manuscript. Dr. Mathilde Cannat reviewed and edited the manuscript. Dr. Javier Escartín reviewed and edited the manuscript.

Chapter 5, "Investigating brittle deformation and rifting processes at the Lucky Strike hydrothermal field, Mid-Atlantic Ridge, from quantitative fault analysis derived from high-resolution bathymetry". The author of this dissertation is the principal contributor of this manuscript in conceptualization, methodology, data curation, and writing of the original draft. Dr. John Jamieson supervised, provided funding, aided in the conceptualization of the study, and reviewed and edited the manuscript.

1.6. References

Alt, J.C., 1995, Sub-seafloor processes in Mid-Ocean Ridge hydrothermal systems, *in* Humphris, S.E., Zierenberg, R.A., Mullineaux, S., and Thomson, R.E. eds., Seafloor hydrothermal systems: Physical, chemical, biological, and geological interactions, Geophysical Monograph, American Geophysical Union, p. 85–114.

Anderson, M.O., Hannington, M.D., Haase, K., Schwarz-Schampera, U., Augustin, N., McConachy, T.F., and Allen, K., 2016, Tectonic focusing of voluminous basaltic eruptions in magma-deficient backarc rifts: Earth and Planetary Science Letters, v. 440, p. 43–55, doi: 10.1016/j.epsl.2016.02.002.

Barreyre, T., Escartín, J., Garcia, R., Cannat, M., Mittelstaedt, E., and Prados, R., 2012, Structure, temporal evolution, and heat flux estimates from the Lucky Strike deep-sea hydrothermal field derived from seafloor image mosaics: Geochemistry, Geophysics, Geosystems, v. 13, p. 1–29, doi: 10.1029/2011GC003990.

Beaulieu, S.E., and Szafrański, K.M., 2020, InterRidge Global Database of Active Submarine Hydrothermal Vent Fields Version 3.4.: PANGAEA, doi: https://doi.org/10.1594/PANGAEA.917894.

Bleeker, W., and van Breemen, O., 2011, New geochronological, stratigraphic, and structural observations on the Kidd-Munro assemblage and the terrane architecture of the south-central Abitibi greenstone belt, Superior craton, Canada, in Results from the Targeted Geoscience Initiative III Kidd-Munro Project, Ontario Geological Survey, v. 6258, p. 142.

Bogdanov, Y.A., Lein, A.Y., Sagalevich, A.M., Ul'yanov, A.A., Dorofeev, S.A., and Ul'yanova, N. V., 2006, Hydrothermal sulfide deposits of the Lucky Strike vent field,

Mid-Atlantic Ridge: Geochemistry International, v. 44, p. 403–418, doi: 10.1134/S0016702906040070.

Cannat, M., Briais, A., Deplus, C., Escartín, J., Georgen, J., Lin, J., Mercouriev, S., Meyzen, C., Muller, M., Pouliquen, G., Rabain, A., and Da Silva, P., 1999, Mid-Atlantic Ridge-Azores hotspot interactions: Along-axis migration of a hotspot-derived event of enhanced magmatism 10 to 4 Ma ago: Earth and Planetary Science Letters, v. 173, p. 257–269, doi: 10.1016/S0012-821X(99)00234-4.

Cathles, L.M., 2011, What processes at mid-ocean ridges tell us about volcanogenic massive sulfide deposits: Mineralium Deposita, v. 46, p. 639–657, doi: 10.1007/s00126-010-0292-9.

Chadwick, W.W., Clague, D.A., Embley, R.W., Perfit, M.R., Butterfield, D.A., Caress, D.W., Paduan, J.B., Martin, J.F., Sasnett, P., Merle, S.G., and Bobbitt, A.M., 2013, The 1998 eruption of Axial Seamount: New insights on submarine lava flow emplacement from high-resolution mapping: Geochemistry, Geophysics, Geosystems, v. 14, p. 3939–3968, doi: 10.1002/ggge.20202.

Charlou, J.L., Donval, J.P., Douville, E., Jean-Baptiste, P., Radford-Knoery, J., Fouquet, Y., Dapoigny, A., and Stievenard, M., 2000, Compared geochemical signatures and the evolution of Menez Gwen (35°50N) and Lucky Strike (37°17N) hydrothermal fluids, south of the Azores Triple Junction on the Mid-Atlantic Ridge: Chemical Geology, v. 171, p. 49–75, doi: 10.1016/S0009-2541(00)00244-8.

Chavagnac, V., Leleu, T., Fontaine, F., Cannat, M., Ceuleneer, G., and Castillo, A., 2018, Spatial Variations in Vent Chemistry at the Lucky Strike Hydrothermal Field, Mid-Atlantic Ridge (37°N): Updates for Sub-seafloor Flow Geometry From the Newly Discovered Capelinhos Vent: Geochemistry, Geophysics, Geosystems, v. 19, p. 4444–4458, doi: 10.1029/2018GC007765.

Cherkashov, G., Kuznetsov, V., Kuksa, K., Tabuns, E., Maksimov, F., and Bel'tenev, V., 2017, Sulfide geochronology along the Northern Equatorial Mid-Atlantic Ridge: Ore Geology Reviews, v. 87, p. 147–154, doi: 10.1016/j.oregeorev.2016.10.015.

Combier, V., Seher, T., Singh, S.C., Crawford, W.C., Cannat, M., Escartín, J., and Dusunur, D., 2015, Three-dimensional geometry of axial magma chamber roof and faults at Lucky Strike volcano on the Mid-Atlantic Ridge: Journal of Geophysical Research : Solid Earth, v. 121, p. 6386–6403, doi: 10.1002/2015JB012282.

Converse, D.R., Holland, H.D., and Edmond, J.M., 1984, Flow rates in the axial hot springs of the East Pacific Rise (21°N): implications for the heat budget and the formation of massive sulfide deposits: Earth and Planetary Science Letters, v. 69, p. 159–175.

Coogan, L.A., and Dosso, S., 2012, An internally consistent, probabilistic, determination of ridge-axis hydrothermal fluxes from basalt-hosted systems: Earth and Planetary Science Letters, v. 323–324, p. 92–101, doi: 10.1016/j.epsl.2012.01.017.

Crawford, W.C., Rai, A., Singh, S.C., Cannat, M., Escartín, J., Wang, H., Daniel, R., and

Combier, V., 2013, Hydrothermal seismicity beneath the summit of Lucky Strike volcano, Mid-Atlantic Ridge: Earth and Planetary Science Letters, v. 373, p. 118–128, doi: 10.1016/j.epsl.2013.04.028.

Ditchburn, R.G., de Ronde, C.E.J., and Barry, B.J., 2012, Radiometric dating of volcanogenic massive sulfides and associated iron oxide crusts with an emphasis on 226Ra/Ba and 228Ra/226Ra in volcanic and hydrothermal processes at intraoceanic Arcs: Economic Geology, v. 107, p. 1635–1648, doi: 10.2113/econgeo.107.8.1635.

Van Dover, C.L., Arnaud-Haond, S., Gianni, M., Helmreich, S., Huber, J.A., Jaeckel, A.L., Metaxas, A., Pendleton, L.H., Petersen, S., Ramirez-Llodra, E., Steinberg, P.E., Tunnicliffe, V., and Yamamoto, H., 2018, Scientific Rationale and International Obligations for Protection of Active Hydrothermal Vent Ecosystems From Deep-Sea Mining: Marine Policy, v. 90, p. 20–28, doi: 10.1016/j.marpol.2018.01.020.

Van Dover, C.L., German, C.R., Speer, K.G., Parson, L.M., and Vrijenhoek, R.C., 2002, Evolution and biogeography of deep-sea vent and seep invertebrates: Science, v. 295, p. 1253–1257, doi: 10.1126/science.1067361.

Dyriw, N.J., Bryan, S.E., Richards, S.W., Parianos, J.M., Arculus, R.J., and Gust, D.A., 2021, Morphotectonic Analysis of the East Manus Basin, Papua New Guinea: Frontiers in Earth Science, v. 8, p. 1–23, doi: 10.3389/feart.2020.596727.

Elderfield, H., and Schultz, A., 1996, Mid-Ocean Ridge hydrothermal fluxes and the chemical composition of the ocean: Ann. Rev. Earth Planet. Sci., v. 24, p. 191–224.

Escartín, J., Barreyre, T., Cannat, M., Garcia, R., Gracias, N., Deschamps, A., Salocchi, A., Sarradin, P.M., and Ballu, V., 2015, Hydrothermal activity along the slow-spreading Lucky Strike ridge segment (Mid-Atlantic Ridge): Distribution, heatflux, and geological controls: Earth and Planetary Science Letters, v. 431, p. 173–185, doi: 10.1016/j.epsl.2015.09.025.

Escartín, J., Cannat, M., and Deschamps, A., 2021, Microbathymetry from AUV and ROV Surveys (MOMARETO'06, MOMAR'08-Leg1 and BATHYLUCK'09 cruises) along the Lucky Strike ridge segment (Mid Atlantic Ridge): SEANOE, doi: 10.17882/80574.

Escartín, J., Soule, S.A., Cannat, M., Fornari, D.J., Düşünür, D., and Garcia, R., 2014, Lucky Strike seamount: Implications for the emplacement and rifting of segment-centered volcanoes at slow spreading mid-ocean ridges: Geochemistry, Geophysics, Geosystems, v. 15, p. 4157–4179, doi: 10.1002/2014GC005563.Received.

Fallon, E.K., Frische, M., Petersen, S., Brooker, R.A., and Scott, T.B., 2019, Geological, mineralogical and textural impacts on the distribution of environmentally toxic trace elements in seafloor massive sulfide occurrences: Minerals, v. 9, p. 1–53, doi: 10.3390/min9030162.

Ferrini, V.L., Fornari, D.J., Shank, T.M., Kinsey, J.C., Tivey, M.A., Soule, S.A., Carbotte, S.M., Whitcomb, L.L., Yoerger, D., and Howland, J., 2007, Submeter bathymetric

mapping of volcanic and hydrothermal features on the East Pacific Rise crest at 9°500N: Geochemistry, Geophysics, Geosystems, v. 8, doi: 10.1029/2006GC001333.

Galley, A.G., Hannington, M.D., and Jonasson, I.R., 2007, Volcanogenic Massive Sulphide Deposits: Mineral Deposits of Canada: A Synthesis of Major Deposit-Types, District Metallogeny, the Evolution of Geological Provinces, and Exploration Methods, p. 141–161.

German, C.R., and Seyfried, W.E., 2014, Hydrothermal Processes: Elsevier Ltd., v. 8, 191–233 p., doi: 10.1016/B978-0-08-095975-7.00607-0.

Golder Associates Pty. Ltd., 2012, Mineral resource estimate, Solwara projet, Bismarck Sea, PNG: Technical Report compiled under NI43-101.:

Graber, S., Petersen, S., Yeo, I., Szitkar, F., Klischies, M., Jamieson, J.W., Hannington, M.D., Rothenbeck, M., Wenzlaff, E., Augustin, N., and Stobbs, I., 2020, Structural Control, Evolution, and Accumulation Rates of Massive Sulfides in the TAG Hydrothermal Field: Geochemistry, Geophysics, Geosystems, doi: 10.1029/2020GC009185.

Hannington, M.D., 2009, Modern submarine hydrothermal systems - a global perspective on distribution, size and tectonic settings, *in* Cousens, B. and Piercey, S.J. eds., Submarine volcanism and mineralization: Modern through ancient, Geological Association of Canada, Mineral Deposits Division, p. 91–146.

Hannington, M.D., 2014, Volcanogenic Massive Sulfide Deposits: Treatise on Geochemistry: Second Edition, v. 13, p. 463–488, doi: 10.1016/B978-0-08-095975-7.01120-7.

Hannington, M.D., Jamieson, J., Monecke, T., and Petersen, S., 2010, Modern Sea-Floor Massive Sulfides and Base Metal Resources: Toward an Estimate of Global Sea-Floor Massive Sulfide Potential: Society of Economic Geologists Special Publication 15, p. 317–338, file://localhost/Users/jescartin/WORK/Referencias/pdfs/Hannington2010.pdf.

Hannington, M.D., Jamieson, J., Monecke, T., Petersen, S., and Beaulieu, S., 2011, The abundance of seafloor massive sulfide deposits: Geology, v. 39, p. 1155–1158, doi: 10.1130/G32468.1.

Hannington, M.D., Jonasson, I.R., Herzig, P.M., and Petersen, S., 1995, Physical and chemical processes of seafloor mineralization at mid-ocean ridges, *in* Humphris, S.E., Zierenberg, R.A., Mullineaux, S., and Thomson, R.E. eds., Seafloor hydrothermal systems: Physical, chemical, biological, and geological interactions, Geophysical Monograph, American Geophysical Union, p. 115–157, doi: 10.1029/GM091p0115.

Hannington, M.D., Poulsen, K.H., Thompson, J.F.., and Sillitoe, R.H., 1999, Volcanogenic gold in the massive sulfide environment, *in* Barrie, C.T. and Hannington, M.D. eds., Volcanic-associated massive sulfide deposits: Processes and examples in modern and ancient settings, Reviews in Economic Geology, v. 8, p. 319–350.

Hannington, M.D., de Ronde, C.E.J., and Petersen, S., 2005, Sea-Floor Tectonics and Submarine Hydrothermal Systems: Economic Geology, v. 100th Anni, p. 111–141.

Humphris, S.E., and Cann, J.R., 2000, Constraints on the energy and chemical balances of the modern TAG and ancient Cyprus seafloor sulfide deposits: Journal of Geophysical Research, v. 105, p. 28477–28488.

Humphris, S.E., Fornari, D.J., Scheirer, D.S., German, C.R., and Parson, L.M., 2002, Geotectonic setting of hydrothermal activity on the summit of Lucky Strike Seamount (37°17'N, Mid-Atlantic Ridge): Geochemistry, Geophysics, Geosystems, v. 3, p. 1–24, doi: 10.1029/2001GC000284.

Jamieson, J.W., Clague, D.A., and Hannington, M.D., 2014, Hydrothermal sulfide accumulation along the Endeavour Segment , Juan de Fuca Ridge: Earth and Planetary Science Letters, v. 395, p. 136–148.

Jamieson, J.W., Hannington, M.D., Clague, D.A., Kelley, D.S., Delaney, J.R., Holden, J.F., Tivey, M.K., and Kimpe, L.E., 2013, Sulfide geochronology along the Endeavour Segment of the Juan de Fuca Ridge: Geochemistry, Geophysics, Geosystems, v. 14, p. 2084–2099, doi: 10.1002/ggge.20133.

Jowitt, S.M., Jenkin, G.R.T., Coogan, L.A., and Naden, J., 2012, Quantifying the release of base metals from source rocks for volcanogenic massive sulfide deposits : Effects of protolith composition and alteration mineralogy: Journal of Geochemical Exploration, v. 118, p. 47–59, doi: 10.1016/j.gexplo.2012.04.005.

Kleinrock, M.C., and Humphris, S.E., 1996, Structural control on sea-floor hydrothermal activity at theTAG active mound: Nature, v. 382, p. 149–153.

Lalou, C., Thompson, G., Arnold, M., Brichet, E., Druffel, E., and Rona, P.A., 1990, Geochronology of TAG and Snakepit hydrothermal fields, Mid-Atlantic Ridge: witness to a long and complex hydrothermal history: Earth and Planetary Science Letters, v. 97, p. 113–128.

Langmuir, C., Humphris, S., Fornari, D., Van Dover, C., Von Damm, K., Tivey, M.K., Colodner, D., Charlou, J.-L., Desonie, D., Wilson, C., Fouquet, Y., Klinkhammer, G., and Bougault, H., 1997, Hydrothermal vents near a mantle hot spot: the Lucky Strike vent field at 37°N on the Mid-Atlantic Ridge: Earth and Planetary Science Letters, v. 148, p. 69–91, doi: 10.1016/S0012-821X(97)00027-7.

Layton-Matthews, D., Peter, J.M., Scott, S.D., and Leybourne, M.I., 2008, Distribution , Mineralogy , and Geochemistry of Selenium in Felsic Volcanic-Hosted Massive Sulfide Deposits of the Finlayson Lake District , Yukon Territory , Canada: Economic Geology, v. 103, p. 61–88.

Lydon, J.W., 1988, Ore deposit models 14. Volcanogenic massive sulphide deposits. Part 2: genetic models: Geoscience Canada, v. 15, p. 43–65.

Manor, M.J., Piercey, S.J., Wall, C.J., and Denisová, N., 2022, High precision CA-ID-

TIMS U-Pb zircon geochronology of felsic rocks in the Finlayson Lake VMS district, Yukon : Linking Paleozoic basin-scale accumulation rates to the occurrence of sub-seafloor replacement-style mineralization: Economic Geology,.

Martin, A.J., Keith, M., McDonald, I., Haase, K.M., McFall, K.A., Klemd, R., and MacLeod, C.J., 2019, Trace element systematics and ore-forming processes in mafic VMS deposits: Evidence from the Troodos ophiolite, Cyprus: Ore Geology Reviews, v. 106, p. 205–225, doi: 10.1016/j.oregeorev.2019.01.024.

Mayer, L., Jakobsson, M., Allen, G., Dorschel, B., Falconer, R., Ferrini, V., Lamarche, G., Snaith, H., and Weatherall, P., 2018, The Nippon Foundation-GEBCO seabed 2030 project: The quest to see the world's oceans completely mapped by 2030: Geosciences (Switzerland), v. 8, doi: 10.3390/geosciences8020063.

Monecke, T., Petersen, S., Hannington, M.D., Grant, H., and Samson, I.M., 2016, The Minor Element Endowment of Modern Sea-Floor Massive Sulfi des and Comparison with Deposits Hosted in Ancient Volcanic Successions, *in* Verplanck, P.L. and Hitzman, M.W. eds., Rare earth and critical elements in ore deposits, Littleton, Colorado, Reviews in Economic Geology, v. 18, p. 245–306.

Münch, U., Lalou, C., Halbach, P., and Fujimoto, H., 2001, Relict hydrothermal events along the super-slow Southwest Indian spreading ridge near 63°56′E- Mineralogy, chemistry and chronology of sulfide samples: Chemical Geology, v. 177, p. 341–349, doi: 10.1016/S0009-2541(00)00418-6.

Natural Resources, C., 2021, Critical metals:, www.nrcan.gc.ca/our-natural-resources/minerals-mining/critical-minerals/23414.

Ondréas, H., Cannat, M., Fouquet, Y., Normand, A., Sarradin, P.M., and Sarrazin, J., 2009, Recent volcanic events and the distribution of hydrothermal venting at the Lucky Strike hydrothermal field, Mid-Atlantic Ridge: Geochemistry, Geophysics, Geosystems, v. 10, doi: 10.1029/2008GC002171.

Patten, C.G.C., Pitcairn, I.K., and Teagle, D.A.H., 2017, Hydrothermal mobilisation of Au and other metals in supra-subduction oceanic crust : Insights from the Troodos ophiolite: Ore Geology Reviews, v. 86, p. 487–508, doi: 10.1016/j.oregeorev.2017.02.019.

Patten, C.G.C., Pitcairn, I.K., Teagle, D.A.H., and Harris, M., 2016a, Mobility of Au and related elements during the hydrothermal alteration of the oceanic crust : implications for the sources of metals in VMS deposits: Mineralium Deposita, v. 51, p. 179–200, doi: 10.1007/s00126-015-0598-8.

Patten, C.G.C., Pitcairn, I.K., Teagle, D.A.H., and Harris, M., 2016b, Sulphide mineral evolution and metal mobility during alteration of the oceanic crust: Insights from ODP Hole 1256D: Geochimica et Cosmochimica Acta, v. 193, p. 132–159, doi: 10.1016/j.gca.2016.08.009.

Pester, N.J., Reeves, E.P., Rough, M.E., Ding, K., Seewald, J.S., and Seyfried, W.E., 2012,

Sub-seafloor phase equilibria in high-temperature hydrothermal fluids of the Lucky Strike Seamount: Geochimica et Cosmochimica Acta, v. 90, p. 303–322, doi: 10.1016/j.gca.2012.05.018.

Petersen, S., Krätschell, A., Augustin, N., Jamieson, J., Hein, J.R., and Hannington, M.D., 2016, News from the seabed – Geological characteristics and resource potential of deep-sea mineral resources: Marine Policy, v. 70, p. 175–187, doi: 10.1016/j.marpol.2016.03.012.

Petersen, S., Lehrmann, B., and Murton, B.J., 2018, Modern Seafloor Hydrothermal Systems: New Perspectives on Ancient Ore-Forming Processes: Elements, v. 14, p. 307–312, doi: 10.2138/gselements.14.5.307.

Rona, P.A., 2003, Resources of the sea floor: Science, v. 299, p. 673–674, doi: 10.1126/science.1080679.

Rona, P.A., and Clague, D.A., 1989, Geologic controls of hydrothermal discharge on the northern Gorda Ridge: Geology, v. 17, p. 1097–1101, doi: 10.1130/0091-7613(1989)017<1097:GCOHDO>2.3.CO;2.

de Ronde, C.E.J., Hannington, M.D., Stoffers, P., Wright, I.C., Ditchburn, R.G., Reyes, A.G., Baker, E.T., Massoth, G.J., Lupton, J.E., Walker, S.L., Greene, R.R., Soong, C.W.R., Ishibashi, J., and Lebon, G.T., 2005, Evolution of a Submarine Magmatic-Hydrothermal System : Brothers Volcano, Southern Kermadec Arc, New Zealand: Economic Geology, v. 100, p. 1097–1133.

Ross, P.-S., Boulerice, A., Mercier-Langevin, P., and McNicoll, V., 2020, Volcanology, chemo-stratigraphy, geochronology, hydrothermal alteration and VMS potential of the Lemoine Member of the Waconichi Formation, Chibougamau district, Abitibi greenstone belt, Québec: Mineralium Deposita, v. 55, p. 21–46, doi: 10.1007/s00126-019-00884-6.

Singh, S.C., Crawford, W.C., Carton, H., Seher, T., Combier, V., Cannat, M., Canales, J.P., Düsünür, D., Escartín, J., and Miranda, J.M., 2006, Discovery of a magma chamber and faults beneath a Mid-Atlantic Ridge hydrothermal field: Nature, v. 442, p. 1029–1032, doi: 10.1038/nature05105.

Wang, Y., Han, X., Jin, X., Qiu, Z., Ma, Z., and Yang, H., 2012, Hydrothermal Activity Events at Kairei Field, Central Indian Ridge 25°S: Resource Geology, v. 62, p. 208–214, doi: 10.1111/j.1751-3928.2012.00189.x.

Wölfl, A.C., Snaith, H., Amirebrahimi, S., Devey, C.W., Dorschel, B., Ferrini, V., Huvenne, V.A.I., Jakobsson, M., Jencks, J., Johnston, G., Lamarche, G., Mayer, L., Millar, D., Pedersen, T.H., et al., 2019, Seafloor mapping - The challenge of a truly global ocean bathymetry: Frontiers in Marine Science, v. 6, p. 1–16, doi: 10.3389/fmars.2019.00283.

2. Age and rate of accumulation of metal-rich hydrothermal deposits on the seafloor: the Lucky Strike Vent Field, Mid-Atlantic Ridge

2.1. Abstract

Hydrothermal venting at the Lucky Strike hydrothermal field, located on the Mid-Atlantic Ridge, is associated with faulting linked to the tectonic dismemberment of a central axial volcano. Radium-226/Ba dating of hydrothermal barite indicates that hydrothermal venting is at least 6,600 years old, and that Lucky Strike is one of the youngest known vent fields on the Mid-Atlantic Ridge, which typically have ages exceeding 20 ka. Deposit volume calculations indicate that the total accumulated mass of the hydrothermal deposits on the seafloor at Lucky Strike is ~1.3 ± 0.2 Mt, and that this mass accumulated at a maximum average rate of 194 ± 28 t/yr. This accumulation rate is comparable to other well characterized mid-ocean ridge hydrothermal sites, such as TAG and Endeavour, but at Lucky Strike is concentrated within a relatively small area of <2.5 km^2.

2.2. Introduction

Hydrothermal deposits form at and below the ocean floor due to sub-seafloor hydrothermal circulation associated with magmatism and faulting (Hannington, 2014, and references therein; Lowell et al. 1995). The ages of these deposits provide insights into the longevity and history of hydrothermal venting and rates at which these deposits form (Jamieson et al., 2014; Lalou et al. 1990). Several hydrothermal sites on volcanic arcs (e.g., de Ronde et al., 2005; Ditchburn et al., 2012) and mid-ocean ridges (MORs) (e.g., Cherkashov et al., 2017; Jamieson et al., 2013; Lalou et al., 1990; Lalou and Brichet, 1982; Münch et al., 2001; Wang et al., 2012) have been dated using U-series dating techniques. Vent fluid flux,

temperatures, and compositions can be used to estimate chemical mass fluxes and deposit growth rates at time scales applicable to human observations (e.g., ranging from direct observation and sampling over seconds to minutes to repeat sampling and observations over years or decades; Barreyre et al., 2012; Lowell et al., 1995; Mittelstaedt et al., 2012; and references therein). However, to determine average rates of accumulation over the lifespan of a vent field, accurate estimates of deposit size are also required, together with age constraints. We define accumulation rate here as the total amount of hydrothermal deposition on the seafloor (measured as volume and converted to mass using estimated average density) relative to the oldest age determined for the site. This is therefore an average rate over the documented lifespan of the system and does not consider that instantaneous rates may be variable over the lifespan of the hydrothermal system (Lalou et al., 1990), nor does it consider sub-seafloor deposition.

Of the seafloor hydrothermal deposits on mid-ocean ridges that have been dated thus far, only the Endeavour and TAG vent fields have been mapped at a high enough resolution to accurately determine the amount of hydrothermal material deposited on the seafloor (Graber et al., 2020; Jamieson et al., 2014). At Endeavour, 1.2 Mt of hydrothermal sulfide/sulfate/silica material accumulated over ~3,000 years, at an average rate of 400 t/yr (Jamieson et al., 2014). At TAG, 29 Mt of material accumulated over 100,000 years at an average rate of 300 t/yr (Graber et al., 2020). However, at TAG, the dating work by Lalou et al. (1990) suggests that active venting occurred over only 20,000 years of the 100,000 year lifespan of the field, indicating that average accumulation rates during discontinuous periods of activity may have been as high as 1,500 t/yr.

The Lucky Strike hydrothermal vent field, located on the Mid-Atlantic Ridge (MAR), is situated on an active axial volcano and is therefore considered to be young, relative to TAG and other MAR-hosted hydrothermal vent fields, which have ages of up to 230 ka (Cherkashov et al., 2017). In this study, we use a similar approach to Jamieson et al. (2014), and report results from ^{226}Ra/Ba dating of hydrothermal barite at Lucky Strike to constrain the history and evolution of the vent field, and mass accumulation rates. We couple these results with deposit tonnage estimates derived from high-resolution (~1 m) bathymetric data to determine the rates of deposit formation. The results of this study provide insights into formation rates for ancient volcanogenic massive sulfide (VMS) deposits.

2.3. Geological setting

The Lucky Strike segment hosts a prominent axial volcano, named the Lucky Strike Seamount that rises up from the central part of the segment. Recent episodes of volcanism produced two volcanic edifices that are aligned along the ridge axis and which are separated by a flat depression that is interpreted to be a remnant fossil lava lake (Figure 2.1A; Humphris et al., 2002; Ondréas et al., 2009). Both volcanic edifices are now cut by a series of ridge-parallel normal faults, with the older, northern, volcanic edifice exhibiting a higher degree of rifting than the younger, southern, volcanic edifice (Humphris et al., 2002). The remains of the fossil lava lake overprint, and are therefore younger, than the faults (Figure 2.1A).

Hydrothermal materials were first recovered in 1992 via dredging (Langmuir et al., 1992), and mounds and chimneys were located in 1993 using the human occupied vehicle (HOV) Alvin (Langmuir et al., 1997). This early exploration work was followed by additional

dives in 1994 using the HOV Nautile, and by autonomous underwater vehicle (AUV) and remotely operated vehicle (ROV) bathymetric mapping coupled with photomosaic imaging (Figure 2.1B and 1C; Barreyre et al., 2012; Fouquet et al., 1995; Langmuir et al., 1997; Ondréas et al., 2009). Hydrothermal venting occurs predominantly around the edges of the fossil lava lake, in clusters such as Sintra, Tour Eiffel, Y3, and others (Figure 2.1 and 2.2). Venting is interpreted to be genetically associated with an underlying axial magma chamber and is spatially associated with the most recent episode of faulting (Singh et al., 2006). Two other isolated hydrothermal vents occur outside of the main vent field; Capelinhos is located 1.4 km east of the central rift axis whereas Ewan occurs 1.5 km south of the main field (Figure 2.1A; Escartín et al., 2015). The spatial association of hydrothermal vents and fault traces, observed both within the main Lucky Strike field and at the Capelinhos vent site, suggests that faulting is a primary control on sub-seafloor fluid channeling, although fluids are likely redistributed where faults intersect the fossil lava lake (Barreyre et al., 2012; Escartín et al., 2015; Humphris et al., 2002).

The deposits at Lucky Strike are composed of a sulfide-sulfate mineral assemblage that is typical of hydrothermal deposits on the MAR (e.g., Bogdanov et al., 2006; Langmuir et al., 1997), with the notable exception of abundant barite, which has been linked to the enriched MOR basalt substrate associated with the Azores hotspot (Langmuir et al., 1997). There are two main modes of deposition of hydrothermal material on the seafloor at Lucky Strike; hydrothermally cemented volcaniclastic breccias; and massive sulfide-sulfate mounds and chimneys (Figure *2.3*). The occurrence of barite allows for the hydrothermal deposits to be dated using the ^{226}Ra/Ba dating method (Ditchburn et al., 2004; de Ronde et al., 2005; Ditchburn et al., 2012; Ditchburn and de Ronde, 2017).

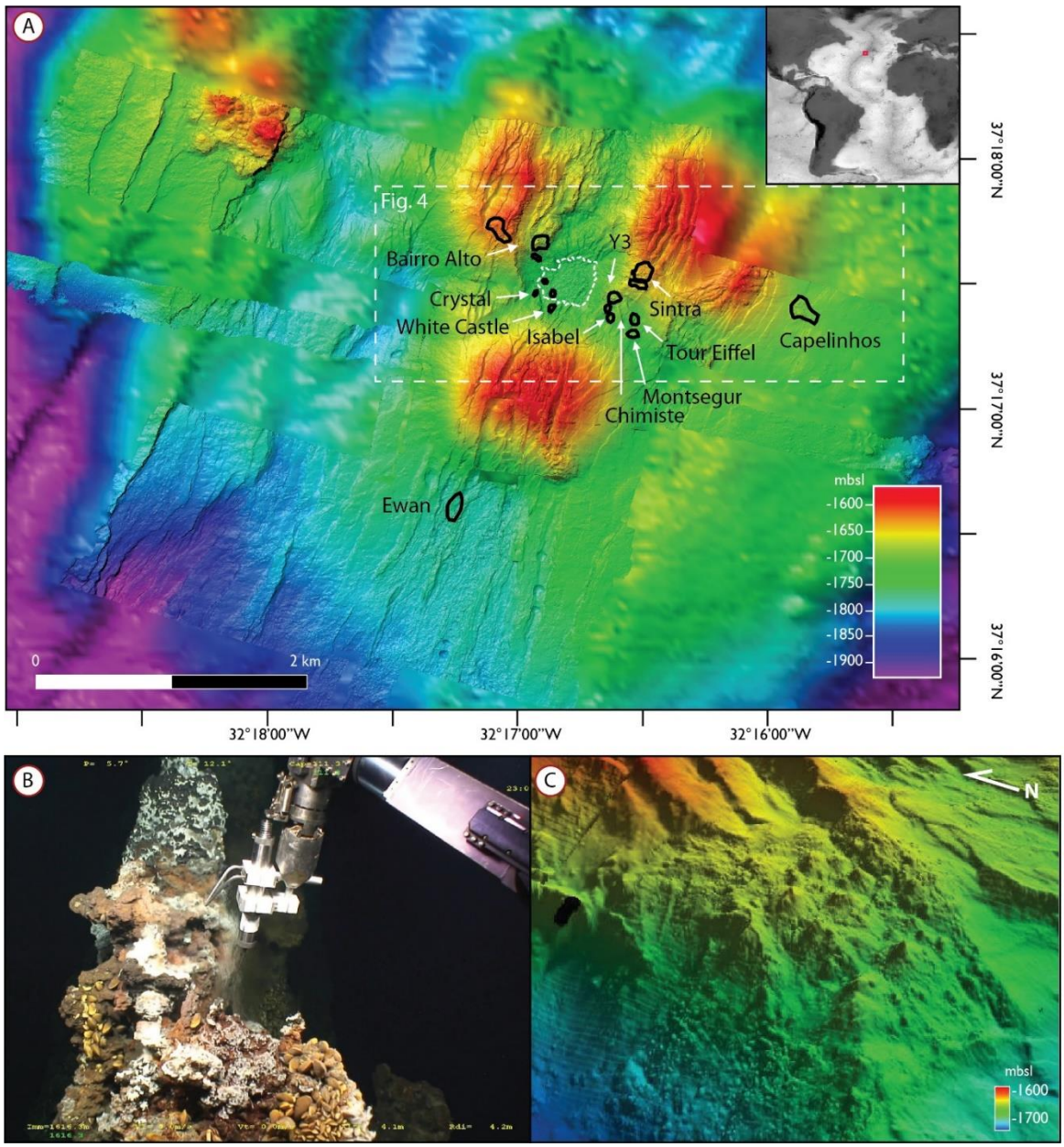

Figure 2.1. A) Bathymetric map with outlines (solid black lines) of hydrothermal deposits at Lucky Strike. The white irregular dashed outline shows the extent of a solidified recent fossil lava lake. High temperature venting (>200°C) occurs within the main vent cluster that surrounds the fossil lava lake, and at Capelinhos. Ewan is a site of diffuse fluid flow. B) Venting of up to 222°C (Charlou et al., 2000) at a sulfide chimney at the Sintra vent complex. C) High-resolution (~1 m) bathymetry shows hydrothermal mounds and chimneys at the Sintra site. Bathymetry sources (Ondréas et al., 2009; Escartín et al., 2015, 2021).

2.4. Methodology

2.4.1. ^{226}Ra/Ba dating

Rock samples for this study were collected from hydrothermal vents using the ROV *Victor 6000* during the Momarsat campaigns from 2011 to 2015 on the R/V *Pourquoi pas ?* and R/V Thalassa (2012). Seventeen barite-rich samples were dated using the ^{226}Ra/Ba method (Ditchburn et al., 2004, 2012; Ditchburn & de Ronde, 2017; Jamieson et al., 2013). Ages are calculated by determining the amount of ^{226}Ra within barite that has decayed since formation:

$$\boldsymbol{t = \frac{\ln(N_0/N) \times 1600\ years}{\ln 2}}$$

where t = time (years), N_0 = initial ^{226}Ra/Ba of the sample at the time of crystallization, N = the measured ^{226}Ra/Ba of the sample, and 1,600 years the half-life of ^{226}Ra. The ^{226}Ra/Ba method relies on the assumption that the initial ^{226}Ra/Ba does not vary significantly over the period of venting (de Ronde et al., 2005). The lower age limit for the ^{226}Ra/Ba dating technique is ~500 years old (Ditchburn et al., 2004, 2012). To determine N_0, two additional samples were collected from precipitates that formed on temperature probes that were deployed in 2009 and 2012 and each recovered 1 year later from two active high temperature vents within the vent field (see zero age data in Table *2.1*).

In addition to using ^{226}Ra/Ba, detectable ^{228}Ra (half-life of 5.75 years) and ^{228}Th (half-life of 1.91 years) activities indicate the presence of relatively young barite in a sample (Ditchburn and de Ronde, 2017). Using the ^{228}Ra/^{226}Ra activity ratios, barite with ages from 3 to 35 years can be dated, and using the ^{228}Th/^{228}Ra activity ratio, barite younger than 12 years can be dated. Previous work, mainly at volcanic arcs, has shown that older

hydrothermal barite can be incorporated into younger samples, thus affecting the overall sample age (Ditchburn & de Ronde, 2017; de Ronde et al., 2014). When these different isotope chronometers are applied to individual samples, the different calculated ages can be used to evaluate the degree of mixing and ages of different generations of barite.

Barium concentrations within the bulk samples were determined by instrumental neutron activation analysis at Activation Laboratories (Ancaster, Ontario, Canada). The accuracy and precision of Ba is better than ± 5%, based on repeat (n = 7) analysis of the GXR-1 standard. Radium-226, ^{228}Ra, and ^{228}Th activities of powdered samples was measured using a Canberra gamma spectrometer with a high-purity germanium well-type detector with a counting time of 24 hours per sample. Raw spectra were converted to isotope activities using the ScienTissiMe software package by ScienTissiMe Inc. The initial N_0 value (1053 ± 43 Bq/kg·wt %) was determined from the slope of the ^{226}Ra activity (Bq/kg) versus Ba (wt %) plot of the two zero-age samples. The age uncertainties were calculated using error propagation of all variables within the age equation, assuming independent and non-correlated variables (Glen, 2021).

2.4.2. Tonnage estimate

The extent of hydrothermal chimneys and mounds on the seafloor were digitized from ~1 m resolution bathymetry (Figure 2.2A) collected during the MOMARETO cruise in 2006 and complemented with MOMAR'08 and Bathyluck'09 surveys, derived from the ROV Victor 6000 and AUV Aster-X surveys (Ondréas et al., 2009; Escartín et al., 2015, 2021). The extent of these hydrothermal deposits was also validated using ROV video imagery and a photomosaic dataset (e.g., Figure 2.2B; Barreyre et al., 2012). Deposit volumes were

calculated using Leapfrog Geo 4.3 software. These estimates are limited to hydrothermal material that has accumulated above the seafloor using an interpolated lower surface to represent the assumed geometry of the seafloor prior to hydrothermal deposition (Figure 2.2C-2E). An uncertainty of 10% is assigned to volume estimates. This uncertainty is derived from the resolution limitations of the bathymetric data and errors associated with defining the areal extent of the hydrothermal deposits in regions where photomosaics were not available. Evidence from VMS deposits studied on land (Galley et al., 2007) and from deep sea drilling (e.g., the active mound at TAG; Hannington et al., 1998), show that sub-seafloor replacement-style hydrothermal mineralization commonly occurs (e.g., Doyle & Allen, 2003; Piercey, 2015). However, in this study we only consider the surficial hydrothermal material, and, as a result, our calculations provide minimum estimates for total accumulated hydrothermal material at Lucky Strike if sub-seafloor mineralization was also included.

To convert volumes to tonnages, a density for the hydrothermal deposits must be determined. An average density of 3.7 t/m^3 (range of 2.5-4.6 t/m^3 for individual samples) was determined for seafloor sulfide and sulfate rich samples from mid-ocean ridges and arc settings (Spagnoli et al., 2016). At the TAG active mound, Hannington et al. (1998) used an average density of 3.7 t/m^3 (range of 3.5-4 t/m^3) to calculate tonnage, whereas Graber et al. (2020) applied a density of 3.5 t/m^3 for the active mound. For an extensive study performed by Nautilus Minerals Inc., 415 hydrothermal deposit samples were analyzed for the resource estimate for the Solwara 1 hydrothermal deposit (Papua New Guinea), located in a backarc setting, and yielded an average density of 3.3 t/m^3 for sulfide-rich samples (Golder Associates Pty. Ltd., 2012). An average density of 3.1 t/m^3 was determined for the

hydrothermal deposits at the Endeavour vent field (Juan de Fuca Ridge), and this value was used for a similar volume-tonnage estimate at that site (Jamieson et al., 2014; Tivey et al., 1999). For this study we use a value of 3.4 ± 0.3 t/m^3, which represents the average reported for mid-ocean ridge and arc settings and the value for the mineralogically similar Endeavour segment (Tivey et al., 1999; Spagnoli et al., 2016).

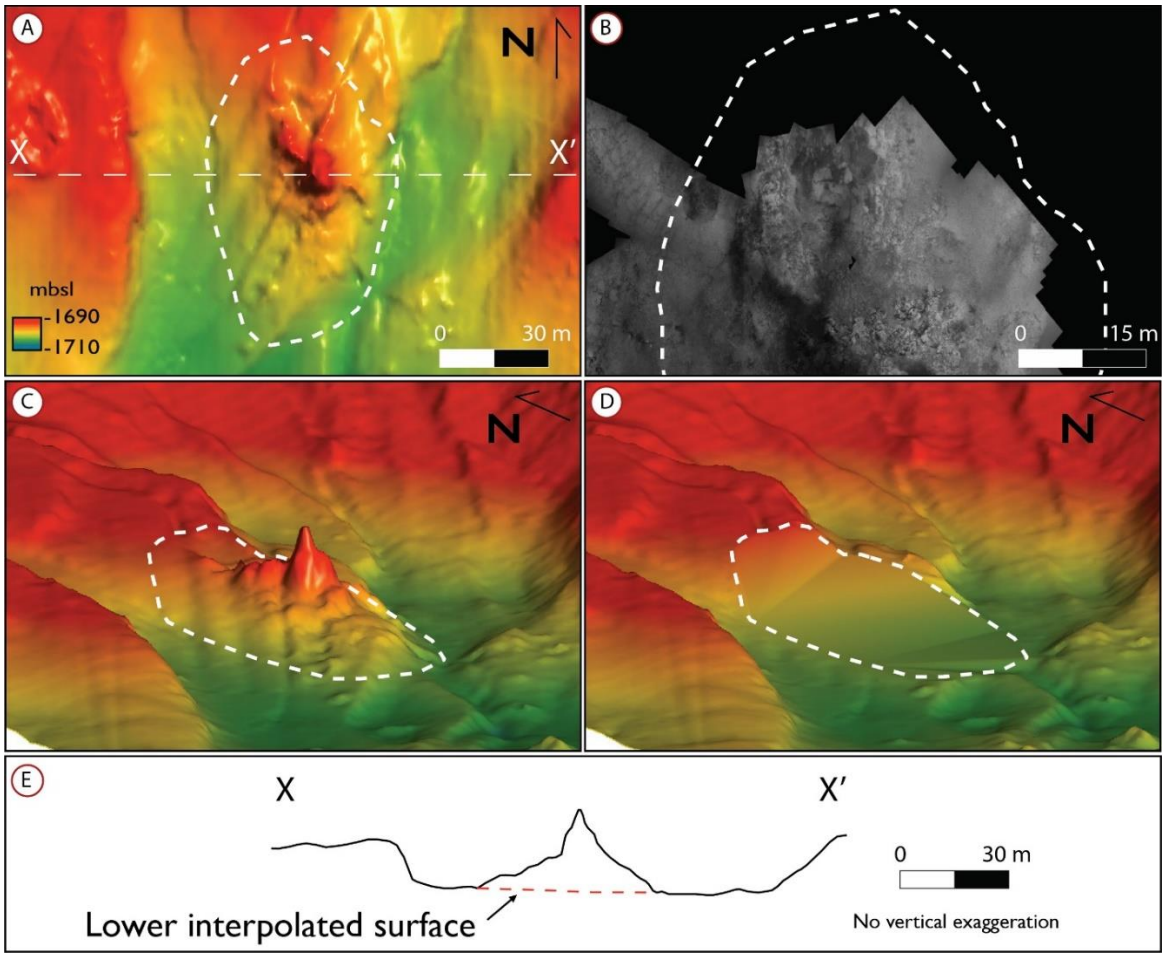

Figure 2.2. Volume calculations of hydrothermal deposits, illustrated using the Tour Eiffel site as an example. A) Plan view of the bathymetry surrounding the Tour Eiffel site. White dashed outline shows the extent of the hydrothermal deposit, based on bathymetric features and visual confirmation from photomosaics of the seafloor. B) Photomosaic coverage of Tour Eiffel site (Bathyluck'09 photomosaic). C) Oblique view of Tour Eiffel site with the dashed white line outlining the extent of the hydrothermal deposit used to define the lower boundary from which volumes were estimated. D) Same view as (C) but with the bathymetry cropped and replaced by the interpolated lower boundary cut-off surface. E) Cross-section X-X' from (A) showing a profile of the Tour Eiffel site including the lower

interpolated surface (red dashed line) that results in a 10% uncertainty for the volume estimate.

2.5. Results

2.5.1. Ages of hydrothermal deposits

Ages of hydrothermal samples from Lucky Strike, using the ^{226}Ra/Ba chronometer, range from zero (actively forming) to 6,647 ± 154 years (Table *2.1*; Figure 2.4). The oldest sample was collected from the Sintra site, located on the eastern side of Lucky Strike (Figure 2.1 and 2.3A). This age overlaps within uncertainties of the next two oldest samples (6,403 ± 534 years and 6,347 ± 171 years) from the Bairro Alto site on the western side of Lucky Strike and the Chimiste site on the eastern side, respectively (Figure 2.1A). The oldest sample dated from Capelinhos has an age of 817 ± 187 years. Six of the seventeen dated samples are hydrothermally cemented volcaniclastic breccias, that have also been previously described as "slabs" (Figure 2.3B-2.3D; Table *2.1*) (Humphris et al., 2002; Langmuir et al., 1997; Ondréas et al., 2009). These slabs are filled by hydrothermal barite (0.27-11 wt.% Ba) and marcasite/pyrite, with the exception of MOM12-504-ROC1 that contains minor amounts of disseminated sphalerite and chalcopyrite. The age of these hydrothermal cements, which generally occur at the base of mound and chimney structures, are amongst the oldest hydrothermal precipitates in this study, and range from 6,403 ± 517 to 2,115 ± 120 years (Figure 2.4; Table *2.1*). By contrast, chimney samples, with the exception of one sample from Sintra, yield younger ages that range from zero (active) to 817 years (Figure 2.3A, 2.3E, and 2.3F). Therefore, the ages of the hydrothermal cements can provide a more confident estimate of the oldest ages for the vent field.

Nine samples have measurable ^{228}Ra and ^{228}Th activities, all from or near actively venting edifices (Table *2.1*). The samples with no measurable ^{228}Ra and ^{228}Th activities are primarily from inactive regions of the vent field (including all of the volcaniclastic breccia, or "slab" samples), although three samples are from active vent sites. By combining the ^{226}Ra/Ba age data with the ^{228}Ra and ^{228}Th results, samples can be grouped into four categories (Table *2.1*): Group I (n=8) comprises the oldest samples dated (>~750 years) and contain no measurable ^{228}Ra or ^{228}Th; Group II (n=3) consists of samples with ^{226}Ra/Ba ages of >500 years and measurable ^{228}Ra or ^{228}Th; Group III (n=2) consists of samples with ^{226}Ra/Ba ages of <500 years and no measurable ^{228}Ra or ^{228}Th; Group IV (n=6) consists of samples with ^{226}Ra/Ba ages of <500 years and measurable ^{228}Ra and ^{228}Th.

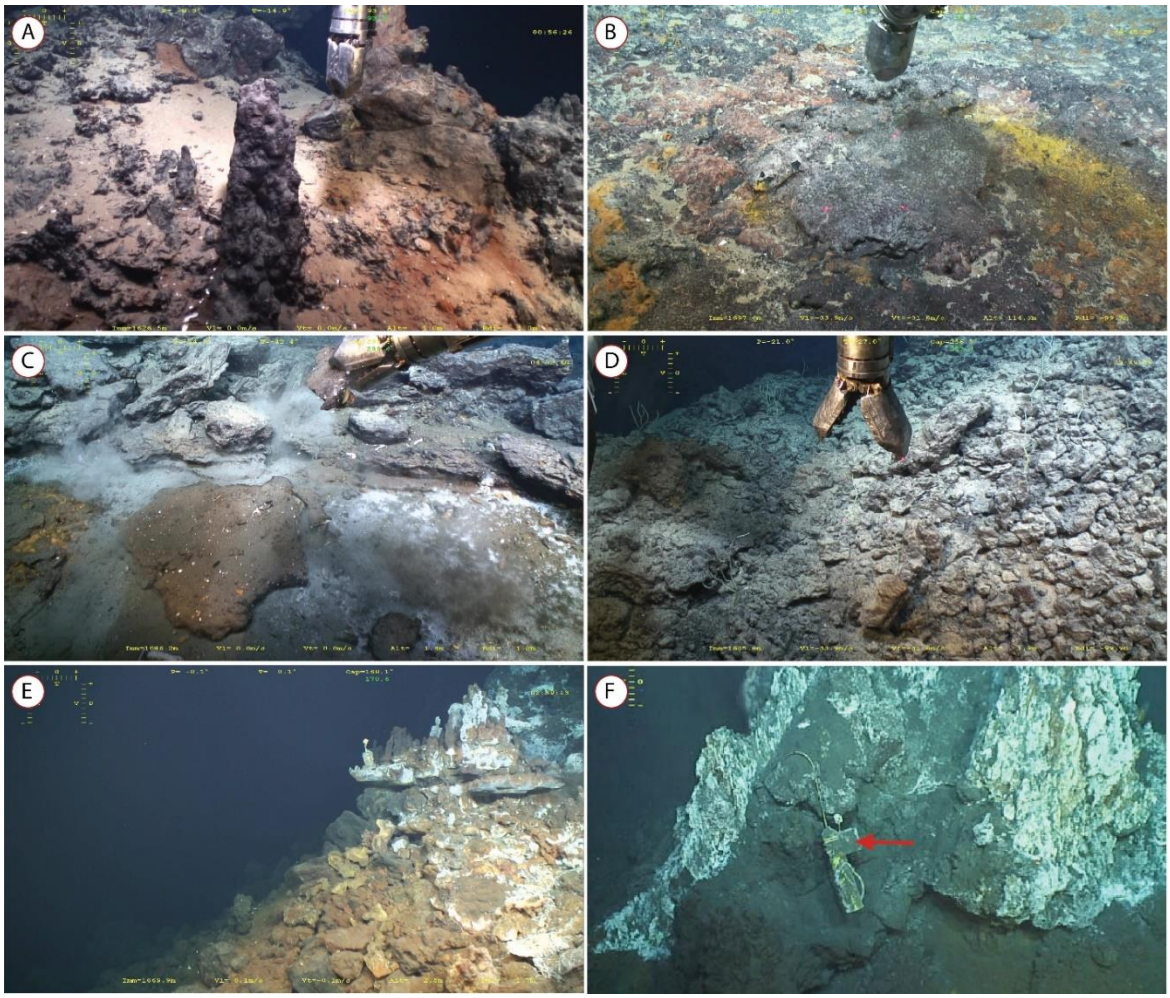

Figure 2.3. Hydrothermal deposit sample types. A) Massive sulfide/sulfate chimney at the base of the Sintra site (sample MOM11-452-ROC1), which has an age of 6,647 ± 154 years (i.e., the oldest dated sample at Lucky Strike). B) Hydrothermally cemented volcaniclastic breccia near Isabel (sample MOM15-607-ROC7), which has an age of 6,347 ± 154 years. C) Hydrothermally cemented volcaniclastic breccia sampled 70 m W of Tour Eiffel (sample MOM15-607-ROC1), which has an age of 4,060 ± 157 years. D) Hydrothermally cemented volcaniclastic breccia located 150 m NW from Bairro Alto (sample MOM15-605-ROC1), which has an age of 6,403 ± 517 years. E) Massive sulfide/sulfate talus at the base of the Capelinhos site (sample MOM13-528-ROC1-S), which has an age of 817 ± 151 years. F) Zero age sample, collected as hydrothermal precipitates that formed on a temperature probe (red arrow) at Crystal vent. Photomicrographs of the cemented breccias can be found in Appendix 4.

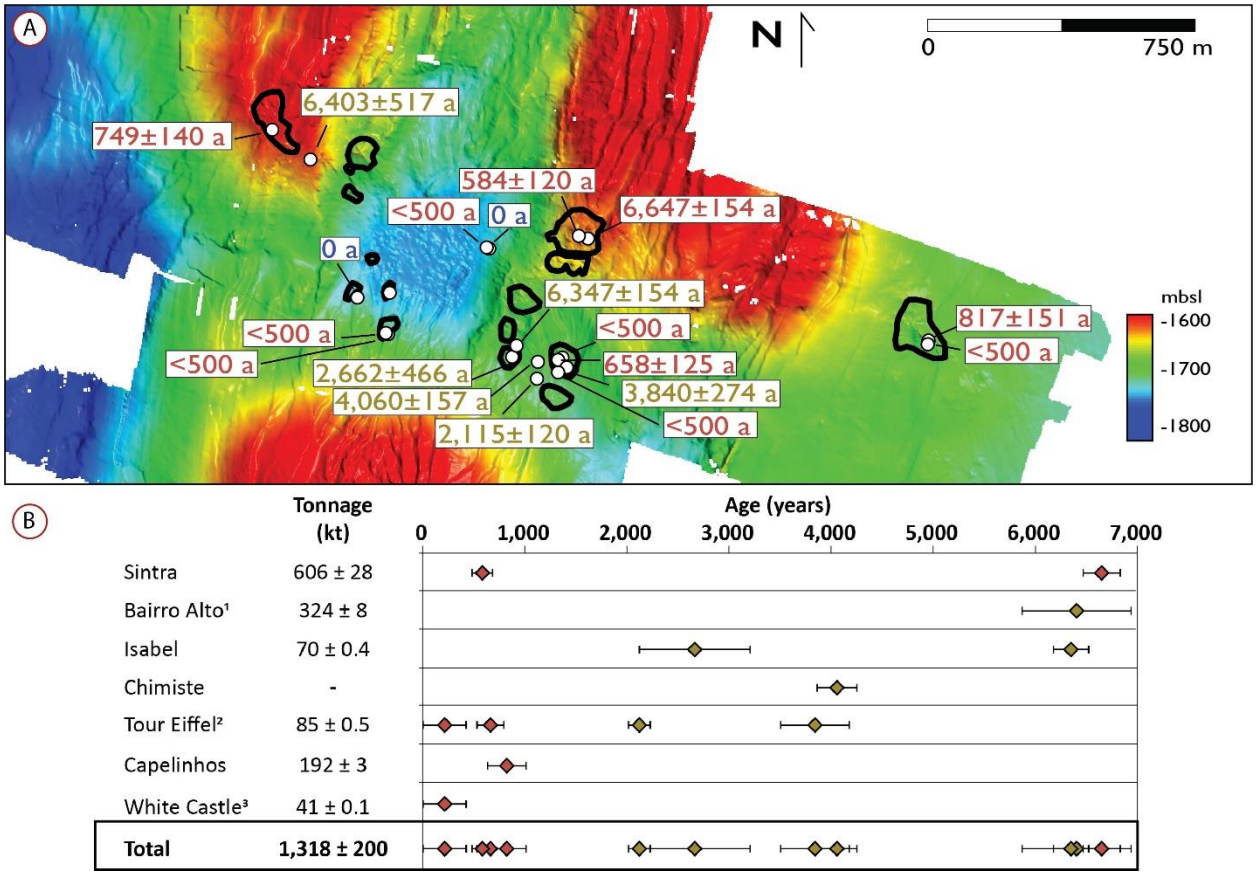

Figure 2.4. A) Map of hydrothermal sites. Black outlines indicate areas where volumes of hydrothermal deposits have been determined. White circles indicate locations of samples dated using the ^{226}Ra/Ba method. The labelled ages in gold correspond to the hydrothermally cemented volcaniclastic rocks, red labels indicate sulfate/sulfide rocks, and blue labels indicate zero-age samples. B) Tonnages, accumulation rates, and ages for sulfide/sulfate samples from different vent edifices at Lucky Strike. Red diamonds are sulfate/sulfide rock samples and gold diamonds correspond to hydrothermally cemented volcaniclastic samples. [1]Bairro Alto includes tonnage from three sites in the northwestern part of the area; [2]Tour Eiffel includes tonnages from Montsegur; [3]White Castle includes tonnages from four sites in the southwestern part of the area.

Table 2.1. ^{226}Ra, ^{228}Ra, and ^{228}Th activities and Ba concentrations for hydrothermal sulfide/sulfate samples from Lucky Strike. Table with sample coordinates and International Geo Sample number (IGSN) can be found in Appendix 1.

Sample	Ba (wt.%)	^{226}Ra activity (Bq/kg)	^{228}Ra activity (Bq/kg)	^{228}Th activity (Bq/kg)	^{226}Ra/Ba Age (years)	^{228}Ra/^{226}Ra age (years)	^{228}Th/^{228}Ra age (years)	Group	Sample type	Description
Y3										
MOM11-454-ROC7	1.93	2083 ± 66	392 ± 19	181 ± 7	<500	26 ± 0.5	1.5 ± 0.2	IV	Massive sulfate/sulfide rock	Base of small active chimney
White Castle										
MOM15-603-ROC5	0.50	665 ± 21	75 ± 6	38 ± 2	<500	30 ± 0.7	1.7 ± 0.3	IV	Massive sulfate/sulfide rock	Block from active edifice
MOM15-603-ROC6	3.83	3764 ± 119			<500	>35	>12	III	Massive sulfate/sulfide rock	Block from active edifice
Off axial graben to the W										
MOM15-605-ROC2	44.4	33790 ± 1502			749 ± 140	>35	>12	I	Massive sulfate/sulfide rock	From inactive site
Tour Eiffel										
MOM11-452-ROC4	0.50	99 ± 4			3840 ± 274	>35	>12	I	Hydrothermally cemented volcaniclastic breccia	At the SE base of Tour Eiffel
MOM11-457-ROC8	3.45	2730 ± 86	240 ± 13	115 ± 4	658 ± 125	32 ± 0.5	1.6 ± 0.2	II	Massive sulfate/sulfide rock	Small inactive chimney W of Tour Eiffel
MOM14-579-ROC1	2.38	2085 ± 66	122 ± 8	56 ± 3	<500	36 ± 0.6	1.5 ± 0.2	IV	Massive sulfate/sulfide rock	Small inactive chimney, two barite generations
MOM13-532-ROC1	9.94	10055 ± 316			<500	>35	>12	III	Massive sulfate/sulfide rock	Block in the E slope of Tour Eiffel
Site 85 m SW of Tour Eiffel										
MOM12-504-ROC1	11.2	4715 ± 148			2115 ± 120	>35	>12	I	Hydrothermally cemented volcaniclastic breccia	Block in inactive area 85 m SW of Tour Eiffel

Sample	Ba (wt.%)	^{226}Ra activity (Bq/kg)	^{228}Ra activity (Bq/kg)	^{228}Th activity (Bq/kg)	^{226}Ra/Ba Age (years)	^{228}Ra/^{226}Ra age (years)	^{228}Th/^{228}Ra age (years)	Group	Sample type	Description
Sintra										
MOM12-502-ROC1	38.1	31140 ± 978	5081 ± 227	2356 ± 76	584 ± 120	27 ± 0.5	1.5 ± 0.2	II	Massive sulfate/sulfide rock	Active chimney
MOM11-452-ROC1	1.42	84 ± 3			6647 ± 154	>35	>12	I	Massive sulfate/sulfide rock	Small inactive chimney on sulfide-rich basement at the base of Sintra
Site 70 m W of Tour Eiffel (Chimiste)										
MOM15-607-ROC1	1.24	225 ± 8			4060 ± 157	>35	>12	I	Hydrothermally cemented volcaniclastic breccia	Fragment next to inactive site 70 m W of Tour Eiffel
Between Isabel and Flores										
MOM15-607-ROC7	1.58	106 ± 4			6347 ± 154	>35	>12	I	Hydrothermally cemented volcaniclastic breccia	20 m SE from Isabel
MOM15-607-ROC6	0.27	88 ± 4			2662 ± 466	>35	>12	I	Hydrothermally cemented volcaniclastic breccia	Southern base of the active site Flores
Site 150 m NW from Bairro Alto										
MOM15-605-ROC1	0.28	18 ± 2			6403 ± 517	>35	>12	I	Hydrothermally cemented volcaniclastic breccia	From inactive site
Capelinhos										
MOM14-583-ROC1-S	4.52	4506 ± 142	266 ± 15	119 ± 5	<500	36 ± 0.6	1.5 ± 0.2	IV	Massive sulfate/sulfide rock	Block from the base of Capelinhos edifice, active high-T vents near, two barite generations
MOM13-528-ROC1-S	1.29	953 ± 30	140 ± 8	62 ± 3	817 ± 151	28 ± 0.6	1.5 ± 0.2	II	Massive sulfate/sulfide rock	Block from the base of Capelinhos edifice, active high-T vents near, two barite generations

Sample	Ba (wt.%)	^{226}Ra activity (Bq/kg)	^{228}Ra activity (Bq/kg)	^{228}Th activity (Bq/kg)	^{226}Ra/Ba Age (years)	^{228}Ra/^{226}Ra age (years)	^{228}Th/^{228}Ra age (years)	Group	Sample type	Description
Zero age										
LS-BS-WHOI (Y3)	3.23	3369 ± 106	791 ± 37	333 ± 11	-	24 ± 13	1.4 ± 0.2	IV	Sample recovered from temperature probe	
HT010-CR12 (Crystal)	0.74	750 ± 24	177 ± 10	75 ± 3	-	24 ± 11	1.4 ± 0.2	IV	Sample recovered from temperature probe	

Note: blank spaces indicate that activities were below the detection limit.

2.5.2. Deposit size and average mass accumulation rate

Deposit size (reported as tonnage) and ages determined in this study are summarized in Figure 2.4. A total of 388,000 m^3, or 1.3 ± 0.2 Mt (converted using an average density of 3.4 ± 0.3 t/m^3) of hydrothermal material is estimated to have accumulated on the seafloor at Lucky Strike at an average rate of 194 ± 28 t/yr, using the maximum age obtained in this study (6,647 years). The calculated overall accumulation rate should be considered a maximum rate because the maximum recorded age for the field (~6,650 years) represents the minimum duration of hydrothermal activity at this site.

2.6. Discussion

2.6.1. Age and Evolution of the Lucky Strike vent field

Hydrothermal venting, and therefore barite precipitation, has occurred throughout the lifespan of the Lucky Strike hydrothermal system, either as continuous venting or at least continuous over prolonged episodes of active venting (e.g., 100s to 1000s of years; Figure 2.4B). Textural evidence, such as barite crystal morphology and cross-cutting relationships for samples at Lucky Strike, indicate a single generation of barite within most samples. However, three samples show evidence for at least two generations of barite (Table *2.1*; Figure 2.5). Either way, the reported $^{226}Ra/Ba$ ages represent not necessarily a discrete age but, more likely, an average age of the barite in that sample. For example, a sample of chimney wall from an actively venting structure with an $^{226}Ra/Ba$ age of 600 years would contain a mixture of barite of ages that range from zero to >600 years. For this reason, all ages should be considered minimum ages.

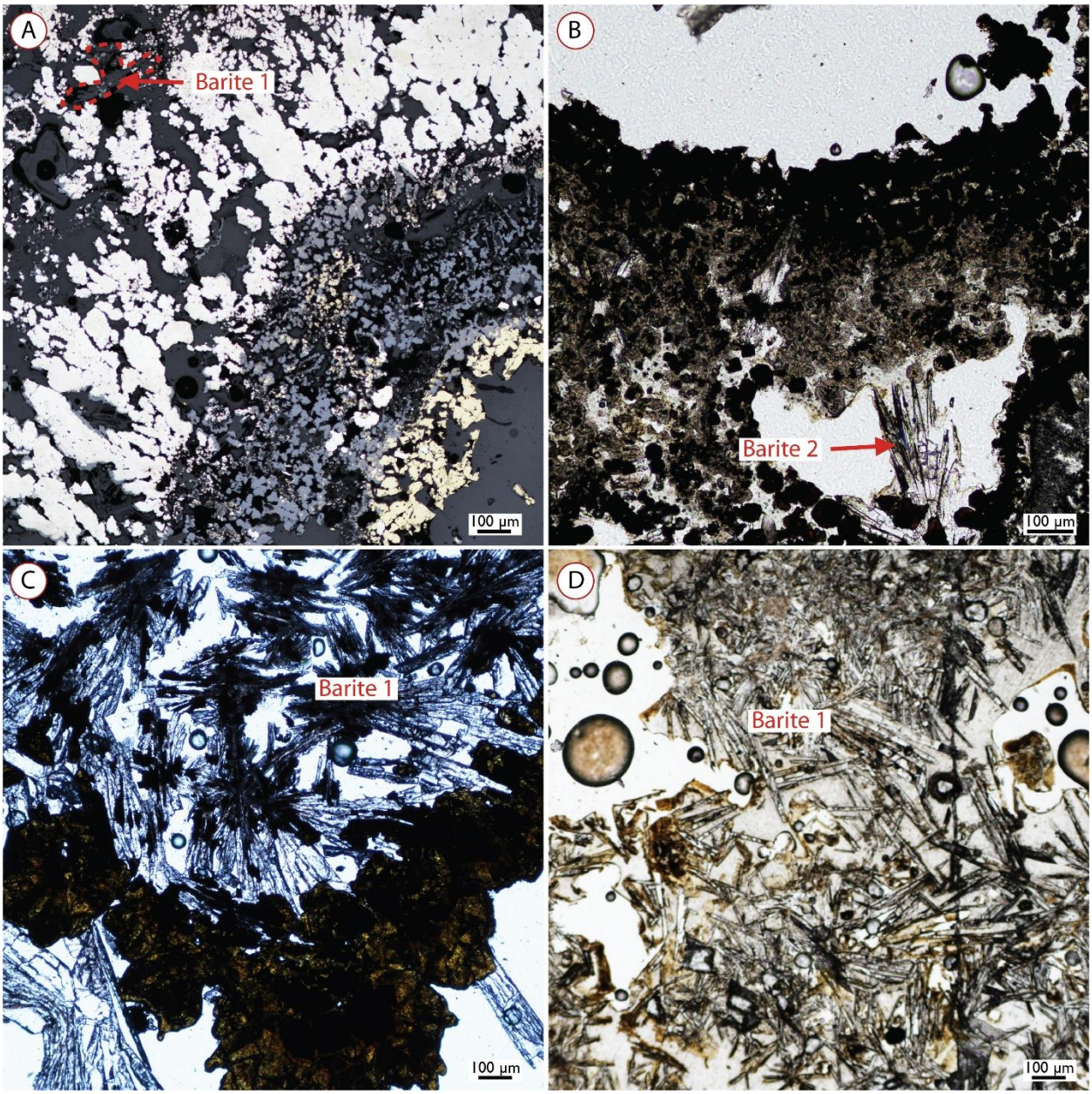

Figure 2.5. A) Photomicrograph of a sample from the Tour Eiffel site (MOM14-579-ROC1) showing a generation of barite that has intergrown with marcasite (early stage). B) Image from the same sample as A but in another area that shows a second generation of barite that has grown infilling vent conduits (late stage). C) Single generation of barite from the Sintra site (MOM12-502-ROC1). D) Single generation of barite at a site located west of the axial graben. Image A is a plane-polarized reflected light photomicrograph. Images B, C, D, are plane-polarized transmitted light photomicrographs.

The presence of barite with mixed ages at Lucky Strike is highlighted by comparing the ^{226}Ra/Ba ages with the ^{228}Ra and ^{228}Th data, as defined in the four sample groups (Table *2.1*). Group I

samples are older than ~500 years and have no measurable ^{228}Ra and ^{228}Th, indicating that these samples contain no barite younger than ~35 years old but likely contain a mixture of older barite. The absence of young barite within Group I samples is consistent with these samples being the oldest samples and collected from inactive regions of the vent field. Group II samples, which were collected from hydrothermally active areas of the vent field, are also older than ~500 years but, unlike Group I samples, do contain measurable ^{228}Ra and ^{228}Th, indicating barite in these samples that ranges in age from recently precipitated (<~12 years, based on ^{228}Th activity) to older than the reported ^{226}Ra/Ba age for each sample. Group III samples are younger than ~500 years and contain no measurable ^{228}Ra and ^{228}Th activities, which indicates absence of younger barite (<~35 years, based on ^{228}Ra activity). The combination of young ages but lack of recent barite is consistent with these samples being collected from inactive areas of otherwise actively venting edifices (Table *2.1*). Group IV consists of samples younger than ~500 years with measurable ^{228}Ra and ^{228}Th activities, which is consistent with these samples being collected from active vents.

A plot of ^{228}Ra/Ba versus ^{226}Ra/Ba for samples that contain measurable ^{228}Ra activity can be used to determine if chimney barite contains a component of older remobilized barite from deeper in the system (de Ronde et al., 2014). A source of old barite with a defined age will result in a mixing line with a y-intercept that defines the ^{226}Ra/Ba ratio, and therefore the age, of the old barite. A ^{228}Ra/Ba versus ^{226}Ra/Ba plot for young samples at Lucky Strike does not result in a linear array, indicating that there is no discrete reservoir of old remobilized barite with a well defined age (Figure 2.6). Instead, a lack of defined linear array is consistent with samples containing barite representing a continuum of mixed ages.

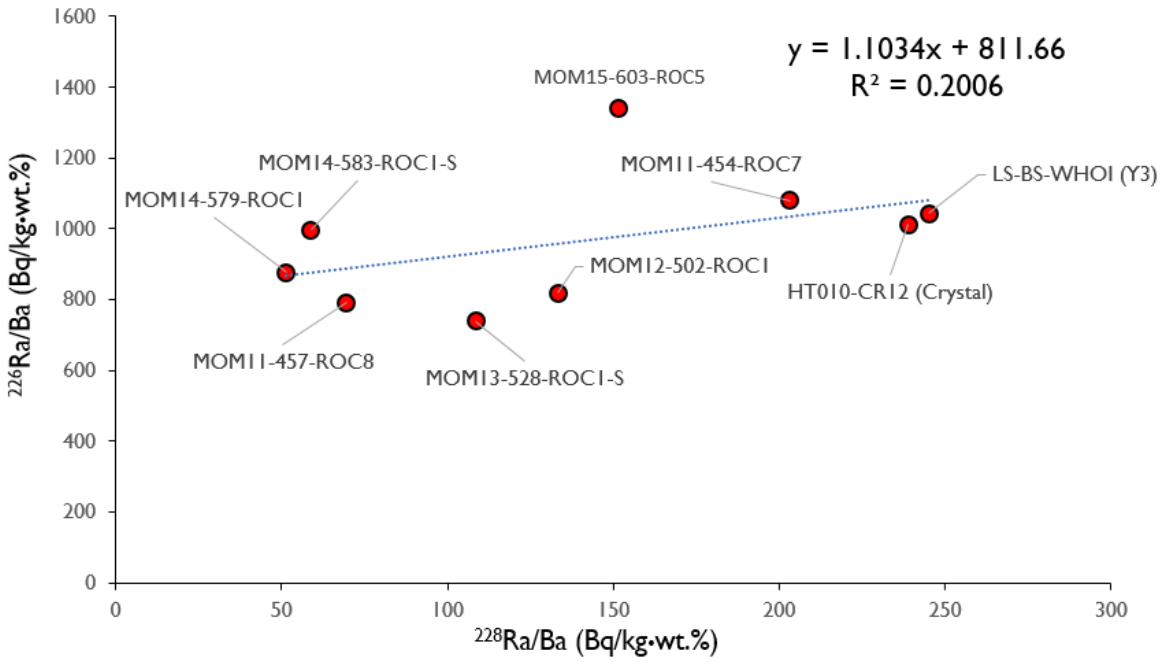

Figure 2.6. ^{228}Ra/Ba versus ^{226}Ra/Ba plot showing a mixing line of new and older barite in hydrothermal samples from the Lucky Strike vent field.

2.6.2. Age and Evolution of the Lucky Strike vent field

The results of the barite dating indicate that there has been hydrothermal activity at Lucky Strike for at least ~6,600 years. The ages determined thus far (n = 17) show some age gaps between ~6,000 and 4,000 years and ~2,000 and 800 years (Figure 2.4B). These age gaps could be interpreted to indicate that venting at Lucky Strike is episodic, as proposed for other sites on the MAR (Lalou et al., 1995; Cherkashov et al., 2017). If so, it is estimated that active hydrothermal venting has occurred for only ~3,400 years, or ~50% of the minimum age of the vent field. However, it is also possible that these age gaps simply reflect the limited number of dated samples. More sampling and dating would be required to resolve if the hydrothermal system at Lucky Strike has been continuous or discontinuous.

The results show that Lucky Strike is one of the youngest known basalt-hosted vent fields along the northern MAR. The youngest known basalt-hosted vent field along the MAR is Snake Pit (i.e., 3.7 ka; Lalou et al., 1993, 1990), and the next youngest, after Lucky Strike, is Puy des Folles (18 ka; Cherkashov et al., 2017). The common characteristic of these relatively young deposits is that they are located directly on the ridge axis and are associated with volcanic edifices. By comparison, the oldest known basalt-hosted hydrothermal deposits along the MAR are 223 ka, from the Peterburgskoye field, which is located 16 km off axis, and the 119 ka Krasnov site, located 8 km from the ridge axis (Cherkashov et al., 2017). The average age of dated samples from the MAR is ~66 ka (Cherkashov et al., 2017).

The rifting event that has resulted in the dismemberment of the two volcanic edifices that host the Lucky Strike hydrothermal deposits is estimated to have initiated at ~60 ka, an age based on spreading rate and distances to the ridge axis and is therefore poorly constrained (Escartín et al., 2014). The fossil lava lake located between the rifted volcanic edifices shows no evidence of rifting and therefore represents the most recent volcanic event in this part of the segment (Humphris et al., 2002; Ondréas et al., 2009). The young ages of the hydrothermal deposits relative to the age of rifting and the spatial association of the venting with the recent fossil lava lake, suggest that the initiation of the hydrothermal system feeding the vent field is related to the recent volcanic event that formed the lava lake. The occurence of hydrothermal deposits surrounding the perimeter of the fossil lava lake suggests that older deposits may have been covered by recent volcanism (e.g., Humphris et al., 2002; Ondréas et al., 2009) and that any record of hydrothermal activity that would predate the recent volcanism has been obliterated.

The oldest known hydrothermal activity at Lucky Strike is recorded both at sites of significant sulfide/sulfate accumulation such as from the base of the Sintra site, and in hydrothermally cemented volcaniclastic breccias away from major hydrothermal edifices where there is no significant accumulation of hydrothermal material on the seafloor. Similar silificied and barite breccias have been described at the Clark Volcano, Kermadec arc, northeast of New Zealand and yielded the oldest dated age at this site (de Ronde et al., 2014). We suggest therefore, that early hydrothermal venting was likely widespread (~2.5 km^2), and evolved to more focused and prolonged fluid flow that resulted in, and continues to form, the sulfide/sulfate mounds and chimney structures. The evolution of hydrothermal venting at Lucky Strike suggests that, for similar investigations of the age and evolution of other hydrothermal vent fields, hydrothermally cemented breccias (if present) may represent the oldest record of hydrothermal venting and should be targeted to provide greater insight into the maximum age of hydrothermal venting within the vent field.

2.6.3. Average hydrothermal mass accumulation rates

The calculated minimum average mass accumulation rate of 194 ± 28 t/yr for Lucky Strike is comparable to other reported mass accumulation rates for seafloor hydrothermal sites, which range from less than 100 to ~800 t/yr (Jamieson et al., 2014 and references therein). However, with the exception of TAG and Endeavour, these calculated rates rely primarily on rough visual estimates of deposit size, as opposed to more precise high-resolution (<2 m) bathymetry used in this study. High-temperature hydrothermal activity at the active mound at TAG began ~50,000 years ago, but may have experienced only ~5,000 to 10,000 years of active venting over that time (Lalou et al., 1995). Any episodicity of hydrothermal venting will increase the average accumulation rate over the lifespan of a hydrothermal system. As a result, the mass accumulation rate for the active mound

at TAG is 54 t/yr when considering the average rate over the lifespan of the mound, but is 360 t/yr when considering only periods of active venting (Jamieson et al., 2014). For Lucky Strike, although there are significant age gaps between samples (e.g., between 4,000 and 6,000 years; Figure 2.4B), the low number of samples dated can not resolve if hydrothermal activity has been episodic or continuous. The average accumulation rate of 194 ± 28 t/yr at Lucky Strike is therefore half of the rate at which the active mound at TAG accumulated during periods of activity. However, if an episodic scenario is assumed, the discontinuous accumulation rate over ~3,400 years of effective activity would be ~350 ± 95 t/yr, which is nearly identical to the rate calculated for TAG.

The scale of observation may have a significant influence when comparing mass accumulation rates between different vent fields as the overall areal extent of vent fields can vary significantly. For example, Lucky Strike and Endeavour have a similar estimated tonnage of 1.2–1.3 Mt (Jamieson et al., 2014); however, the higher accumulation rate of 400 t/yr along the Endeavour segment reflects high fluid fluxes associated with the large size of the vent field, which is distributed over ~60 km^2 of seafloor, compared to the Lucky Strike where vents cluster over an area of <2.5 km^2 (Jamieson et al., 2014). At both sites, venting generally occurs directly above the underlying axial magma chamber (with the exception of Capelinhos at Lucky Strike). At Lucky Strike, the axial magma chamber is thought to be located ~3 km below the seafloor and extends ~7 km along axis (Singh et al., 2006). In contrast, the magma chamber at Endeavour, although 2–3 km deep, extends up to 24 km along axis (van Ark et al., 2007), thus covering a much longer ridge section that hosts active hydrothermal venting. It is therefore important to consider the size of the vent field when comparing accumulation rates between different fields. From a

hydrothermal mineral accumulation perspective, Lucky Strike represents a site where focused fluid flow has resulted in accumulation over a relatively small area, which is optimal from an ore deposit formation perspective.

Total hydrothermal fluid flux at Lucky Strike is estimated to range from 5.7 to 32 kg/s, based on heat flux measurements and the partitioning of high temperature focused fluid flow and lower temperature diffuse flow constrained using the seafloor photomosaic imagery (Barreyre et al., 2012; Barreyre, 2013). This flux range, combined with average vent fluid concentrations from Charlou et al. (2000) for the primary mineral forming elements (i.e., Cu, Zn, Fe, Si, Mn, S, Ba, Sr, and Ca), results in a dissolved hydrothermal mass flux to the seafloor of 352 to 1966 t/yr, which is significantly higher than the average mass accumulation rate. This difference can be largely attributed to the venting and dispersal of a proportion of the dissolved mass flux in hydrothermal plumes discharging into the overlying water column (e.g. Von Damm, 1990; Elderfield & Schultz, 1996; German & Angel, 1995). The proportion of dissolved hydrothermal mass flux retained in the chimneys and mounds at the seafloor, or "depositional efficiency" at Lucky Strike field is thus estimated to be between 9 and 51%. This range of values is similar to, or higher than other percent efficiency estimates, such as 5% for the Endeavour Field (Jamieson et al., 2014) and 30% for TAG (Humphris & Cann, 2000).

Overall, considering only accumulation during periods of hydrothermal activity, differences in accumulation rates at different vent fields result from differences in hydrothermal fluid flux (which may or may not correlate with vent field size), the efficiency of mineral precipitation, and the proportion of minerals that precipitate on the sub-seafloor. If these variables are considered

individually, higher fluid fluxes will increase the rate of mineral precipitation, and higher degrees of mixing between ascending hydrothermal fluids and local seawater prior to venting will cause increased mineral precipitation within the deposit (and hence a lower proportion of metals lost to plumes) and a higher mass accumulation rate.

2.6.4. Implications for the formation of VMS deposits

This study focuses on the accumulation of hydrothermal material at the seafloor, and therefore quantifiable in terms of volume/tonnage using bathymetric data. However, significant hydrothermal mineralization can also occur within the immediate subsurface below hydrothermal vents, and ancient VMS deposits are commonly interpreted to comprise sulfide mineralization that accumulated both at the seafloor and as replacement below the seafloor (e.g., Franklin et al., 2005; Galley et al., 2007; Piercey, 2015), and therefore deposit mass accumulation becomes decoupled from volume accumulation at the seafloor. As a result, the rates of formation calculated for hydrothermal deposits on the seafloor using the methods described here cannot be directly compared to rates of formation of VMS deposits that likely include a component of sub-seafloor replacement mineralization. Instead, the seafloor rates represent minimum estimates for total seafloor and sub-seafloor mineralization. The application of drilling and or geophysical methods would be necessary to include the sub-seafloor component of any rate and tonnage calculations (Galley et al., 2021; Murton et al., 2019).

The degree of subsurface mineral precipitation is controlled largely by the porosity and permeability of the immediate substrate through which fluid flow occurs. At TAG, Graber et al. (2020) estimated an additional 30% of sulfide material in the sub-seafloor, based on drilling observations at the active mound at TAG (Hannington et al., 1998). However, using seismic

surveys at TAG, Murton et al. (2019) suggested that sub-seafloor deposits can range from 2 to 5 times the amount that is above the seafloor as mounds and chimneys. Drilling at sediment-hosted Middle Valley resulted in an estimate of at least the same amount of sulfide material in the subsurface compared to the mound material above the seafloor (Zierenberg et al., 1998). However, sediment-hosted deposits represent an extreme endmember of sub-seafloor mineralization due to the high porosity of the substrate. Another consideration for Lucky Strike is the possibility of unaccounted hydrothermal accumulation at the seafloor that was buried under the fossil lava lake. In summary, for Lucky Strike the calculated volume-based rate of accumulation should be considered as a minimum mass accumulation rate when considering the additional inclusion of sub-seafloor mineralization. Nevertheless, if we consider a scenario similar to TAG, where the mass of subsurface hydrothermal material is up to five times the amount that occurs at the surface, then the total mass accumulation rate for Lucky Strike would be 900 t/yr, which is still comparable to other sites on the seafloor (Graber et al., 2020; Jamieson et al., 2014).

Accumulation rates have been estimated for some ancient VMS deposits, where the duration of ore formation is constrained by measured ages of volcanic rocks stratigraphically above and below the hydrothermal deposits, and deposit tonnages include deposition both above and below the seafloor. Using these constraints, the Archean Kidd Creek deposit in Ontario, Canada, formed at a minimum rate of ~170 t/yr (Bleeker & van Breemen, 2011; Bleeker & Parrish, 1996; Hannington et al., 2017). Similarly, calculated accumulation rates for deposits within the Devonian-Mississippian Finlayson Lake VMS district in the Yukon Territory, Canada, include 75–800 t/yr for the Kudz Ze Kayah deposit, ~8 t/yr for the GP4F deposit, and 40–200 t/yr for the Wolverine deposit (Manor et al., 2022). Therefore, although the lack of sub-seafloor data prevents direct

comparisons between the modern seafloor and ancient deposits, the estimated accumulation rates from VMS deposits are comparable (within the same order of magnitude) to rates from the modern seafloor hydrothermal deposits. Based on the minimum accumulation rate estimated in this study (~194 t/yr), the average mafic-dominated VMS deposit (~4.8 Mt; Mosier et al., 2009) can form in under 25,000 years.

2.7. Conclusions

Results from ^{226}Ra/Ba dating of hydrothermal deposits within the Lucky Strike vent field indicate that the vent field is at least 6,600 years old, which is relatively young compared to other dated deposits along the MAR. Combined ^{226}Ra, ^{228}Ra, and ^{228}Th activities indicate that the ^{226}Ra/Ba ages represent average barite ages within each sample. Based on the number and distribution of sample ages, whether hydrothermal venting has been continuous or episodic remains unresolved. The relatively young age of the vent field is consistent with the hydrothermal field being located on a volcanically active ridge axis, where recent volcanism may have buried older deposits. The generally older age of the hydrothermally cemented volcaniclastic breccias suggests an initial stage of widespread hydrothermal activity that later evolved into more focused fluid flow at discrete sites that are represented by the major mound deposits.

A minimum of 1.3 Mt of hydrothermal material is estimated to have accumulated on the seafloor at Lucky Strike. This estimate does not account for hydrothermal sulfide-sulfate precipitation below the seafloor and thus should not be considered a resource estimate for this vent field. The calculated average mass accumulation rate at the seafloor is ~194 ± 28 t/yr. If an episodic venting scenario is considered, the accumulation rate over the active periods would be ~350 ± 95 t/yr. Although these accumulation rates are comparable to other sites along MORs, the Lucky Strike deposits notably occur within a relatively small seafloor footprint compared to other well-

characterized vent fields. The rates of accumulation at Lucky Strike along with other sites from the seafloor are similar to estimated rates of formation for some ancient volcanogenic massive sulfide deposits.

2.8. Acknowledgements

This work was supported by the Canada Research Chair Program, an NSERC Discovery Grant, and RDC Leverage Grant to J.W. Jamieson. DSM acknowledges support from the NSERC iMAGE-CREATE program.

2.9. References

van Ark, E. M., Detrick, R. S., Canales, J. P., Carbotte, S. M., Harding, A. J., Kent, G. M., et al. (2007). Seismic structure of the endeavour segment, Juan de Fuca Ridge: Correlations with seismicity and hydrothermal activity. *Journal of Geophysical Research: Solid Earth*, *112*(2), 1–22. https://doi.org/10.1029/2005JB004210

Barreyre, T. (2013). *Dynamics and heat fluxes of the Lucky Strike hydrothermal field (Mid-Atlantic Ridge, 37°17'N)*. Institut de Physique du Globe de Paris Université Paris Diderot.

Barreyre, T., Escartín, J., Garcia, R., Cannat, M., Mittelstaedt, E., & Prados, R. (2012). Structure, temporal evolution, and heat flux estimates from the Lucky Strike deep-sea hydrothermal field derived from seafloor image mosaics. *Geochemistry, Geophysics, Geosystems*, *13*(4), 1–29. https://doi.org/10.1029/2011GC003990

Bleeker, W., & van Breemen, O. (2011). New geochronological, stratigraphic, and structural observations on the Kidd-Munro assemblage and the terrane architecture of the south-central Abitibi greenstone belt, Superior craton, Canada. In *Results from the Targeted Geoscience Initiative III Kidd-Munro Project, Ontario Geological Survey* (Vol. 6258, p. 142).

Bleeker, W., & Parrish, R. R. (1996). Stratigraphy and U-Pb zircon geochronology of Kidd Creek: Implications for the formation of giant volcanogenic massive sulphide deposits and the tectonic history of the Abitibi greenstone belt. *Canadian Journal of Earth Sciences*, *33*, 1213–1231.

Bogdanov, Y. A., Lein, A. Y., Sagalevich, A. M., Ul'yanov, A. A., Dorofeev, S. A., & Ul'yanova, N. V. (2006). Hydrothermal sulfide deposits of the Lucky Strike vent field, Mid-Atlantic Ridge. *Geochemistry International*, *44*(4), 403–418. https://doi.org/10.1134/S0016702906040070

Charlou, J. L., Donval, J. P., Douville, E., Jean-Baptiste, P., Radford-Knoery, J., Fouquet, Y., et

al. (2000). Compared geochemical signatures and the evolution of Menez Gwen (35°50N) and Lucky Strike (37°17N) hydrothermal fluids, south of the Azores Triple Junction on the Mid-Atlantic Ridge. *Chemical Geology*, *171*(1–2), 49–75. https://doi.org/10.1016/S0009-2541(00)00244-8

Cherkashov, G., Kuznetsov, V., Kuksa, K., Tabuns, E., Maksimov, F., & Bel'tenev, V. (2017). Sulfide geochronology along the Northern Equatorial Mid-Atlantic Ridge. *Ore Geology Reviews*, *87*, 147–154. https://doi.org/10.1016/j.oregeorev.2016.10.015

Von Damm, K. L. (1990). Seafloor hydrothermal activity: black smoker chemistry and chimneys. *Annual Review of Earth & Planetary Sciences*, *18*, 173–204. https://doi.org/10.1146/annurev.ea.18.050190.001133

Ditchburn, R. G., & de Ronde, C. E. J. (2017). Evidence for Remobilization of Barite Affecting Implications for the Evolution of Sea-Floor Volcanogenic Massive Sulfides, 1231–1245. https://doi.org/10.5382/econgeo.2017.4508

Ditchburn, R. G., Graham, I. J., Barry, B. J., & de Ronde, C. E. J. (2004). Uranium series disequilibrium dating of black smoker chimneys. *New Zealand Science Review*, *61*, 54–56.

Ditchburn, R. G., de Ronde, C. E. J., & Barry, B. J. (2012). Radiometric dating of volcanogenic massive sulfides and associated iron oxide crusts with an emphasis on 226Ra/Ba and 228Ra/226Ra in volcanic and hydrothermal processes at intraoceanic Arcs. *Economic Geology*, *107*(8), 1635–1648. https://doi.org/10.2113/econgeo.107.8.1635

Doyle, M. G., & Allen, R. L. (2003). Subsea-floor replacement in volcanic-hosted massive sulfide deposits. *Ore Geology Reviews*, *23*, 183–222. https://doi.org/10.1016/S0169-1368(03)00035-0

Elderfield, H., & Schultz, A. (1996). Mid-Ocean Ridge hydrothermal fluxes and the chemical composition of the ocean. *Ann. Rev. Earth Planet. Sci.*, *24*, 191–224.

Escartín, J., Soule, S. A., Cannat, M., Fornari, D. J., Düşünür, D., & Garcia, R. (2014). Lucky Strike seamount: Implications for the emplacement and rifting of segment-centered volcanoes at slow spreading mid-ocean ridges. *Geochemistry, Geophysics, Geosystems*, *15*, 4157–4179. https://doi.org/10.1002/2014GC005563.Received

Escartín, J., Barreyre, T., Cannat, M., Garcia, R., Gracias, N., Deschamps, A., et al. (2015). Hydrothermal activity along the slow-spreading Lucky Strike ridge segment (Mid-Atlantic Ridge): Distribution, heatflux, and geological controls. *Earth and Planetary Science Letters*, *431*, 173–185. https://doi.org/10.1016/j.epsl.2015.09.025

Escartín, J., Cannat, M., & Deschamps, A. (2021). Microbathymetry from AUV and ROV Surveys (MOMARETO'06, MOMAR'08-Leg1 and BATHYLUCK'09 cruises) along the Lucky Strike ridge segment (Mid Atlantic Ridge). *SEANOE*. https://doi.org/10.17882/80574

Fouquet, Y., Ondréas, H., Charlou, J. L., Donval, J.-P., Radford-Knoery, J., Costa, I., et al. (1995). Atlantic lava lakes and hot vents. *Nature*, *377*(6546), 201. https://doi.org/10.1038/377201a0

Franklin, J. M., Gibson, H. . L., Jonasson, I. R., & Galley, A. G. (2005). Volcanogenic Massive Sulfide Deposits. *Economic Geology 100th Anniversary Volume*, 523–560. https://doi.org/10.1016/B978-0-08-095975-7.01120-7

Galley, A. G., Hannington, M. D., & Jonasson, I. R. (2007). Volcanogenic massive sulphide deposits. *Geological Association of Canada*, (5), 141–161.

Galley, C., Lelièvre, P., Haroon, A., Graber, S., Jamieson, J. W., Szitkar, F., et al. (2021). Magnetic and Gravity Surface Geometry Inverse Modelling of the TAG Active Mound. *Journal of Geophysical Research: Solid Earth*.

German, C. R., & Angel, M. V. (1995). Hydrothermal fluxes of metals to the oceans: A comparison with anthropogenic discharge. *Geological Society Special Publication*, *87*(87), 365–372. https://doi.org/10.1144/GSL.SP.1995.087.01.28

Glen, S., 2021, Error Propagation (Propagation of Uncertainty): From StatisticsHowTo.com: Elementary Statistics for the rest of us!, https://www.statisticshowto.com/error-propagation/.

Golder Associates Pty. Ltd. (2012). Mineral resource estimate, Solwara projet, Bismarck Sea, PNG: Technical Report compiled under NI43-101.

Graber, S., Petersen, S., Yeo, I., Szitkar, F., Klischies, M., Jamieson, J. W., et al. (2020). Structural Control, Evolution, and Accumulation Rates of Massive Sulfides in the TAG Hydrothermal Field. *Geochemistry, Geophysics, Geosystems*. https://doi.org/10.1029/2020GC009185

Hannington, M. D. (2014). Volcanogenic Massive Sulfide Deposits. *Treatise on Geochemistry: Second Edition*, *13*, 463–488. https://doi.org/10.1016/B978-0-08-095975-7.01120-7

Hannington, M. D., Galley, A. G., Herzig, P. M., Petersen, S., & Charles, K. (1998). Comparison of the TAG mound and stockwork complex with Cyprus-type massive sulfide deposits. *Proceedings of the Ocean Drilling Programm, Scientific Results*, *158*, 389–415.

Hannington, M. D., Gemmell, T., & Monecke, T. (2017). The Kidd Creek Volcanogenic Massive Sulfide Deposit—An Update. In T. Monecke, P. Mercier-Langevin, & B. Dubé (Eds.), *Archean Base and Precious Metal Deposits, Southern Abitibi Greenstone Belt, Canada* (Vol. 19, pp. 81–102). Littleton, Colorado: Reviews in Economic Geology. https://doi.org/10.5382/Rev.19.03

Humphris, S.E., Fornari, D. J., Scheirer, D. S., German, C. R., & Parson, L. M. (2002). Geotectonic setting of hydrothermal activity on the summit of Lucky Strike Seamount (37°17'N, Mid-Atlantic Ridge). *Geochemistry, Geophysics, Geosystems*, *3*(8), 1–24. https://doi.org/10.1029/2001GC000284

Humphris, S. E., & Cann, J. R. (2000). Constraints on the energy and chemical balances of the modern TAG and ancient Cyprus seafloor sulfide deposits. *Journal of Geophysical Research*, *105*, 28477–28488.

Jamieson, J W, Clague, D. A., & Hannington, M. D. (2014). Hydrothermal sulfide accumulation

along the Endeavour Segment , Juan de Fuca Ridge. *Earth and Planetary Science Letters*, *395*, 136–148.

Jamieson, J. W., Hannington, M. D., Clague, D. A., Kelley, D. S., Delaney, J. R., Holden, J. F., et al. (2013). Sulfide geochronology along the Endeavour Segment of the Juan de Fuca Ridge. *Geochemistry, Geophysics, Geosystems*, *14*(7), 2084–2099. https://doi.org/10.1002/ggge.20133

Lalou, C., & Brichet, E. (1982). Ages and implications of East Pacific Rise sulphide deposits 21˚N. *Nature*, *300*, 169–171.

Lalou, C., Thompson, G., Arnold, M., Brichet, E., Druffel, E., & Rona, P. A. (1990). Geochronology of TAG and Snakepit hydrothermal fields, Mid-Atlantic Ridge: witness to a long and complex hydrothermal history. *Earth and Planetary Science Letters*, *97*, 113–128.

Lalou, C., Reyss, J.-L., Brichet, E., Arnold, M., Thompson, G., Fouquet, Y., & Rona, A. (1993). New Age Data for Mid-Atlantic Ridge Hydrothermal sites: TAG and Snakepit Chronology Revisited. *Journal of Geophysical Research*, *98(B6)*, 9705–9713. https://doi.org/10.1029/92JB01898

Lalou, C., Reyss, J.-L., Brichet, E., Rona, P. A., & Thompson, G. (1995). Hydrothermal activity on a 10(5)-year scale at a slow-spreading ridge, TAG hydrothermal field, Mid-Atlantic Ridge 26˚N. *Journal of Geophysical Research : Solid Earth*, *100*(B9), 17855–17862.

Langmuir, C., Humphris, S., Fornari, D., Van Dover, C., Von Damm, K., Tivey, M. K., et al. (1997). Hydrothermal vents near a mantle hot spot: the Lucky Strike vent field at 37°N on the Mid-Atlantic Ridge. *Earth and Planetary Science Letters*, *148*(1–2), 69–91. https://doi.org/10.1016/S0012-821X(97)00027-7

Langmuir, C. H., Klinkhammer, G., Bougault, H., & and Shipboard Scientific Party. (1992). *FAZAR Cruise Report*. Palisades, N.Y.

Lowell, R. P., Rona, P. A., & Von Herzen, R. P. (1995). Seafloor hydrothermal systems. *Journal of Geophysical Research*, *100*(10), 327–352.

Manor, M. J., Piercey, S. J., Wall, C. J., & Denisová, N. (2022). High precision CA-ID-TIMS U-Pb zircon geochronology of felsic rocks in the Finlayson Lake VMS district, Yukon : Linking Paleozoic basin-scale accumulation rates to the occurrence of sub-seafloor replacement-style mineralization. *Economic Geology*.

Mittelstaedt, E., Escartín, J., Gracias, N., Olive, J., Barreyre, T., Davaille, A., et al. (2012). Quantifying diffuse and discrete venting at the Tour Eiffel vent site, Lucky Strike hydrothermal field. *Geochemistry, Geophysics, Geosystems*, *13*(4). https://doi.org/10.1029/2011GC003991

Mosier, B. D. L., Berger, V. I., & Singer, D. A. (2009). *Volcanogenic Massive Sulfide Deposits of the World — Database and Grade and Tonnage Models*.

Münch, U., Lalou, C., Halbach, P., & Fujimoto, H. (2001). Relict hydrothermal events along the super-slow Southwest Indian spreading ridge near 63°56′E- Mineralogy, chemistry and chronology of sulfide samples. *Chemical Geology*, *177*(3–4), 341–349. https://doi.org/10.1016/S0009-2541(00)00418-6

Murton, B. J., Lehrmann, B., Dutrieux, A. M., Martins, S., de la Iglesia, A. G., Stobbs, I. J., et al. (2019). Geological fate of seafloor massive sulphides at the TAG hydrothermal field (Mid-Atlantic Ridge). *Ore Geology Reviews*, *107*(March), 903–925. https://doi.org/10.1016/j.oregeorev.2019.03.005

Ondréas, H., Cannat, M., Fouquet, Y., Normand, A., Sarradin, P. M., & Sarrazin, J. (2009). Recent volcanic events and the distribution of hydrothermal venting at the Lucky Strike hydrothermal field, Mid-Atlantic Ridge. *Geochemistry, Geophysics, Geosystems*, *10*(2). https://doi.org/10.1029/2008GC002171

Piercey, S. J. (2015). A semipermeable interface model for the genesis of sub-seafloor replacement-type volcanogenic massive sulfide (VMS) deposits. *Economic Geology*, *110*(7), 1655–1660.

de Ronde, C. E. J., Hannington, M. D., Stoffers, P., Wright, I. C., Ditchburn, R. G., Reyes, A. G., et al. (2005). Evolution of a Submarine Magmatic-Hydrothermal System : Brothers Volcano, Southern Kermadec Arc, New Zealand. *Economic Geology*, *100*, 1097–1133.

de Ronde, C. E. J., Walker, S. L., Ditchburn, R. G., Tontini, F. C., Hannington, M. D., Merle, S. G., et al. (2014). The Anatomy of a Buried Submarine Hydrothermal System , Clark Volcano , Kermadec Arc , New Zealand, 2261–2292.

Singh, S. C., Crawford, W. C., Carton, H., Seher, T., Combier, V., Cannat, M., et al. (2006). Discovery of a magma chamber and faults beneath a Mid-Atlantic Ridge hydrothermal field. *Nature*, *442*(7106), 1029–1032. https://doi.org/10.1038/nature05105

Spagnoli, G., Hannington, M. D., Bairlein, K., Hördt, A., Jegen, M., Petersen, S., & Laurila, T. (2016). Electrical properties of seafloor massive sulfides. *Geo-Marine Letters*, *36*, 235–245. https://doi.org/10.1007/s00367-016-0439-5

Tivey, M. K., Stakes, D. S., Cook, T. L., Hannington, M. D., & Petersen, S. (1999). A model for growth of steep-sided vent structures on the Endeavour Segment of the Juan de Fuca Ridge: Results of a petrologic and geochemical study. *Journal of Geophysical Research: Solid Earth*, *104*(B10), 22859–22883. https://doi.org/10.1029/1999JB900107

Wang, Y., Han, X., Jin, X., Qiu, Z., Ma, Z., & Yang, H. (2012). Hydrothermal Activity Events at Kairei Field, Central Indian Ridge 25°S. *Resource Geology*, *62*(2), 208–214. https://doi.org/10.1111/j.1751-3928.2012.00189.x

Zierenberg, R. A., Fouquet, Y., Miller, D. J., Bahr, J. M., Baker, P. A., Bjerkgard, T., et al. (1998). The deep structure of a sea-floor hydrothermal deposit. *Nature*, *392*(April), 485–488.

3. Effects of substrate composition and subsurface fluid pathways on the geochemistry of the seafloor hydrothermal deposits at the Lucky Strike Vent Field, Mid-Atlantic Ridge

3.1. Abstract

The Lucky Strike vent field, located on the Mid-Atlantic Ridge (MAR), is hosted on enriched mid-ocean ridge basalt associated with the nearby Azores hotspot. In this study, we present bulk rock geochemistry coupled with *in situ* sulfur isotope analysis of hydrothermal samples from Lucky Strike. We assess the geological controls on the differences in the major and trace element content and sulfur isotopic composition of the hydrothermal deposits within the vent field. The hydrothermal deposits contain elevated concentrations of elements typically enriched in E-MORB, such as Mo, Ba, and Sr, compared to typical values for other hydrothermal deposits hosted on the MAR. The range in sulfur isotope compositions of hydrothermal marcasite and chalcopyrite (-2.5 to 8.7‰) is similar to the range recorded at other sediment-free basalt-hosted seafloor hydrothermal sites. However, at Lucky Strike, the Capelinhos vent, situated 1.4 km east of the main field, is enriched in ^{34}S (by ~3.5‰ for both marcasite and chalcopyrite), relative to the main field. This difference reflects contrasting sub-seafloor fluid/rock interactions at these two sites, including sub-seafloor sulfide precipitation at the main field that results in <20% of reduced sulfur within the upwelling hydrothermal fluid reaching the seafloor. We also compare the geochemistry of the hydrothermal deposits at Lucky Strike to other hydrothermal sites along the MAR and show that the average hydrothermal deposit Ba/Co is useful to discriminate between E-MORB and other mafic/ultramafic hosted deposits.

3.2. Introduction

Sub-seafloor magmatism drives hydrothermal circulation and the formation of metal and sulfur-rich mineral deposits at or below the seafloor (Hannington, 2014; Lydon, 1988; Tivey, 2007). The geochemistry of seafloor hydrothermal deposits is controlled by several factors, including the composition of the sub-seafloor lithosphere with which the circulating fluids react, temperature, pressure, the presence and type of sediment, and magmatic volatile input into the system (Doe, 1994; Hannington et al., 1995, 2005). At Lucky Strike, a vent field located south of the Azores on the Mid-Atlantic Ridge (MAR), the deposits are composed largely of a suite of hydrothermal minerals (pyrite, chalcopyrite, sphalerite, marcasite, anhydrite, and amorphous silica) that are typical for basalt-hosted seafloor hydrothermal deposits (Fouquet et al., 1993; Kase et al., 1990; Langmuir et al., 1997; Petersen et al., 2000). However, the deposits at Lucky Strike also contain abundant barite, which Langmuir et al. (1997) link to an enriched mid-ocean basalt (E-MORB) substrate associated with the nearby Azores hotspot.

The mineralogy and distribution of major and trace metals within the Lucky Strike hydrothermal deposits are not uniform, suggesting vent field scale variations in vent fluid composition (Bogdanov et al., 2006; Chavagnac et al., 2018). Both spatial and temporal variations in fluid chlorinity and CO_2 concentrations have been documented, indicating sub-seafloor fluid phase separation and effects of magma replenishment, respectively (Chavagnac et al., 2018; Von Damm et al., 1998; Langmuir et al., 1997; Pester et al., 2012). Results from previous sulfur isotope analyses from the main field at Lucky Strike indicate typical $\delta^{34}S$ values for mid-ocean ridge hosted hydrothermal systems of between ~0 and 10‰ (Rouxel et al., 2004). In this study, we present new mineralogical, bulk geochemical, and *in situ* sulfur isotope data from hydrothermal samples (n=23) collected during the 2011–2015 MoMARsat maintenance cruises of the EMSO-Azores observatory (European Multidisciplinary Seafloor and water-column Observatory) from

several of the hydrothermal edifices at Lucky Strike (Cannat et al., 2011; Cannat and Sarradin, 2012; Blandin et al., 2013; Sarradin and Cannat, 2014, 2015). We document the spatial variations in composition (mineralogical, geochemical, and in S isotopes) of the hydrothermal deposits to 1) evaluate the mineralogical controls on minor and trace element partitioning within the deposits; and 2) link these variations to the geological controls on hydrothermal venting conditions at the vent field scale.

In this study we also further investigate the influence of the Azores hotspot on the composition of hydrothermal deposits along the MAR. We develop geochemical criteria based on major and trace element compositions of hydrothermal deposits from MAR-hosted vent fields to fingerprint specific host rock compositions, which can vary from E-MORB to ultramafic rock.

Insights into the local and regional geological controls on the compositions of seafloor hydrothermal deposits is becoming increasingly important due to the growing interest in the economic potential of these deposits. Large seafloor hydrothermal deposits with high concentrations of base and precious metals (e.g., Cu, Zn, Au, and Ag) are potential targets for future mining (Hannington et al., 2011; Petersen et al., 2016; Rona, 2003). However, environmentally deleterious metals such as As, Cd, Se, Sb, which occur as trace metals within the sulfide minerals can also accumulate (Fallon et al., 2019; Hannington et al., 1999; Layton-Matthews et al., 2008; Martin et al., 2019). Results from this study will contribute to the understanding of the controls of substrate composition on the metal endowment, and therefore provide a framework for predictive assessment of the economic potential and associated environmental risks of exploiting seafloor massive sulfide deposits (SMS) based on geological setting on mid-ocean ridges.

3.3. Geological setting

The Lucky Strike segment is located along the slow-spreading Mid-Atlantic Ridge, approximately 360 km southwest of the Azores archipelago, near the triple junction between the North American, African, and Eurasian plates (Figure 3.1) (Cannat et al., 1999; Escartín et al., 2001). This segment is currently spreading at a full rate of ~20–25 mm/yr (Cannat et al., 1999; Argus et al., 2011), and is bound to the north by a non-transform offset with the Menez Gwen segment and to the south by a non-transform offset with the North Famous segment (Figure 3.1). The Lucky Strike segment formed as a product of rifting of an oceanic plateau associated with the Azores hotspot that began at ~10 Ma (Cannat et al., 1999; Escartín et al., 2001; Gente et al., 2003). The melt anomaly associated with the Azores hotspot is propagating southward, along the ridge, forming a V-shaped ridge that indicates shallowing of the ridges and its flanks towards the Azores hotspot, which is interpreted based on gravity and bathymetric data as a temporal and spatial variations in melt supply to the ridge axis that result from ridge-hotspot interactions (Cannat et al., 1999; Escartín et al., 2001).

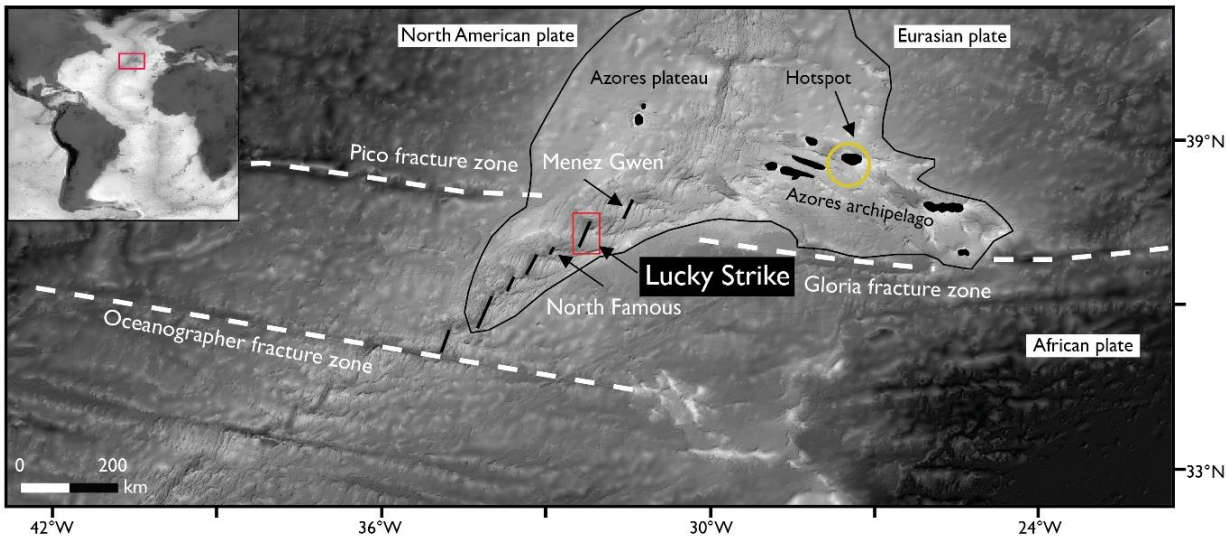

Figure 3.1. Location of the Lucky Strike segment on the Mid-Atlantic Ridge and its geotectonic context. The black outline highlights the bathymetric high of the Azores plateau and the yellow circle is the location of the Azores hotspot (Gente et al., 2003).

The Lucky Strike segment is ~70 km long, with a prominent axial volcano, named the Lucky Strike Seamount, that rises to 1500 mbsl in the central part of the segment from bathymetric lows of ~3500 mbsl towards the northern end of the segment and ~3200 mbsl towards the southern end of the segment, and is bounded by an overall ~20 km wide fault-bounded rift valley (Figure 3.2). Bathymetry and sidescan sonar imagery record cyclic volcanic (magmatic) crustal construction followed by tectonic (rifting) phases (Escartín et al., 2014). Recent volcanic episodes produced two volcanic centers that are aligned along the ridge axis and separated by a flat depression that is interpreted to be a recent but now fossil lava lake (Figure 3.3A) (Humphris et al., 2002; Ondréas et al., 2009). Both volcanic structures are now cut by a series of ridge-parallel normal faults, with the older, northern, volcanic edifice experiencing a higher degree of rifting than the younger, southern, volcanic edifice (Figure 3.3A) (Escartín et al., 2014; Humphris et al., 2002). The Lucky Strike rift valley floor is paved by volcanic rocks that range in composition from transitional mid-ocean ridge basalt (T-MORB) to E-MORB (Gale et al., 2011). Basalts with a more E-MORB

affinity are found towards the center of the segment, whereas the T-MORB compositions are distributed along the rest of the segment. The stratigraphy of the lava flows indicate that E-MORB lavas are crosscut by T-MORB lavas (Gale et al., 2011; Langmuir et al., 1997). Lava morphologies vary from sheeted flows to pillow lavas, with sheeted flows dominant in the neovolcanic zone that hosts the hydrothermal fields (Escartín et al., 2014; Gini et al. 2021).

Focused hydrothermal activity is restricted to the central region of the Lucky Strike Seamount (Figure 3.3). Seismic reflection studies have identified an axial magma chamber that lies ~3.5 km below the seafloor, and normal faults that propagate below the axial volcano (Singh et al., 2006; Combier et al., 2015). Microseismicity data suggest that hydrothermal circulation occurs primarily along-axis, and extends into the crust to within a few hundred meters of the axial magma chamber reflector in the narrow faulted area at the volcano summit (Crawford et al., 2013). The location of the vent field is also associated with a crustal magnetic low caused by hydrothermal alteration of the underlying rocks (Miranda et al., 2005).

At the vent field scale, venting and hydrothermal deposits are associated with normal faults and occur, for the most part, near a fossil lava lake at the volcano summit (Figure 3.3) (Barreyre et al., 2012; Escartín et al., 2015; Fouquet et al., 1994; Ondréas et al., 2009). Focused venting also occurs 1.4 km to the east of the central ridge axis at a site called Capelinhos (Escartín et al., 2015). The spatial association of hydrothermal venting with faulting suggest that faulting is the primary control on the location of fluid discharge (Barreyre et al., 2012; Escartín et al., 2015). Diffuse venting has been documented at Ewan, located 1.5 km south of the main field (Figure 3.3) (Escartín et al., 2015). The maximum temperature measured is 340°C at the main Lucky Strike field (South Crystal) and 324°C at Capelinhos (Barreyre et al., 2014; Chavagnac et al., 2018). The hydrothermal deposits at Lucky Strike were identified in previous studies via dredging, followed

by autonomous underwater vehicle (AUV) and remotely operated vehicle (ROV) bathymetric mapping coupled with photomosaic imaging (Barreyre et al., 2012; Escartín et al., 2015; Langmuir et al., 1997; Langmuir et al., 1992; Ondréas et al., 2009). Observations from time series imaging of the seafloor, acquired in 1996, 2006, 2008, and 2009, suggest that the heat flux associated with hydrothermal venting is decreasing, likely as a result of cooling of the axial magma chamber that is driving the fluid circulation in this system (Barreyre et al., 2012). Radioisotope (^{226}Ra) dating of hydrothermal barite indicates that hydrothermal venting at this site has been ongoing for at least 6,600 years and has accumulated at an average rate of ~194 t/yr (Sánchez-Mora et al., 2022).

Rock samples for this study were collected using the Victor 6000 ROV during the MoMARsat cruises from 2011 to 2015 on the R/V Pourquoi Pas ? and R/V Thalassa in 2012. Sampling mainly focused on hydrothermal deposits on several sites within the main vent field as well as on Capelinhos (Table *3.1*). Samples for the main field at Lucky Strike (n=19) and Capelinhos (n=4) range from sulfide blocks at the bases of hydrothermal edifices to active and inactive sulfide-rich chimneys and samples that precipitated on temperature probes (Table *3.1*).

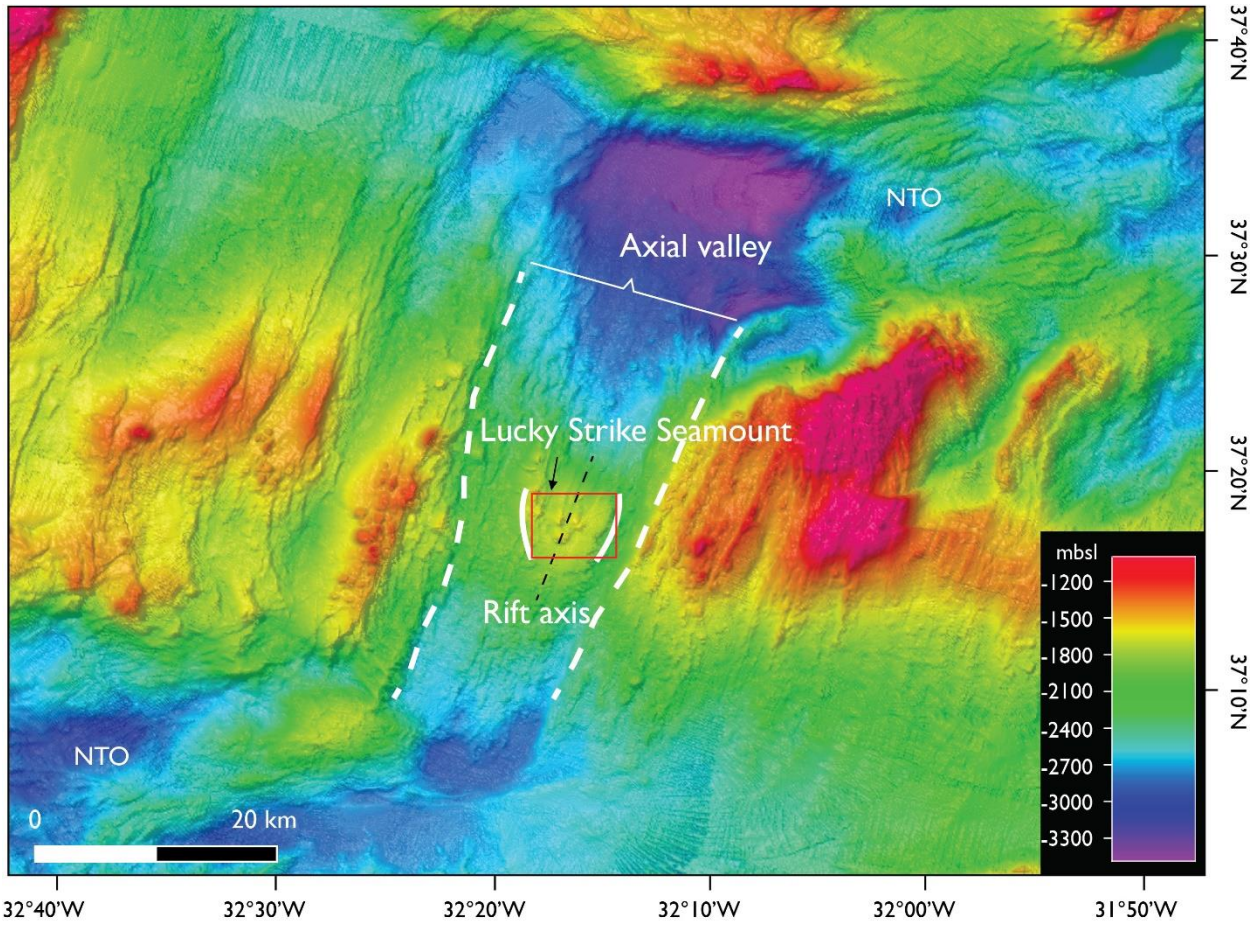

Figure 3.2. Segment scale bathymetric map of Lucky Strike (~40 m resolution). Red rectangle shows the area of study (Figure 3.3A). White solid lines show approximate extent of the Lucky Strike Seamount. The white dashed lines are the axial valley walls. NTO are non-transform offsets. Bathymetry from the Sudaçores cruise (Cannat et al., 1999; Escartín et al., 2001).

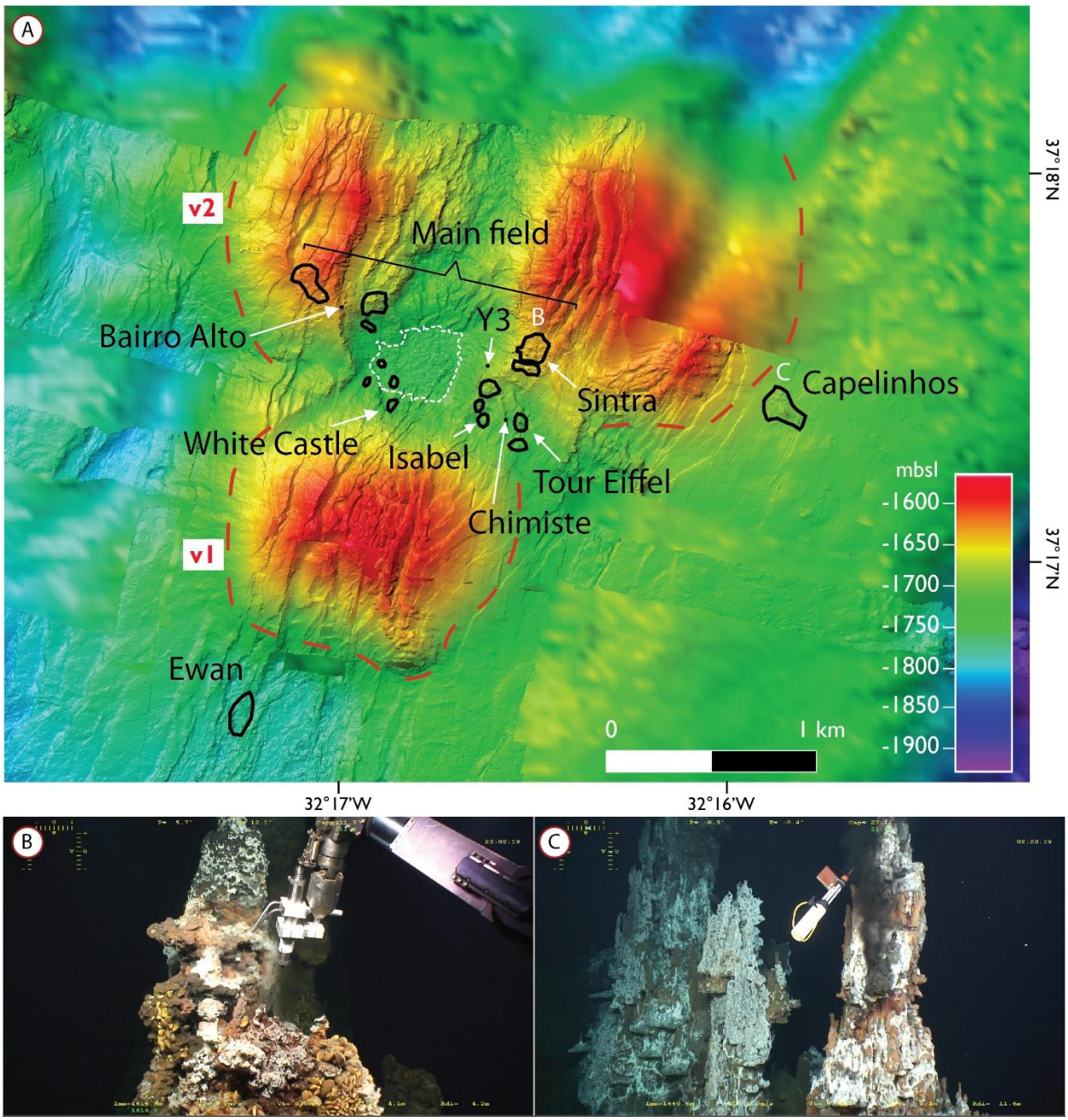

Figure 3.3. A) Outlines of the main hydrothermal areas from the Lucky Strike hydrothermal system. High temperature venting of 340°C (T_{max}) occurs at the main Lucky Strike hydrothermal field and 324°C fluid (T_{max}) at Capelinhos. Ewan is a site of diffuse venting (Barreyre et al., 2014; Escartín et al., 2015). The dashed red lines show the volcanic rifted structures v2 (higher degree of rifting) to the north and v1 in the south. White dashed outline is a fossil lava lake. B) Venting of 222°C fluid (T_{max});(Von Damm et al., 1998) at a sulfide chimney at the Sintra vent complex within the main Lucky Strike hydrothermal field. The length of the robotic arm is ~75 cm. C) Chimneys and high-temperature venting at the Capelinhos site (Chavagnac et al., 2018). The temperature probe is ~1 m long. Bathymetry sources: Ondréas et al. (2009) and Escartín et al. (2015).

3.4. Methodology

3.4.1. Bulk geochemistry

For bulk multi-element geochemistry, 23 samples were crushed at Memorial University using a ring pulverizer with a tungsten carbide grinding container and then analyzed at Activation Laboratories LTD (Actlabs, Ancaster, Ontario, Canada). Samples were analyzed using: 1) instrumental neutron activation analysis (INAA) for Au, Ag, As, Ba, Co, Fe, Na, Sb, Se, and Zn; and 2) Na_2O_2 fusion and inductively coupled plasma optical emission spectroscopy (ICP-OES) and mass spectrometry (ICP-MS) for Ca, Mo, Ni, Sr, Al, Cd, Cu, Ga, Ge, In, Mg, Mn, Pb, S, Si, Sn, Tl, and V (Hoffman, 1992). Accuracy and precision for INAA values are both better than ±5%, based on repeat (n=7) analysis of the GXR-1 standard. For the Na_2O_2 fusion ICP method, accuracy is better than ±7%, based on repeat (n=3) measurement of the OREAS 922 standard, with the exceptions of Ni and Sr, for which accuracy is 17%. Precision for the ICP method is better than 10%, except for Ni and Pb, which have precisions of 20% and 12%, respectively.

3.4.2. *In situ* sulfur isotope measurements

In situ sulfur isotope measurements were performed using a Cameca IMS 4f Secondary Ion Mass Spectrometer at the MAF-IIC Microanalysis Facility at Memorial University, following the methods of Brueckner et al. (2015). Sulfide-bearing samples (n=16) were embedded in epoxy in a 25.4 mm diameter aluminum ring and prepared as polished mounts, and sputter coated with 300 Å of Au to mitigate charging under primary ion bombardment. Isotopic analyses (n=52) were performed by bombarding the sample with a 0.8–1.0 nA primary ion microbeam accelerated through a 10 keV potential and focused into a 15-20 μm diameter spot. Each spot was pre-sputtered for 120 s using a 10 μm raster to exclude exotic material in the polished surface from the analysis. Negatively charged sputtered secondary ions were accelerated into the mass spectrometer through

a 4.5 keV potential. Signals for $^{32}S^-$, $^{34}S^-$ and a background position at 31.67 Da were obtained by cyclical magnetic peak switching. Standard counting time and peak sequence used were 0.5 s at the background position, 2.0 s on $^{32}S^-$, and 6.0 s on $^{34}S^-$. A typical analysis consisted of accumulating 80 peak cycles. All peak signals were collected with an ETP 133H multiple-dynode electron multiplier (em) and processed through ECL-based pulse-counting electronics with an overall dead time of 11 ns. The production and detection of sputtered secondary ions produces an instrumental mass fractionation (IMF) bias between the actual $^{34}S/^{32}S$ of the sample and that measured by the mass spectrometer. The magnitude of the IMF varies substantially between sulfide minerals. For this reason, the $^{34}S/^{32}S$ measured in samples of pyrite were corrected for IMF by comparison to replicate measurements of in-house reference materials UL9B (pyrite; $\delta^{34}S$: +16.3‰) and a Norilsk chalcopyrite ($\delta^{34}S$: +8.4‰). Measured $^{34}S/^{32}S$ values are transformed to the Vienna Cañon Diablo Troilite (V-CDT) scale using $^{34}S/^{32}S_{VCDT}$ = 0.0441626 (Ding et al., 2001). Data are presented in standard delta notation:

$$\delta^{34}S = \left(\frac{(R)_{sample}}{(R)_{V-CDT}} - 1\right) \times 1000$$

Where R = $^{34}S/^{32}S$. Analyses yield internal precisions on individual $\delta^{34}S$ determinations of better than ±0.3‰ (1σ) and the overall reproducibility, based on replicate standards analyses, is typically better than ±0.45‰ (1σ).

3.5. Results

3.5.1. Mineralogy and geochemistry

3.5.1.1. Mineralogy

Rock samples from Lucky Strike were collected primarily from the hydrothermally active Sintra, Tour Eiffel, Chimiste, Isabel, White Castle and Bairro Alto edifices (Figure 3.3A; Ondréas et al., 2009). Within the samples, mineral distributions change from the exterior to the interior of the chimneys, as typically described at black smoker deposits (Fouquet et al., 2010; Hannington et al., 1995; Haymon, 1983), with a lower temperature mineral assemblage of barite, anhydrite, marcasite, and pyrite with millimeter-scale goethite rims dominating the exterior of the chimney, and a higher-temperature mineral assemblage of sphalerite and chalcopyrite dominating the interior and lining fluid conduits (Figure 3.4A-E). Early marcasite forms plumose, colloform, or ring-like textures. Later stage marcasite is massive and euhedral. Subhedral to euhedral pyrite overgrows marcasite and is interpreted to have co-precipitated with sphalerite and exhibits a range of textures, from plumose to subhedral and massive (Figure 3.4D, F, G). Late stage chalcopyrite has massive and euhedral textures and is commonly replacing or overgrowing sphalerite (Figure 3.4D, H, I). Supergene alteration consists of exterior goethite rinds and atacamite (Figure 3.4F), and secondary covellite and bornite replacing chalcopyrite (Figure 3.4G). No major mineralogical differences are identified between Sintra, Tour Eiffel, and White Castle, except for an absence of pyrite in samples collected from Sintra, and absence of covellite in samples from White Castle.

Samples from Capelinhos show similar mineralogical assemblages and textural characteristics to the main Lucky Strike field, with lower temperature assemblages in the outer chimney walls that transition to higher temperature assemblages towards the interior. However, the primary difference is the occurrence of a second generation of sphalerite (Sph2), chalcopyrite (Cpy2), and barite (Ba2), that overprint previous generations (Figure 3.4G, H, I) suggesting temporal fluctuations in temperature of mineralizing fluids (Eldridge et al., 1983). Supergene alteration includes replacement of chalcopyrite by covellite and minor bornite, goethite, and atacamite.

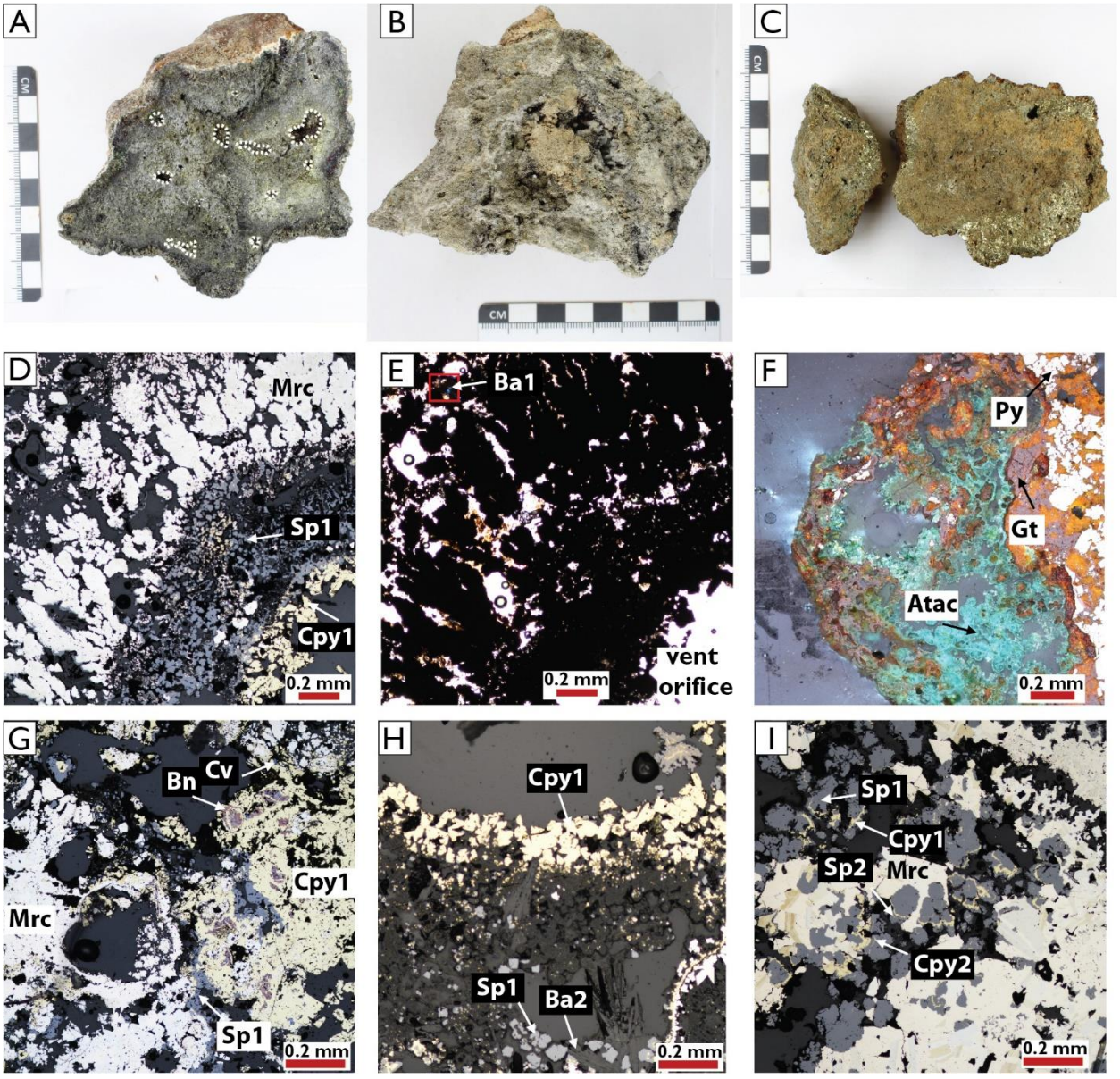

Figure 3.4. The main mineral assemblages of hydrothermal deposits at Lucky Strike. A) Typical chimney sample from Tour Eiffel (MOM14-579-ROC1) with sulfate and Fe-sulfide minerals dominating the exterior, and chalcopyrite and sphalerite in the interior, and lining the open fluid conduits (in white dashed lines). B) Sample collected from the side of the Sintra (MOM12-502-ROC1) edifice, with abundant barite, anhydrite, marcasite, and sphalerite. C) Chimney fragment from Tour Eiffel (MOM13-532-ROC2), dominated by marcasite and chalcopyrite. D) Typical mineralogical transition, from barite and marcasite towards the exterior, to sphalerite and chalcopyrite lining an interior high-temperature fluid conduit. Sample from the Tour Eiffel site (MOM14-579-ROC1). E) The same photomicrograph as D but under transmitted, crossed polarized light. F) Supergene alteration consisting of atacamite and goethite occurring on outer chimney walls. Sample from the Chimiste site (MOM15-PL607_ROC3). G) Supergene alteration, with minor bornite and covellite replacing chalcopyrite. Sample from the Capelinhos site (MOM14-PL583-ROC4). H) Sphalerite overgrown by chalcopyrite in a vent orifice and a second

generation of acicular barite infilling voids. Sample from the inner part of a chimney from Tour Eiffel (MOM14-579-ROC1). I) Sphalerite and chalcopyrite overgrown by a second generation of sphalerite and chalcopyrite and marcasite from the Capelinhos site (MOM14-PL583-ROC4). Images D, G, H, and I are plane-polarized reflected light photomicrographs. Image F was taken under cross-polarized reflected light.

3.5.1.2. Bulk geochemistry of hydrothermal deposits

Table *3.1* summarizes 28-element geochemical analysis of 19 sulfide-rich samples from Lucky Strike and sulfide-rich hydrothermal precipitates on the temperature probes. Notable results include average base metal concentrations of 7.2 wt.% Cu, with a range of 0.012–26.4 wt.% Cu, 5.9 wt.% Zn, with a range of 0.037–37.4 wt.% Zn, 6.5 wt.% Ba, with a range of 0.027–44.4 wt.% Ba, and 630 ppb Au, with a range of 8–2030 ppb Au. Additionally, the samples contain concentrations of Sr of up to 5940 ppm, Mo of up to 351 ppm, and Se of up to 2570 ppm. Rare earth element concentrations are generally below detection limits. There are no significant elemental enrichments or depletions associated with the different vent sites at Lucky Strike. The composition of the temperature probe precipitates have notably lower concentrations of Zn, Pb, Ba, Au, and Ag, compared to the chimney and crust samples.

Principal component analysis (PCA) was performed to identify statistical trends in the chimney sample geochemical dataset, using correlation matrices. The analysis was performed using the 28 elements of which at least 50% of the samples contained concentrations greater than their respective detection limits. Where reported concentrations were below detection limits, a value representing 65% of the detection limit was used (Palarea-Albaladejo et al., 2014). A sensitivity analysis using different thresholds for percentages of samples below detection limit and different values to represent the analyses below detection limit resulted in negligible changes to the results of the PCA analysis. A centred-log-ratio transformation was applied to the raw data to avoid

closure problems and spurious correlations (Pawlowsky-Glahn and Egozcue, 2006). The centred-log-ratio transformation (clr(x)) was calculated using the following equation:

$$\mathrm{clr}(\boldsymbol{x}) = [ln(x_1/(x_1 \cdot x_2 \ldots x_D))^{1/D}) , ln(x_2/(x_1 \cdot x_2 \ldots x_D))^{1/D}), \ldots, ln(x_D/(x_1 \cdot x_2 \ldots x_D)^{1/D})]$$

where D = the number of samples.

The PCA (Figure 3.5) reveals a cluster of elements associated with high-temperature sulfide minerals (e.g., Co, Cu, Se and Sn) with a negative PC1 loading, and a second cluster of elements associated with lower-temperature sulfide minerals (Ga, Sb, Zn, Cd, Mn, Si) with a positive PC1 loading. Principal component 2 has positive loadings for sulfide mineral associated elements (transition and post-transition metals), and negative loadings for sulfate and oxide minerals associated elements (alkaline earth metals such as Ba, Sr, Ca, and Mg) but also Ni. Principal component 1 accounts for 37% of the variability in the dataset and PC2 accounts for 17% of the variability.

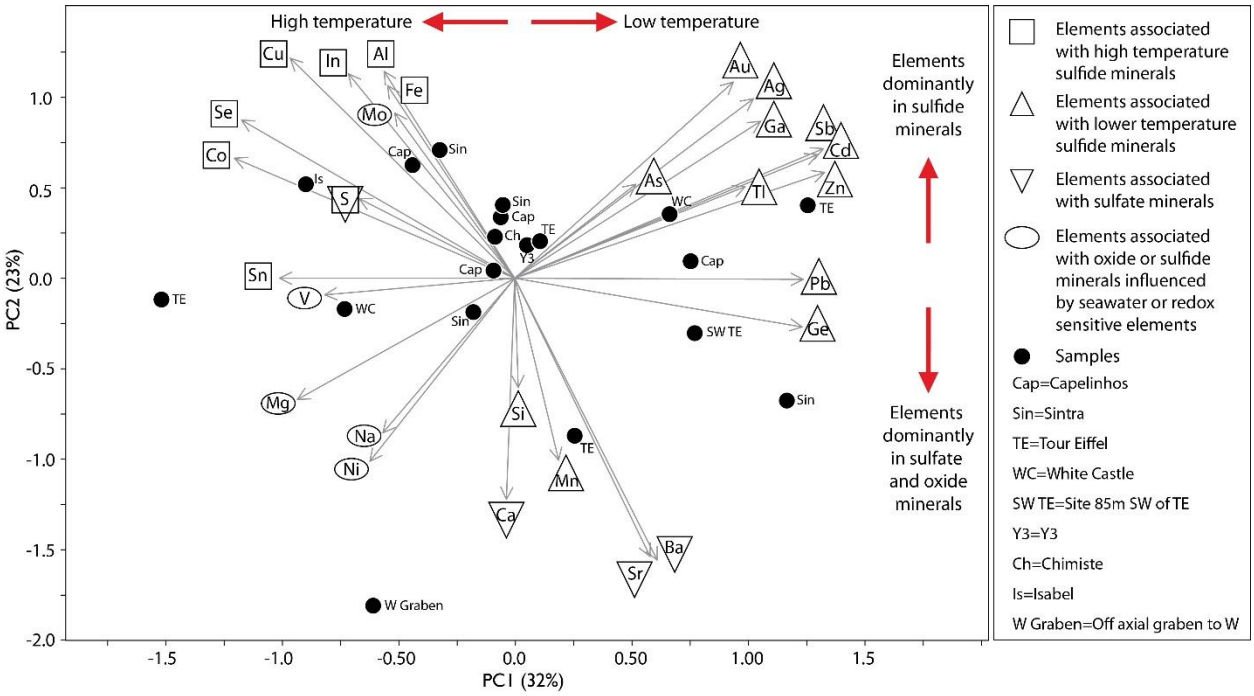

Figure 3.5. Principal component analysis of bulk rock geochemistry (black dots) from the main Lucky Strike and Capelinhos hydrothermal sites. Elements in squares are associated with high temperature sulfide minerals; elements in upright triangles are associated with lower temperature sulfide minerals; elements in inverted triangles are associated with sulfate minerals; elements in ovals are associated with seawater or redox sensitive (Mo, V, and Ni).

Table 3.1 Chemical composition of hydrothermal samples from Lucky Strike vent field (see Appendix 2 for full dataset that includes additional elements that were largely below detection limit).

Analyte Symbol	Latitude	Longitude	Description	IGSN	Cu (wt.%)	Zn (wt.%)	Pb (ppm)	Fe (wt.%)	S (wt.%)	Si (wt.%)	Al (wt.%)	Ca (wt.%)	Na (wt.%)	Mg (wt.%)	Ba (ppm)	Sr (ppm)	Mo (ppm)
Detection Limit					0.0002	0.001	0.8	0.01	0.01	0.01	0.01	0.01	0.001	0.01	20	3	1
Analysis Method					FUS	INAA	FUS	INAA	FUS	FUS	FUS	FUS	INAA	FUS	INAA	FUS	FUS
Capelinhos (1678 mbsl)																	
MOM14-583-ROC1-S	37.28973	-32.281042	Block from the base of Capelinhos edifice	CNRS0000007069	5.4	1.01	113	21.8	27	11.9	0.04	0.09	0.12	<0.01	45200	1150	33
MOM14-PL583-ROC4	37.289418	-32.263983	Fragment A of active chimney	CNRS0000007072	5.09	2.49	193	42.4	50.1	0.04	0.03	0.48	0.08	<0.01	1760	97	37
MOM14-PL583-ROC4	37.289418	-32.263983	Fragment B of active chimney	CNRS0000007072	11.4	1.53	137	40	45.3	0.22	0.11	0.05	0.22	<0.01	330	20	40
MOM13-528-ROC1-S	37.289467	-32.263972	Block from the base of Capelinhos edifice	N/A	0.0459	6.64	716	35.4	46.9	0.17	0.05	0.07	0.16	0.01	12900	737	69
Y3 (1730 mbsl)																	
MOM11-454-ROC7	37.291867	-32.277817	Base of small active chimney	CNRS0000007017	4.02	7.57	489	31.5	41.5	1.56	0.5	0.19	0.3	0.02	19300	850	318
White Castle (1705 mbsl)																	
MOM15-603-ROC5	37.28973	-32.281042	Block from active edifice	CNRS0000007099	1.41	27.6	887	12.3	34.7	2.94	0.64	0.07	0.25	0.03	4960	239	121
MOM15-603-ROC6	37.28973	-32.281042	Block from active edifice	CNRS0000007100	10.1	0.614	209	27.3	35.8	5.45	0.36	0.1	0.18	0.04	38300	1700	351
Off axial graben to the W (1612 mbsl)																	
MOM15-605-ROC2	37.295229	-32.284963	From inactive site	CNRS0000007103	0.035	0.048	31.3	0.56	6.29	0.6	<0.01	0.16	0.12	0.02	444000	5940	7
Tour Eiffel (1696 mbsl)																	
MOM11-457-ROC8	37.289033	-32.275667	Small inactive chimney W of Tour Eiffel	CNRS0000007018	1.52	37.4	823	17.5	38.5	0.95	0.08	0.1	0.06	<0.01	34500	1040	59
MOM14-579-ROC1	37.290722	-32.281038	Small inactive chimney	CNRS0000007062	7.36	7.62	454	28.5	36.7	5.36	0.61	0.1	0.19	0.01	23800	667	167
MOM13-532-ROC1	37.288933	-32.275417	Block in the E slope of Tour Eiffel		0.012	0.128	746	26.3	33.2	4.63	<0.01	0.1	0.14	<0.01	99400	2080	25
MOM13-532-ROC2	37.288933	-32.275417	Block of sulfide at base of Tour Eiffel	N/A	19.4	0.037	19.9	31.7	41.3	0.51	0.18	0.07	0.28	0.05	950	48	22
Site 85 m SW of Tour Eiffel (1691 mbsl)																	
MOM12-504-ROC1	37.288583	-32.276333	Block in inactive area 85 m SW of Tour Eiffel	CNRS0000007053	1.02	10.8	502	11.2	17.7	13.6	0.28	0.15	0.38	0.03	112000	1420	66
Sintra (1630 mbsl)																	

Analyte Symbol	Latitude	Longitude	Description	IGSN	Cu (wt.%)	Zn (wt.%)	Pb (ppm)	Fe (wt.%)	S (wt.%)	Si (wt.%)	Al (wt.%)	Ca (wt.%)	Na (wt.%)	Mg (wt.%)	Ba (ppm)	Sr (ppm)	Mo (ppm)
Detection Limit					0.0002	0.001	0.8	0.01	0.01	0.01	0.01	0.01	0.001	0.01	20	3	1
Analysis Method					FUS	INAA	FUS	INAA	FUS	FUS	FUS	FUS	INAA	FUS	INAA	FUS	FUS
MOM11-452-ROC1	37.292083	-32.274717	Small inactive chimney on sulfide-rich basement at the base of Sintra	CNRS0000007011	2.45	0.554	993	38.8	38.1	0.91	0.15	0.84	0.41	0.11	14200	407	67
MOM11-452-ROC2	37.292083	-32.2747	Fragments of inactive chimney	CNRS0000007012	25.6	0.593	379	31.9	37.4	0.32	0.15	0.04	0.21	0.02	310	24	100
MOM11-452-ROC3	37.292033	-32.274717	Fragments of inactive chimney	CNRS0000007013	26.4	1.57	306	26.7	33.5	1.77	0.26	0.06	0.21	0.03	2870	41	59
MOM12-502-ROC1	37.292167	-32.2750	Active chimney	CNRS0000007051	0.036	5.08	541	4.74	9.41	0.3	<0.01	0.17	0.29	<0.01	381000	5110	11
Isabel (1703 mbsl)																	
MOM15-PL607_ROC5	37.28912	-32.277405	Sulfide block	CNRS0000007108	13.5	0.22	177	35.1	40.3	0.51	0.23	0.05	0.23	0.03	380	23	267
Chimiste (1687 mbsl)																	
MOM15-PL607_ROC3	37.289291	-32.276545	Sulfide block	CNRS0000007106	1.27	0.562	354	30.3	38.6	12.3	0.19	0.04	0.2	<0.01	270	20	69
Temperature probe precipitates																	
Cyprès (1740 mbsl)																	
MOM14-HN29008-ROCK	37.290787	-32.280972	Precipitate on temperature probe	N/A	8.5	0.049	8.1	44.3	48.5	0.08	0.03	0.34	0.05	0.02	<20	36	6
Crystal (1730 mbsl)																	
HT010-CR12	37.29088	-32.28202	Precipitate on temperature probe	N/A	2.41	2.12	230	10.3	29.2	0.42	0.17	17.4	0.21	0.07	7420	2100	444
Cimendef (1702 mbsl)																	
MOM14-HT007-ROCK	37.288083	-32.275838	Precipitate on temperature probe	N/A	5.25	0.098	18.2	44.8	50.8	0.22	0.09	1	0.07	0.04	560	132	11
Y3 (1730 mbsl)																	
LS-BS-WHOI	37.29187	-32.27785	Precipitate on temperature probe	N/A	15.2	2.13	201	30.1	35.6	3.27	0.24	0.13	0.1	<0.01	32300	1360	212

FUS = analysis by ICP-OES or ICP-MS, with samples prepared by fusion with a Na_2O_2 flux
INAA = analysis by instrumental neutron activation

Table 3.1. *(continued)* Chemical composition of hydrothermal samples from Lucky Strike vent field (see Appendix 2 for full dataset that includes additional elements that were largely below detection limit).

Analyte Symbol	V (ppm)	Ni (ppm)	Co (ppm)	Se (ppm)	Au (ppb)	Ag (ppm)	As (ppm)	Ga (ppm)	Ge (ppm)	Sb (ppm)	Cd (ppm)	Tl (ppm)	In (ppm)	Sn (ppm)	Mn (ppm)
Detection Limit	5	10	0.1	0.5	2	2	1	0.2	0.7	0.1	2	0.1	0.2	0.5	3
Analysis Method	FUS	FUS	INAA	INAA	INAA	INAA	INAA	FUS	FUS	INAA	FUS	FUS	FUS	FUS	FUS
Capelinhos (1678 mbsl)															
MOM14-583-ROC1-S	<5	<10	277	<0.5	258	22	128	27.5	6.8	11.4	43	5.4	10.1	3.7	55
MOM14-PL583-ROC4	<5	10	158	131	256	21	291	27.4	14.8	15	55	16.2	2.6	5.3	76
MOM14-PL583-ROC4	9	10	258	150	237	22	229	15	10.8	11.4	30	5.5	6	3.3	38
MOM13-528-ROC1-S	<5	10	14.1	<0.5	323	39	236	51.4	22.8	49.9	213	61.9	1	1	91
Y3 (1730 mbsl)															
MOM11-454-ROC7	110	10	337	127	625	88	307	45.8	33.2	23.7	288	44	1.4	2.5	634
White Castle (1705 mbsl)															
MOM15-603-ROC5	<5	<10	64.6	42.6	748	152	277	63.8	60.8	50	1250	27.6	0.7	3.5	464
MOM15-603-ROC6	51	30	604	237	205	9	142	8.2	21.9	5	17	10.7	3.4	2.3	193
Off axial graben to the W (1612 mbsl)															
MOM15-605-ROC2	6	10	7.4	<0.5	8	<2	14	1.1	3.4	0.8	<2	<0.1	<0.2	1.7	369
Tour Eiffel (1696 mbsl)															
MOM11-457-ROC8	6	10	33	<0.5	2030	278	346	354	68.2	166	1700	42.6	5.7	1.1	424
MOM14-579-ROC1	122	40	107	179	724	76	387	62.6	29.8	36.9	288	38.5	4.2	2.3	349
MOM13-532-ROC1	<5	20	48.5	<0.5	309	<2	449	1.7	23.1	2.3	4	151	<0.2	1	205
MOM13-532-ROC2	12	10	167	2570	73	<2	99	1.7	5.7	1.6	<2	1.2	2.5	6.3	60
Site 85 m SW of Tour Eiffel (1691 mbsl)															
MOM12-504-ROC1	35	20	50.6	<0.5	1750	165	642	55.3	43	82.8	291	21.6	0.6	0.6	1240
Sintra (1630 mbsl)															
MOM11-452-ROC1	131	20	467	69.9	1340	49	635	46.5	19.9	39	9	23.4	12.7	1.1	1830
MOM11-452-ROC2	20	10	225	346	1010	94	223	36.5	19.5	19	25	6.5	10.5	4.2	113
MOM11-452-ROC3	16	10	47.5	106	677	59	242	28	24.1	28	59	13.4	6.9	1.6	153
MOM12-502-ROC1	<5	<10	8.5	<0.5	369	89	168	10.4	50.9	29.5	98	36.9	<0.2	0.9	65
Isabel (1703 mbsl)															

Analyte Symbol	V (ppm)	Ni (ppm)	Co (ppm)	Se (ppm)	Au (ppb)	Ag (ppm)	As (ppm)	Ga (ppm)	Ge (ppm)	Sb (ppm)	Cd (ppm)	Tl (ppm)	In (ppm)	Sn (ppm)	Mn (ppm)
Detection Limit	5	10	0.1	0.5	2	2	1	0.2	0.7	0.1	2	0.1	0.2	0.5	3
Analysis Method	FUS	FUS	INAA	INAA	INAA	INAA	INAA	FUS	FUS	INAA	FUS	FUS	FUS	FUS	FUS
MOM15-PL607_ROC5	44	10	409	907	539	44	268	5.1	6.9	6.3	6	9.8	6.3	5.9	211
Chimiste (1687 mbsl)															
MOM15-PL607_ROC3	<5	20	89.2	28.9	496	59	477	3.4	8.1	9.6	27	18.4	0.3	1	353
Temperature probe precipitates															
Cyprès (1740 mbsl)															
MOM14-HN29008-ROCK	<5	60	559	227	37	6	85	0.7	5.1	0.5	<2	<0.1	8.4	17.7	11
Crystal (1730 mbsl)															
HT010-CR12	57	1450	101	70.6	189	28	97	12.2	9.7	12.4	122	9.2	2.5	3	92
Cimendef (1702 mbsl)															
MOM14-HT007-ROCK	<5	20	86.8	385	47	<2	96	1.4	5.8	1.1	3	1.3	1.7	2.2	25
Y3 (1730 mbsl)															
LS-BS-WHOI	58	30	198	490	228	52	120	17.8	19.9	8.3	92	21	3.1	2.3	341

FUS = analysis by ICP-OES or ICP-MS, with samples prepared by fusion with a Na_2O_2 flux
INAA = analysis by instrumental neutron activation

Table 3.2. In situ sulfur isotope compositions of marcasite (mrc), pyrite (py), and chalcopyrite (cpy) from Lucky Strike. SEM= standard error of the mean.

	Mineral	Texture	Mineral assemblage	$\delta^{34}S$ (‰)	SEM
Capelinhos site					
MOM14-PL583-ROC4_Cpy1	Cpy	euhedral/massive	marcasite-chalcopyrite	7.7	0.5
MOM14-PL583-ROC4_Cpy3	Cpy	massive	chalcopyrite	6.3	0.2
MOM14-PL583-ROC4_Cpy1	Cpy	massive	chalcopyrite	6.5	0.2
MOM14-PL583-ROC4_Cpy2	Cpy	massive	chalcopyrite	6.5	0.2
MOM14-583-ROC1-S _Cpy1	Cpy	euhedral	marcasite-chalcopyrite	7.2	0.3
MOM14-583-ROC1-S _Cpy2	Cpy	euhedral/massive	marcasite-chalcopyrite	4.7	0.6
MOM13-528-ROC1-S_Cp1	Cpy	cpy disease	sphalerite-chalcopyrite	8.7	0.5
MOM13-528-ROC1-S_Mrc2	Mrc	plumose	marcasite-barite-sphalerite	3.4	0.3
MOM13-528-ROC1-S_Mrc1	Mrc	plumose	marcasite-barite-sphalerite	3.9	0.4
MOM14-583-ROC1-S_Mrc2	Mrc	massive/subhedral	marcasite-chalcopyrite	5.2	0.3
MOM14-583-ROC1-S_Mrc1	Mrc	atoll/ring	marcasite-chalcopyrite	4.0	0.8
MOM14-PL583-ROC4_Mrc1	Mrc	atoll/ring	marcasite	1.7	0.6
MOM14-PL583-ROC4_Mrc2	Mrc	euhedral/massive	marcasite	4.4	0.7
Main Field-Chimiste					
MOM15-PL607_ROC3_Mrc1	Mrc	euhedral	marcasite	-0.5	0.3
Main Field-Isabel					
MOM15-PL607_11_ROC5_Cpy1	Cpy	massive	marcasite-chalcopyrite	2.8	0.2
MOM15-PL607_11_ROC5_Cpy2	Cpy	euhedral	marcasite-chalcopyrite	2.8	0.5
MOM15-PL607_11_ROC5_Mrc1	Mrc	colloform	marcasite-chalcopyrite	-2.4	0.3
MOM15-PL607_11_ROC5_Mrc2	Mrc	plumose	marcasite-chalcopyrite	-0.7	0.4
Main Field-Sintra					
MOM11-452-ROC3_Cpy2	Cpy	euhedral/massive	chalcopyrite-sphalerite	2.0	0.3
MOM11-452-ROC3_Cpy1	Cpy	euhedral/massive	chalcopyrite-sphalerite	3.3	0.4
MOM11-452-ROC3_Cpy3	Cpy	euhedral/massive	chalcopyrite	2.1	0.3
MOM11-452-ROC2_Cpy2	Cpy	massive	chalcopyrite-marcasite-covellite	4.7	0.4
MOM11-452-ROC2_Cpy1	Cpy	massive	chalcopyrite-marcasite-covellite	6.0	0.4
MOM11-452-ROC3_Mrc1	Mrc	atoll/ring	marcasite-chalcopyrite	-0.7	0.3
MOM11-452-ROC1_Mrc2	Mrc	colloform	marcasite-barite	-0.6	0.4
MOM12-502-ROC1_Mrc1	Mrc	colloform	marcasite-barite	1.1	0.5
MOM11-452-ROC1_Mrc1	Mrc	colloform	marcasite-barite	1.1	0.6
MOM11-452-ROC2_Mrc1	Mrc	euhedral	marcasite-chalcopyrite	0.9	0.3
Main Field-Tour Eiffel					
MOM13-532-ROC2_Cpy1	Cpy	massive	marcasite-chalcopyrite	4.3	0.3

	Mineral	Texture	Mineral assemblage	$\delta^{34}S$ (‰)	SEM
MOM11-457-ROC8_Cpy1	Cpy	massive	chalcopyrite-sphalerite	4.8	0.3
MOM14-579-ROC1_Cpy3	Cpy	euhedral	chalcopyrite-sphalerite	5.3	0.4
MOM13-532-ROC2_Mrc1	Py	euhedral/massive	marcasite-chalcopyrite	1.6	0.3
MOM12-504-ROC1_Mrc1	Mrc	colloform	barite-marcasite	-0.3	0.6
MOM11-457-ROC8_Mrc1	Mrc	plumose	marcasite-barite	0.1	0.4
MOM13-532-ROC1_Mrc2	Mrc	colloform	marcasite	0.9	0.3
MOM13-532-ROC1_Mrc6	Mrc	colloform	marcasite	0.9	0.3
MOM13-532-ROC1_Mrc4	Mrc	colloform	marcasite	1.0	0.2
MOM13-532-ROC1_Mrc3	Mrc	colloform	marcasite	1.1	0.2
MOM13-532-ROC1_Mrc5	Mrc	colloform	marcasite	1.3	0.3
MOM13-532-ROC1_Mrc7	Mrc	massive	marcasite-sphalerite	1.4	0.5
MOM13-532-ROC1_Mrc1	Mrc	colloform	marcasite	1.5	0.7
MOM14-579-ROC1_Mrc2	Mrc	plumose	barite-marcasite	1.3	0.3
MOM14-579-ROC1_Mrc1	Mrc	atoll/ring	barite-marcasite	2.0	0.3
Main Field-White Castle					
MOM15-603-ROC6_Cpy1	Cpy	euhedral	chalcopyrite-sphalerite	3.1	0.4
MOM15-603-ROC6_Mrc1	Py	euhedral	marcasite	1.5	0.3
Main Field-Y3					
LS-BS-WHOI_Cpy3	Cpy	euhedral	chalcopyrite-sphalerite	1.0	0.3
LS-BS-WHOI_Cpy1	Cpy	euhedral	chalcopyrite-sphalerite	1.8	0.4
LS-BS-WHOI_Cpy2	Cpy	euhedral	chalcopyrite-sphalerite	1.8	0.5
MOM11-454-ROC7_Cpy1	Cpy	euhedral	chalcopyrite-sphalerite	3.7	0.4
LS-BS-WHOI_Mrc1	Mrc	plumose	marcasite-barite	-1.0	0.3
MOM11-454-ROC7_Mrc1	Mrc	plumose	marcasite	-2.5	0.2
MOM11-454-ROC7_Mrc2	Py	plumose/euhedral	marcasite	-0.8	0.3

3.5.2. *In situ* sulfur isotopes

Table *3.2* summarizes results from *in situ* sulfur isotope measurements for marcasite and chalcopyrite (Figure 3.6 and 3.7). The $\delta^{34}S$ values for marcasite and pyrite (n=30) average 1.0‰ ($1\sigma = 1.8$) and vary from -2.5 to 5.2‰. Values for chalcopyrite (n=22) average 4.4‰ ($1\sigma = 2.1$) and range from 1.0 to 8.7‰. Notable low (negative) $\delta^{34}S$ values of -2.5 and -2.4‰ where obtained on marcasite from the Y3 and Isabel sites, respectively, which are part of the main field. Average marcasite and chalcopyrite sulfur isotope compositions from

the main field (0.3‰, n=24, and 3.3‰, n=15, respectively) are lower than those for Capelinhos (3.7‰, n=6, and 6.8‰, n=7, respectively; Figure 3.7). Marcasite $\delta^{34}S$ values do not vary significantly as a function of texture at the main field (Figure 3.6). At both sites, chalcopyrite is, on average, isotopically heavier by ~3‰ than marcasite (Figure 3.7). There is no apparent correlation between $\delta^{34}S$ values and age for the seventeen samples for which both S isotope and age data are available (Sánchez-Mora et al., 2022).

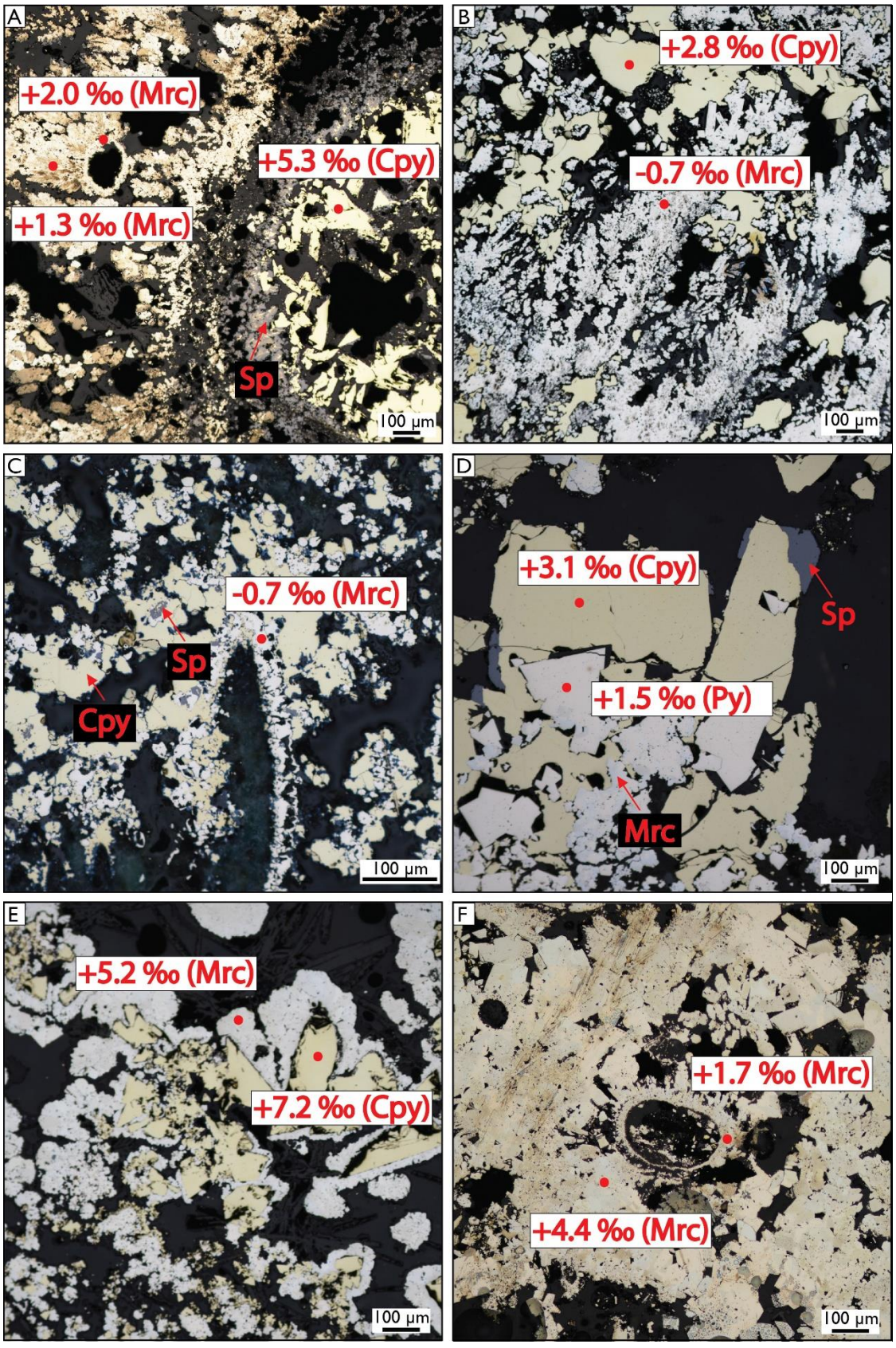
A
+2.0 ‰ (Mrc)
+5.3 ‰ (Cpy)
+1.3 ‰ (Mrc)
Sp
100 µm
B
+2.8 ‰ (Cpy)
-0.7 ‰ (Mrc)
100 µm
C
-0.7 ‰ (Mrc)
Sp
Cpy
100 µm
D
+3.1 ‰ (Cpy)
Sp
+1.5 ‰ (Py)
Mrc
100 µm
E
+5.2 ‰ (Mrc)
+7.2 ‰ (Cpy)
100 µm
F
+1.7 ‰ (Mrc)
+4.4 ‰ (Mrc)
100 µm

Figure 3.6. Thin section photomicrographs (plane polarized reflected light) showing locations of $\delta^{34}S$ spot analysis: A) Partially infilled vent orifice with a low-temperature assemblage of atoll-like marcasite with plumose marcasite overgrowths, barite and sphalerite, overprinted by high-temperature euhedral chalcopyrite. Sample from the Tour Eiffel site (MOM14-579-ROC1). B) Plumose marcasite overprinted by euhedral chalcopyrite. Samples from the Isabel site (MOM15-PL607-ROC5). C) Atoll-like marcasite overprinted by massive chalcopyrite. Sample from the Sintra site (MOM11-452-ROC3). D) Euhedral pyrite overprinted by euhedral chalcopyrite. Sample from the White Castle site (MOM15-603-ROC6). E) Anhedral marcasite with later anhedral chalcopyrite infilling. Sample from the Capelinhos site (MOM14-583-ROC1-S). F) Atoll-like marcasite overprinted by massive marcasite. Sample from Capelinhos (MOM14-PL583-ROC4). All the spot analyses in photomicrographs can be found in Appendix 5.

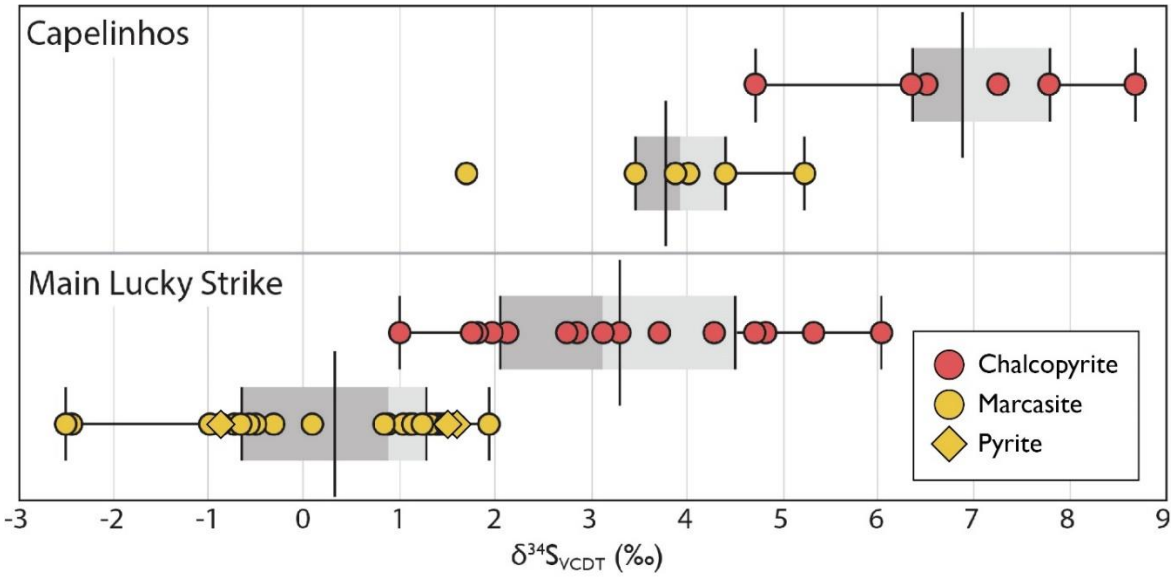

Figure 3.7. Box plot of in situ sulfur isotope $\delta^{34}S$ values for marcasite, pyrite, and chalcopyrite at Lucky Strike, divided by sites. Box and whiskers of quartiles, boxes represent 50% of the data, median is between the boxes, and black line is the average.

3.6. Discussion

The bulk, minor and trace element geochemical data presented in this study expands on the data originally presented by Bogdanov et al. (2006) by including a more extensive suite of elements such as Au, Ag, As, Ba, Mo, Sb, Se, Sb, Si, and Sn (see Table *3.1*). Additionally,

this study includes data from samples from other areas of the vent field not included in the study by Bogdanov et al. (2006), including the Capelinhos site, for which no data has been published to date. Results from the principal component analysis reflect the strong temperature control and influence of seawater on the mineral associations and trace element distributions within the deposits (Figure 3.5). An analysis of the distribution of the different sites within the Lucky Strike vent field that occur at different water depth within the field (Table *3.1*) over the PC1 and PC2 space contrast with the interpretation of Bogdanov et al. (2006), who suggested that, due to phase separation occurring at the seafloor or in the shallow sub-seafloor, the highest temperature fluids occur at the deepest vents within the vent field. This phase separation was hypothesized to be a main control on the variability of composition of the hydrothermal deposits (Bogdanov et al., 2006). However, our data indicates no systematic variation in bulk geochemistry with water depth or deposit age (~6,600 years to present; Sánchez-Mora et al., 2022). Therefore, differences in mineral assemblages and geochemistry likely only reflects the stage (low- or high- temperature) at which the sample was formed and not necessarily linked to phase separation.

3.6.1. Controls on minor and trace element distributions at Lucky Strike and other MAR black smoker fields

Minor and trace elements occur within the main mineral phases (chalcopyrite, marcasite, pyrite and sphalerite) in hydrothermal sulfide deposits and can be incorporated into their crystal structure or can occur as micro- or nano-scale inclusions as well as in gangue minerals (Cook et al., 2016; Monecke et al., 2016; Fontboté et al., 2017). Minor and trace element distribution is generally evaluated via microanalytical techniques such as an

electron microprobe and/or laser ablation ICP-MS (e.g., Berkenbosch et al., 2019; Grant et al., 2018; Keith et al., 2016; Melekestseva et al., 2017). Our approach uses PCA on bulk geochemistry of hydrothermal samples from the Lucky Strike vent field to determine the minor and trace element variability, which we compared to previous geochemical work conducted at Lucky Strike by Bogdanov et al. (2006) and compared to other similar studies on mid-ocean ridges.

The mineralogy of the Lucky Strike hydrothermal deposits are typical for basalt hosted mid-ocean ridge deposits, which is generally dominated by marcasite, pyrite, sphalerite, and chalcopyrite with the notable exception of the high abundance of barite, which has been linked to high Ba concentrations in the underlying E-MORB substrate (Langmuir et al., 1992). High-temperature interiors of chimneys are dominated by chalcopyrite and euhedral pyrite and marcasite. Concentrations of In, Se, Co and Sn correlate with the major mineral-forming elements (Cu, Fe, and S) that comprise this high-temperature mineral assemblage (Figure 3.5). These associations have been documented in other seafloor hydrothermal sites (e.g., Auclair et al., 1987; Hannington et al., 1991). Cobalt has been previously documented to be concentrated in marcasite and pyrite at Lucky Strike (Bogdanov et al., 2006). The correlation between Co with Cu and Fe that are associated with the precipitation of minerals at high-temperatures suggests that Co is hosted in euhedral pyrite and marcasite that precipitated associated with these high-temperature mineral assemblages (Figure 3.5). At the basalt-hosted TAG hydrothermal field further south on the MAR, In is hosted primarily as a trace metal within chalcopyrite and marcasite, Sn is largely hosted within chalcopyrite, and Se is largely hosted in chalcopyrite and pyrite to a lesser extent (Grant et al., 2018). Similarly, Lein et al. (2010) and Bogdanov et al. (2008) report high concentrations of In

within high-temperature mineral assemblages at Menez Gwen and Broken Spur, respectively, both also located at the MAR to the North and South of Lucky Strike, respectively. Selenium has also been documented to occur primarily within chalcopyrite at Lucky Strike (Rouxel et al., 2004), but also in pyrite in a range of other seafloor hydrothermal deposits (e.g., Monecke et al., 2016, and references therein). Selenium commonly substitutes for S in Cu and Fe sulfides (Monecke et al., 2016, and references therein). The PCA results show a strong correlation between Se and Cu for both PC1 and PC2, confirming the results of Rouxel et al. (2004) that the Se at Lucky Strike is likely hosted primarily in chalcopyrite. Cobalt often substitutes for Fe in pyrite, sphalerite, or chalcopyrite (Grant et al., 2018). At Lucky Strike, Co, like Se, correlates strongly with Cu and is also likely primarily substituting in chalcopyrite or high-temperature pyrite (Figure 3.5). Indium commonly substitutes for Zn in sphalerite or Fe in chalcopyrite, or it can occur as inclusions in pyrite (Monecke et al., 2016; Grant et al., 2018). The PCA results indicate that either chalcopyrite or pyrite is the primary mineral host for In at Lucky Strike (Figure 3.5).

The lower temperature exteriors of chimneys from Lucky Strike are dominated by sphalerite (ZnS), barite ($BaSO_4$), plumose marcasite and amorphous silica. Silver, Au, As, Ga, Cd, Sb, Tl, Pb, and Ge abundances correlate with the major mineral-forming elements (Zn, Ba, and Si) of this lower temperature mineral suite. The association of some of these trace elements (As, Sb, Cd, Mn, and Ag) with lower temperature minerals in the PCA (Figure 3.5) such as marcasite and sphalerite has been documented at Lucky Strike (Bogdanov et al., 2006) as well as at other hydrothermal deposits hosted on the MAR, including Menez Gwen (Lein et al., 2010), TAG (Grant et al., 2018), Broken Spur

(Bogdanov et al., 2008). Arsenic and antimony typically substitute for Fe in pyrite but Sb can also occur as inclusions in sphalerite (Monecke et al., 2016; Grant et al., 2018). The PCA results show a strong correlation between Sb and Zn, suggesting that Sb is largely hosted as inclusions in sphalerite (Figure 3.5). Arsenic has a weaker correlation with Zn, suggesting that sphalerite is not the only mineralogical host for As. The PCA shift for As towards Fe suggests that pyrite may be a secondary host (Figure 3.5). Gallium and germanium commonly substitute for Zn in sphalerite, and both elements correlate closely with Zn at Lucky Strike (Grant et al., 2018). Thallium can typically occur as a substitution for Fe or Zn in pyrite or sphalerite but can also be incorporated as inclusions (Grant et al., 2018). The PCA results suggest that, at Lucky Strike, Tl is primarily substituting for forming inclusions in sphalerite.

The elements Ca, Ba, and Sr, which are associated with the sulfate minerals anhydrite and barite, have a distinct negative loading with respect to PC2. Barium and Sr have minor positive loadings and Ca has a minor negative loading with respect to PC1 (Figure 3.5). The minor negative loading of Ca with respect to PC1 is consistent with anhydrite occurring primarily in association with the high-temperature sulfide mineral suite due to its absence at lower temperatures due to its retrograde solubility at temperatures below 150°C (Blount and Dickson, 1969). In contrast, Ba and Sr have a positive loading with respect to PC1, consistent with the typical association of barite with lower-temperature sulfide minerals (Jamieson et al., 2016). The proximity of Sr to Ba in Figure 3.5 is likely the result of barite being significantly more abundant than anhydrite at Lucky Strike, as indicated by the higher Ba concentrations (and higher barite contents) in the samples compared to Ca.

Magnesium, V, Ni, and to a lesser extent, Mo and Na have a negative loading with respect to PC1 (Figure 3.5). At TAG, redox-sensitive elements such as V, Ni, and Mo are associated with the precipitation of pyrite and marcasite that has interacted with cold, Na- and Mg-rich seawater towards the exteriors of vents (Grant et al., 2018). Alternatively, Ni, and V can also be associated with the formation and scavenging of Fe-oxyhydroxides (German and Seyfried, 2014). Regardless, the negative loading with respect to PC2 discriminates elements associated with sulfate and oxide minerals that precipitate upon direct interactions with seawater, which is consistent with the three samples with the lowest PC2 loadings that are barite and Fe-oxyhydroxides rich. Overall, the PCA effectively differentiates the elemental associations that are controlled mainly by temperature and the main mineral types (sulfide, sulfate, oxides, or oxyhydroxide minerals).

3.6.2. Differences in S isotope compositions between the main Lucky Strike field and Capelinhos

The overall sulfur isotope compositions of the sulfide deposits at Lucky Strike range between -2.5 and 8.7‰ (Figure 3.7), which is within the range of average $\delta^{34}S$ values for sulfide minerals at other sediment-free and basalt-hosted mid-ocean ridge hydrothermal deposits (Hannington et al., 2005; Zeng et al., 2017). The range in $\delta^{34}S$ values for the main field reported in this study are similar to those reported by Rouxel et al. (2004). The mineralogy of the Capelinhos site is similar to the mineralogy of the deposits at the main field, which is consistent with evidence from vent fluid trace element concentrations that correlate with chlorinity and indicate a common hydrothermal fluid source for these sites (Chavagnac et al., 2018). However, the S isotope compositions of sulfide minerals from

Capelinhos are ~3.5‰ higher than the average values at the main field (Figure 3.7). The range at Capelinhos is comparable to other sediment-free fast to slow spreading mid-ocean ridges sites such as TAG, East Pacific Rise South, and Axial Seamount (Hannington et al., 2005; Zeng et al., 2017).

At mid-ocean ridge-hosted hydrothermal sites, $\delta^{34}S$ values of between ~0 and 10‰ are typically interpreted to be a result of two component mixing between igneous-derived sulfur ($\delta^{34}S \approx 0$‰) leached from mid-ocean ridge crust and seawater sulfate ($\delta^{34}S = 21$‰); (Hannington et al., 2005; Shanks, 2001; Zeng et al., 2017). It is possible that the more positive $\delta^{34}S$ values for sulfide minerals at Capelinhos are due to a higher relative contribution of reduced sulfur derived from seawater sulfate or a longer fluid flow pathway feeding the Capelinhos vents, or a combination of both (Chavagnac et al., 2018; Escartín et al., 2015). Also, in sediment free environments, the addition of isotopically-light H_2S associated with disproportionation of magmatic SO_2 can also drive the overall system towards lower $\delta^{34}S$ values (Gamo et al., 1997; Shanks, 2001; McDermott et al., 2015). Fluctuations in vent fluid CO_2 content (Pester et al., 2012) and recent magmatic intrusions detected from seismicity at Lucky Strike (Dziak et al., 2004) indicate that magmatic volatiles may contribute to the hydrothermal system. A higher proportion of such volatiles could result in the relatively lower $\delta^{34}S$ values in the hydrothermal precipitates in the main field. However, CO_2 fluid data is not available for Capelinhos to assess differences in volatile input between this site and the main field. In addition, there is no mineralogical evidence of direct magmatic volatile input, such as the presence of high-sulfidation alteration assemblages, sulfosalts, and elevated concentrations of volatile associated trace elements such as Bi, Se, and Te (de Ronde et al., 2011; Martin et al., 2019). Rouxel et al.

(2004) speculated that, at Lucky Strike, there is also a component of a fractionated sulfur source associated with microbial activity below the fossil lava lake. These interpretations highlight the ambiguity inherent in the interpretation of $\delta^{34}S$ values on their own and the requirement of additional information to assess processes driving different sulfur isotope compositions at Lucky Strike.

Vent fluids at the main field are also depleted in Fe, enriched in Cl, and contain higher $^{87}Sr/^{86}Sr$, relative to Capelinhos fluids (Chavagnac et al., 2018). Chavagnac et al. (2018) interpret the higher $^{87}Sr/^{86}Sr$ at the main field to indicate higher water/rock ratios, even though the field lies directly above the heat source and the overall flow pathway is likely shorter. Longer residence times for fluids venting at the main field may result from locally reduced permeability. The fossil lava lake may act as a hydrological cap for ascending fluids, promoting lower overall permeabilities in the subsurface (Arnulf et al., 2014) leading to increased interaction with altered basalts, thus driving the $\delta^{34}S$ values of the fluids and deposits closer to zero (Figure 3.8).

Chavagnac et al. (2018) report a ~65% depletion in the dissolved Fe concentration of the fluids from the main field, relative to Capelinhos. Concentrations of other dissolved species (e.g., Mg, Mn, Na, and SO_4) and vent fluid pH indicate that this depletion is not a result of seawater dilution. Therefore it was suggested that significant amounts of precipitation of Fe-bearing minerals occurs in the sub-seafloor below the main field (Chavagnac et al., 2018). The precipitation of pyrite/marcasite would result in a temperature-dependent S isotope fractionation between the precipitated pyrite/marcasite and reduced S in the fluid. The fraction of reduced S removed from the fluid due to sub-seafloor pyrite/marcasite

precipitation can be modelled over a range of temperatures as an open system Rayleigh distillation:

$$R = R_0 f^{(\alpha-1)}$$

where R is the isotopic ratio of the fraction f of reduced sulfur remaining in the fluid after pyrite/marcasite precipitation, R_0 is the initial sulfur isotope ratio of the fluid, and α is the fractionation factor ($\alpha = R_{Py}/R_{H2S}$). Compared to the vent fluids at the main field, the composition of the endmember venting fluids at Capelinhos have been interpreted to be more representative of the fluids within the deeper part of the hydrothermal reaction zone, based on the linear correlation of trace elements and chlorinity in the hydrothermal fluids at Lucky Strike (Pester et al., 2012; Chavagnac et al., 2018). The $\delta^{34}S$ values from sulfide minerals at Capelinhos can therefore be used to represent R_0 (i.e., the isotopic composition of the ascending fluids below the main field) and the $\delta^{34}S$ values from the main field represent R. The temperature dependent fractionation factors (α), determine the different mass fractions (f) at which the ~3.5‰ difference between Capelinhos and main Lucky Strike can be obtained. If fractionation factors are used between H_2S and pyrite (Ohmoto and Rye, 1979) from 150 and 350°C , fractions of 0.21 to 0.034 are obtained, respectively (Hannington, 2014).

Results from sulfur isotope modelling suggest that at least ~80% of the original H_2S in the hydrothermal fluid at the main field precipitated below the seafloor, dominantly as pyrite/marcasite (Figure 3.8). A similar proportion (75%) of major and trace element deposition below the seafloor has been estimated at the seawater-dominated Reykjanes geothermal system in Iceland, which is considered an analogue to seafloor systems (Grant

et al., 2020). The average value of H_2S in hydrothermal fluids at the main field vents is 2.7 mmol/kg (Charlou et al., 2000). If this value represents less than 20% of the original H_2S concentration, the original fluid H_2S concentration would have been greater than ~14 mmol/kg. The amount of reduced S trapped in the subsurface as pyrite/marcasite is reasonably consistent with the amount of Fe estimated to have been trapped in the subsurface based on differences in vent fluid chemistry between the main field and Capelinhos (Chavagnac et al., 2018).

Chalcopyrite is another Fe-bearing mineral that could have precipitated and trapped both Fe and S in the subsurface and commonly forms in the upflow zones of seafloor hydrothermal systems (Franklin et al., 2005; Galley et al., 2007). However, the fractionation factors between chalcopyrite and H_2S at sub-seafloor hydrothermal conditions are extremely low (e.g., <0.3 (1000lnα) at 150°C, Ohmoto and Rye, 1979) and very large amounts of reduced sulfur would have to precipitate in the subsurface to generate the predicted fractionations, requiring initial fluid H_2S concentrations of >300,000 mmol. For comparison, maximum reported H_2S concentrations for vent fluids are on the order of 110 mmol (Von Damm et al., 1995). Therefore, although chalcopyrite may be precipitating in the sub-seafloor, the isotopic differences between Capelinhos and the main field suggest that pyrite is the primary sulfide phase being precipitated. This interpretation is consistent with evidence from subsea drilling at TAG and from VMS deposits that show that upflow zones can be enriched in chalcopyrite but are dominated by pyrite (Galley et al., 2007; Knott et al., 1998).

It should be noted that the calculations and results presented above assume isotopic equilibrium between the vent fluid and minerals. In seafloor hydrothermal systems, isotopic

equilibrium can be evaluated by comparing known temperatures of formation to temperatures calculated between mineral pairs-based equilibrium sulfur isotope fractionation. For example, there is a uniform difference in isotopic composition of ~3‰ between neighboring chalcopyrite and marcasite crystals at both the main field and Capelinhos (Figure 3.6). This difference is independent of sample location and depositional age as there is no significant variation in $\delta^{34}S$ values and mineral textures (e.g., plumose vs. euhedral marcasite) (Sánchez-Mora et al. 2022). The isotopic enrichment in ^{34}S in chalcopyrite, relative to marcasite, is consistent with equilibrium fractionation processes. Under equilibrium conditions, a 3‰ fractionation between chalcopyrite and marcasite corresponds to a crystallization temperature of 114°C (using fractionation factors by Kajiwara and Krouse, 1971). This temperature is too low for typical crystallization temperatures for chalcopyrite (>250˚C) although marcasite can form at temperatures of up to 240˚C under hydrothermal conditions (Hannington et al., 1995; Murowchick & Barnes, 1986), indicating that these mineral phases were not in isotopic equilibrium at the time of formation. This is consistent with textural evidence that indicates that these mineral phases did not co-precipitate (Figure 3.6), and the difference in isotopic composition between the two mineral phases is likely a result of either equilibrium or non-equilibrium isotopic partitioning between each mineral phase and the hydrothermal fluid at different temperatures of mineral formation and/or other possible kinetic isotopic effects, such as effects of microbial processes during marcasite formation (Juniper et al., 1988). Overall, an important outcome from this analysis is that subsurface sulfide mineral precipitation can change the S isotopic composition of the vent fluid and surficial deposits (Figure 3.8), yielding surficial isotopic compositions that are indistinguishable from isotopic

compositions that result from simple two-component mixing between mantle sulfur and reduced seawater sulfate (Ohmoto and Lasaga, 1982; Ono et al., 2007).

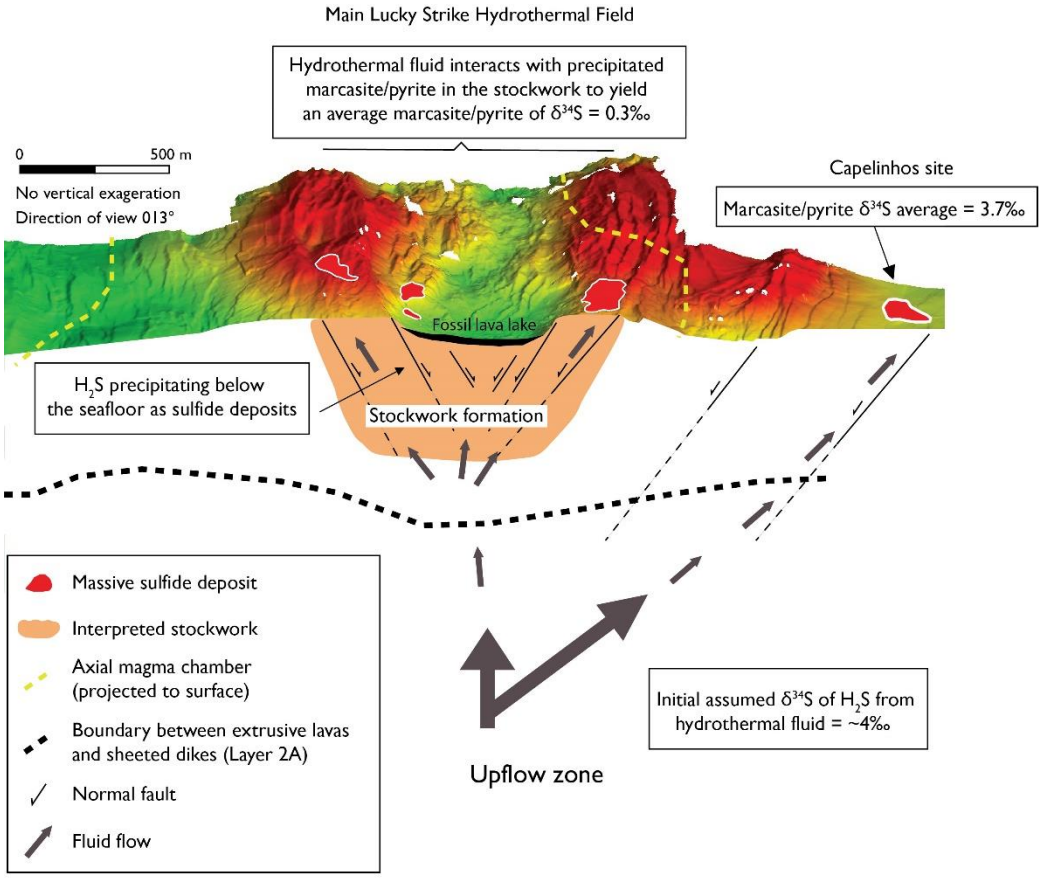

Figure 3.8. Summary sketch of the location and faulting at the Lucky Strike hydrothermal field. The stockwork is interpreted based on the sulfur isotope data from this study. Axial magma chamber (~3.5 km depth) outline from Combier et al. (2015) and layer 2A from Seher et al. (2010), both derived from seismic reflection data.

3.6.3. Geological controls on the composition of Lucky Strike and other vent fields along the Mid-Atlantic Ridge

The most distinctive compositional characteristic of both Lucky Strike and Menez Gwen (a vent field located ~90 km northeast from Lucky Strike, closer to the Azores hotspot) is

the abundance of barite (Bogdanov et al., 2005; Lein et al., 2010). Compared to other basalt or ultramafic-hosted vent fields along the MAR that are not hotspot influenced, such as TAG, Snake Pit, and Rainbow, Lucky Strike contains significantly more barite, and higher concentrations of Ba, Sr and Mo, but lower Au and Sn (Figure 3.9); (Bogdanov et al., 2002; Fouquet et al., 1993; Grant et al., 2018; Honnorez et al., 1990; Krasnov et al., 1995; Marques et al., 2007). The basaltic substrate at Lucky Strike and Menez Gwen is dominated by E-MORB (Gale et al., 2011; Langmuir et al., 1997), which is enriched by 10 to 30 times in incompatible elements (e.g., Ba and Sr) compared to the normal mid-ocean ridge basalts (N-MORB) that host TAG and Snake Pit (Hannington et al., 2005). The E-MORB substrate composition and associated enrichment in incompatible elements (Ba and Sr) was originally linked to enhanced melting of the metasomatized mantle associated with the Azores hotspot (Langmuir et al., 1997). However, other mechanisms for the genesis of E-MORB at mid-ocean ridges have since been proposed, including a low degree of melting that metasomatizes a depleted mantle source prior to the main melting episodes (Gale et al., 2011), and subduction of oceanic crust that then results in the source melting region beneath mid-ocean ridges (Hofman, 2014).

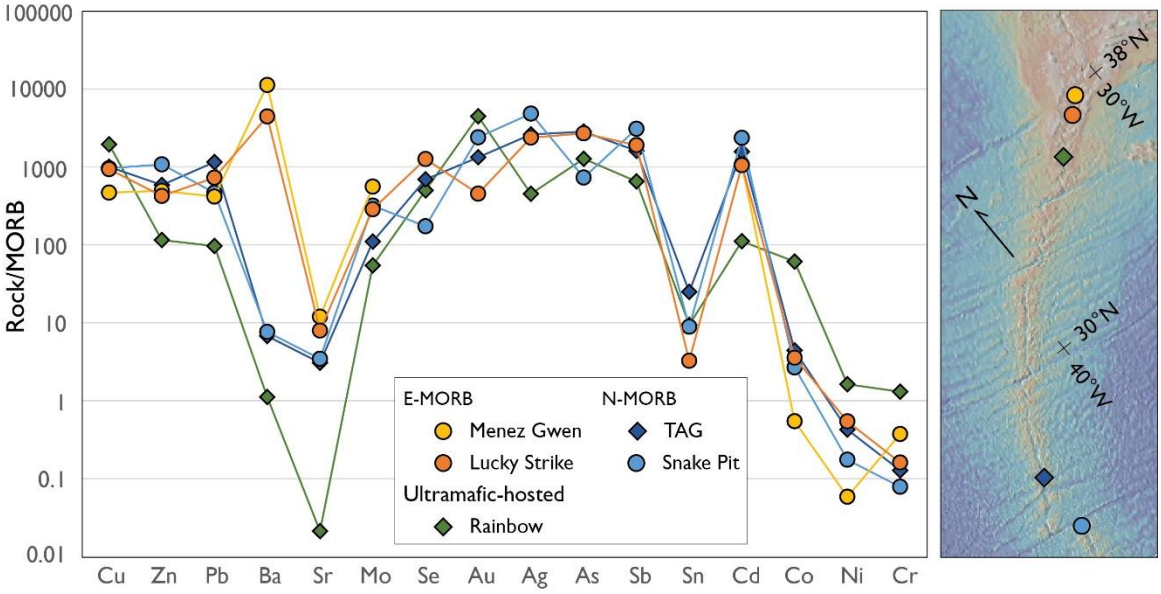

Figure 3.9. Average bulk geochemistry of hydrothermal samples of selected Mid-Atlantic Ridge hosted hydrothermal sites, normalized to average mid-ocean ridge basalt composition (Arevalo and McDonough, 2010). The diamond symbol indicates sites hosted in detachment fault systems. Lucky Strike data is from this study and Bogdanov et al. (2006), Menez Gwen (Bogdanov et al., 2005), TAG (Hannington et al., 1991; Hannington, 1993; Krasnov et al., 1995; Lisitsyn et al., 1990; Rona et al., 1993; Thompson et al., 1988), Snake Pit (Hannington et al., 1991; Hannington, 1989; Honnorez et al., 1990; Kase et al., 1990; Krasnov et al., 1995; Fouquet et al., 1993), and Rainbow (Bogdanov et al., 2002; Marques et al., 2007). Menez Gwen (n=12), Lucky Strike (n=50), Rainbow (n=6), TAG (n=190), and Snake Pit (n=105). Full dataset provided in Appendix 3 which is based primarily on the global database of seafloor hydrothermal systems from Hannington et al. (2004).

In contrast to E-MORB hosted Lucky Strike and Menez Gwen, the active TAG mound, which contains relatively low concentrations of Ba and Sr, is hosted within N-MORB in an active detachment fault zone (Humphris et al., 2015). Rainbow is hosted in ultramafic rocks but is influenced by basaltic rocks in the vicinity of the hydrothermal site. Rainbow has relatively high Ni and Co contents, which is typical for ultramafic-hosted sites (Marques et

al., 2007; Mozgova et al., 2008). At ultramafic sites, serpentinization causes the release of Co and Ni during the alteration of primary silicate minerals such as olivine (Marques et al., 2007). Barium enrichment in E-MORB hosted hydrothermal sites and Co enrichment in ultramafic hosted hydrothermal sites have been widely documented (e.g., Hannington et al., 2005). The Ba/Co within hydrothermal deposits can therefore be used to discriminate E-MORB hosted deposits from deposits hosted on other mafic and ultramafic substrates at sites where the composition of host rock is not known (Figure 3.10A). To test the utility of this ratio, a compilation of four groups of substrate types were compiled (Appendix 3) for which bulk geochemistry of hydrothermal deposits was available: 1) E-MORB (Lucky Strike, Menez Gwen, and Endeavour); 2) N-MORB (TAG, Snake Pit, and Broken Spur); 3) ultramafic (Rainbow and Logatchev); and 4) mixed mafic and ultramafic (Beebe, Kairei, Yuhuang-1, and Daxi; Figure 3.10A, B). The median Ba/Co values are 180, 3, 3, and 0.006 for E-MORB, N-MORB, ultramafic, and mixed mafic/ultramafic groups, respectively (Figure 3.10B). However, concentrations of Ba and Co can also be significantly affected by temperature during mineral precipitation, with Co associated with high-temperature mineral assemblages and Ba associated with lower-temperature mineral assemblages (Figure 3.5). Therefore, to test whether changes in Ba/Co values primarily reflect substrate composition or temperature, the ratios are plotted against Cu/Zn, another geochemical proxy for temperature, for the different substrate groups (Figure 3.10). Elevated Cu values are associated with precipitation of high-temperature chalcopyrite (250–350°C) and high Zn values are associated with precipitation of sphalerite at lower temperatures (<250°C; Figure 3.5; Hannington, 2014). For the E-MORB group, the Ba/Co values show a general negative trend, relative to Cu/Zn, which reflects the temperature dependence of both ratios

within a group. However, when comparing data from different substrate groups, the Ba/Co shows a trend associated with different substrates that is independent of Cu/Zn (Figure 3.10).

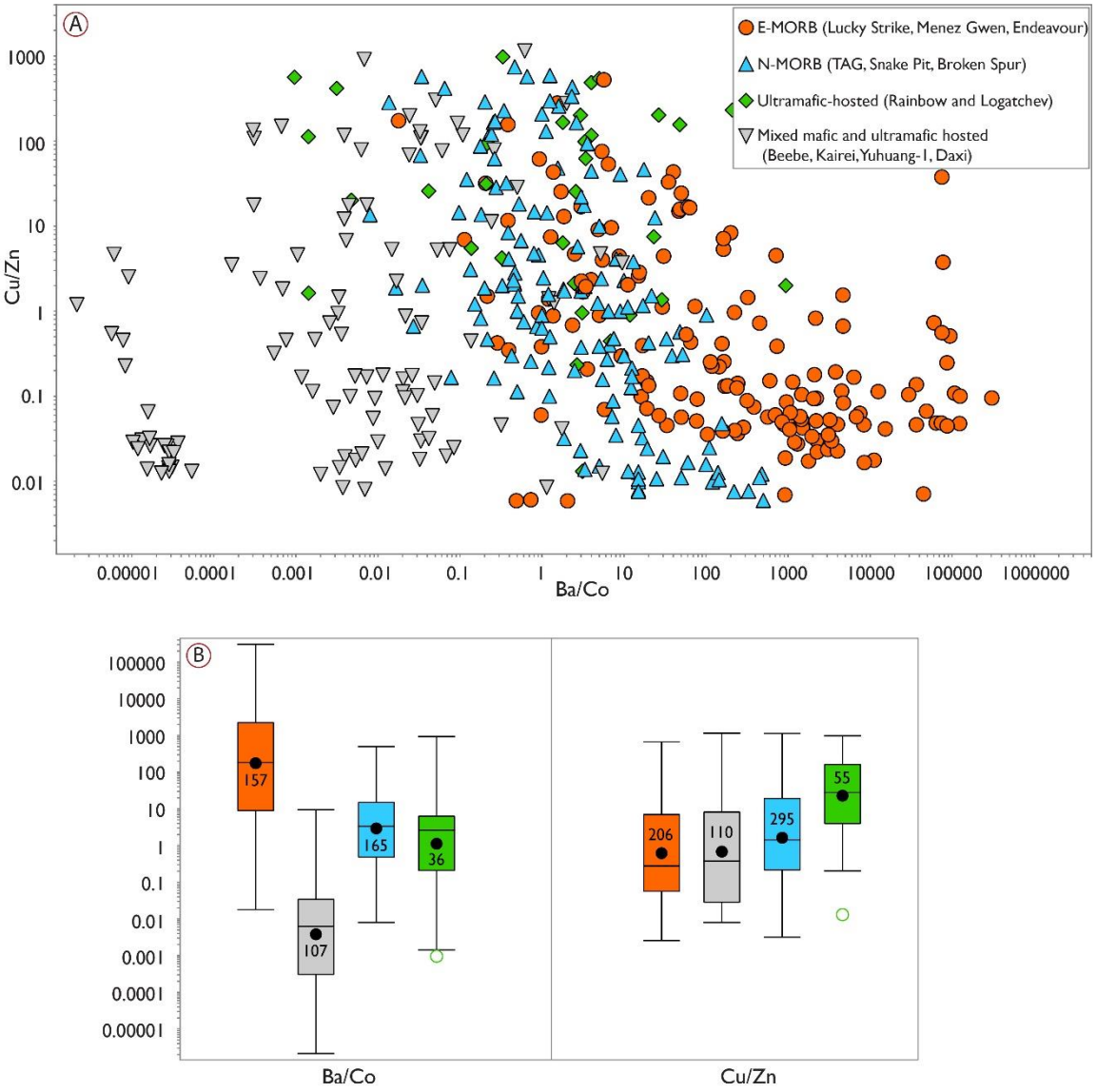

Figure 3.10. A) Ratios from selected SMS deposits grouped according to host rock in mid-ocean ridges. Ba/Co vs Cu/Zn. Ba/Co used as a proxy for proximity to a hotspot, Cu/Zn used as a proxy of temperature of formation. B) Box and whisker plots of quartiles for Ba/Co and Cu/Zn (boxes with black line for median, black dot for mean, and number of samples). E-MORB includes data from Lucky Strike (this study and Bogdanov et al.

(2006)), Menez Gwen (Bogdanov et al., 2005), and Endeavour (Morgan and Selk, 1984; Samson, 1986; Tivey and Delaney, 1986; Tivey et al., 1999; Hannington et al., 2004; Toffolo et al., 2020). N-MORB includes TAG (Hannington et al., 1991; Hannington, 1993; Krasnov et al., 1995; Lisitsyn et al., 1990; Rona et al., 1993; Thompson et al., 1988), Snake Pit (Hannington et al., 1991; Hannington, 1989; Honnorez et al., 1990; Kase et al., 1990; Krasnov et al., 1995; Fouquet et al., 1993; Hannington et al., 2004; Toffolo et al., 2020), and Broken Spur (Bogdanov et al., 1995; Bogdanov et al., 2008; Lisitsyn et al., 1999; Peresypkin et al., 1999; Hannington et al., 2004; Toffolo et al., 2020). Ultramafic-hosted includes Rainbow (Marques et al., 2007) and Logatchev (Bogdanov et al., 1997; Krasnov et al., 1995; Lisitsyn et al., 1999; Mozgova et al., 1999; Murphy & Meyer, 1998; Peresypkin et al., 1999). Mixed mafic and ultramafic includes Beebe (Webber et al., 2015), Kairei (Wang et al., 2014), Yuhuang-1 (Liao et al., 2018), and Daxi (Wang et al., 2021). Data in Appendix 3 which is largely based on the global database of seafloor hydrothermal systems from Hannington et al. (2004).

3.7. Conclusions

The hydrothermal deposits at Lucky Strike are composed of a mineral assemblage typical of basalt-hosted mid-ocean ridge hydrothermal deposits, except for the presence of abundant barite. Principal component analysis discriminates the minor and trace element distribution between high and low temperature mineral assemblages and the precipitation of minerals that result from direct interaction with seawater. The mineralogy and geochemical composition of the off-axis Capelinhos site is similar to the deposits from the main field. However, the sulfur isotopic composition of Capelinhos is heavier by ~3.5‰ compared to the rest of Lucky Strike. These differences reflect variations in length and/or permeability in the pathways of the uprising hydrothermal fluid and distinct fluid/rock interactions at each of these sites, including evidence from S isotope modelling of extensive sub-seafloor marcasite/pyrite mineralization below the main site. Here, S isotopic data corroborate previously reported variations in fluid chemistry between different sites that indicate that >80% of the available H_2S in the ascending hydrothermal fluid precipitates in

a stockwork zone below the seafloor. These results highlight that the interpretation of S isotope compositions for hydrothermal deposits along mid-ocean ridges cannot necessarily be interpreted simply within the context of a two-component mixing model between mantle- and seawater-derived sulfur sources, and that sub-seafloor mineralization and isotopic exchange can also affect the isotopic compositions of surficial sulfide deposits.

The Ba/Co value of hydrothermal deposits provides a temperature-independent geochemical tool to discriminate the composition of the substrate beneath hydrothermal vent fields at mid-ocean ridges, especially E-MORB hosted site that have a distinct elevated Ba/Co. High Ba/Co at Lucky Strike and Menez Gwen indicate an E-MORB substrate associated with the Azores hotspot. In contrast, low Ba/Co is associated with hydrothermal sites hosted in N-MORB, ultramafic, and sites that have a mixed mafic and ultramafic substrate.

3.8. Acknowledgements

This work was supported by the Canada Research Chair Program, an NSERC Discovery Grant, and RDC Leverage Grant to J.W. Jamieson. DSM acknowledges support from the NSERC iMAGE-CREATE program.

3.9. References

Arevalo, R. J., & McDonough, W. F. (2010). Chemical variations and regional diversity observed in MORB. *Chemical Geology*, *271*, 70–85.

Argus, D. F., Gordon, R. G., & Demets, C. (2011). Geologically current motion of 56 plates relative to the no-net-rotation reference frame. *Geochemistry, Geophysics, Geosystems*, *12*(11), 1–13. https://doi.org/10.1029/2011GC003751

Arnulf, A. F., Harding, A. J., Kent, G. M., Singh, S. C., & Crawford, W. C. (2014). Constraints on the shallow velocity structure of the Lucky Strike Volcano, Mid-

Atlantic Ridge, from downward continued multichannel streamer data. *Journal of Geophysical Research, Solid Earth*, *119*, 1119–1144. https://doi.org/10.1002/2013JB010500

Auclair, G., Fouquet, Y., & Bohn, M. (1987). Distribution of selenium in high-temperature hydrothermal sulfide deposits at 13° North, East Pacific Rise. *The Canadian Mineralogist*, *25*, 577–587.

Barreyre, T., Escartín, J., Sohn, R. A., Cannat, M., Ballu, V., & Crawford, W. C. (2014). Temporal variability and tidal modulation of hydrothermal exit-fluid temperatures at the Lucky Strike deep-sea vent field, Mid-Atlantic Ridge. *Journal of Geophysical Research: Solid Earth*, *119*, 2543–2566. https://doi.org/10.1002/2013JB010478

Barreyre, T., Escartín, J., Garcia, R., Cannat, M., Mittelstaedt, E., & Prados, R. (2012). Structure, temporal evolution, and heat flux estimates from the Lucky Strike deep-sea hydrothermal field derived from seafloor image mosaics. *Geochemistry, Geophysics, Geosystems*, *13*(4), 1–29. https://doi.org/10.1029/2011GC003990

Berkenbosch, H. A., de Ronde, C. E. J., Ryan, C. G., McNeill, A. W., Howard, D. L., Gemmell, J. B., & Danyushevsky, L. V. (2019). Trace element mapping of copper- and zinc-rich black smoker chimneys from brothers volcano, kermadec arc, using synchrotron radiation XFM and LA-ICP-MS. *Economic Geology*, *114*(1), 67–92. https://doi.org/10.5382/econgeo.2019.4620

Blandin, J., Sarradin, P. M., & Cannat, M. (2013). MOMARSAT2013 cruise, RV Pourquoi pas ? https://doi.org/10.17600/13030040

Blount, C. W., & Dickson, F. W. (1969). The solubility of anhydrite (CaSO4) in NaCl-H2O from 100 to 450°C and 1 to 1000 bars. *Geochimica et Cosmochimica Acta*, *33*, 227–245. https://doi.org/10.1016/0016-7037(69)90140-9

Bogdanov, Y. A., Gurich, E., & Kuptsov, V. (1995). Relict sulfide mounds at the TAG hydrothermal field of the Mid-Atlantic Ridge (26° N, 45° W). *Oceanology*, *34*, 534–542.

Bogdanov, Y. A., Bortnikov, N. S., Sagalevich, A. M., Gurvich, E. G., & Vikent'ev, I. V. (1997). New type of mineral-forming systems: Black smokers of the hydrothermal field at 14° 45' N MAR. *Geologiya Rudnykh (Geology of Ore Deposits)*, *39*, 68–90.

Bogdanov, Y. A., Bortnikov, N. S., Vikent'ev, I. V., Lein, A. Y., Gurvich, E. G., Sagalevich, A. M., et al. (2002). Mineralogical-Geochemical Peculiarities of Hydrothermal Sulfide Ores and Fluids in the Rainbow Field Associated with Serpentinites, Mid-Atlantic Ridge (36°14'). *Geology of Ore Deposits*, *44*(6), 444–473.

Bogdanov, Y. A., Lein, A. Y., & Sagalevich, A. M. (2005). Chemical Composition of the Hydrothermal Deposits of the Menez Gwen Vent Field (Mid-Atlantic Ridge). *Marine Geology*, *45*(6), 849–856.

Bogdanov, Y. A., Lein, A. Y., Sagalevich, A. M., Ul'yanov, A. A., Dorofeev, S. A., & Ul'yanova, N. V. (2006). Hydrothermal sulfide deposits of the Lucky Strike vent field, Mid-Atlantic Ridge. *Geochemistry International*, *44*(4), 403–418. https://doi.org/10.1134/S0016702906040070

Bogdanov, Y. A., Lein, A. Y., Maslennikov, V. V., Li, S., & Ul'yanov, A. A. (2008). Mineralogical – Geochemical Features of Sulfide Ores from the Broken Spur Hydrothermal Vent Field. *Oceanology*, *48*, 679–700. https://doi.org/10.1134/S000143700805007X

Brueckner, S.M., Piercey, S.J., Layne, G.D., Piercey, G., and Sylvester, P.J., 2015, Variations of sulphur isotope signatures in sulphides from the metamorphosed Ming Cu(−Au) volcanogenic massive sulphide deposit, Newfoundland Appalachians, Canada: Mineralium Deposita, v. 50, p. 619–640, doi: 10.1007/s00126-014-0567-7.

Cannat, M., & Sarradin, P. M. (2012). MOMARSAT2012 cruise, RV Thalassa. https://doi.org/10.17600/12040050

Cannat, M., Briais, A., Deplus, C., Escartín, J., Georgen, J., Lin, J., et al. (1999). Mid-Atlantic Ridge-Azores hotspot interactions: Along-axis migration of a hotspot-derived event of enhanced magmatism 10 to 4 Ma ago. *Earth and Planetary Science Letters*, *173*(3), 257–269. https://doi.org/10.1016/S0012-821X(99)00234-4

Cannat, M., Blandin, J., & Sarradin, P. M. (2011). MOMARSAT2011 cruise, RV Pourquoi pas ? https://doi.org/10.17600/11030070

Charlou, J. L., Donval, J. P., Douville, E., Jean-Baptiste, P., Radford-Knoery, J., Fouquet, Y., et al. (2000). Compared geochemical signatures and the evolution of Menez Gwen (35°50N) and Lucky Strike (37°17N) hydrothermal fluids, south of the Azores Triple Junction on the Mid-Atlantic Ridge. *Chemical Geology*, *171*(1–2), 49–75. https://doi.org/10.1016/S0009-2541(00)00244-8

Chavagnac, V., Leleu, T., Fontaine, F., Cannat, M., Ceuleneer, G., & Castillo, A. (2018). Spatial Variations in Vent Chemistry at the Lucky Strike Hydrothermal Field, Mid-Atlantic Ridge (37°N): Updates for Sub-seafloor Flow Geometry From the Newly Discovered Capelinhos Vent. *Geochemistry, Geophysics, Geosystems*, *19*(11), 4444–4458. https://doi.org/10.1029/2018GC007765

Combier, V., Seher, T., Singh, S. C., Crawford, W. C., Cannat, M., Escartín, J., & Dusunur, D. (2015). Three-dimensional geometry of axial magma chamber roof and faults at Lucky Strike volcano on the Mid-Atlantic Ridge. *Journal of Geophysical Research : Solid Earth*, *121*, 6386–6403. https://doi.org/10.1002/2015JB012282.Received

Cook, N., Ciobanu, C. L., George, L., Zhu, Z. Y., Wade, B., & Ehrig, K. (2016). Trace element analysis of minerals in magmatic-hydrothermal ores by laser ablation inductively-coupled plasma mass spectrometry: Approaches and opportunities. *Minerals*, *6*(4). https://doi.org/10.3390/min6040111

Crawford, W. C., Rai, A., Singh, S. C., Cannat, M., Escartín, J., Wang, H., et al. (2013). Hydrothermal seismicity beneath the summit of Lucky Strike volcano, Mid-Atlantic Ridge. *Earth and Planetary Science Letters*, *373*, 118–128. https://doi.org/10.1016/j.epsl.2013.04.028

Von Damm, K. L., Oosting, S. E., Kozlowski, R., Buttermore, L. G., Colodner, D. C., Edmonds, H. N., et al. (1995). Evolution of East Pacific Rise hydrothermal vent fluids following a volcanic eruption. *Nature*, *375*(6526), 47–50. https://doi.org/10.1038/375047a0

Von Damm, K. L., Bray, A. M., Buttermore, L. G., & Oosting, S. E. (1998). The geochemical controls on vent fluids from the Lucky Strike vent field , Mid-Atlantic Ridge. *Earth and Planetary Science Letters*, *160*, 521–536.

Ding, T., Valkiers, S., Kipphardt, H., De Bièvre, P., Taylor, P. D. P., Gonfiantini, R., & Krouse, R. (2001). Calibrated sulfur isotope abundance ratios of three IAEA sulfur isotope reference materials and V-CDT with a reassessment of the atomic weight of sulfur. *Geochimica et Cosmochimica Acta*, *65*(15), 2433–2437.

Doe, B. R. (1994). Zinc, Copper, and Lead in Midocean Ridge Basalts and the Source-Rock Control on Zn/Pb in Ocean-Ridge Hydrothermal Deposits. *Geochimica Et Cosmochimica Acta*, *58*(10), 2215–2223.

Dziak, R. P., Smith, D. K., Bohnenstiehl, D. W. R., Fox, C. G., Desbruyeres, D., Matsumoto, H., et al. (2004). Evidence of a recent magma dike intrusion at the slow spreading Lucky Strike segment, Mid-Atlantic Ridge. *Journal of Geophysical Research B: Solid Earth*, *109*(12), 1–15. https://doi.org/10.1029/2004JB003141

Eldridge, C. S., Barton, P. B., & Ohmoto, H. (1983). Mineral textures and their bearing on formation of the Kuroko orebodies. In H. Ohmoto & B. J. Skinner (Eds.), *The Kuroko and related volcanogenic massive sulfide deposits* (pp. 241–281). Economic Geology Monographs.

Escartín, J., Cannat, M., Pouliquen, G., Rabain, A., & Lin, J. (2001). Crustal thickness of V-shaped ridges south of the Azores: Interaction of the Mid-Atlantic Ridge (36°–39°N) and the Azores hot spot. *Journal of Geophysical Research*, *106*(B10), 21719–21735. https://doi.org/10.1029/2001JB000224

Escartín, J., Soule, S. A., Cannat, M., Fornari, D. J., Düşünür, D., & Garcia, R. (2014). Lucky Strike seamount: Implications for the emplacement and rifting of segment-centered volcanoes at slow spreading mid-ocean ridges. *Geochemistry, Geophysics, Geosystems*, *15*, 4157–4179. https://doi.org/10.1002/2014GC005563.Received

Escartín, J., Barreyre, T., Cannat, M., Garcia, R., Gracias, N., Deschamps, A., et al. (2015). Hydrothermal activity along the slow-spreading Lucky Strike ridge segment (Mid-Atlantic Ridge): Distribution, heatflux, and geological controls. *Earth and Planetary Science Letters*, *431*, 173–185. https://doi.org/10.1016/j.epsl.2015.09.025

Fallon, E. K., Frische, M., Petersen, S., Brooker, R. A., & Scott, T. B. (2019). Geological, mineralogical and textural impacts on the distribution of environmentally toxic trace elements in seafloor massive sulfide occurrences. *Minerals*, *9*(3), 1–53. https://doi.org/10.3390/min9030162

Fontboté, L., Kouzmanov, K., Chiaradia, M., & Pokrovski, G. S. (2017). Sulfide minerals in hydrothermal deposits. *Elements*, *13*(2), 97–103. https://doi.org/10.2113/gselements.13.2.97

Fouquet, Y., Wafik, A., Cambon, P., Mevel, C., Meyer, G., & Gente, P. (1993). Tectonic Setting and Mineralogical and Geochemical Zonation in the Snake Pit Sulfide Deposit (Mid-Atlantic Ridge at 23°N). *Economic Geology*, *88*, 2018–2036.

Fouquet, Y., Charlou, J.-L., Costa, I., Donval, J.-P., Radford-Knoery, J., Pellé, H., et al. (1994). A detailed study of the Lucky Strike hydrothermal site and discovery of a new hydrothermal site: Menez Gwen. In *Preliminary results on the DIVA1 Cruise (5-29 May, 1994)* (pp. 14–17). InterRidge Newsletter.

Fouquet, Y., Cambon, P., Etoubleau, J., Charlou, J. L., Ondréas, H., Barriga, F. J. A. S., et al. (2010). Geodiversity of hydrothermal processes along the Mid-Atlantic ridge and ultramafic-hosted mineralization: A new type of oceanic Cu-Zn-Co-Au volcanogenic massive sulfide deposit. *Geophysical Monograph Series*, *188*, 321–367. https://doi.org/10.1029/2008GM000746

Franklin, J. M., Gibson, H. . L., Jonasson, I. R., & Galley, A. G. (2005). Volcanogenic Massive Sulfide Deposits. *Economic Geology 100th Anniversary Volume*, 523–560. https://doi.org/10.1016/B978-0-08-095975-7.01120-7

Gale, A., Escrig, S., Gier, E. J., Langmuir, C. H., & Goldstein, S. L. (2011). Enriched basalts at segment centers: The Lucky Strike (37°17'N) and Menez Gwen (37°50'N) segments of the Mid-Atlantic Ridge. *Geochemistry, Geophysics, Geosystems*, *12*(6). https://doi.org/10.1029/2010GC003446

Galley, A.G., Hannington, M. D., & Jonasson, I. R. (2007). Volcanogenic Massive Sulphide Deposits. *Mineral Deposits of Canada: A Synthesis of Major Deposit-Types, District Metallogeny, the Evolution of Geological Provinces, and Exploration Methods*, (5), 141–161.

Galley, A. G, Hannington, M. D., & Jonasson, I. R. (2007). Volcanogenic massive sulphide deposits. *Geological Association of Canada*, (5), 141–161.

Gamo, T., Okamura, K., Charlou, J., Urabe, T., Auzende, J., Ishibashi, J., et al. (1997). Acidic and sulfate-rich hydrothermal fluids from the Manus back-arc basin , Papua New Guinea. *Geology*, *25*, 139–142. https://doi.org/10.1130/0091-7613(1997)025<0139

Gente, P., Dyment, J., Maia, M., & Goslin, J. (2003). Interaction between the Mid-Atlantic

Ridge and the Azores hot spot during the last 85 Myr: Emplacement and rifting of the hot spot-derived plateaus. *Geochemistry, Geophysics, Geosystems*, *4*(10), 1–23. https://doi.org/10.1029/2003GC000527

German, C. R., & Seyfried, W. E. (2014). *Hydrothermal Processes*. *Treatise on Geochemistry* (2nd ed., Vol. 8). Elsevier Ltd. https://doi.org/10.1016/B978-0-08-095975-7.00607-0

Gini, C., Escartín, J., Cannat, M., & Barreyre, T. (2021). Extrusive upper crust formation at slow-spreading ridges: Fault steering of lava flows. *Earth and Planetary Science Letters*, *576*, 117202. https://doi.org/10.1016/j.epsl.2021.117202

Gale, A., Escrig, S., Gier, E.J., Langmuir, C.H., and Goldstein, S.L., 2011, Enriched basalts at segment centers: The Lucky Strike (37°17'N) and Menez Gwen (37°50'N) segments of the Mid-Atlantic Ridge: Geochemistry, Geophysics, Geosystems, v. 12, doi: 10.1029/2010GC003446.

Grant, H. L. J., Hannington, M. D., Petersen, S., Frische, M., & Fuchs, S. H. (2018). Constraints on the behavior of trace elements in the actively-forming TAG deposit, Mid-Atlantic Ridge, based on LA-ICP-MS analyses of pyrite. *Chemical Geology*, (July), 1–27. https://doi.org/10.1016/j.chemgeo.2018.08.019

Grant, H. L. J., Hannington, M. D., Hardardóttir, V., Fuchs, S. H., & Schumann, D. (2020). Trace metal distributions in sulfide scales of the seawater-dominated Reykjanes geothermal system: Constraints on sub-seafloor hydrothermal mineralizing processes and metal fluxes. *Ore Geology Reviews*, *116*(May 2019), 103145. https://doi.org/10.1016/j.oregeorev.2019.103145

Hannington, M., Herzig, P., Scott, S., Thompson, G., & Rona, P. (1991). Comparative mineralogy and geochemistry of gold-bearing sulfide deposits on the mid-ocean ridges. *Marine Geology*, *101*(1–4), 217–248. https://doi.org/10.1016/0025-3227(91)90073-D

Hannington, M. D., Jamieson, J., Monecke, T., Petersen, S., & Beaulieu, S. (2011). The abundance of seafloor massive sulfide deposits. *Geology*, *39*(12), 1155–1158. https://doi.org/10.1130/G32468.1

Hannington, M. D. (1989). *The geochemistry of gold in modern seafloor hydrothermal systems and implications for gold mineralization in ancient volcanogenic massive sulfides*. *Unpublished Ph.D. thesis*. University of Toronto.

Hannington, M. D. (1993). The formation of atacamite during weathering of sulfides on the modern seafloor. *Canadian Mineralogist*, *31*(4), 945–956.

Hannington, M. D. (2014). Volcanogenic Massive Sulfide Deposits. *Treatise on Geochemistry: Second Edition*, *13*, 463–488. https://doi.org/10.1016/B978-0-08-095975-7.01120-7

Hannington, M. D., Jonasson, I. R., Herzig, P. M., & Petersen, S. (1995). Physical and chemical processes of seafloor mineralization at mid-ocean ridges. In Susan E. Humphris, R. A. Zierenberg, S. Mullineaux, & R. E. Thomson (Eds.), *Seafloor hydrothermal systems: Physical, chemical, biological, and geological interactions, Geophysical Monograph* (pp. 115–157). American Geophysical Union. https://doi.org/10.1029/GM091p0115

Hannington, M. D., Poulsen, K. H., Thompson, J. F. ., & Sillitoe, R. H. (1999). Volcanogenic gold in the massive sulfide environment. In C. T. Barrie & M. D. Hannington (Eds.), *Volcanic-associated massive sulfide deposits: Processes and examples in modern and ancient settings* (Vol. 8, pp. 319–350). Reviews in Economic Geology.

Hannington, M.D., Petersen, S., Herzig, P.M., and Jonasson, I.R., 2004, A global database of seafloor hydrothermal systems, including a digital database of geochemical analyses of seafloor polymetallic sulfides: Open File 4598, Geological Survey of Canada, doi: https://doi.org/10.4095/215065.

Hannington, M. D., de Ronde, C. E. J., & Petersen, S. (2005). Sea-Floor Tectonics and Submarine Hydrothermal Systems. Economic Geology, 100th Anni, 111–141.

Haymon, R. M. (1983). Growth history of hydrothermal black smoker chimneys. *Nature*, *301*, 695–698.

Hoffman, E. L. (1992). Instrumental neutron activation in geoanalysis. *Journal of Geochemical Exploration*, *44*, 297–319.

Hofmann, A.W., 2014, Sampling Mantle Heterogeneity through Oceanic Basalts: Isotopes and Trace Elements: Elsevier Ltd., v. 3, 67–101 p., doi: 10.1016/B978-0-08-095975-7.00203-5.

Honnorez, C. M., Honnorez-Guerstein, B. M., & Tomschi, H. P. (1990). Mineralogy and chemistry of sulfide deposits drilled from hydrothermal mound of the Snake Pit active field, MAR. In R. Detrick, J. B. Honnorez, W. B. Bryan, & T. Juteau (Eds.), *Proceedings of the Ocean Drilling Program, Scientific Results* (Vol. 106/109, pp. 145–162). College Station.

Humphris, S.E., Fornari, D. J., Scheirer, D. S., German, C. R., & Parson, L. M. (2002). Geotectonic setting of hydrothermal activity on the summit of Lucky Strike Seamount (37°17'N, Mid-Atlantic Ridge). *Geochemistry, Geophysics, Geosystems*, *3*(8), 1–24. https://doi.org/10.1029/2001GC000284

Humphris, S. E., Tivey, M. K., & Tivey, M. A. (2015). The Trans-Atlantic Geotraverse hydrothermal field: A hydrothermal system on an active detachment fault. *Deep-Sea Research Part II: Topical Studies in Oceanography*, *121*, 8–16. https://doi.org/10.1016/j.dsr2.2015.02.015

Jamieson, J. W., Hannington, M. D., Tivey, M. K., Hansteen, T., Williamson, N. M. B., Stewart, M., et al. (2016). Precipitation and growth of barite within hydrothermal vent deposits from the Endeavour Segment, Juan de Fuca Ridge. *Geochimica et Cosmochimica Acta*, *173*, 64–85. https://doi.org/10.1016/j.gca.2015.10.021

Juniper, S. K., Tunnicliffe, V., & Fontaine, A. R. (1988). Biological influences on mineral deposition at deep-sea hydrothermal vents. *NOAA National Undersea Research Program Report*, *88*(4), 99–118.

Kajiwara, Y., & Krouse, H. R. (1971). Sulfur Isotope Partitioning in Metallic Sulfide Systems. *Canadian Journal of Earth Sciences*, *8*(1397).

Kase, K., Yamamoto, M., & Shibata, T. (1990). Copper-rich sulfide deposit 23°N, Mid-Atlantic Ridge: Chemical composition, mineral chemistry, and sulfur isotopes. In R. Detrick, J. Honnorez, W. B. Bryan, & T. Juteau (Eds.), *Proceedings of the Ocean Drilling Programm, Scientific Results* (Vol. 106/109, pp. 163–177). College Station.

Keith, M., Häckel, F., Haase, K. M., Schwarz-Schampera, U., & Klemd, R. (2016). Trace element systematics of pyrite from submarine hydrothermal vents. *Ore Geology Reviews*, *72*, 728–745. https://doi.org/10.1016/j.oregeorev.2015.07.012

Knott, R., Fouquet, Y., Honnorez, J., Petersen, S., & Bohn, M. (1998). Petrology of hydrothermal mineralization: a vertical section through the TAG mound. *Proceedings of the Ocean Drilling Program: Scientific Results*, *158*, 5–26. https://doi.org/10.2973/odp.proc.sr.158.201.1998

Krasnov, S. G., Cherkashev, G. A., Stepanova, T. V., Batuyev, B. N., Krotov, A. G., Malin, B. V., et al. (1995). Detailed geological studies of hydrothermal fields in the North Atlantic. In L. M. Parson, C. L. Walker, & D. R. Dixon (Eds.), *Hydrothermal Vents and Processes* (pp. 43–64). Geological Society Special Publication.

Langmuir, C., Humphris, S., Fornari, D., Van Dover, C., Von Damm, K., Tivey, M. K., et al. (1997). Hydrothermal vents near a mantle hot spot: the Lucky Strike vent field at 37°N on the Mid-Atlantic Ridge. *Earth and Planetary Science Letters*, *148*(1–2), 69–91. https://doi.org/10.1016/S0012-821X(97)00027-7

Langmuir, C. H., Klinkhammer, G., Bougault, H., & and Shipboard Scientific Party. (1992). *FAZAR Cruise Report*. Palisades, N.Y.

Layton-Matthews, D., Peter, J. M., Scott, S. D., & Leybourne, M. I. (2008). Distribution , Mineralogy , and Geochemistry of Selenium in Felsic Volcanic-Hosted Massive Sulfide Deposits of the Finlayson Lake District , Yukon Territory , Canada. *Economic Geology*, *103*, 61–88.

Lein, A. Y., Bogdanov, Y. A., Maslennikov, V. V., Li, S., Ulyanova, N. V., Maslennikova, S. P., & Ulyanov, A. A. (2010). Sulfide Minerals in the Menez Gwen Nonmetallic Hydrothermal Field (Mid Atlantic Ridge). *Lithology and Mineral Resources*, *45*(4),

305–323. https://doi.org/10.1134/S0024490210040012

Liao, S., Tao, C., Li, H., Barriga, F. J. A. S., Liang, J., Yang, W., et al. (2018). Bulk geochemistry, sulfur isotope characteristics of the Yuhuang-1 hydrothermal field on the ultraslow-spreading Southwest Indian Ridge. *Ore Geology Reviews*, *96*(April), 13–27. https://doi.org/10.1016/j.oregeorev.2018.04.007

Lisitsyn, A. P., Bogdanov, Y. A., & Gurvich, E. G. (1990). *Hydrothermal formations of the ocean rift zone*. Nauk Publisher.

Lisitsyn, A. P., Lapukhov, A. S., Simonov, V. A., Sidenko, N. V., Mazurov, M. P., Bogdanov, Y. A., & Batuev, V. N. (1999). Noble metals in ore-forming hydrothermal systems of modern oceans. *Doklady Earth Sciences*, *369*, 1198–1200.

Lydon, J. W. (1988). Ore deposit models 14. Volcanogenic massive sulphide deposits. Part 2: genetic models. *Geoscience Canada*, *15*(1), 43–65.

Marques, A. F., Barriga, F. J. A. S., & Scott, S. D. (2007). Sulfide mineralization in an ultramafic-rock hosted seafloor hydrothermal system : From serpentinization to the formation of Cu–Zn–(Co)-rich massive sulfides. *Marine Geology*, *245*, 20–39. https://doi.org/10.1016/j.margeo.2007.05.007

Martin, A. J., Keith, M., McDonald, I., Haase, K. M., McFall, K. A., Klemd, R., & MacLeod, C. J. (2019). Trace element systematics and ore-forming processes in mafic VMS deposits: Evidence from the Troodos ophiolite, Cyprus. *Ore Geology Reviews*, *106*(January), 205–225. https://doi.org/10.1016/j.oregeorev.2019.01.024

McDermott, J. M., Ono, S., Tivey, M. K., Seewald, J. S., Shanks, W. C., & Solow, A. R. (2015). Identification of sulfur sources and isotopic equilibria in submarine hot-springs using multiple sulfur isotopes. *Geochimica et Cosmochimica Acta*, *160*, 169–187. https://doi.org/10.1016/j.gca.2015.02.016

Melekestseva, I. Y., Maslennikov, V. V., Tret'yakov, G. A., Nimis, P., Beltenev, V. E., Rozhdestvenskaya, I. I., et al. (2017). Gold-And silver-rich massive sulfides from the semenov-2 hydrothermal field, 13°31.13'N, Mid-Atlantic ridge: A case of magmatic contribution? *Economic Geology*, *112*(4), 741–773. https://doi.org/10.2113/econgeo.112.4.741

Miranda, J. M., Luis, J. F., Lourenço, N., & Santos, F. M. (2005). Identification of the magnetization low of the Lucky strike hydrothermal vent using surface magnetic data. *Journal of Geophysical Research: Solid Earth*, *110*(4), 1–9. https://doi.org/10.1029/2004JB003085

Monecke, T., Petersen, S., Hannington, M. D., Grant, H., & Samson, I. M. (2016). The Minor Element Endowment of Modern Sea-Floor Massive Sulfi des and Comparison with Deposits Hosted in Ancient Volcanic Successions. In P. L. Verplanck & M. W. Hitzman (Eds.), *Rare earth and critical elements in ore deposits* (Vol. 18, pp. 245–

306). Littleton, Colorado: Reviews in Economic Geology.

Morgan, C. L., & Selk, B. W. (1984). Ore assays of massive sulfides from three spreading centers. *Proceedings of the Annual Offshore Technology Conference*, *1984-May*, 9–16. https://doi.org/10.4043/4777-ms

Mozgova, N. N., Efimov, A. V., Borodaev, Y. S., Krasnov, S. G., Cherkashev, G. A., Stepanova, T. V., & Ashadze, A. M. (1999). Mineralogy and chemistry of massive sulfides from the Logatchev Hydrothermal Field (14°45' N Mid-Atlantic Ridge). *Exploration and Mining Geology*, *8*, 379–395.

Mozgova, N. N., Trubkin, N. V., Borodaev, Y. S., Cherkashev, G. A., Stepanova, T. V., Semkova, T. A., & Uspenskaya, T. Y. (2008). Mineralogy of massive sulfides from the Ashadze hydrothermal field 13°N, Mid-Atlantic Ridge. *Canadian Mineralogist*, *46*, 545–567.

Murowchick, J. B., & Barnes, H. L. (1986). Marcasite precipitation from hydrothermal solutions. *Geochimica et Cosmochimica Acta*, *50*(12), 2615–2629. https://doi.org/10.1016/0016-7037(86)90214-0

Murphy, P. J., & Meyer, G. (1998). A gold-copper association in ultramafic-hosted hydrothermal sulfides from the Mid-Atlantic ridge. *Economic Geology*, *93*, 1076–1083.

Ohmoto, H., & Lasaga, A. C. (1982). Kinetics of reactions between aqueous sulfates and sulfides in hydrothermal systems. *Geochimica et Cosmochimica Acta*, *46*(10), 1727–1745. https://doi.org/10.1016/0016-7037(82)90113-2

Ohmoto, H., & Rye, R. O. (1979). Isotope of sulfur and carbon. In H. L. Barnes (Ed.), *Geochemistry of Hydrothermal deposits* (pp. 509–567). New York: John Wiley and Sons.

Ondréas, H., Cannat, M., Fouquet, Y., Normand, A., Sarradin, P. M., & Sarrazin, J. (2009). Recent volcanic events and the distribution of hydrothermal venting at the Lucky Strike hydrothermal field, Mid-Atlantic Ridge. *Geochemistry, Geophysics, Geosystems*, *10*(2). https://doi.org/10.1029/2008GC002171

Ono, S., Shanks, W. C., Rouxel, O. J., & Rumble, D. (2007). S-33 constraints on the seawater sulfate contribution in modern seafloor hydrothermal vent sulfides. *Geochimica et Cosmochimica Acta*, *71*(5), 1170–1182. https://doi.org/10.1016/j.gca.2006.11.017

Palarea-Albaladejo, J., Martín-Fernández, J. A., & Buccianti, A. (2014). Compositional methods for estimating elemental concentrations below the limit of detection in practice using R. *Journal of Geochemical Exploration*, *141*, 71–77. https://doi.org/10.1016/j.gexplo.2013.09.003

Pawlowsky-Glahn, V., & Egozcue, J. J. (2006). Compositional data and their analysis : an

introduction. *Geological Society, London, Special Publications*, *264*, 1–10.

Peresypkin, V. I., Lein, A. Y., Bogdanov, Y. A., & Nortinkov, N. S. (1999). On the nature of lipids in hydrothermal formations at the Broken Spur and vent fields of the Mid-Atlantic Ridge. *Exploration and Mining Geology*, *8*, 365–377.

Pester, N. J., Reeves, E. P., Rough, M. E., Ding, K., Seewald, J. S., & Seyfried, W. E. (2012). Sub-seafloor phase equilibria in high-temperature hydrothermal fluids of the Lucky Strike Seamount. *Geochimica et Cosmochimica Acta*, *90*, 303–322. https://doi.org/10.1016/j.gca.2012.05.018

Petersen, S., Herzig, P. M., & Hannington, M. D. (2000). Third dimension of a presently forming VMS deposit: TAG hydrothermal mound, Mid-Atlantic Ridge, 26°N. *Mineralium Deposita*, *35*(2–3), 233–259. https://doi.org/10.1007/s001260050018

Petersen, S., Krätschell, A., Augustin, N., Jamieson, J., Hein, J. R., & Hannington, M. D. (2016). News from the seabed – Geological characteristics and resource potential of deep-sea mineral resources. *Marine Policy*, *70*, 175–187. https://doi.org/10.1016/j.marpol.2016.03.012

Rona, P. A. (2003). Resources of the sea floor. *Science*, *299*(5607), 673–674. https://doi.org/10.1126/science.1080679

Rona, P. A., Hannington, M. D., Raman, C. V., Thompson, G., Tivey, M. K., Humphris, S. E., et al. (1993). Active and relict sea-floor hydrothermal mineralization at the TAG hydrothermal field, mid-Atlantic ridge. *Economic Geology*, *88*(8), 1989–2017. https://doi.org/10.2113/gsecongeo.88.8.1989

de Ronde, C. E. J., Massoth, G. J., Butterfield, D. A., Christenson, B. W., Ishibashi, J., Ditchburn, R. G., et al. (2011). Submarine hydrothermal activity and gold-rich mineralization at Brothers Volcano, Kermadec Arc, New Zealand. *Mineralium Deposita*, *46*(5), 541–584. https://doi.org/10.1007/s00126-011-0345-8

Rouxel, O., Fouquet, Y., & Ludden, J. N. (2004). Subsurface processes at the lucky strike hydrothermal field, Mid-Atlantic ridge: Evidence from sulfur, selenium, and iron isotopes. *Geochimica et Cosmochimica Acta*, *68*(10), 2295–2311. https://doi.org/10.1016/j.gca.2003.11.029

Samson, J. (1986). Compilation of Information on Polymetallic Sulfide Deposits and Occurrences off the West Coast of Canada. *Canada Oil and Gas Lands Administration*, 1–58.

Sánchez-Mora, D., Jamieson, J. W., Escartín, J., Barreyre, T., & Cannat, M. (2022). Age and rates of formation of metal-rich hydrothermal deposits on the seafloor: example from the Lucky Strike Vent Field, Mid-Atlantic Ridge. *Journal of Geophysical Research: Solid Earth*

Sarradin, P. M., & Cannat, M. (2014). MOMARSAT2014 cruise, RV Pourquoi pas ?

https://doi.org/10.17600/14000300

Sarradin, P. M., & Cannat, M. (2015). MOMARSAT2015 cruise, RV Pourquoi pas ? https://doi.org/10.17600/15000200

Seher, T., Crawford, W. C., Singh, S. C., & Cannat, M. (2010). Seismic layer 2A variations in the Lucky Strike segment at the Mid-Atlantic Ridge from reflection measurements. *Journal of Geophysical Research: Solid Earth*, *115*(7), 1–20. https://doi.org/10.1029/2009JB006783

Shanks, W. C. I. (2001). Stable Isotopes in Seafloor Hydrothermal Systems: Vent fluid, hydrothermal deposits, hydrothermal alteration, and microbial processes. In J. W. Valley & D. R. Cole (Eds.), *Stable Isotope Geochemistry* (pp. 469–525). Washington, D.C.: Reviews in Mineralogy & Geochemistry.

Singh, S. C., Crawford, W. C., Carton, H., Seher, T., Combier, V., Cannat, M., et al. (2006). Discovery of a magma chamber and faults beneath a Mid-Atlantic Ridge hydrothermal field. *Nature*, *442*(7106), 1029–1032. https://doi.org/10.1038/nature05105

Thompson, G., Humphris, S. E., Schroeder, B., Sulanowska, M., & Rona, P. A. (1988). Active vents and massive sulfides at 26°N (TAG) and 23°N (Snakepit) on the Mid-Atlantic Ridge. *Canadian Mineralogist*, *26*, 697–711.

Tivey, M. K., & Delaney, J. R. (1986). Growth of large sulfide structures on the Endeavour segment of the Juan de Fuca ridge. *Earth and Planetary Science Letters*, *77*(3–4), 303–317. https://doi.org/10.1016/0012-821X(86)90142-1

Tivey, M. K., (2007). Generation of Seafloor Hydrothermal Vent Fluids and Associated Mineral Deposits. *Oceanography*, *20*(1), 50–65. https://doi.org/10.5670/oceanog.2007.80

Tivey, M. K., Stakes, D. S., Cook, T. L., Hannington, M. D., & Petersen, S. (1999). A model for growth of steep-sided vent structures on the Endeavour Segment of the Juan de Fuca Ridge: Results of a petrologic and geochemical study. *Journal of Geophysical Research: Solid Earth*, *104*(B10), 22859–22883. https://doi.org/10.1029/1999JB900107

Toffolo, L., Nimis, P., Tret'yakov, G. A., Melekestseva, I. Y., & Beltenev, V. E. (2020). Seafloor massive sulfides from mid-ocean ridges: Exploring the causes of their geochemical variability with multivariate analysis. *Earth-Science Reviews*, *201*(February 2019), 102958. https://doi.org/10.1016/j.earscirev.2019.102958

Wang, Y., Han, X., Petersen, S., Jin, X., Qiu, Z., & Zhu, J. (2014). Mineralogy and geochemistry of hydrothermal precipitates from Kairei hydrothermal field, Central Indian Ridge. *Marine Geology*, *354*, 69–80. https://doi.org/10.1016/j.margeo.2014.05.003

Wang, Y., Han, X., Zhou, Y., Qiu, Z., Yu, X., Petersen, S., et al. (2021). The Daxi Vent

Field: An active mafic-hosted hydrothermal system at a non-transform offset on the slow-spreading Carlsberg Ridge, 6°48′N. *Ore Geology Reviews*, *129*(April 2020), 103888. https://doi.org/10.1016/j.oregeorev.2020.103888

Webber, A. P., Roberts, S., Murton, B. J., & Hodgkinson, M. R. S. (2015). Geology, sulfide geochemistry and supercritical venting at the Beebe Hydrothermal Vent Field, Cayman Trough. *Geochemistry, Geophysics, Geosystems*, (February 2013), 2661–2678. https://doi.org/10.1002/2015GC005879.Received

Zeng, Z., Ma, Y., Chen, S., Selby, D., Wang, X., & Yin, X. (2017). Sulfur and lead isotopic compositions of massive sulfides from deep-sea hydrothermal systems: Implications for ore genesis and fluid circulation. *Ore Geology Reviews*, *87*, 155–171. https://doi.org/10.1016/j.oregeorev.2016.10.014

4. Efficiency of metal precipitation at seafloor hydrothermal vents

4.1. Abstract

Submarine hydrothermal circulation results in the mobilization and transport of metals to the seafloor. The proportion of mobilized metals that are retained at the seafloor at sites of hydrothermal discharge can be quantified by calculating the metal depositional efficiency, which is the proportion of metals retained at the seafloor, relative to the amount of metals dissolved and transported by the ascending fluid. The depositional efficiency of hydrothermal systems has been a longstanding question, due to its importance to understand ocean metal budgets, alteration of oceanic crust, and ore-forming processes at the seafloor. Here, we use a combination of vent fluid composition and flux estimates, U-series geochronology of hydrothermal deposits, and deposit mass estimates to calculate metal-specific depositional efficiencies at the Lucky Strike vent field, on the Mid-Atlantic Ridge. Our calculations show that depositional efficiencies vary significantly for different metals, with values of 38–99 % for Cu, 64–78 % for Zn, 14–76% for Fe, and <1% for Mn and Si. The relative trapping efficiency of different metals corresponds to the temperature-dependent solubilities of their respective host minerals. The efficient trapping of Cu and Zn at the seafloor is significantly higher than previous estimates and indicates that metal-rich seafloor massive sulfide (SMS) deposits can form over relatively short timescales of thousands of years.

4.2. Introduction

Hydrothermal circulation of seawater through oceanic crust along submarine tectonic boundaries results in the leaching, mobilization, and transport of metals to the seafloor. Upon reaching the seafloor, mixing of hydrothermal fluid with seawater causes metal

sulfide minerals to precipitate. A proportion of the mobilized metals precipitate either below the seafloor in metal-rich stockwork vein networks or replacement of the host rock, or at the seafloor forming metal sulfide-rich chimneys and mounds. The remaining metals vent into the overlying ocean water column as black "smoke" (Elderfield and Schultz, 1996; German and Seyfried, 2014). The depositional efficiency of a discharge site is a quantitative measure of the relative proportion of metals mobilized by the hydrothermal system that precipitate and are retained at or below the seafloor. Previous investigations of depositional efficiency at seafloor hydrothermal vent sites have produced results that indicate that most of the mobilized metals are lost to the hydrothermal plume (Converse et al., 1984; Humphris and Cann, 2000; Cathles, 2011; Hannington, 2011; Jowitt et al., 2012; Jamieson et al., 2014; Patten et al., 2016b, 2017). These studies relied on data collected at the deposit or vent field scale. Jamieson et al. (2014) calculated a depositional efficiency of combined metals, Si, and S of 30% for the TAG active mound using chemical mass balance estimates based on vent fluid flux and hydrothermal deposit tonnage from Humphris and Cann (2000). Jamieson et al. (2014) also combined vent field age, total mound and chimney tonnage, hydrothermal fluid flux estimates, and deposit composition to calculate a total metal sulfide depositional efficiency of 5% for the Endeavour vent field. A different approach, using the composition of protolith and the altered source rocks from ophiolites and seafloor drilling, resulted in calculated efficiency of precipitation estimates of 60% for Cu, 20% for Zn at TAG, and 33% for Cu and 4% for Zn for the Troodos ophiolite (Jowitt et al., 2012; Patten et al., 2016a, 2017). In these studies, the foremost limitation to calculate efficiency estimates was the high uncertainties associated with the input parameters and reliance on assumptions, especially with respect to heat and chemical flux

calculations (Jamieson et al., 2014). Here, we investigate the efficiency of precipitation at the scale of individual vents or vent clusters, which allows for more precise input parameters, but at the expense of being able to extrapolate to the deposit or vent field scale. The inputs required for our calculations include the composition and size of the deposit, vent fluid composition and flux, and the duration of hydrothermal activity. The Lucky Strike vent field, on the northern Mid-Atlantic Ridge, is one of the few vent fields for which all necessary data are available to calculate a chemical mass balance and depositional efficiency for individual vents (Figure 4.1). We apply mass balance calculations to two vent complexes, Sintra and Tour Eiffel, which together account for ~50% of the total mass of hydrothermal material accumulated on the seafloor at Lucky Strike. These sites were chosen because the required input parameters for these sites (mass, age, fluid flux, deposit and fluid composition) are well-constrained (Charlou et al., 2000; Barreyre et al., 2012; Mittelstaedt et al., 2012; Sánchez-Mora et al., 2022a; Sánchez-Mora et al., 2022b). The Sintra site is a vent complex that consists of multiple coalesced mounds and inactive chimneys with one active vent (Figure 4.1). The complex has an estimated mass of 525,000 tons (Sánchez-Mora et al., 2022b). The smaller Tour Eiffel vent complex contains approximately eight individual black smoker vents (Figure 4.1) and has an estimated mass of 55,000 tons, making it more comparable in size to one of several individual mounds (~15) within Sintra (Sánchez-Mora et al., 2022b). The maximum recorded vent fluid temperatures are 222˚C at Sintra and 324˚C at Tour Eiffel (Von Damm et al., 1998; Charlou et al., 2000). Results from ^{226}Ra/Ba dating of hydrothermal barite indicate minimum vent ages of ~6,650 years and 3,850 years for Sintra and Tour Eiffel, respectively (Sánchez-Mora et al., 2022b). These data, combined with deposit volumes and mass estimates from

high resolution (~1 m) bathymetry (Sánchez-Mora et al. 2022b), bulk metal concentrations from surface grab samples (Sánchez-Mora et al. 2022a), vent fluid chemistry (Charlou et al., 2000), and fluid flux estimates (Mittelstaedt et al., 2012, and this study) are used to calculate the fractions of metals that are retained in the deposit, precipitated at the seafloor, and dispersed as a hydrothermal plume (Table 4.1).

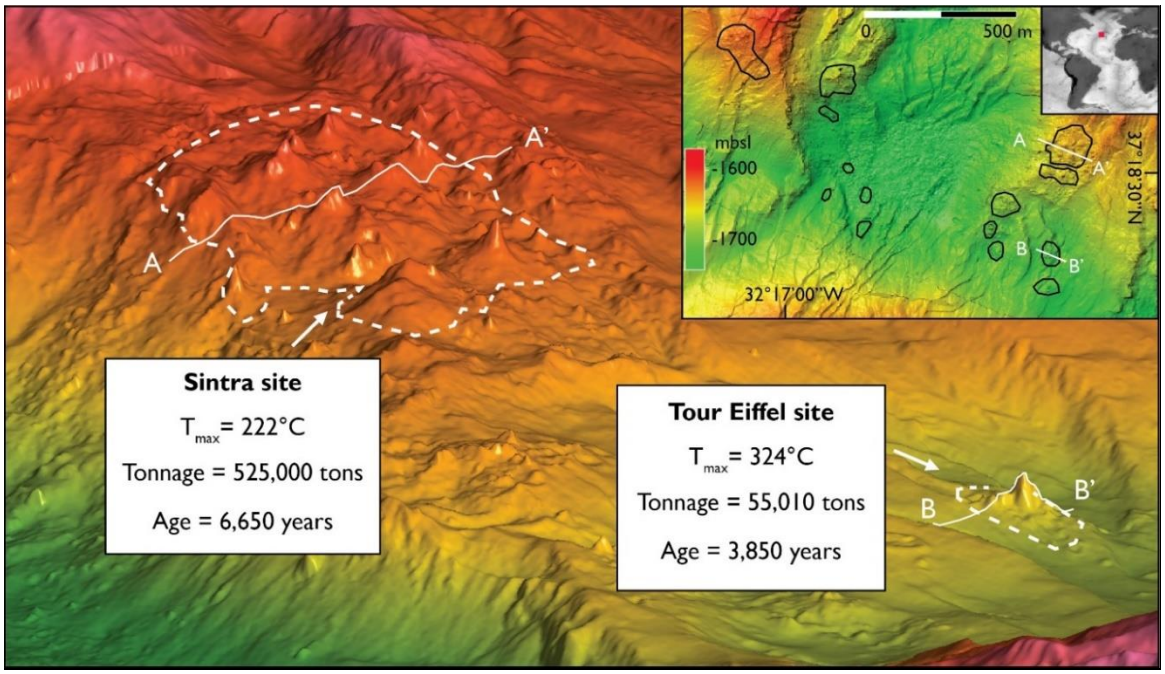

Figure 4.1. Oblique view of ~1 m resolution bathymetric map from the Lucky Strike vent field, looking northeast. The white dashed lines show the extent of the Sintra and Tour Eiffel hydrothermal complexes. The solid white lines indicate the locations of cross-section profiles presented in Figure 4.2. Profile A–A' is 180 m and B–B' is 90 m. The inset map shows the bathymetric map of the main Lucky Strike vent field with the outlines (solid black) of the hydrothermal deposits. Ages, tonnages, and T_{max} from (Charlou et al., 2000; Chavagnac et al., 2018; Sánchez-Mora et al., 2022b).

4.3. Fluid flux estimates

Fluid flux estimates were calculated using the following equation:

$$M_f = Q_f / C_f T_f$$

where M_f (kg/s) is the fluid mass flux, Q_f (MW) is the heat flux, T_f (°C) is the maximum recorded fluid temperature, and C_f is the heat capacity of water (5.2 $kJ \cdot kg^{-1} \cdot °C^{-1}$). Results presented in this study are combined with previously calculated heat fluxes from Mittelstaedt et al. (2012) for Tour Eiffel and from Barreyre et al. (2012) for the overall Lucky Strike vent field. Heat fluxes were calculated using Particle Image Velocimetry (PIV), a video analysis technique that tracks the change in position of features in a video frame by frame. If the scale of the imagery can be determined (e.g., by having an object of known dimensions in the same plane as the moving features) and the video frame rate is known, velocities (in this case smoke discharge from a vent) can be calculated. Heat flux can be calculated from velocities if the area of the vent orifice can also be determined (again, with an object of known dimensions in the field of view) and the vent fluid temperature is known (Mittelstaedt et al., 2012). For Sintra, the estimated present day heat flux ranges from 2 to 20 MW (Q_f). Using this range for heat flux, and C_f=5.2 $kJ \cdot kg^{-1} \cdot C^{-1}$ and T_f=222°C, Sintra is venting fluid at a rate of of 2–17 kg/s. For Tour Eiffel, the heat flux ranges from 1 to 45 MW (Q_f), and, based on T_f=324°C, results in a calculated fluid flux of 1–27 kg/s. These heat flux estimates include both focused/high temperature and lower temperature diffuse flow. At Tour Eiffel, the diffuse to discrete ratio was determined to be ~18, with discrete venting output of ~1 MW (Mittelstaedt et al., 2012). These calculated fluid fluxes are comparable to estimates from entire vent fields, such as 86 kg/s at 9˚50'N

(~30 active vents) on the East Pacific Rise, 36 kg/s at ASHES (~7 active vents), at Axial volcano on the Juan de Fuca Ridge, and 56 kg/s at Kairei (~7 active vents) in the Central Indian Ridge (Macdonald et al., 1980; Rona and Trivett, 1992; Hashimoto et al., 2001; Lowell et al., 2013).

4.4. Efficiency of metal entrapment

Metal depositional efficiency was calculated using the following equation:

$$\text{Depositional Efficiency (\%)} = \frac{\text{Metal trapped}}{\text{Metal trapped} + \text{Metal lost to plume}} \times 100\%$$

This equation assumes that vent fluids collected at chimney orifices represent the only source of metal loss to the plume, and the composition of the fluids is the product of the modification of initial sub-seafloor upwelling fluid by precipitation of minerals upon mixing with seawater, either within the chimneys and mounds, or in the shallow sub-seafloor. The amount of metal trapped at each site is determined from bulk geochemical analysis and deposit size (Table 4.1). The amount of metal that has exited the seafloor as a dissolved or particulate component of the vent fluid is calculated from the end-member concentration of metal in the fluid, the fluid flux, and the amount of time for which the vent has been active.

Metal fluxes to the overlying water column were calculated using average fluid compositions and estimated maximum fluid fluxes from each site (Table 4.1). Results of these calculations indicate that depositional efficiencies differ significantly for different elements, with Cu, Zn, and Fe having efficiencies that range from 10 to 99%, and Si and

Mn having efficiencies of at least two orders of magnitude lower (Table 4.1). The associated uncertainties for the calculated depositional efficiencies were determined by propagating the uncertainties of each parameter through the equation (Table 4.1). However, the calculated uncertainty values are likely a minimum estimates due to unquantified uncertainties associated with the input data, including: 1) the average bulk geochemical data for each vent complex was determined from only a limited number of surface grab samples, and these values may not be representative of the composition of the interior of the vents; 2) the calculations assume that vent fluid composition and flux have not changed significantly over the lifespan of the vents; 3) the U-series geochronology provides only a minimum ages for the vents, and the reported efficiencies should therefore be considered maximum values; and 4) in contrast, the calculations underestimate depositional efficiency by considering only the hydrothermal material that has accumulated on the seafloor, and not hydrothermal mineralization that may also occur in a stockwork zone beneath the vent complexes (Jamieson et al., 2014). With respect to the stability of vent fluid composition, sampling and monitoring at Lucky Strike over the past ~20 years indicates relative stability in fluid temperature and composition over this period (Von Damm et al., 1998; Pester et al., 2012; Chavagnac et al., 2018). Vent fluid stability over similar timespans has also been documented at the Endeavour vent field (Seyfried et al., 2004), the Lau Basin (Du Preez and Fisher, 2018) and the Mid-Atlantic Ridge (Logatchev-1, Nibelungen, Turtle Pits, Red Lion, and Menez Gwen) (Koschinsky et al., 2020). For sub-seafloor precipitation, at the active TAG mound, Humphris and Cann (2000) estimated that the sub-seafloor stringer zone contains 44% of the amount of sulfide material exposed at the seafloor. However, results from seismic reflection surveys indicate that the total amount of sulfide material at

the entire TAG field can be up to 2–5 times greater than that deposited above the seafloor (Murton et al., 2019). Accounting for a similar degree of sub-seafloor mineralization at Lucky Strike would result in an increase in calculated depositional efficiencies.

The degree of sub-seafloor sulfide precipitation raises the question of the availability of sulfur for the precipitation of the sulfide deposits at the seafloor. Charlou et al. (2000) report vent fluid H_2S concentrations of 2700 μmol/L, which is in stoichiometric excess relative to the combined vent fluid Fe, Cu, and Zn concentrations (308 μmol/L, 10.6 μmol/L, and 29 μmol/L, respectively; Charlou et al., 2000), indicating that, even with significant sub-seafloor precipitation, S remains in excess relative to base metals in the vent fluid, and is therefore not a limiting factor for the precipitation of massive sulfide deposits at the surface. For comparison, the active mound at TAG has a vent fluid metal excess, relative to S (H_2S=3500 μmol/L, Cu=150 μmol/L, Fe=5590 μmol/L, and Zn= 46 μmol/L; James and Elderfield, 1996).

To assess how much the uncertainties of the different input parameters (Table 4.1) change the calculated efficiencies, a sensitivity analysis of the calculations was performed, using Cu from the Sintra site as a test case. Using the minimum and maximum estimates of heat flux (2–15 MW) the efficiency for Cu varies from 99.19% to 99.89%, respectively. The uncertainty in age of 6493–6801 years for Sintra results in a variation of 99.17% and 99.20% (using a heat flux of 15 MW). The uncertainty of the estimated volumes is ±10% and results in a variation of 99.10% to 99.26%. The uncertainty of densities is ±25% and using the lowest density the efficiency would be 98.91% and the highest would yield a value of 99.35%. The Cu composition of the hydrothermal deposits has a range of 2.5–26 wt. %, which yields efficiencies that range from 95.64% to 99.58%, respectively. The

temperature of the fluid has only a 1% uncertainty (Charlou et al., 2000), however, if at Sintra we use the same temperature as at Tour Eiffel (324°C), the efficiency of Cu varies from 99.19% to 99.44%. Likewise, if for Sintra the same fluid Cu composition of Tour Eiffel (26 μmol/L) is applied, the efficiency decreases to 94.10%. Finally, if we consider a scenario where each of the ~15 mound/chimney structures formed under the same conditions of Tour Eiffel (temperature and Cu composition) and use a heat flux of 15 times the maximum heat flux at Sintra (225 MW), the calculated Cu efficiency would be 60%. Therefore, we see that the most sensitive parameters are: 1) the composition of the fluids where we see a difference of 5% lower in the efficiency estimate when the composition of the fluid is increase by nearly an order of magnitude (3.4 to 26 μmol/L); 2) the composition of the hydrothermal deposits where again an increase in the inputed composition by an order of magnitude (2.5 to 26 Cu wt.%) results in a decrease of 5% of depositional efficiency; and 3) an assumed heat flux of an order of magnitude higher (15 to 225 MW) results in the greatest change in calculated depositional efficiency, from 99% to 60%.

Table 4.1. Compositions of seafloor massive sulfides and fluid compositions used to calculate entrapment efficiencies.

		Cu	Zn	Fe	Si	Mn
Heat flux (MW)[a]	Tour Eiffel[a]			1–45		
	Sintra			2–20		
Fluid flux (kg/s)	Tour Eiffel			27±5		
	Sintra			13±3		
Vent fluid composition (μmol/L)[b]	Tour Eiffel	26±0.001	16.5±0.0008	624±0.02	13,400±0.1	289±0.009
	Sintra	3.4±0.0002	12.5±0.0006	260±0.01	11,500±0.1	228±0.008
Deposit composition (wt.%)[c]	Tour Eiffel (n=5)	5.9±0.4	11.2±0.6	23±1.2	5±0.4	0.04556±0.003
	Sintra (n=4)	13.6±0.95	1.9±0.1	25.5±1.3	0.8±0.06	0.1±0.003
	Lucky Strike (n=23)	7.3±0.5	5.1±0.3	27.1±1.4	3±0.2	0.03±0.002
Deposit mass[a] (t)[d]	Tour Eiffel	3,200±900	6,200±1700	12,700±3600	2,800±800	25±7
	Sintra	71,700±20000	10,300±2800	134,500±37000	800±200	50±14
Deposit minimum age (yr)[d]	Tour Eiffel			3,840±274		
	Sintra			6,647±154		
Vent metal flux (t/yr)	Tour Eiffel	1.4±0.3	0.9±0.2	21±5	318±70	10±2
	Sintra	0.1±0.02	0.5±0.06	6.5±1	180±26	5.7±0.9
Deposit accumulation rate* (t/yr)	Tour Eiffel	0.8±0.2	1.6±0.5	3.3±1	0.7±0.2	0.007±0.002
	Sintra	11±3	1.5±0.4	20±6	0.1±0.02	0.008±0.002
Precipitation efficiency* (%)	Tour Eiffel	>38	>64	>14	<0.5	<0.1
	Sintra	>99	>78	>76	<0.7	<1

a-(Mittelstaedt et al., 2012)
b-(Charlou et al., 2000)
c-(Sánchez-Mora et al. 2022a)
d-(Sánchez-Mora et al. 2022b)

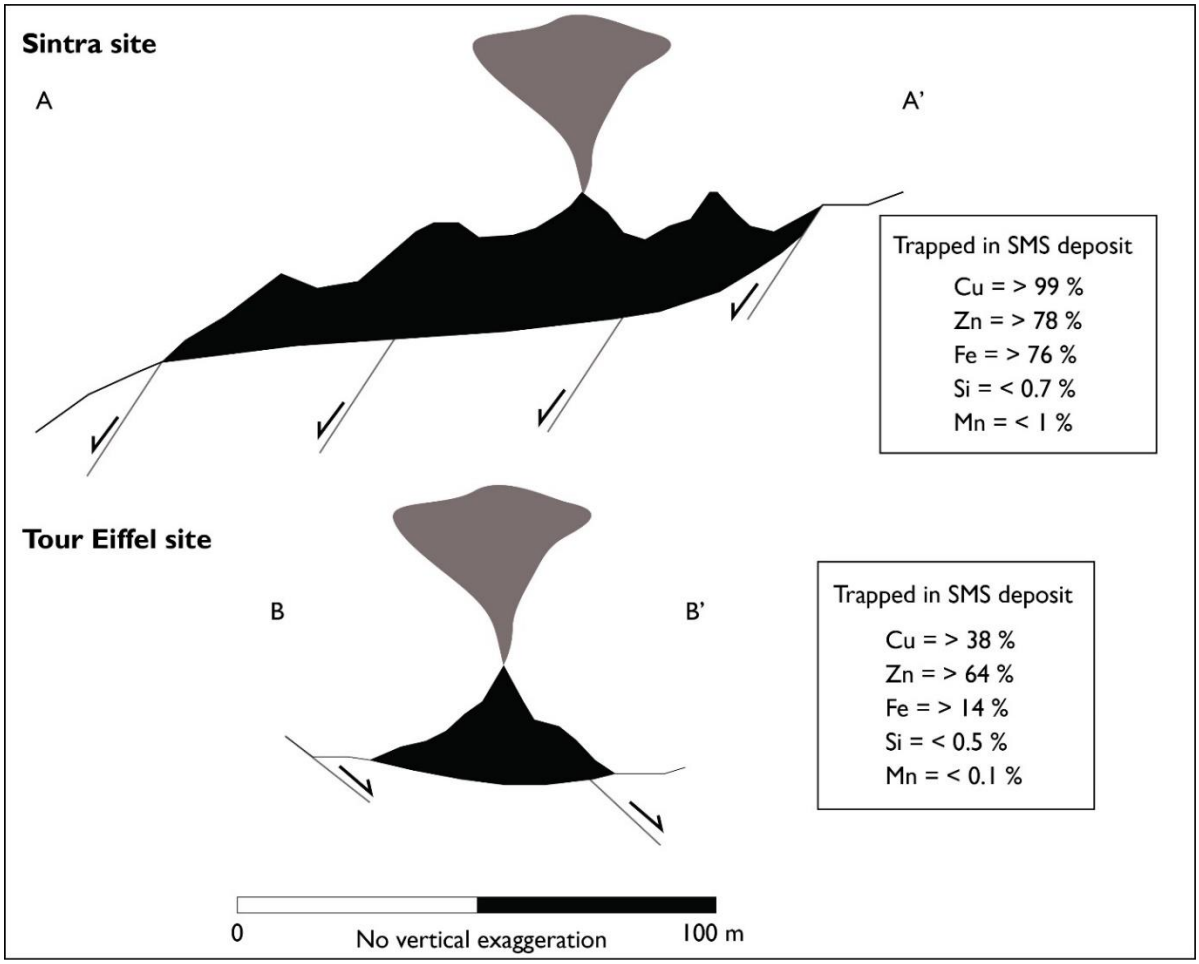

Figure 4.2. Summary profiles of metal precipitation efficiencies for the Sintra and Tour Eiffel sites (see Figure 4.1 for location). Location of normal faults interpreted from surface bathymetry.

4.5. Effects of temperature dependent mineral solubilities on depositional efficiency

At both Tour Eiffel and Sintra, the differences in metal-specific depositional efficiencies generally follow an expected pattern where elements associated with minerals that precipitate at higher temperature, such as Cu in chalcopyrite, Zn in sphalerite, and Fe primarily in pyrite, marcasite and pyrrhotite, but also chalcopyrite and sphalerite, are trapped more efficiently than elements associated with phases that precipitate at lower

temperatures, such as Si in amorphous silica and Mn in Mn-oxide crusts (Table 4.2: Hannington et al., 1995). The relatively lower efficiency of Cu precipitation at Tour Eiffel is a notable exception to this pattern.

Table 4.2. Comparison of depositional efficiency to temperature of precipitation of host mineral.

Metal	**Primary mineral**	**Temperature of precipitation (°C)***	**Depositional efficiency Lucky Strike (%)**	**Depositional efficiency TAG (%)**	**Depositional efficiency Endeavour (%)**
Cu	Chalcopyrite	250–350[1]	38–99	3–19	27–70
Zn	Sphalerite	<250[1]	64–78	1–11	28–70
Fe	Pyrite	<300 and >350[2]	10–77	1–8	<1
Si	Amorphous Silica	120–140[3]	<1	0.5–2.5	<1
Mn	Mn oxide	<25[4]	<1	<1	<1

*Temperature of a typical mid-ocean ridge basalt-hosted vent fluid. [1] (Hannington, 2014), [2] (Grant et al., 2018; Petersen et al., 1998), [3] (Jamieson et al., 2016), [4] (Gammons and Seward, 1996).

The differences in depositional efficiencies between Sintra and Tour Eiffel indicate that depositional efficiencies can vary significantly between different vents within a single field. The higher efficiencies at Sintra are consistent with the lower fluid venting temperature and associated higher degree of sulfide mineral precipitation (Table 4.1). Sintra is also older, larger, and has a greater overall depositional accumulation rate than Tour Eiffel (Table 4.1). For Sintra, a suggested past hydrothermal flux of 25 kg/s (Barreyre et al., 2012) would lower the calculated efficiency of precipitation by ~3% for Cu, Zn, and Fe and <0.5% for Si and Mn. The overall greater efficiency of precipitation at Sintra could be related to

greater sub-seafloor permeability and seawater mixing associated with its intersection with a greater number of faults, relative to Tour Eiffel (Figure 4.2). Alternatively, a decline in hydrothermal activity at Sintra (Barreyre et al., 2012) compared to Tour Eiffel could potentially also be relevant to precipitate more metals at depth below Sintra.

4.6. Scale-dependent depositional efficiency calculations

The chemical mass balance approach for calculating the depositional efficiencies for vents within Lucky Strike can be applied to other sediment-free hydrothermal sites for which similar data are available, albeit applied to the vent field scale instead of individual vents or vent clusters. For example, at the TAG active mound, which has a diameter of 250 m and height of 40 m, the estimated depositional efficiency ranges from 3–19% for Cu, 1–11% for Zn, 1–8% for Fe, 0.5–2.5% for Si, and <1% for Mn, based on a range of estimated heat flux of 225–2000 MW (Rona et al., 1993; James and Elderfield, 1996; Humphris and Cann, 2000). In addition to the difference in size of the TAG mound, which is significantly larger than Sintra or Tour Eiffel, the estimates for the TAG mound are based on a higher range of heat flux (compared to 20 and 45 MW for Sintra and Tour Eiffel, respectively) that was used to estimate the amount of metal lost to the plume (James and Elderfield, 1996; Humphris and Cann, 2000). If a similar heat flux is used for TAG as in this study (assuming 45 MW and 10,000 years of active venting), the efficiency of precipitation (Cu=31%, Zn=19%, Fe=13%, Si=4%, Mn<1%) would be comparable to that of Tour Eiffel but lower than estimates from Sintra.

For the Endeavour vent field, which stretches over 15 km of ridge segment, an estimated efficiency of <5% was determined for total base metals, silica, and sulfur, based on total

deposit size, age, and fluid and heat flux estimates (Jamieson et al., 2014). However, the efficiency, recalculated for the same elements as this study (Cu, Zn, Fe, Si, and Mn), using the same heat flux of 400–2500 MW that has been previously estimated at this site, results in values that range from 27–70% for Cu, 28–70% for Zn, <1% for Fe, Si, and Mn (Ginster et al., 1994; Von Damm, 1995; Jamieson et al., 2014). These values are strikingly similar to the values calculated for Lucky Strike, with the exception of Fe. For all three vent fields, the depositional efficiencies show a similar pattern of decreasing efficiency with decreasing temperature of associated mineral precipitation. The lower calculated efficiencies at TAG and, to a lesser extent, Endeavour, may reflect an overall higher proportion of high-temperature venting and associated loss of metals to the plume.

The calculated accumulation rates for TAG, Endeavour, and Lucky Strike (360 t/yr, 400 t/yr, and 194 t/y, respectively), based on age and volume estimates, are relatively similar to each other. However, there is a significant difference in the areal extent of each of these sites. Area-normalized mass accumulation rates are 21 t/yr·km^2 for TAG, 7 t/yr·km^2 for Endeavour, and 78 t/yr·km^2 for Lucky Strike. The higher areally-normalized accumulation rate at Lucky Strike is likely related to the higher depositional efficiency at this site.

4.7. Implications for metal fluxes to the oceans and rates of ore-forming processes

This study shows that the efficiency of precipitation of hydrothermal vents are highly variable, but can be high, with the potential for most of the mobilized metals to accumulate at the seafloor and sub-seafloor and not vent into the ocean. Hannington (2011) estimated a global precipitation efficiency assuming a mass accumulation rate range of 1,200–12,000 t/yr for hydrothermal massive sulfide deposits and a flux into the oceans of ~1 million tons

per year of metal and sulfur, which yields an efficiency of <1%. If global efficiencies are higher, either the associated global accumulation rates are also higher than these estimates or global flux to the oceans is lower. However, the variability of efficiencies between different vent sites within a single vent field indicate that caution must be used when extrapolating from the scale of a single vent or vent complex to the deposit, vent field, or global scale.

High depositional efficiencies represent optimal ore-forming conditions at the seafloor by maximizing the trapping of the target metals of potential economic value and minimize the diluting effects of elements that are not of economic value. Based on the calculated depositional efficiencies for Cu, Zn, Fe, Mn, and Si, a vent fluid temperature window of between ~150 to 250°C would maximize the trapping of the primary target base metals of economic interest (Cu and Zn) while minimizing the precipitation of elements that contribute to diluting gangue minerals (Mn and Si).

4.8. Acknowledgments

This work was supported by the Canada Research Chair Program, an NSERC Discovery Grant, and RDC Leverage Grant to J.W. Jamieson. DSM acknowledges support from the NSERC iMAGE-CREATE program.

4.9. References

Barreyre, T., Escartín, J., Garcia, R., Cannat, M., Mittelstaedt, E., and Prados, R., 2012, Structure, temporal evolution, and heat flux estimates from the Lucky Strike deep-sea hydrothermal field derived from seafloor image mosaics: Geochemistry, Geophysics,

Geosystems, v. 13, p. 1–29, doi: 10.1029/2011GC003990.

Cathles, L.M., 2011, What processes at mid-ocean ridges tell us about volcanogenic massive sulfide deposits: Mineralium Deposita, v. 46, p. 639–657, doi: 10.1007/s00126-010-0292-9.

Charlou, J.L., Donval, J.P., Douville, E., Jean-Baptiste, P., Radford-Knoery, J., Fouquet, Y., Dapoigny, A., and Stievenard, M., 2000, Compared geochemical signatures and the evolution of Menez Gwen (35°50N) and Lucky Strike (37°17N) hydrothermal fluids, south of the Azores Triple Junction on the Mid-Atlantic Ridge: Chemical Geology, v. 171, p. 49–75, doi: 10.1016/S0009-2541(00)00244-8.

Chavagnac, V., Leleu, T., Fontaine, F., Cannat, M., Ceuleneer, G., and Castillo, A., 2018, Spatial Variations in Vent Chemistry at the Lucky Strike Hydrothermal Field, Mid-Atlantic Ridge (37°N): Updates for Sub-seafloor Flow Geometry From the Newly Discovered Capelinhos Vent: Geochemistry, Geophysics, Geosystems, v. 19, p. 4444–4458, doi: 10.1029/2018GC007765.

Converse, D.R., Holland, H.D., and Edmond, J.M., 1984, Flow rates in the axial hot springs of the East Pacific Rise (21°N): implications for the heat budget and the formation of massive sulfide deposits: Earth and Planetary Science Letters, v. 69, p. 159–175.

Von Damm, K.L., 1995, Controls on the Chemistry and Temporal Variability of Seafloor Hydrothermal Fluids, *in* Humphris, S.E., Zierenberg, R.A., Mullineaux, S., and Thomson, R.E. eds., Seafloor hydrothermal systems: Physical, chemical, biological, and geological interactions, Geophysical Monograph, American Geophysical Union, v. 91, p. 222–247, doi: 10.1029/GM091p0222.

Von Damm, K.L., Bray, A.M., Buttermore, L.G., and Oosting, S.E., 1998, The geochemical controls on vent fluids from the Lucky Strike vent field , Mid-Atlantic Ridge: Earth and Planetary Science Letters, v. 160, p. 521–536.

Elderfield, H., and Schultz, A., 1996, Mid-Ocean Ridge hydrothermal fluxes and the chemical composition of the ocean: Ann. Rev. Earth Planet. Sci., v. 24, p. 191–224.

Gammons, C.H., and Seward, T.M., 1996, Stability of manganese (II) chloride complexes from 25 to 300°C: Geochimica et Cosmochimica Acta, v. 60, p. 4295–4311, doi: 10.1016/S0016-7037(96)00275-X.

German, C.R., and Seyfried, W.E., 2014, Hydrothermal Processes: Elsevier Ltd., v. 8, 191–233 p., doi: 10.1016/B978-0-08-095975-7.00607-0.

Ginster, U., Mottl, M.J., and Von Herzen, R.P., 1994, Heat flux from black smokers on the Endeavour and Cleft segments , Juan de Fuca Ridge: Journal of Geophysical Research, v. 99, p. 4937–4950.

Graber, S., Petersen, S., Yeo, I., Szitkar, F., Klischies, M., Jamieson, J.W., Hannington, M.D., Rothenbeck, M., Wenzlaff, E., Augustin, N., and Stobbs, I., 2020, Structural Control, Evolution, and Accumulation Rates of Massive Sulfides in the TAG

Hydrothermal Field: Geochemistry, Geophysics, Geosystems, doi: 10.1029/2020GC009185.

Grant, H.L.J., Hannington, M.D., Petersen, S., Frische, M., and Fuchs, S.H., 2018, Constraints on the behavior of trace elements in the actively-forming TAG deposit, Mid-Atlantic Ridge, based on LA-ICP-MS analyses of pyrite: Chemical Geology, p. 1–27, doi: 10.1016/j.chemgeo.2018.08.019.

Hannington, M., 2011, Comments on "What processes at mid-ocean ridges tell us about volcanogenic massive sulfide deposits" by L.M. Cathles: Mineralium Deposita, v. 46, p. 659–663, doi: 10.1007/s00126-011-0329-8.

Hannington, M.D., 2014, Volcanogenic Massive Sulfide Deposits: Treatise on Geochemistry: Second Edition, v. 13, p. 463–488, doi: 10.1016/B978-0-08-095975-7.01120-7.

Hannington, M.D., Galley, A.G., Herzig, P.M., and Petersen, S., 1998, Comparison of the TAG mound and stockwork complex with Cyprus-type massive sulfide deposits, *in* Herzig, P.M., Humphris, S.E., Miller, D.J., and Zierenberg, R.A. eds., Proceedings of the Ocean Drilling Program, Scientific Results, v. 158, p. 389–415.

Hashimoto, J., Ohta, S., Gamo, T., Chiba, H., Yamaguchi, T., Tsuchida, S., Okudaira, T., Watabe, H., Yamanaka, T., and Kitazawa, M., 2001, First hydrothermal vent communities from the Indian Ocean discovered: Zoological Science, v. 18, p. 717–721, doi: 10.2108/zsj.18.717.

Humphris, S.E., and Cann, J.R., 2000, Constraints on the energy and chemical balances of the modern TAG and ancient Cyprus seafloor sulfide deposits: Journal of Geophysical Research, v. 105, p. 28477–28488.

James, R.H., and Elderfield, H., 1996, Chemistry of ore-forming fluids and mineral formation rates in an active hydrothermal sulfide deposit on the Mid-Atlantic Ridge: Geology, v. 24, p. 1147–1150, doi: 10.1130/0091-7613(1996)024<1147:COOFFA>2.3.CO;2.

Jamieson, J.W., Clague, D.A., and Hannington, M.D., 2014, Hydrothermal sulfide accumulation along the Endeavour Segment , Juan de Fuca Ridge: Earth and Planetary Science Letters, v. 395, p. 136–148.

Jamieson, J.W., Hannington, M.D., Tivey, M.K., Hansteen, T., Williamson, N.M.B., Stewart, M., Fietzke, J., Butterfield, D., Frische, M., Allen, L., Cousens, B., and Langer, J., 2016, Precipitation and growth of barite within hydrothermal vent deposits from the Endeavour Segment, Juan de Fuca Ridge: Geochimica et Cosmochimica Acta, v. 173, p. 64–85, doi: 10.1016/j.gca.2015.10.021.

Jowitt, S.M., Jenkin, G.R.T., Coogan, L.A., and Naden, J., 2012, Quantifying the release of base metals from source rocks for volcanogenic massive sulfide deposits : Effects of protolith composition and alteration mineralogy: Journal of Geochemical Exploration, v. 118, p. 47–59, doi: 10.1016/j.gexplo.2012.04.005.

Koschinsky, A., Schmidt, K., and Garbe-schönberg, D., 2020, Geochemical time series of hydrothermal fluids from the slow-spreading Mid-Atlantic Ridge : Implications of medium-term stability: Chemical Geology, v. 552, p. 119760, doi: 10.1016/j.chemgeo.2020.119760.

Lowell, R.P., Farough, A., Hoover, J., and Cummings, K., 2013, Characteristics of magma-driven hydrothermal systems at oceanic spreading centers: Geochemistry, Geophysics, Geosystems, v. 14, p. 1756–1770, doi: 10.1002/ggge.20109.

Macdonald, K.C., Becker, K., Spiess, F.N., and Ballard, R.D., 1980, Hydrothermal heat flux of the "black smoker" vents on the East Pacific Rise: Earth and Planetary Science Letters, v. 48, p. 1–7, doi: 10.1016/0012-821X(80)90163-6.

Mittelstaedt, E., Escartín, J., Gracias, N., Olive, J., Barreyre, T., Davaille, A., Cannat, M., and Garcia, R., 2012, Quantifying diffuse and discrete venting at the Tour Eiffel vent site, Lucky Strike hydrothermal field: Geochemistry, Geophysics, Geosystems, v. 13, doi: 10.1029/2011GC003991.

Murton, B.J., Lehrmann, B., Dutrieux, A.M., Martins, S., de la Iglesia, A.G., Stobbs, I.J., Barriga, F.J.A.S., Bialas, J., Dannowski, A., Vardy, M.E., North, L.J., Yeo, I.A.L.M., Lusty, P.A.J., and Petersen, S., 2019, Geological fate of seafloor massive sulphides at the TAG hydrothermal field (Mid-Atlantic Ridge): Ore Geology Reviews, v. 107, p. 903–925, doi: 10.1016/j.oregeorev.2019.03.005.

Patten, C.G.C., Pitcairn, I.K., and Teagle, D.A.H., 2017, Hydrothermal mobilisation of Au and other metals in supra-subduction oceanic crust : Insights from the Troodos ophiolite: Ore Geology Reviews, v. 86, p. 487–508, doi: 10.1016/j.oregeorev.2017.02.019.

Patten, C.G.C., Pitcairn, I.K., Teagle, D.A.H., and Harris, M., 2016a, Mobility of Au and related elements during the hydrothermal alteration of the oceanic crust : implications for the sources of metals in VMS deposits: Mineralium Deposita, v. 51, p. 179–200, doi: 10.1007/s00126-015-0598-8.

Patten, C.G.C., Pitcairn, I.K., Teagle, D.A.H., and Harris, M., 2016b, Sulphide mineral evolution and metal mobility during alteration of the oceanic crust: Insights from ODP Hole 1256D: Geochimica et Cosmochimica Acta, v. 193, p. 132–159, doi: 10.1016/j.gca.2016.08.009.

Pester, N.J., Reeves, E.P., Rough, M.E., Ding, K., Seewald, J.S., and Seyfried, W.E., 2012, Sub-seafloor phase equilibria in high-temperature hydrothermal fluids of the Lucky Strike Seamount: Geochimica et Cosmochimica Acta, v. 90, p. 303–322, doi: 10.1016/j.gca.2012.05.018.

Petersen, S., Herzig, P.M., and Hannington, M.D., 1998, Fluid inclusion studies as a guide to the temperature regime within the TAG hydrothermal mound, 26°N, Mid-Atlantic Ridge., *in* Herzig, P.M., Humphris, S.E., and Zierenberg, R.A. eds., Proceedings of the Ocean Drilling Program, Scientific Results, College Station, Ocean Drilling

Program, p. 163–178.

Du Preez, C., and Fisher, C.R., 2018, Long-Term Stability of Back-Arc Basin Hydrothermal Vents: Frontiers in Marince Science, v. 5, p. 1–10, doi: 10.3389/fmars.2018.00054.

Rona, P.A., Hannington, M.D., Raman, C. V., Thompson, G., Tivey, M.K., Humphris, S.E., Lalou, C., and Petersen, S., 1993, Active and relict sea-floor hydrothermal mineralization at the TAG hydrothermal field, mid-Atlantic ridge: Economic Geology, v. 88, p. 1989–2017, doi: 10.2113/gsecongeo.88.8.1989.

Rona, P.A., and Trivett, D.A., 1992, Discrete and diffuse heat transfer at ashes vent field, Axial Volcano, Juan de Fuca Ridge: Earth and Planetary Science Letters, v. 109, p. 57–71, doi: 10.1016/0012-821X(92)90074-6.

Sánchez-Mora, D., Jamieson, J.W., Cannat, M., Escartín, J., and Barreyre, T., 2022a, Effects of substrate composition and subsurface fluid pathways on the geochemistry of seafloor hydrothermal deposits at the Lucky Strike Vent Field, Mid-Atlantic Ridge:

Sánchez-Mora, D., Jamieson, J.W., Escartín, J., Barreyre, T., and Cannat, M., 2022b, Age and rates of formation of metal-rich hydrothermal deposits on the seafloor: example from the Lucky Strike Vent Field, Mid-Atlantic Ridge:

Seyfried, W.E., Seewald, J.S., Berndt, M.E., Ding, K., and Foustoukos, D.I., 2004, Chemistry of hydrothermal vent fluids from the Main Endeavour Field , northern Juan de Fuca Ridge : Geochemical controls in the aftermath of June 1999 seismic events: Journal of Geophysical Research, v. 108, p. 1–23, doi: 10.1029/2002JB001957.

5. Investigating brittle deformation and rifting processes at the Lucky Strike hydrothermal field, Mid-Atlantic Ridge, from quantitative fault analysis derived from high-resolution bathymetry

5.1. Abstract

Faulting within oceanic lithosphere is one of the primary controls on hydrothermal fluid circulation and the formation of hydrothermal deposits on the seafloor. The locations and geometries of faults can be determined from bathymetric expressions at the seafloor. In an effort to optimize the amount of data extractable from a bathymetric dataset, we use the 3D software Leapfrog Geo to visualize faults on the seafloor and digitize their orientation and slip to investigate the relationship between rift-related regional stress fields and the location of hydrothermal discharge at the Lucky Strike hydrothermal vent field, Mid-Atlantic Ridge. Results indicate that the location of hydrothermal venting and seafloor massive sulfide deposits is controlled by enhanced permeability resulting from local scale offsets in the orientation of stress fields associated with the rifting of two axial volcanoes upon which the vent field is situated. This offset in stress field orientation results in the formation of relay ramps and fault linkages where the faults that cross-cut the southern volcano interact with the faults that cross-cut the northern volcano, creating areas of enhanced permeability. The bathymetric data show that underlapping of west-dipping faults on the eastern flank of the rift control the venting of hydrothermal fluids at distances of up to 1.4 km from the central ridge axis. These results demonstrate the value of digitization and orientation analysis of geological deformation features identified from high-resolution bathymetric models of the seafloor for investigating controls on hydrothermal fluid circulation along mid-ocean ridges.

5.2. Introduction

Faults have been widely recognized as a primary control on the location of hydrothermal mineral deposits on land (Gibson et al., 1997; Vearncombe et al., 1998; Rowland and Sibson, 2004; Micklethwaite et al., 2010; Blenkinsop et al., 2020) and at the seafloor (Kleinrock and Humphris, 1996; Curewitz and Karson, 1997; deMartin et al., 2007; McCaig et al., 2007; Humphris et al., 2015; Graber et al., 2020). To decipher the structural controls on the location of mineral deposits on land, extensive mapping of faults and other structural features is required to determine the geometry and kinematics of deformation and their relation to hydrothermal fluid circulation (Micklethwaite et al., 2010; Blenkinsop et al., 2020). Mapping of these features is complicated by post-formational processes such as erosion, deformation, and modification of the surficial environment through human and other biological processes. For deposits forming on the seafloor, such as seafloor massive sulfide (SMS) deposits that form at sites of high-temperature hydrothermal venting, the challenges are in some ways simpler, and in other ways more complicated than structural mapping on land. For example, SMS deposits form along mid-ocean ridges also along submarine arcs, rifted arcs, back-arcs, and fore arc, which are modern, volcanically and tectonically active geological environments, and are thus not overprinted by subsequent geological or biological processes that alter the primary geological features. However, collecting reliable, high-quality geological data from the seafloor and sub-seafloor is much more technically challenging and costly than collecting similar data from dry land and its subsurface. Digital bathymetric models of the deep ocean floor are acquired using

multibeam echosounders. The resolution of the data can vary from <1 m to ~100 m, depending on the depth, and whether the data is being collected from a surface vessel or an underwater vehicle. Structural geology studies at the seafloor commonly rely on 2D lineament analysis of bathymetric data sets of varying resolutions (Kleinrock and Humphris, 1996; Anderson et al., 2017; Anderson et al., 2021; Graber et al., 2020). Even though lineament analysis can be a valuable tool to determine trends that can explain the location of hydrothermal deposits or hydrothermal venting at a regional scale, this analysis only uses the strike of structures and not dip, and therefore the geometry of the faults is not fully resolved (Anderson et al., 2017; Graber et al., 2020; Dyriw et al., 2021). To determine the dip of a structure using bathymetric data it is critical that the resolution of the data is not only high enough to resolve the fault, but also high enough to accurately resolve features on the exposed fault scarp in order to avoid measuring dips of, for example, scree slopes. Due to increasing acquisition of high-resolution (<5 m) bathymetry in our underexplored oceans (Wölfl et al., 2019), we propose the use of 3D software (Leapfrog Geo), which is primarily used in the mineral exploration industry on land, to extract additional information from faults such as dip and displacement to better understand the geometric controls on hydrothermal deposits and venting locations on the seafloor. Here, we present a case study from the Lucky Strike hydrothermal field, which is located on an actively rifting volcanic complex. We identified and measured the orientations of the rift faults, and used these data to assess the regional stress fields associated with rifting, and investigate the controls of the rift-related faults on the location of hydrothermal venting and associated seafloor massive sulfide deposit formation.

5.3. Geological setting

The Lucky Strike segment is located approximately 360 km southwest of the Azores archipelago on the slow-spreading Mid-Atlantic Ridge, near the the triple junction between the North American, African, and Eurasian plates (Cannat et al., 1999; Escartín et al., 2001).

The Lucky Strike segment is ~70 km long with a prominent axial volcano, named the Lucky Strike Seamount, that rises to 1500 mbsl in the central part of the segment from bathymetric lows of ~3500 mbsl towards the ends of the segment (Figure. 5.1). The Lucky Strike Seamount consists of a central volcanic edifice that lies within a ~20 km wide fault-bounded rift valley, and is situated above a 7 km long, 4 km wide axial magma chamber that lies ~3.5 km below the seafloor and is the heat source driving the hydrothermal system (Singh et al., 2006; Combier et al., 2015; Escartín et al., 2015). A series of rifted volcanic highs within the volcanic edifice indicates episodic changes between tectonic and volcanic dominated phases of seafloor spreading (Humphris et al., 2002). The most recent volcanic activity and current hydrothermal activity occurs above the axial magma chamber, in the center of the volcano (Ondréas et al., 2009; Escartín et al., 2014, 2015). This most recent episode of volcanism produced two volcanic edifices that are aligned along the ridge axis, and separated by a flat depression (Figure. 5.2) that is interpreted to be a recent fossil lava lake (Humphris et al., 2002; Ondréas et al., 2009). Both edifices are now cut by a series of ridge-parallel normal faults (Figure. 5.2), with the older, northern, edifice experiencing a higher degree of rifting than the younger, southern, edifice (Humphris et al., 2002). The recent fossil lava lake appears to cover and therefore be younger than the rift-related faults.

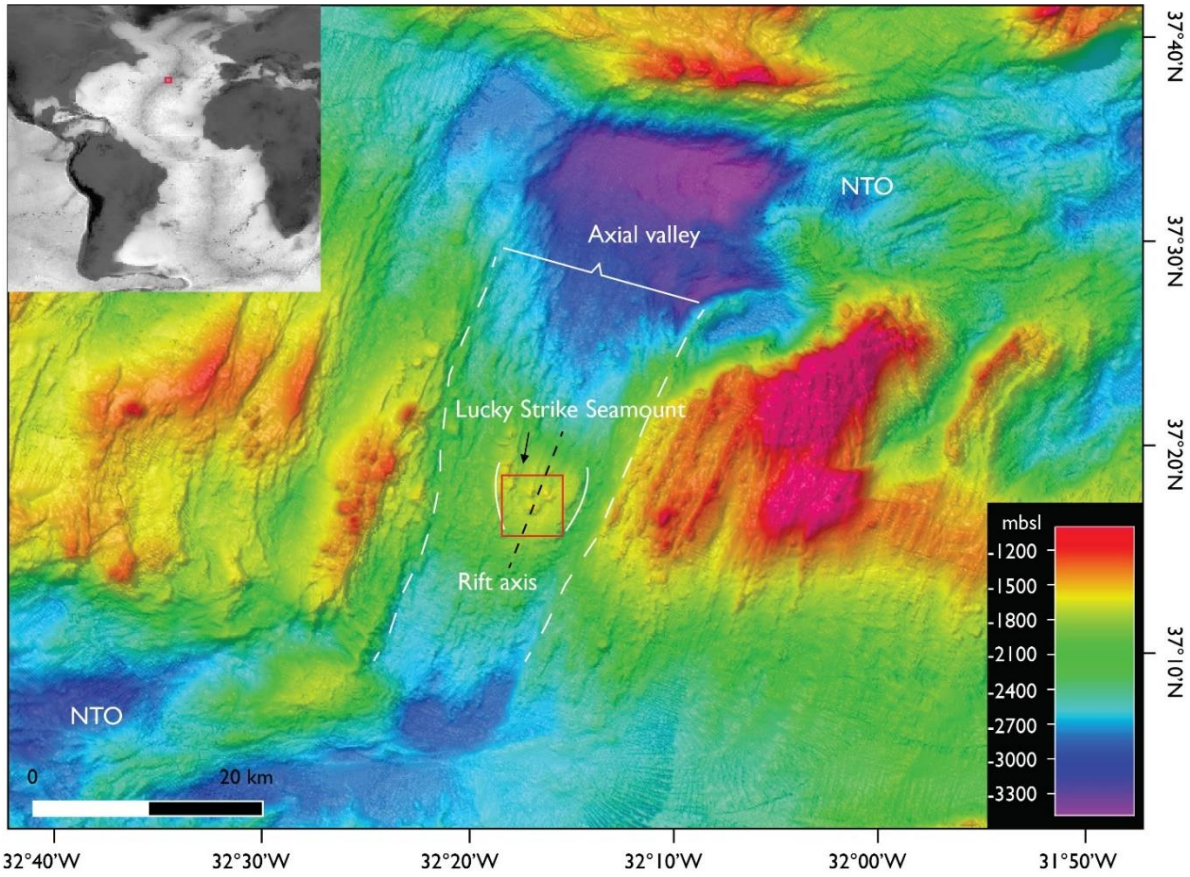

Figure. 5.1. Segment scale bathymetric map of Lucky Strike (~40 m resolution). Inset map shows location along the Mid-Atlantic Ridge. Red rectangle show area of study (Figure. 5.2). White solid lines show approximate extent of the Lucky Strike Seamount. Bathymetric data is from the Sudaçores program (Cannat et al., 1999; Escartín et al., 2001).

The Lucky Strike hydrothermal field is located in the center of the volcanic complex and is interpreted to be genetically associated with underlying axial magma chamber and the most recent faulting (Escartín et al., 2015). Vent sites within the field are situated around the edges of the remnant fossil lava lake between the two rifted volcanic edifices (Figure. 5.2). The occurence of Capelinhos, an active site located 1.4 km away from the ridge axis that is spatial association with a normal fault suggests that faults are a primary control on fluid discharge (Escartín et al., 2015). Radioisotope dating of hydrothermal barite indicates

that the Lucky Strike vent field is at least 6,600 years old (Sánchez-Mora et al. 2022). Analysis of high-resolution bathymetric digital elevation model of the vent field indicates that ~1.3 Mt of hydrothermal material has accumulated on the seafloor (Sánchez-Mora et al. 2022).

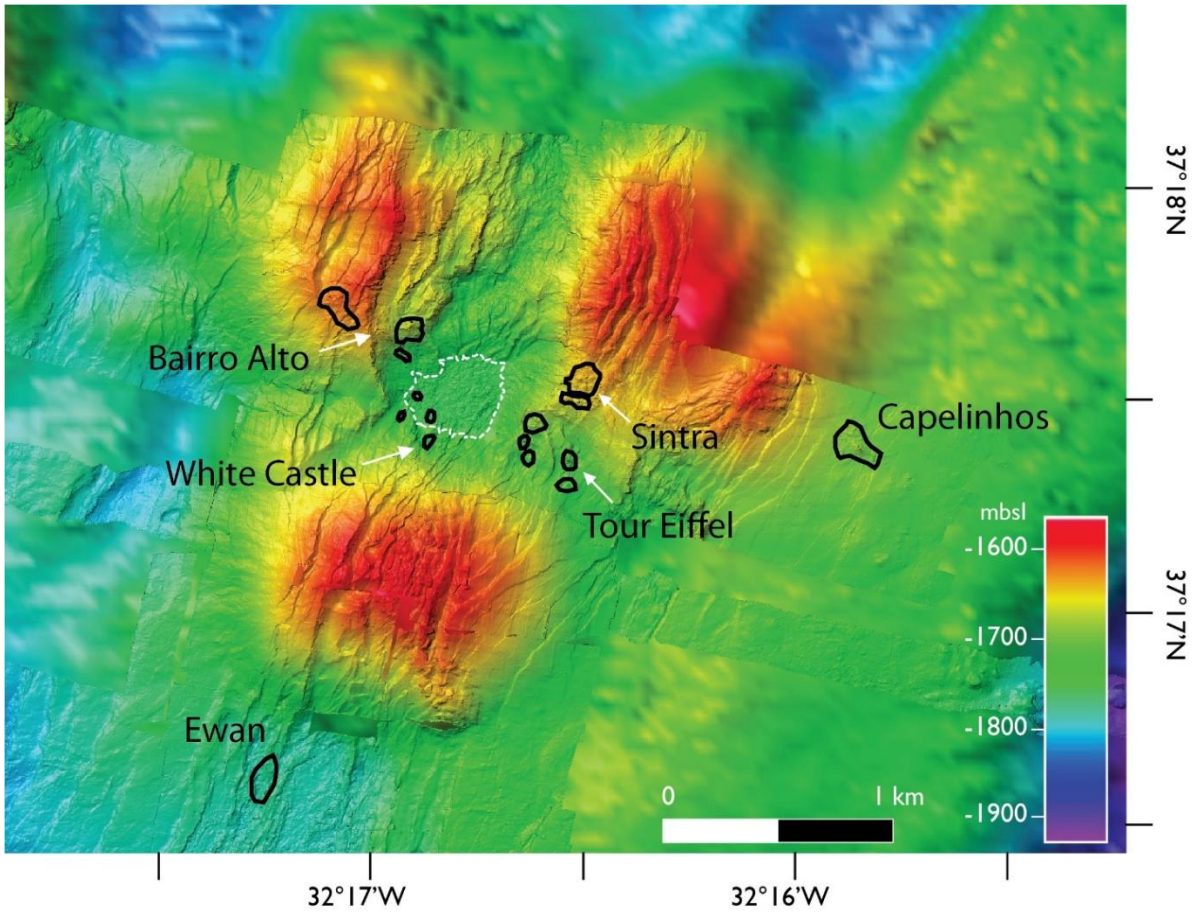

Figure. 5.2. Outlines of hydrothermal sites from the Lucky Strike segment. High temperature venting (>200°C) occurs at the main Lucky Strike hydrothermal field and Capelinhos. Ewan is a site of diffuse flow. White dashed outline indicates the extent of the fossil lava lake. Bathymetry sources (Ondréas et al., 2009; Escartín et al., 2015, 2021).

5.4. Methodology

5.4.1. Structural measurements

Rift-related faults associated with the tectonic and volcanic evolution of the Lucky Strike segment were identified using ~1 m resolution bathymetric data collected using the remotely-operated vehicle *Victor 6000* and autonomous underwater vehicle *Aster-X* (Figure. 5.3) (Ondréas et al., 2009; Escartín et al., 2015). Fault orientations and displacements were quantified by applying the structural modelling tool in Leapfrog Geo 4.0 software. This tool calculates orientation (strike and dip) data from specified point locations on a surface. Surface orientations at each point (represented as oriented disks in Figure. 5.4) are calculated by adjusting the disks manually to best represent the orientation of the fault scarp surface. Seventy-one normal faults with a fault scarp of at least 5 m were identifed in the bathymetric data, ranging in length from 100 to 1500 m. The orientations of exposed normal fault scarps were determined for the 71 faults on the Lucky Strike Seamount (Figure. 5.4A). For each fault, the number of individual orientation measurements ranged from two to 26, and average around seven, with the number of measurements depending primarily on the length of each fault. The faults are grouped based on average dip direction and dip and are summarized in Table 5.1. All faults in the study area have some degree of strike curvature, and the strike of a single fault can vary by up to 107° but is typically between 30–40°. Dip variability can be up to 27° but is generally between 5–15°. Individual fault scarps are highlighted with the aid of a bathymetry-derived slope map (Figure. 5.3A, 5.4).

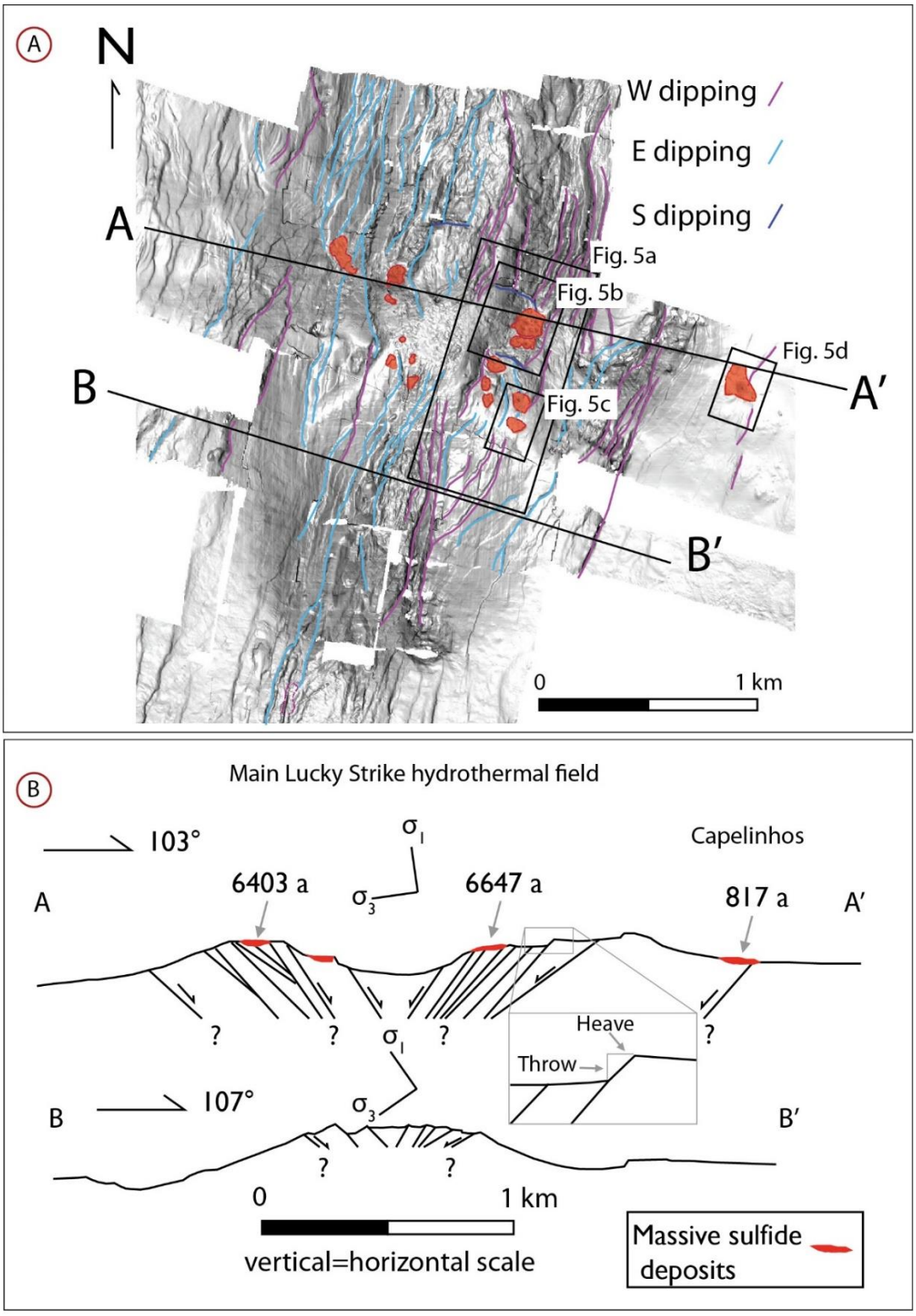

Figure. 5.3. A) Map of the main faults found in the proximity to the Lucky Strike hydrothermal field. B) Cross-sections showing the measured dip and seafloor massive

sulfide deposits with labelled ages from Sánchez-Mora et al. (2022). The measured net slip and estimated heave and throw for each fault was determined in the planes of these cross sections (Table 5.2).

The normal slip (i.e. orthogonal displacement) for individual faults was measured with the Leapfrog measuring tool (Figure. 5.4). Dip and dip direction were measured at multiple locations along individual faults in order to generate average orientations. Measurements were taken at the steepest and smoothest parts of the scarps to avoid talus deposits at the base of the scarps. The net slip was measured from the top of the fault scarps down to lowest part of the scarp, following the dip direction of the fault. Areas where talus was abundant were avoided. The heave (horizontal displacement), and throw (vertical displacement) were calculated using this net slip and the dip of each fault (Figure. 5.3B). The orientation data were used to calculate orthogonal stress fields associated with rifting, using OpenStereo software (Grohmann and Campanha, 2010), where the orientation of the maximum principal stress (σ_1) occurs at 30° to the average orientation of normal fault sets on a plane perpendicular (dashed blue lines Figure 5.5A) to the average fault plane orientation. The orientation of the minimum principle stress (σ_3) occurs 90° to σ_1 along this same perpendicular plane, and the orientation of σ_2, is orthogonal to the plane formed by σ_1 and σ_3.

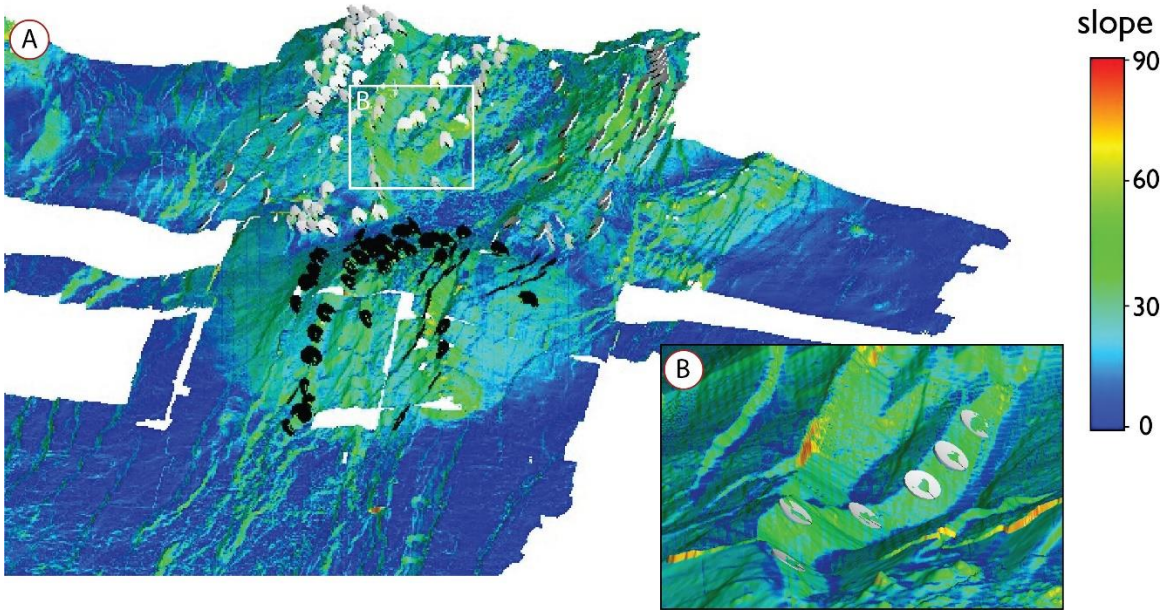

Figure. 5.4. A) Slope map, looking north, of the central volcano within the Lucky Strike Seamount, with disks (white and black for the northern and southern volcanic centers, respectively) representing the locations of structural measurements. B) Close-up (looking north) of individual structural measurment points on the western lobe of the northern edifice.

5.5. Results

5.5.1. Fault orientations and slip

5.5.1.1. Fault orientations

The normal faults that cross-cut the Lucky Strike Seamount are subdivided into northern and southern faults, based on whether the faults occur on the northern or southern volcanic edifice. Faults are also divided into western and eastern zones, defined based on the side of the ridge axis on which they occur. Results of measurements of average fault orientations and principle stress orientations are presented in Table 5.1 and Figure. 5.5B. The orientation of the minimum principle stress axis, σ_3, representing the orientation of maximum tension associated with rifting, averages 6-283 and 35-286 (plunge-trend) in the northern and

southern volcanic centers, respectively. These orientations are consistent with the the 110-290° azimuth of spreading defined by plate motion studies (DeMets et al., 1990).

Table 5.1. Mean structural orientations and stress regimes from the central volcanic complex on the Lucky Strike Seamount.

	Northern edifice NW section	Southern edifice SW section	Northern edifice NE section	Southern edifice SE section
	n=24	n=12	n=24	n=11
Mean principal orientation (Dip dir/dip)[a]	107/51	107/43	276/45	289/51
Intersections N and S (plunge-trend)[b]	0-197		39-240	
	North	South		
Sigma 1 (plunge-trend)[c]	81-058	55-109		
Sigma 2 (plunge-trend)[c]	6-193	2-017		
Sigma 3 (plunge-trend)[c]	6-283	35-286		

a = Calculated by averaging dip and dip directions on the measured faults.
b = Calculated by determining the line of intersection of the average planes from the northern edifices with the southern edifices, the data is divided to where these average planes intersect in the east and the west.
c = Principal stress orientations (linear directions) calculated from faults cross-cutting the northern edifice (eastern and western sections) and southern edifice (eastern and western sections). It is assumed that all faults are normal.

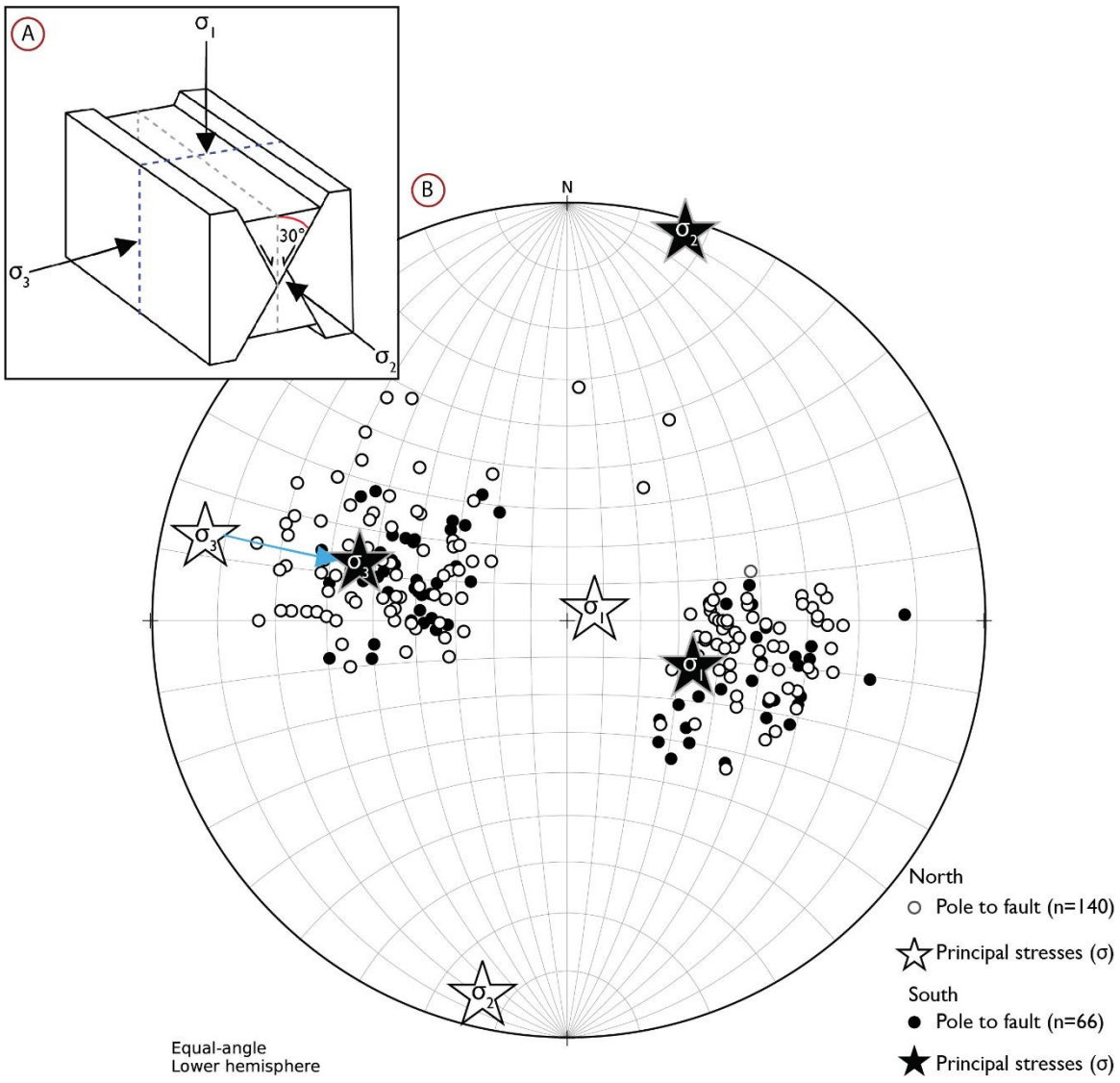

Figure. 5.5. A) Diagram illustrating the principal stress axes in relation to faulting. Dashed blue lines represent the σ_1- σ_3 plane and the gray lines the σ_1- σ_2 plane. Modified from van der Pluijm and Marshak (2004). B) Equal angle stereonet showing orientations (plotted as poles to planes) of rift faults, and resulting calculated principle stress axes along the Lucky Strike Seamount. Principle stress axis σ_1 represents the maximum principle stress and σ_3 represents the minimum principle stress (or maximum tensile stress). The blue arrow shows a 29° shift in the orientation of σ_3 between the northern and southern edifice. Spreading direction of 110° from (DeMets et al., 1990).

5.5.1.2. Fault slip

Cumulative net slip, heave (horizontal displacement), and throw (vertical displacement) were determined from fault measurements for each side of the ridge axis for both the northern and southern volcanic centers (Table *5.2* and Figure. 5.3). In general, the northern areas have higher cumulative net slip and therefore also higher heave and throw.

Table 5.2. Measured net slip in faults.

	Cumulative net slip (m)	**Cumulative heave (m)**	**Cumulative throw (m)**
NW (n=24)	556.5	372.06	405.03
NE (n=22)	525	344.14	393.06
SW (n=12)	242	172.08	168.21
SE (n=11)	154	109.39	105.50

5.6. Discussion

5.6.1. Location of seafloor massive sulfide deposits and local stress regimes

Hydrothermal venting at Lucky Strike is concentrated along the southern flank of the rifted northern edifice and the trough between the northern and southern edifices (Figure. 5.2). The higher amount of cumulative fault slip at the northern edifice indicates that the northern edifice is older and has undergone a higher degree of rifting than the younger southern edifice, which is evident from the larger number of faults cutting the northern volcanic edifice and also the dismemberment of this volcanic structure that can be seen in the bathymetry (Figure 5.6A) (Table *5.2*). The increased permeability and fault density

associated with the higher degree of faulting results in preferential channeling of ascending fluids beneath the northern edifice (Figure. 5.3A,B).

Calculations of principle stress axes based on fault orientations of the northern and southern rift faults indicate that the direction of maximum tension (σ_3) is parallel to the relative movement of the plates away from the ridge axis (110°; Figure. 5.5B; Table *5.1*). However, the results indicate that the plunge component of maximum tension is rotated ~30° from near horizontal at the northern edifice to plunging westward by ~35° at the southern edifice. This rotation of σ_3 between faults cutting the northern and southern volcanic edifices and therefore the rotation in the stress field is hypothesized to enhance the permeability of the region where these faults intersect. Sigma-2, which represents the stress axis with an orientation orthogonal to the maximum and minimum stress axes, and is generally parallel to the ridge axis, shows no significant rotation, suggesting no horizontal rotation in the stress field (Curewitz and Karson, 1997; Fossen and Rotevatn, 2016). This enhanced permeability and heat source directly below, has been imaged from seismic reflection data (Singh et al., 2006; Combier et al., 2015) and corresponds to the location of most of the present and past hydrothermal venting at the seafloor.

5.6.2. Relay ramps and fault linkage/interaction

Relay ramps form at the intersection of two faults, where displacement or strain is transferred from one fault to the other (Fossen and Rotevatn, 2016). The geometry of faulting at the main Lucky Strike field forms relay ramps where the faults that cross-cut the southern edifice intersect the faults that cross-cut the northern edifice (Figure. 5.6A, B). Relay ramps are commonly highly fractured and have an increased structural complexity,

with a larger number of fractures at a wider range of orientations compared to single, isolated faults (Kim et al., 2004; Fossen and Rotevatn, 2016). Relay ramps and also associated with rotation of the local stress field (Kattenhorn et al., 2000). Within this relay ramp structure hydrothermal deposits at Lucky Strike seem to be associated with two different local structural settings. The first setting consists of deposits that form at the intersection of west dipping faults with south dipping faults. These intersections form an isolated compartment (Figure. 5.6C) where upwelling fluids are focused and bounded by the faults and therefore focusing fluid discharge to form the deposits at Sintra. The second setting is related to the linkage of faults between the north and south towards the southeastern sector of the main Lucky Strike field, where deposits are located at fault terminations (Figure. 5.6D), which have been previously recognized as sites with high permeability (Micklethwaite et al., 2010). At the Capelinhos site (located 1.4 km from the central ridge axis) the hydrothermal deposits and venting are controlled by a west dipping set of underlapping permeable faults that may or may not join to become one fault at depth (Figure. 5.6E) (Micklethwaite et al., 2010).

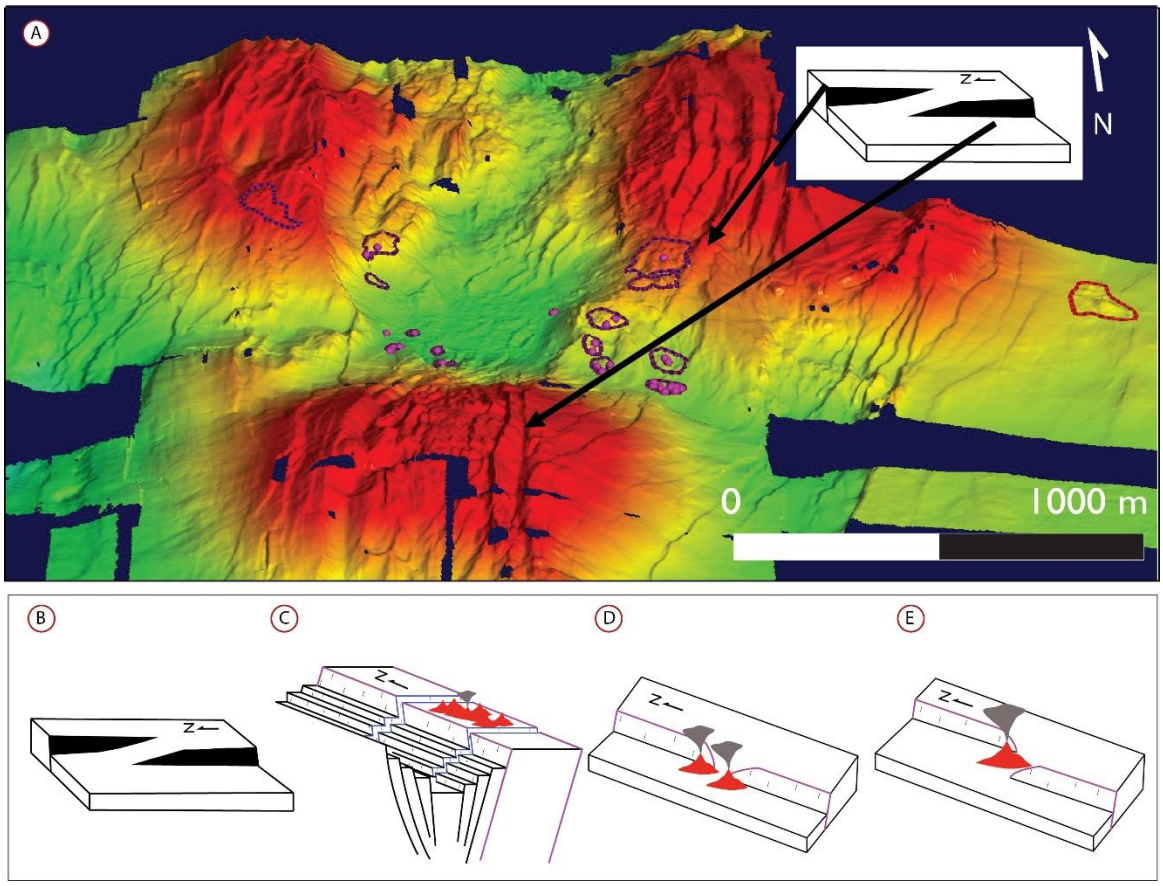

Figure. 5.6. Local structural controls on the location of hydrothermal deposits and venting at the Lucky Strike vent field (locations shown in Figure. 5.3). A) Oblique view of the Lucky Strike vent field showing the location of the major relay ramp. Outlines are SMS deposits and in purple point venting sites. B) Relay ramp at the main Lucky Strike field. C) Structural compartment formed by west dipping faults and south dipping faults under the main Lucky Strike field. D) Fault linkages between the north and south faults on the main Lucky Strike field. E) West dipping set of underlapping structures on the Capelinhos site.

5.7. Conclusions

The use of the Leapfrog Geo software is demonstrated here to be an effective tool to visualize and extract 3-dimensional structural orientation data from high-resolution bathymetric data. Here, this approach is applied to evaluating the stress fields associated with rifting at the Lucky Strike seamount, and controls of the resulting deformation on hydrothermal fluid flow in the crust. This structural analysis that is based on bathymetric

data is especially useful when no seismic reflection data have been collected or where the resolution of the seismic data are not high enough to resolve small scale faulting. The hydrothermal deposits and venting at the Lucky Strike hydrothermal field are largely spatially controlled by enhanced permeability associated with the spatial intersections of faults produced by stress fields with different orientations.

Our approach in this study shows a simple but new application of 3D software to extract dip of structures from bathymetric data. The use of this workflow adds a fundamental piece of information in the study of faults at the seafloor and can be applied in other sites where high-resolution bathymetry is available and fault scarps are distinguishable.

5.8. Acknowledgments

This work was supported by the Canada Research Chair Program, an NSERC Discovery Grant, and RDC Leverage Grant to J.W. Jamieson. DSM acknowledges support from the NSERC iMAGE-CREATE program.

5.9. References

Anderson, M.O., Chadwick, W.W., Hannington, M.D., Merle, S.G., Resing, J.A., Baker, E.T., Butterfield, D.A., Walker, S.L., and Augustin, N., 2017, Geological interpretation of volcanism and segmentation of the Mariana back-arc spreading center between 12.7˚N and 18.3˚N: Geochemistry, Geophysics, Geosystems, v. 18, p. 2240–2274, doi: 10.1002/2017GC006813.Received.

Anderson, M.O., Norris-Julseth, C., Rubin, K.H., Haase, K., Hannington, M.D., Baxter, A.T., and Stewart, M.S., 2021, Geologic and Structural Evolution of the NE Lau Basin, Tonga: Morphotectonic Analysis and Classification of Structures Using Shallow Seismicity: Frontiers in Earth Science, v. 9, p. 1–24, doi: 10.3389/feart.2021.665185.

Blenkinsop, T.G., Oliver, N.H.S., Dirks, P.G.H.M., Nugus, M., Tripp, G., and Sanislav, I.,

2020, Structural Geology Applied to the Evaluation of Hydrothermal Gold Deposits, *in* Rowland, J. V. and Rhys, D.A. eds., Applied Structural Geology of Ore-Forming Hydrothermal Systems, Reviews in Economic Geology, p. 1–23, doi: 10.5382/rev.21.01.

Cannat, M., Briais, A., Deplus, C., Escartín, J., Georgen, J., Lin, J., Mercouriev, S., Meyzen, C., Muller, M., Pouliquen, G., Rabain, A., and Da Silva, P., 1999, Mid-Atlantic Ridge-Azores hotspot interactions: Along-axis migration of a hotspot-derived event of enhanced magmatism 10 to 4 Ma ago: Earth and Planetary Science Letters, v. 173, p. 257–269, doi: 10.1016/S0012-821X(99)00234-4.

Combier, V., Seher, T., Singh, S.C., Crawford, W.C., Cannat, M., Escartín, J., and Dusunur, D., 2015, Three-dimensional geometry of axial magma chamber roof and faults at Lucky Strike volcano on the Mid-Atlantic Ridge: Journal of Geophysical Research : Solid Earth, v. 121, p. 6386–6403, doi: 10.1002/2015JB012282.Received.

Curewitz, D., and Karson, J.A., 1997, Structural settings of hydrothermal outflow: Fracture permeability maintained by fault propagation and interaction: Journal of Volcanology and Geothermal Research, v. 79, p. 149–168, doi: 10.1016/S0377-0273(97)00027-9.

deMartin, B.J., Sohn, R.A., Canales, J.P., and Humphris, S.E., 2007, Kinematics and geometry of active detachment faulting beneath the Trans-Atlantic geotraverse (TAG) hydrothermal field on the Mid-Atlantic Ridge: Geology, v. 35, p. 711–714, doi: 10.1130/G23718A.1.

DeMets, C., Gordon, R.G., Argus, D.F., and Stein, S., 1990, Current plate motions: Geophysical Journal International, v. 101, p. 425–478, doi: 10.1111/j.1365-246X.1990.tb06579.x.

Dyriw, N.J., Bryan, S.E., Richards, S.W., Parianos, J.M., Arculus, R.J., and Gust, D.A., 2021, Morphotectonic Analysis of the East Manus Basin, Papua New Guinea: Frontiers in Earth Science, v. 8, p. 1–23, doi: 10.3389/feart.2020.596727.

Escartín, J., Barreyre, T., Cannat, M., Garcia, R., Gracias, N., Deschamps, A., Salocchi, A., Sarradin, P.M., and Ballu, V., 2015, Hydrothermal activity along the slow-spreading Lucky Strike ridge segment (Mid-Atlantic Ridge): Distribution, heatflux, and geological controls: Earth and Planetary Science Letters, v. 431, p. 173–185, doi: 10.1016/j.epsl.2015.09.025.

Escartín, J., Cannat, M., and Deschamps, A., 2021, Microbathymetry from AUV and ROV Surveys (MOMARETO'06, MOMAR'08-Leg1 and BATHYLUCK'09 cruises) along the Lucky Strike ridge segment (Mid Atlantic Ridge): SEANOE, doi: 10.17882/80574.

Escartín, J., Cannat, M., Pouliquen, G., Rabain, A., and Lin, J., 2001, Crustal thickness of V-shaped ridges south of the Azores: Interaction of the Mid-Atlantic Ridge (36°–39°N) and the Azores hot spot: Journal of Geophysical Research, v. 106, p. 21719–21735, doi: 10.1029/2001JB000224.

Escartín, J., Soule, S.A., Cannat, M., Fornari, D.J., Düşünür, D., and Garcia, R., 2014, Lucky Strike seamount: Implications for the emplacement and rifting of segment-centered volcanoes at slow spreading mid-ocean ridges: Geochemistry, Geophysics, Geosystems, v. 15, p. 4157–4179, doi: 10.1002/2014GC005563.Received.

Fossen, H., and Rotevatn, A., 2016, Fault linkage and relay structures in extensional settings — A review: Earth Science Reviews, v. 154, p. 14–28, doi:

10.1016/j.earscirev.2015.11.014.
Gibson, H.L., Morton, R.L., and Hudak, G.J., 1997, Submarine volcanic processes, deposits, and environments favorable for the location of volcanic-associated massive sulfide deposits, *in* Barrie, C.T. and Hannington, M.D. eds., Volcanic-associated massive sulfide deposits: Processes and examples in modern and ancient settings, Reviews in Economic Geology, p. 13–52.
Graber, S., Petersen, S., Yeo, I., Szitkar, F., Klischies, M., Jamieson, J.W., Hannington, M.D., Rothenbeck, M., Wenzlaff, E., Augustin, N., and Stobbs, I., 2020, Structural Control, Evolution, and Accumulation Rates of Massive Sulfides in the TAG Hydrothermal Field: Geochemistry, Geophysics, Geosystems, doi: 10.1029/2020GC009185.
Grohmann, C.H., and Campanha, G.A., 2010, OpenStereo: Open source, cross-platform software for structural geology analysis: AGU Abstract, p. 2.
Humphris, S.E., Fornari, D.J., Scheirer, D.S., German, C.R., and Parson, L.M., 2002, Geotectonic setting of hydrothermal activity on the summit of Lucky Strike Seamount (37°17'N, Mid-Atlantic Ridge): Geochemistry, Geophysics, Geosystems, v. 3, p. 1–24, doi: 10.1029/2001GC000284.
Humphris, S.E., Tivey, M.K., and Tivey, M.A., 2015, The Trans-Atlantic Geotraverse hydrothermal field: A hydrothermal system on an active detachment fault: Deep-Sea Research Part II: Topical Studies in Oceanography, v. 121, p. 8–16, doi: 10.1016/j.dsr2.2015.02.015.
Kattenhorn, S.A., Aydin, A., and Pollard, D.D., 2000, Joints at high angles to normal fault strike: Journal of Structural Geology, v. 22, p. 1–23, file:///Users/jescartin/WORK/Referencias/pdfs/Kattenhorn2000.pdf.
Kim, Y.S., Peacock, D.C.P., and Sanderson, D.J., 2004, Fault damage zones: Journal of Structural Geology, v. 26, p. 503–517, doi: 10.1016/j.jsg.2003.08.002.
Kleinrock, M.C., and Humphris, S.E., 1996, Structural control on sea-floor hydrothermal activity at theTAG active mound: Nature, v. 382, p. 149–153.
McCaig, A.M., Cliff, R.A., Escartín, J., Fallick, A.E., and MacLeod, C.J., 2007, Oceanic detachment faults focus very large volumes of black smoker fluids: Geology, doi: 10.1130/G23657A.1.
Micklethwaite, S., Sheldon, H.A., and Baker, T., 2010, Active fault and shear processes and their implications for mineral deposit formation and discovery: Journal of Structural Geology, v. 32, p. 151–165, doi: 10.1016/j.jsg.2009.10.009.
Ondréas, H., Cannat, M., Fouquet, Y., Normand, A., Sarradin, P.M., and Sarrazin, J., 2009, Recent volcanic events and the distribution of hydrothermal venting at the Lucky Strike hydrothermal field, Mid-Atlantic Ridge: Geochemistry, Geophysics, Geosystems, v. 10, doi: 10.1029/2008GC002171.
Rowland, J. V., and Sibson, R.H., 2004, Structural controls on hydrothermal flow in a segmented rift system, Taupo Volcanic Zone, New Zealand: Geofluids, v. 4, p. 259–283, doi: 10.1111/j.1468-8123.2004.00091.x.
Sánchez-Mora, D., Jamieson, J.W., Escartín, J., Barreyre, T., and Cannat, M., 2022. Age and rates of formation of metal-rich hydrothermal deposits on the seafloor: example from the Lucky Strike Vent Field, Mid-Atlantic Ridge: Journal of Geophysical Research: Solid Earth

Singh, S.C., Crawford, W.C., Carton, H., Seher, T., Combier, V., Cannat, M., Canales, J.P., Düsünür, D., Escartín, J., and Miranda, J.M., 2006, Discovery of a magma chamber and faults beneath a Mid-Atlantic Ridge hydrothermal field: Nature, v. 442, p. 1029–1032, doi: 10.1038/nature05105.

van der Pluijm, B.A., and Marshak, S., 2004, Earth Structure: An Introduction to structural geology and tectonics: W.W. Norton & Company, 656 p.

Vearncombe, S., Vearncombe, J.R., and Barley, M.E., 1998, Fault and stratigraphic controls on volcanogenic massive sulphide deposits in the Strelley Belt, Pilbara Craton, Western Australia: Precambrian Research, v. 88, p. 67–82, doi: 10.1016/s0301-9268(97)00064-8.

Wölfl, A.C., Snaith, H., Amirebrahimi, S., Devey, C.W., Dorschel, B., Ferrini, V., Huvenne, V.A.I., Jakobsson, M., Jencks, J., Johnston, G., Lamarche, G., Mayer, L., Millar, D., Pedersen, T.H., et al., 2019, Seafloor mapping - The challenge of a truly global ocean bathymetry: Frontiers in Marine Science, v. 6, p. 1–16, doi: 10.3389/fmars.2019.00283.

6. Summary

This dissertation focuses on the formation of metal-rich seafloor hydrothermal deposits at the Lucky Strike vent field, located on the Mid-Atlantic Ridge. The vent field consists of hydrothermal deposits located close to the ridge spreading axis, referred to as the main Lucky Strike vent field, and a newly discovered site called Capelinhos that is located 1.4 km east from the main field. Dating of these metal-rich deposits indicates that hydrothermal activity at the Lucky Strike segment has been active for at least ~6,600 years. High-resolution seafloor bathymetry highlights the spatial relationship between hydrothermal mineral deposits and faults that crosscut volcanic edifices close to the ridge spreading axis. The geochronology and mineral paragenesis of Lucky Strike hydrothermal precipitates indicate that hydrothermal venting evolved from lower temperature mineral assemblages (e.g., marcasite and barite, <250˚C) that occur as replacement and filling of volcaniclastic breccias to high-temperature mineral assemblages (chalcopyrite, sphalerite, and marcasite, >250˚C) that form the massive sulfide deposits. The total amount of hydrothermal precipitates deposited above the seafloor at Lucky Strike is estimated to be ~1.3 Mt. The oldest age determined in this study along with the total mass of hydrothermal deposits results in an average seafloor accumulation rate of ~194 t/yr, which is comparable to other sites on the seafloor (e.g., TAG and Endeavour; Graber et al., 2020; Jamieson et al., 2014). These rates are also comparable to estimates available for volcanogenic massive sulfide deposits that are considered as ancient analogues for seafloor hydrothermal vents. However, rates of formation of SMS deposits cannot necessarily be directly compared to

VMS deposits because rates of SMS formation, using the method presented in this thesis, cannot account for sub-seafloor mineralization (Bleeker & van Breemen, 2011; Bleeker & Parrish, 1996; Manor et al., submitted).

The mineralogy and bulk composition of the Lucky Strike vent field are typical of basalt-hosted seafloor hydrothermal systems, except for elevated Ba, Sr, and Mo concentrations and the high abundance of barite. The average bulk composition of massive sulfide deposit samples does not vary spatially or temporally within the vent field. Sulfur isotope measurements were performed on the main Lucky Strike vent field and Capelinhos to investigate possible differences in the sulfur source for the sulfide minerals between the two sites. The results indicated that the sulfide minerals from main Lucky Strike have relatively lighter $\delta^{34}S$ values that suggest different sub-seafloor fluid pathways at these two sites. The results also suggest that <20% of the available reduced sulfur reaches the seafloor at the main Lucky Strike vent field and the rest is precipitated as sulfide minerals in the sub-seafloor.

The efficiency of metal precipitation at Lucky Strike was estimated using age, tonnage, and composition of the hydrothermal deposits, and fluid fluxes and vent fluid chemistry. The efficiency of precipitation was estimated to be up to 99% for Cu, 78% for Zn, 76% for Fe, and <1% for Si and Mn, and temperature was identified as a key variable affecting the depositional efficiency. The depositional efficiency also varies spatially between the Sintra and Tour Eiffel hydrothermal deposits. Sintra, where depositional efficiencies are higher, is larger, older, and cooler with a temperature of 222°C, compared to the Tour Eiffel site where the maximum measured fluid temperature is 323˚C. These estimates of depositional

efficiency are notably higher than previous estimates and show that sediment-starved mid-ocean ridge hydrothermal systems can be highly efficient at trapping metals that would otherwise be lost to the ocean. These estimates also indicate a high degree of variability at the vent field scale and therefore any extrapolations at different scales must be done with caution.

Fault analysis of high-resolution (~1 m) bathymetry using the Leapfrog Geo software has proven to be a useful tool to extract structural information of these datasets, which includes strike, dip, and net slip. The fault analysis indicates that the SMS deposits and hydrothermal venting are controlled by enhanced permeability associated with the spatial intersections and interaction of fault relay ramps and different types of fault linkages.

6.1. Findings

- The use of precipitates deposited on a temperature probe instrument can be used to determine the initial $^{226}Ra/Ba$ at the time of barite precipitation, allowing more accurate ages to be established for the $^{226}Ra/Ba$ method.
- Hydrothermally cemented breccias at Lucky Strike occur at the bases of mounds and chimneys of hydrothermal deposits and yielded on average the oldest ages.
- The hydrothermal deposits at Lucky Strike are young (~6,600 years old) compared to other sites on the Mid-Atlantic Ridge, that are, on average, 66,000 years old (Cherkashov et al., 2017).
- The hydrothermal deposits formed at a rate of ~194 t/yr, which is comparable to other vent sites on the seafloor.

- The ~1.3 Mt of hydrothermal material estimated at Lucky Strike is distributed over a relatively small area of <2.5 km^2. For comparison, a similar amount of material has accumulated at the Endeavour segment over an area of ~60 km^2 (Jamieson et al., 2014).
- The bulk composition of massive sulfide deposits at main Lucky Strike does not vary significantly, either spatially or temporally.
- The sulfur isotopic composition varies between main Lucky Strike and Capelinhos. This variation is likely related to different fluid pathways at both sites.
- The difference in average sulfur isotope compositions between the main Lucky Strike site and Capelinhos occurs in response to sub-seafloor precipitation of sulfide minerals below the main Lucky Strike site as opposed to different sources of sulfur to the system.
- The bulk composition of hydrothermal deposits with characteristically high Ba, Sr, and Mo at Lucky Strike, relative to other basalt-hosted hydrothermal deposits, reflects the composition of the substrate, and the high Ba/Co reflects proximity to the Azores hot spot, which has an E-MORB signature.
- The estimated precipitation efficiency of metals at the Lucky Strike vent field is higher than previous estimates at the TAG active mound and Endeavour vent field.
- The efficiency of precipitation varies between different elements and the temperature of the vent fluid. The precipitation efficiency can be up to 99% for Cu, 78% for Zn, 76% for Fe, and <1% for Si and Mn.

- Efficiency of precipitation within the Lucky Strike vent field varies between the smaller and younger Tour Eiffel site and the older and larger Sintra site.
- Leapfrog Geo software is a useful tool to extract structural data (strike, dip, and net slip) from high-resolution bathymetry.
- Relay ramps and fault linkages are the areas (of enhanced permeability) where most of the SMS deposits and venting occur at the Lucky Strike vent field.

6.2. Recommendations

Future studies investigating the age of hydrothermal deposits in sediment-free environments should be coupled with high-resolution bathymetry to facilitate more accurate estimates of the volume/tonnage of hydrothermal deposits in the vent field, which is a key aspect to consider when calculating the depositional efficiency and accumulation rate of metals in these systems. This approach could then be applied to other environments (e.g., ultramafic hosted vent sites) to assess if the geological setting influences the accumulation rate and depositional efficiency of metals in hydrothermal precipitates. To enable more accurate comparisons to be drawn between seafloor massive sulfide deposits and volcanogenic massive sulfide deposits, studies of the sub-seafloor (i.e., deep sea drilling or geophysical investigations) should be conducted at Lucky Strike in order to determine the extent and composition of sub-seafloor sulfide mineralization.

Given the results in Chapter 3, where the sulfur isotopic difference between two hydrothermal sites with different fluid pathways and different fluid/rock interactions is documented, it is suggested that variations in sulfur isotope ratios in sulfide minerals in

hydrothermal systems do not follow a simple two-component mixing model between igneous derived sulfur and reduced seawater sulfate. These results indicate that sub-seafloor mineralization can shift $\delta^{34}S$ to lighter values and therefore, additional geological evidence such as vent fluid chemistry should be carefully evaluated in addition to interpretations from sulfur isotope analyses.

A similar approach to the mass balance calculations to estimate metal depositional efficiency method in Chapter 4, which involves the age, tonnage, and composition of hydrothermal deposits as well as vent fluid flux and vent fluid chemistry can be used to estimate the chemical fluxes and the efficiency of metal precipitation in other seafloor hydrothermal sites. The use of this approach would be needed to document the variability between different geological environments (e.g., arc vs. MOR) or vent fields in the same environment but with different spreading rates, or to see if a typical value can be determined and if there are limits to these values. However, the depositional efficiency estimates from this study show that these can be highly variable even within a vent field and that there seems to be a scale effect on these efficiencies. Therefore, any extrapolations of these efficiency estimates to other scales (chimney to vent field scale) and sites must be treated with caution. The application of the method developed in this thesis to other vent sites will be critical for providing datasets that are directly comparable to depositional efficiencies calculated at Lucky Strike. This would allow us to evaluate the factors that control metal depositional efficiencies at other vent sites and ultimately the processes that enhance the depositional efficiency of metals in hydrothermal vent sites and therefore form larger, more economically viable SMS deposits (Humphris & Cann, 2000; Jamieson et al., 2014; Patten et al., 2016).

6.3. Implications for mineral exploration

6.3.1. Implications for SMS deposit exploration on the modern seafloor

The presence of a central volcano at the Lucky Strike segment and its correlation with the location of the hydrothermal deposits indicate that hydrothermal venting occurs in a relatively small area (<2.5 km^2) and is spatially associated with recent volcanic eruptions at Lucky Strike. In this scenario, the magmatism related to the central volcano provides a focused heat source that drives focused hydrothermal circulation. Therefore, areas of focused high-volume igneous activity like central volcanos that have undergone rift-related faulting should be targeted for active hydrothermal vents and SMS deposits. In addition, the fault analysis at Lucky Strike suggest that relay ramps and fault linkages are areas where these deposits preferentially form and can be targets to explore for inactive SMS deposit sites.

The rate of accumulation of hydrothermal deposits could potentially be used to predict either the age or tonnage as an initial estimate, where one of these parameters has been estimated and the other is unknown. This prediction would be useful to prioritize exploration on the seafloor. For example if a sample has been collected by dredging from an active vent field on the seafloor and an old age is determined then it is possible that that area can have a large accumulation of hydrothermal deposits. However, very few sites on the seafloor have been studied in enough detail to determine accurate accumulation rates. Therefore, more data are required to accurately correlate accumulation rates with the age and tonnage of vent sites.

6.3.2. Implications for exploration for volcanogenic massive sulfide deposits

Lessons learned from seafloor hydrothermal deposits can potentially be applied to VMS deposit exploration. For example, if central volcanoes can be identified by detailed mapping in an on-land volcanic terrane, this could be a potential guide for areas that might host relatively large deposits in small areas. This association of VMS deposits with areas with voluminous volcanism has been previously recognized by VMS exploration geologists (Gibson et al., 2007; Franklin et al., 2005; Galley 2003; Cathles et al., 1997; Lydon 1984). The rates of accumulation can potentially be used as a minimum estimate of the formation rate in mafic-dominated VMS deposits where precise ages have not been or cannot be determined, but the tonnage is known. For example the average mafic-dominated VMS deposit is ~4.8 Mt, and, assuming an accumulation rate of 194 t/yr, the average deposit can form in ~25,000 years, and likely faster as sub-seafloor mineralization is an integral part of VMS deposits (Mosier et al., 2009). This relatively rapid formation time suggests that VMS deposits form over discrete time intervals and therefore discrete stratigraphic intervals. Even giant deposits such as Kidd Creek may have formed at similar or faster rates than 170 t/yr (Bleeker & van Breemen, 2011; Bleeker & Parrish, 1996; Hannington et al., 2017).

6.4. Future research

Exploration and study of seafloor hydrothermal vents is often expensive, technically challenging, and requires a multidisciplinary approach (e.g., geology, geophysics, and biology), and therefore sampling is often not optimized for geological studies. However,

analysis of a more extensive suite of samples from the Lucky Strike vent field would be valuable for determining with more certainty if hydrothermal activity has been continuous or discontinuous at this site, as discrete gaps exist in our data. Any future sampling strategy should target the hydrothermally cemented breccias that, in most cases, yielded the oldest ages, as well as mound and chimney samples, to get a full range of sample ages.

Detailed mineral chemistry (e.g., electron microprobe and laser ablation inductively-coupled plasma mass spectrometry) of sulfide minerals would be useful to see if the principal component analysis from Chapter 3 does accurately predict elemental distribution within the sulfide minerals (e.g., Cu and Se). Analysis of mineral chemistry would also be useful to determine primary controls in minor and trace element distributions within the sulfide minerals, similar to the approach by Grant et al. (2018) at TAG.

Vent field scale geophysical studies, like seismic reflection, magnetic, gravity, electromagnetic, and induced polarity surveys would be beneficial for defining the extent of subsurface mineralization and hydrothermal alteration. Drilling below the main Lucky Strike vent field would be optimal to understand the sub-seafloor mineralization and provide a detailed understanding of the 3D geometry of the uppermost part of the hydrothermal system. Ultimately, these additional datasets would allow for a more accurate estimation of deposit tonnage to be calculated. Acquisition of sub-seafloor data would also allow comparisons to be made with VMS deposits, where a significant proportion of the sulfide mineralization may have formed below the seafloor.

6.5. Conclusions

This dissertation highlights the importance of a coupled analytical approach utilizing geochronology, mineralogy, geochemistry, and sulfur isotopic studies within a sound geological framework provided by high-resolution bathymetric data. The integration of new data with previous datasets, in particular, high-resolution bathymetry, vent fluid chemistry, and heat flux estimates, has allowed for an in-depth understanding of the spatial and temporal variability in hydrothermal venting at Lucky Strike. This study has direct implications for understating the evolution of hydrothermal vent sites with time, the flux of metals into the ocean, and demonstrates the effectiveness of a holistic multidisciplinary approach in understanding the formation of seafloor hydrothermal vent sites.

6.6. References

Bleeker, W., & van Breemen, O. (2011). New geochronological, stratigraphic, and structural observations on the Kidd-Munro assemblage and the terrane architecture of the south-central Abitibi greenstone belt, Superior craton, Canada. In *Results from the Targeted Geoscience Initiative III Kidd-Munro Project, Ontario Geological Survey* (Vol. 6258, p. 142).

Bleeker, W., & Parrish, R. R. (1996). Stratigraphy and U-Pb zircon geochronology of Kidd Creek: Implications for the formation of giant volcanogenic massive sulphide deposits and the tectonic history of the Abitibi greenstone belt. *Canadian Journal of Earth Sciences*, *33*, 1213–1231.

Cathles, L.M., Erendi, A.H.J., and Barrie, T., (1997). How long can a hydrothermal system be sustained by a single intrusive event? Economic Geology, v. 92, p. 766–771, doi: 10.2113/gsecongeo.92.7-8.766.

Cherkashov, G., Kuznetsov, V., Kuksa, K., Tabuns, E., Maksimov, F., & Bel'tenev, V. (2017). Sulfide geochronology along the Northern Equatorial Mid-Atlantic Ridge. *Ore Geology Reviews*, *87*, 147–154. https://doi.org/10.1016/j.oregeorev.2016.10.015

Franklin, J.M., Gibson, H.. L., Jonasson, I.R., and Galley, A.G., (2005). Volcanogenic Massive Sulfide Deposits: Economic Geology 100th Anniversary Volume, p. 523–560, doi: 10.1016/B978-0-08-095975-7.01120-7.

Galley, A.G., (2003). Composite synvolcanic intrusions associated with Precambrian VMS-related hydrothermal systems: Mineralium Deposita, v. 38, p. 443–473, doi: 10.1007/s00126-002-0300-9.

Galley, A. G., Hannington, M. D., & Jonasson, I. R. (2007). Volcanogenic massive sulphide deposits. *Geological Association of Canada*, (5), 141–161.

Gibson, H. L., Allen, R. L., Riverin, G., & Lane, T. E. (2007). The VMS Model : Advances and Application to Exploration Targeting. *Proceedings - Fifth Decennial International Conference on Mineral Exploration - Ore Deposits and Exploration Technology*, 713-730 pp.

Graber, S., Petersen, S., Yeo, I., Szitkar, F., Klischies, M., Jamieson, J. W., et al. (2020). Structural Control, Evolution, and Accumulation Rates of Massive Sulfides in the TAG Hydrothermal Field. *Geochemistry, Geophysics, Geosystems*. https://doi.org/10.1029/2020GC009185

Grant, H. L. J., Hannington, M. D., Petersen, S., Frische, M., & Fuchs, S. H. (2018). Constraints on the behavior of trace elements in the actively-forming TAG deposit, Mid-Atlantic Ridge, based on LA-ICP-MS analyses of pyrite. *Chemical Geology*, (July), 1–27. https://doi.org/10.1016/j.chemgeo.2018.08.019

Hannington, M. D., Gemmell, T., & Monecke, T. (2017). The Kidd Creek Volcanogenic Massive Sulfide Deposit—An Update. In T. Monecke, P. Mercier-Langevin, & B. Dubé (Eds.), *Archean Base and Precious Metal Deposits, Southern Abitibi Greenstone Belt, Canada* (Vol. 19, pp. 81–102). Littleton, Colorado: Reviews in Economic Geology. https://doi.org/10.5382/Rev.19.03

Humphris, S. E., & Cann, J. R. (2000). Constraints on the energy and chemical balances of the modern TAG and ancient Cyprus seafloor sulfide deposits. *Journal of Geophysical Research*, *105*, 28477–28488.

Jamieson, J. W., Clague, D. A., & Hannington, M. D. (2014). Hydrothermal sulfide accumulation along the Endeavour Segment , Juan de Fuca Ridge. *Earth and Planetary Science Letters*, *395*, 136–148.

Lydon, J.W., (1984). Ore deposit models 8. Volcanogenic massive sulphide deposits. Part I: A descriptive model: Geoscience Canada, v. 11, p. 195–202.

Manor, M. J., Piercey, S. J., Wall, C. J., & Denisová, N. (2022). High precision CA-ID-TIMS U-Pb zircon geochronology of felsic rocks in the Finlayson Lake VMS district, Yukon : Linking Paleozoic basin-scale accumulation rates to the occurrence of sub-seafloor replacement-style mineralization. *Economic Geology*.

Mosier, B. D. L., Berger, V. I., & Singer, D. A. (2009). *Volcanogenic Massive Sulfide Deposits of the World — Database and Grade and Tonnage Models*.

Patten, C. G. C., Pitcairn, I. K., Teagle, D. A. H., & Harris, M. (2016). Mobility of Au and related elements during the hydrothermal alteration of the oceanic crust : implications for the sources of metals in VMS deposits. *Mineralium Deposita*, *51*, 179–200. https://doi.org/10.1007/s00126-015-0598-8

7. Appendices

Appendix 1 : Extended table of ^{226}Ra, ^{228}Ra, and ^{228}Th activities and Ba concentrations for hydrothermal sulfide/sulfate samples from Lucky Strike.

Sample	IGSN	Latitude	Longitude	Ba (wt.%)	^{226}Ra activity (Bq/kg)	^{228}Ra activity (Bq/kg)	^{228}Th activity (Bq/kg)	^{226}Ra/Ba Age (years)	$^{228}Ra/^{226}Ra$ age (years)	$^{228}Th/^{228}Ra$ age (years)	Group	Sample type	Description
Y3													
MOM11-454-ROC7	CNRS0000007017	37.29187	-32.27782	1.93	2083 ± 66	392 ± 19	181 ± 7	<500	26 ± 0.5	1.5 ± 0.2	IV	Massive sulfate/sulfide rock	Base of small active chimney
White Castle													
MOM15-603-ROC5	CNRS0000007099	37.28973	-32.28104	0.50	665 ± 21	75 ± 6	38 ± 2	<500	30 ± 0.7	1.7 ± 0.3	IV	Massive sulfate/sulfide rock	Block from active edifice
MOM15-603-ROC6	CNRS0000007100	37.28973	-32.28104	3.83	3764 ± 119			<500	>35	>12	III	Massive sulfate/sulfide rock	Block from active edifice
Off axial graben to the W													
MOM15-605-ROC2	CNRS0000007103	37.29523	-32.28496	44.4	33790 ± 1502			749 ± 140	>35	>12	I	Massive sulfate/sulfide rock	From inactive site
Tour Eiffel													
MOM11-452-ROC4	CNRS0000007014	37.28887	-32.27542	0.50	99 ± 4			3840 ± 274	>35	>12	I	Hydrothermally cemented volcaniclastic breccia	At the SE base of Tour Eiffel
MOM11-457-ROC8	CNRS0000007018	37.28903	-32.27567	3.45	2730 ± 86	240 ± 13	115 ± 4	658 ± 125	32 ± 0.5	1.6 ± 0.2	II	Massive sulfate/sulfide rock	Small inactive chimney W of Tour Eiffel
MOM14-579-ROC1	CNRS0000007062	37.29072	-32.28104	2.38	2085 ± 66	122 ± 8	56 ± 3	<500	36 ± 0.6	1.5 ± 0.2	IV	Massive sulfate/sulfide rock	Small inactive chimney, two barite generations
MOM13-532-ROC1	N/A	37.28893	-32.27542	9.94	10055 ± 316			<500	>35	>12	III	Massive sulfate/sulfide rock	Block in the E slope of Tour Eiffel

Sample	IGSN	Latitude	Longitude	Ba (wt.%)	^{226}Ra activity (Bq/kg)	^{228}Ra activity (Bq/kg)	^{228}Th activity (Bq/kg)	^{226}Ra/Ba Age (years)	^{228}Ra/^{226}Ra age (years)	^{228}Th/^{228}Ra age (years)	Group	Sample type	Description
Site 85 m SW of Tour Eiffel													
MOM12-504-ROC1	CNRS0000007053	37.28858	-32.27633	11.2	4715 ± 148			2115 ± 120	>35	>12	I	Hydrothermally cemented volcaniclastic breccia	Block in inactive area 85 m SW of Tour Eiffel
Sintra													
MOM12-502-ROC1	CNRS0000007051	37.29217	-32.27500	38.1	31140 ± 978	5081 ± 227	2356 ± 76	584 ± 120	27 ± 0.5	1.5 ± 0.2	II	Massive sulfate/sulfide rock	Active chimney
MOM11-452-ROC1	CNRS0000007011	37.29208	-32.27472	1.42	84 ± 3			6647 ± 154	>35	>12	I	Massive sulfate/sulfide rock	Small inactive chimney on sulfide-rich basement at the base of Sintra
Site 70 m W of Tour Eiffel (Chimiste)													
MOM15-607-ROC1	CNRS0000007104	37.28902	-32.27632	1.24	225 ± 8			4060 ± 157	>35	>12	I	Hydrothermally cemented volcaniclastic breccia	Fragment next to inactive site 70 m W of Tour Eiffel
Between Isabel and Flores													
MOM15-607-ROC7	CNRS0000007110	37.28940	-32.27699	1.58	106 ± 4			6347 ± 154	>35	>12	I	Hydrothermally cemented volcaniclastic breccia	20 m SE from Isabel
MOM15-607-ROC6	CNRS0000007109	37.28913	-32.27715	0.27	88 ± 4			2662 ± 466	>35	>12	I	Hydrothermally cemented volcaniclastic breccia	Southern base of the active site Flores
Site 150 m NW from Bairro Alto													
MOM15-605-ROC1	CNRS0000007102	37.29415	-32.28346	0.28	18 ± 2			6403 ± 517	>35	>12	I	Hydrothermally cemented volcaniclastic breccia	From inactive site

Sample	IGSN	Latitude	Longitude	Ba (wt.%)	^{226}Ra activity (Bq/kg)	^{228}Ra activity (Bq/kg)	^{228}Th activity (Bq/kg)	^{226}Ra/Ba Age (years)	^{228}Ra/^{226}Ra age (years)	^{228}Th/^{228}Ra age (years)	Group	Sample type	Description
Capelinhos													
MOM14-583-ROC1-S	CNRS0000007069	37.28973	-32.28104	4.52	4506 ± 142	266 ± 15	119 ± 5	<500	36 ± 0.6	1.5 ± 0.2	IV	Massive sulfate/sulfide rock	Block from the base of Capelinhos edifice, active high-T vents near, two barite generations
MOM13-528-ROC1-S	N/A	37.28947	-32.26397	1.29	953 ± 30	140 ± 8	62 ± 3	817 ± 151	28 ± 0.6	1.5 ± 0.2	II	Massive sulfate/sulfide rock	Block from the base of Capelinhos edifice, active high-T vents near, two barite generations
Zero age													
LS-BS-WHOI (Y3)	N/A	37.29187	-32.27785	3.23	3369 ± 106	791 ± 37	333 ± 11	-	24 ± 13	1.4 ± 0.2	IV	Sample recovered from temperature probe	
HT010-CR12 (Crystal)	N/A	37.29088	-32.28202	0.74	750 ± 24	177 ± 10	75 ± 3	-	24 ± 11	1.4 ± 0.2	IV	Sample recovered from temperature probe	

Appendix 2 : Geochemistry of Lucky Strike hydrothermal samples – full elements

Analyte Symbol	Latitude	Longitude	Description	IGSN	Cu (ppm)	Zn (ppm)	Pb (ppm)	Fe (%)	S (%)
Detection Limit					2	10	0.8	0.01	0.01
Analysis Method					FUS	INAA	FUS	INAA	FUS
Capelinhos									
MOM14-583-ROC1-S	37.28973	-32.281042	Block from the base of Capelinhos edifice	CNRS0000007069	54000	10100	113	21.8	27
MOM14-PL583-ROC4	37.289418	-32.263983	Fragment A of active chimney	CNRS0000007072	50900	24900	193	42.4	50.1
MOM14-PL583-ROC4	37.289418	-32.263983	Fragment B of active chimney	CNRS0000007072	114000	15300	137	40	45.3
MOM13-528-ROC1-S	37.289467	-32.263972	Block from the base of Capelinhos edifice	N/A	459	66400	716	35.4	46.9
Y3									
MOM11-454-ROC7	37.291867	-32.277817	Base of small active chimney	CNRS0000007017	40200	75700	489	31.5	41.5
LS-BS-WHOI	37.29187	-32.27785	Precipitate on temperature probe	N/A	152000	21300	201	30.1	35.6
White Castle									
MOM15-603-ROC5	37.28973	-32.281042	Block from active edifice	CNRS0000007099	14100	276000	887	12.3	34.7
MOM15-603-ROC6	37.28973	-32.281042	Block from active edifice	CNRS0000007100	101000	6140	209	27.3	35.8
Off axial graben to the W									
MOM15-605-ROC2	37.295229	-32.284963	From inactive site	CNRS0000007103	350	480	31.3	0.56	6.29
Tour Eiffel									
MOM11-457-ROC8	37.289033	-32.275667	Small inactive chimney W of Tour Eiffel	CNRS0000007018	15200	374000	823	17.5	38.5
MOM14-579-ROC1	37.290722	-32.281038	Small inactive chimney	CNRS0000007062	73600	76200	454	28.5	36.7
MOM13-532-ROC1	37.288933	-32.275417	Block in the E slope of Tour Eiffel		120	1280	746	26.3	33.2
MOM13-532-ROC2	37.288933	-32.275417	Block of sulfide at base of Tour Eiffel	N/A	194000	370	19.9	31.7	41.3
Site 85 m SW of Tour Eiffel									
MOM12-504-ROC1	37.288583	-32.276333	Block in inactive area 85 m SW of Tour Eiffel	CNRS0000007053	10200	108000	502	11.2	17.7
Sintra									
MOM11-452-ROC1	37.292083	-32.274717	Small inactive chimney on sulfide-rich basement at the base of Sintra	CNRS0000007011	24500	5540	993	38.8	38.1
MOM11-452-ROC2	37.292083	-32.2747	Fragments of inactive chimney	CNRS0000007012	256000	5930	379	31.9	37.4
MOM11-452-ROC3	37.292033	-32.274717	Fragments of inactive chimney	CNRS0000007013	264000	15700	306	26.7	33.5
MOM12-502-ROC1	37.292167	-32.275	Active chimney	CNRS0000007051	360	50800	541	4.74	9.41
Isabel									
MOM15-PL607_ROC5	37.28912	-32.277405	Sulfide block	CNRS0000007108	135000	2200	177	35.1	40.3
Chimiste									
MOM15-PL607_ROC3	37.289291	-32.276545	Sulfide block	CNRS0000007106	12700	5620	354	30.3	38.6
Cyprès									

Analyte Symbol	Latitude	Longitude	Description	IGSN	Cu (ppm)	Zn (ppm)	Pb (ppm)	Fe (%)	S (%)
Detection Limit					2	10	0.8	0.01	0.01
Analysis Method					FUS	INAA	FUS	INAA	FUS
MOM14-HN29008-ROCK	37.290787	-32.280972	Precipitate on temperature probe	N/A	85000	490	8.1	44.3	48.5
Crystal									
HT010-CR12	37.29088	-32.28202	Precipitate on temperature probe	N/A	24100	21200	230	10.3	29.2
Cimendef									
MOM14-HT007-ROCK	37.288083	-32.275838	Precipitate on temperature probe	N/A	52500	980	18.2	44.8	50.8

Appendix 2: *continued* Geochemistry of Lucky Strike hydrothermal samples – full elements.

Analyte Symbol	Si (%)	Al (%)	Ca (%)	Na (%)	Mg (%)	Ba (ppm)	Sr (ppm)	Mo (ppm)	V (ppm)	Ni (ppm)	Co (ppm)	Se (ppm)	Au (ppb)	Ag (ppm)	As (ppm)
Detection Limit	0.01	0.01	0.01	0.001	0.01	20	3	1	5	10	0.1	0.5	2	2	1
Analysis Method	FUS	FUS	FUS	INAA	FUS	INAA	FUS	FUS	FUS	FUS	INAA	INAA	INAA	INAA	INAA
Capelinhos															
MOM14-583-ROC1-S	11.9	0.04	0.09	0.12	<0.01	45200	1150	33	<5	<10	277	<0.5	258	22	128
MOM14-PL583-ROC4	0.04	0.03	0.48	0.08	<0.01	1760	97	37	<5	10	158	131	256	21	291
MOM14-PL583-ROC4	0.22	0.11	0.05	0.22	<0.01	330	20	40	9	10	258	150	237	22	229
MOM13-528-ROC1-S	0.17	0.05	0.07	0.16	0.01	12900	737	69	<5	10	14.1	<0.5	323	39	236
Y3															
MOM11-454-ROC7	1.56	0.5	0.19	0.3	0.02	19300	850	318	110	10	337	127	625	88	307
LS-BS-WHOI	3.27	0.24	0.13	0.1	<0.01	32300	1360	212	58	30	198	490	228	52	120
White Castle															
MOM15-603-ROC5	2.94	0.64	0.07	0.25	0.03	4960	239	121	<5	<10	64.6	42.6	748	152	277
MOM15-603-ROC6	5.45	0.36	0.1	0.18	0.04	38300	1700	351	51	30	604	237	205	9	142
Off axial graben to the W															
MOM15-605-ROC2	0.6	<0.01	0.16	0.12	0.02	444000	5940	7	6	10	7.4	<0.5	8	<2	14
Tour Eiffel															
MOM11-457-ROC8	0.95	0.08	0.1	0.06	<0.01	34500	1040	59	6	10	33	<0.5	2030	278	346
MOM14-579-ROC1	5.36	0.61	0.1	0.19	0.01	23800	667	167	122	40	107	179	724	76	387
MOM13-532-ROC1	4.63	<0.01	0.1	0.14	<0.01	99400	2080	25	<5	20	48.5	<0.5	309	<2	449
MOM13-532-ROC2	0.51	0.18	0.07	0.28	0.05	950	48	22	12	10	167	2570	73	<2	99
Site 85 m SW of Tour Eiffel															
MOM12-504-ROC1	13.6	0.28	0.15	0.38	0.03	112000	1420	66	35	20	50.6	<0.5	1750	165	642
Sintra															
MOM11-452-ROC1	0.91	0.15	0.84	0.41	0.11	14200	407	67	131	20	467	69.9	1340	49	635
MOM11-452-ROC2	0.32	0.15	0.04	0.21	0.02	310	24	100	20	10	225	346	1010	94	223
MOM11-452-ROC3	1.77	0.26	0.06	0.21	0.03	2870	41	59	16	10	47.5	106	677	59	242
MOM12-502-ROC1	0.3	<0.01	0.17	0.29	<0.01	381000	5110	11	<5	<10	8.5	<0.5	369	89	168
Isabel															

Analyte Symbol	Si (%)	Al (%)	Ca (%)	Na (%)	Mg (%)	Ba (ppm)	Sr (ppm)	Mo (ppm)	V (ppm)	Ni (ppm)	Co (ppm)	Se (ppm)	Au (ppb)	Ag (ppm)	As (ppm)
Detection Limit	0.01	0.01	0.01	0.001	0.01	20	3	1	5	10	0.1	0.5	2	2	1
Analysis Method	FUS	FUS	FUS	INAA	FUS	INAA	FUS	FUS	FUS	FUS	INAA	INAA	INAA	INAA	INAA
MOM15-PL607_ROC5	0.51	0.23	0.05	0.23	0.03	380	23	267	44	10	409	907	539	44	268
Chimiste															
MOM15-PL607_ROC3	12.3	0.19	0.04	0.2	<0.01	270	20	69	<5	20	89.2	28.9	496	59	477
Cyprès															
MOM14-HN29008-ROCK	0.08	0.03	0.34	0.05	0.02	<20	36	6	<5	60	559	227	37	6	85
Crystal															
HT010-CR12	0.42	0.17	17.4	0.21	0.07	7420	2100	444	57	1450	101	70.6	189	28	97
Cimendef															
MOM14-HT007-ROCK	0.22	0.09	1	0.07	0.04	560	132	11	<5	20	86.8	385	47	<2	96

Appendix 2: *continued* Geochemistry of Lucky Strike hydrothermal samples – full elements.

Analyte Symbol	Ga (ppm)	Ge (ppm)	Sb (ppm)	Cd (ppm)	Tl (ppm)	In (ppm)	Sn (ppm)	Mn (ppm)	Br (ppm)	Cr (ppm)	Cs (ppm)	Hf (ppm)	Ir (ppb)	Rb (ppm)	Sc (ppm)
Detection Limit	0.2	0.7	0.1	2	0.1	0.2	0.5	3	0.5	0.5	0.1	0.2	2	0.4	0.01
Analysis Method	FUS	FUS	INAA	FUS	FUS	FUS	FUS	FUS	INAA	INAA	FUS	INAA	INAA	FUS	INAA
Capelinhos															
MOM14-583-ROC1-S	27.5	6.8	11.4	43	5.4	10.1	3.7	55	8.4	<0.5	1.2	<0.2	<2	4.4	<0.01
MOM14-PL583-ROC4	27.4	14.8	15	55	16.2	2.6	5.3	76	5.7	3.2	1.3	<0.2	<2	2.7	<0.01
MOM14-PL583-ROC4	15	10.8	11.4	30	5.5	6	3.3	38	9.1	<0.5	0.6	<0.2	<2	1.5	<0.01
MOM13-528-ROC1-S	51.4	22.8	49.9	213	61.9	1	1	91	11.4	11.3	0.8	<0.2	<2	2.1	0.11
Y3															
MOM11-454-ROC7	45.8	33.2	23.7	288	44	1.4	2.5	634	15.6	<0.5	3.1	<0.2	<2	4.6	<0.01
LS-BS-WHOI	17.8	19.9	8.3	92	21	3.1	2.3	341	9.6	<0.5	1.2	<0.2	<2	3.1	0.39
White Castle															
MOM15-603-ROC5	63.8	60.8	50	1250	27.6	0.7	3.5	464	15.2	<0.5	0.2	<0.2	<2	1	<0.01
MOM15-603-ROC6	8.2	21.9	5	17	10.7	3.4	2.3	193	17.5	<0.5	1.1	<0.2	<2	2.6	1.03
Off axial graben to the W															
MOM15-605-ROC2	1.1	3.4	0.8	<2	<0.1	<0.2	1.7	369	6.6	<0.5	0.6	<0.2	<2	1.3	0.09
Tour Eiffel															
MOM11-457-ROC8	354	68.2	166	1700	42.6	5.7	1.1	424	3.3	<0.5	1.1	<0.2	<2	2.5	<0.01
MOM14-579-ROC1	62.6	29.8	36.9	288	38.5	4.2	2.3	349	9	<0.5	4.4	<0.2	<2	4.3	<0.01
MOM13-532-ROC1	1.7	23.1	2.3	4	151	<0.2	1	205	11	<0.5	1.3	<0.2	<2	3.2	<0.01
MOM13-532-ROC2	1.7	5.7	1.6	<2	1.2	2.5	6.3	60	23.4	<0.5	1.4	<0.2	<2	2.4	0.22
Site 85 m SW of Tour Eiffel															
MOM12-504-ROC1	55.3	43	82.8	291	21.6	0.6	0.6	1240	63.1	<0.5	0.4	<0.2	<2	1.9	0.12
Sintra															
MOM11-452-ROC1	46.5	19.9	39	9	23.4	12.7	1.1	1830	19.5	4.6	0.4	<0.2	<2	1.9	0.36

Analyte Symbol	Ga (ppm)	Ge (ppm)	Sb (ppm)	Cd (ppm)	Tl (ppm)	In (ppm)	Sn (ppm)	Mn (ppm)	Br (ppm)	Cr (ppm)	Cs (ppm)	Hf (ppm)	Ir (ppb)	Rb (ppm)	Sc (ppm)
Detection Limit	0.2	0.7	0.1	2	0.1	0.2	0.5	3	0.5	0.5	0.1	0.2	2	0.4	0.01
Analysis Method	FUS	FUS	INAA	FUS	FUS	FUS	FUS	FUS	INAA	INAA	FUS	INAA	INAA	FUS	INAA
MOM11-452-ROC2	36.5	19.5	19	25	6.5	10.5	4.2	113	22	<0.5	1	<0.2	<2	2.1	0.14
MOM11-452-ROC3	28	24.1	28	59	13.4	6.9	1.6	153	14	<0.5	1.5	<0.2	<2	1.8	0.35
MOM12-502-ROC1	10.4	50.9	29.5	98	36.9	<0.2	0.9	65	9	<0.5	0.9	<0.2	<2	1.2	<0.01
Isabel															
MOM15-PL607_ROC5	5.1	6.9	6.3	6	9.8	6.3	5.9	211	34.8	<0.5	1.4	<0.2	<2	2.2	0.36
Chimiste															
MOM15-PL607_ROC3	3.4	8.1	9.6	27	18.4	0.3	1	353	33.8	<0.5	1.2	<0.2	<2	2.6	0.5
Cyprès															
MOM14-HN29008-ROCK	0.7	5.1	0.5	<2	<0.1	8.4	17.7	11	<0.5	<0.5	1.6	<0.2	<2	1.8	<0.01
Crystal															
HT010-CR12	12.2	9.7	12.4	122	9.2	2.5	3	92	311	1780	0.7	<0.2	<2	1.3	0.23
Cimendef															
MOM14-HT007-ROCK	1.4	5.8	1.1	3	1.3	1.7	2.2	25	<0.5	6.1	6.1	<0.2	<2	13.3	0.32

Appendix 2: *continued* Geochemistry of Lucky Strike hydrothermal samples – full elements.

Analyte Symbol	Ta (ppm)	Th (ppm)	U (ppm)	La (ppm)	Ce (ppm)	Nd (ppm)	Sm (ppm)	Eu (ppm)	Tb (ppm)	Yb (ppm)	Lu (ppm)	Mass	B (ppm)	Be (ppm)	Bi (ppm)
Detection Limit	0.2	0.1	0.1	0.05	1	1	0.01	0.05	0.1	0.05	0.01		10	3	2
Analysis Method	FUS	INAA	INAA	INAA	INAA	INAA	INAA	INAA	INAA	INAA	INAA	INAA	FUS	FUS	FUS
Capelinhos															
MOM14-583-ROC1-S	2.4	<0.1	<0.1	1.39	<1	<1	0.17	<0.05	<0.1	<0.05	<0.01	1.006	<10	<3	<2
MOM14-PL583-ROC4	1.4	<0.1	<0.1	0.14	<1	<1	<0.01	<0.05	<0.1	<0.05	<0.01	1.058	<10	<3	<2
MOM14-PL583-ROC4	0.7	<0.1	<0.1	<0.05	<1	<1	<0.01	<0.05	<0.1	<0.05	<0.01	1.03	<10	<3	<2
MOM13-528-ROC1-S	0.6	<0.1	<0.1	0.23	<1	<1	<0.01	<0.05	<0.1	<0.05	<0.01	1.062	<10	<3	<2
Y3															
MOM11-454-ROC7	0.8	<0.1	<0.1	0.88	<1	10	<0.01	<0.05	<0.1	<0.05	<0.01	1.058	<10	<3	<2
LS-BS-WHOI	1.2	<0.1	<0.1	1.53	<1	20	0.04	<0.05	<0.1	<0.05	<0.01	1.007	<10	<3	<2
White Castle															
MOM15-603-ROC5	0.2	<0.1	<0.1	0.39	<1	<1	<0.01	<0.05	<0.1	<0.05	0.07	1.003	<10	<3	<2
MOM15-603-ROC6	1.1	<0.1	<0.1	2.9	<1	27	<0.01	<0.05	<0.1	<0.05	<0.01	1.031	<10	<3	<2
Off axial graben to the W															
MOM15-605-ROC2	0.3	<0.1	<0.1	4.46	<1	457	<0.01	<0.05	<0.1	<0.05	<0.01	1.03	<10	<3	<2
Tour Eiffel															
MOM11-457-ROC8	1.1	<0.1	<0.1	1.07	<1	<1	<0.01	<0.05	<0.1	<0.05	0.14	1.013	<10	<3	<2
MOM14-579-ROC1	1	<0.1	<0.1	1.05	<1	<1	<0.01	<0.05	<0.1	<0.05	<0.01	1.082	<10	<3	<2
MOM13-532-ROC1	3.1	<0.1	<0.1	2.22	<1	87	<0.01	<0.05	<0.1	<0.05	<0.01	1.013	<10	<3	<2

Analyte Symbol	Ta (ppm)	Th (ppm)	U (ppm)	La (ppm)	Ce (ppm)	Nd (ppm)	Sm (ppm)	Eu (ppm)	Tb (ppm)	Yb (ppm)	Lu (ppm)	Mass	B (ppm)	Be (ppm)	Bi (ppm)
Detection Limit	0.2	0.1	0.1	0.05	1	1	0.01	0.05	0.1	0.05	0.01		10	3	2
Analysis Method	FUS	INAA	INAA	INAA	INAA	INAA	INAA	INAA	INAA	INAA	INAA	INAA	FUS	FUS	FUS
MOM13-532-ROC2	3	<0.1	<0.1	<0.05	<1	<1	<0.01	<0.05	<0.1	<0.05	<0.01	1.001	<10	<3	<2
Site 85 m SW of Tour Eiffel															
MOM12-504-ROC1	1.6	<0.1	<0.1	2.78	5	60	<0.01	<0.05	<0.1	<0.05	<0.01	1.057	<10	<3	<2
Sintra															
MOM11-452-ROC1	0.7	<0.1	<0.1	3.52	<1	11	0.46	<0.05	<0.1	<0.05	0.03	1.046	30	<3	<2
MOM11-452-ROC2	0.5	<0.1	0.9	<0.05	<1	<1	<0.01	<0.05	<0.1	<0.05	<0.01	1.077	<10	<3	<2
MOM11-452-ROC3	0.5	<0.1	<0.1	0.23	<1	<1	<0.01	<0.05	<0.1	<0.05	<0.01	1.036	<10	<3	<2
MOM12-502-ROC1	0.4	<0.1	<0.1	2.75	<1	168	0.06	<0.05	<0.1	<0.05	<0.01	1.02	<10	<3	<2
Isabel															
MOM15-PL607_ROC5	1.2	<0.1	<0.1	<0.05	<1	<1	<0.01	<0.05	<0.1	<0.05	<0.01	1.015	<10	<3	<2
Chimiste															
MOM15-PL607_ROC3	1.7	0.2	<0.1	<0.05	<1	<1	0.02	<0.05	<0.1	<0.05	<0.01	1.014	<10	<3	<2
Cyprès															
MOM14-HN29008-ROCK	3.6	<0.1	1	0.13	<1	<1	<0.01	<0.05	<0.1	<0.05	<0.01	1.029	<10	<3	<2
Crystal															
HT010-CR12	1.3	<0.1	<0.1	0.7	<1	<1	0.09	<0.05	<0.1	<0.05	0.01	1.028	30	<3	<2
Cimendef															
MOM14-HT007-ROCK	2.6	0.4	<0.1	0.2	<1	<1	<0.01	<0.05	<0.1	<0.05	<0.01	1.06	<10	<3	<2

Appendix 2: *continued* Geochemistry of Lucky Strike hydrothermal samples – full elements.

Analyte Symbol	Dy (ppm)	Er (ppm)	Gd (ppm)	Ho (ppm)	K (%)	Li (ppm)	Nb (ppm)	Pr (ppm)	Te (ppm)	Ti (%)	Tm (ppm)	Y (ppm)
Detection Limit	0.3	0.1	0.1	0.2	0.1	3	2.4	0.1	6	0.01	0.1	0.1
Analysis Method	FUS	FUS	FUS	FUS	FUS	FUS	FUS	FUS	FUS	FUS	FUS	FUS
Capelinhos												
MOM14-583-ROC1-S	<0.3	<0.1	<0.1	<0.2	<0.1	9	<2.4	<0.1	<6	<0.01	<0.1	0.2
MOM14-PL583-ROC4	<0.3	<0.1	<0.1	<0.2	<0.1	6	<2.4	<0.1	<6	<0.01	<0.1	0.2
MOM14-PL583-ROC4	<0.3	<0.1	<0.1	<0.2	<0.1	<3	<2.4	<0.1	<6	<0.01	<0.1	0.2
MOM13-528-ROC1-S	<0.3	<0.1	<0.1	<0.2	<0.1	10	<2.4	<0.1	<6	<0.01	<0.1	0.2
Y3												
MOM11-454-ROC7	<0.3	<0.1	<0.1	<0.2	<0.1	7	<2.4	<0.1	<6	<0.01	<0.1	0.2
LS-BS-WHOI	<0.3	<0.1	0.4	<0.2	<0.1	7	<2.4	<0.1	<6	<0.01	<0.1	0.6
White Castle												
MOM15-603-ROC5	<0.3	<0.1	<0.1	<0.2	<0.1	<3	<2.4	<0.1	<6	<0.01	<0.1	<0.1
MOM15-603-ROC6	<0.3	<0.1	0.6	<0.2	<0.1	<3	<2.4	0.1	<6	<0.01	<0.1	0.6
Off axial graben to the W												
MOM15-605-ROC2	<0.3	<0.1	3.7	<0.2	<0.1	<3	<2.4	0.1	<6	<0.01	0.1	3.5
Tour Eiffel												

Analyte Symbol	Dy (ppm)	Er (ppm)	Gd (ppm)	Ho (ppm)	K (%)	Li (ppm)	Nb (ppm)	Pr (ppm)	Te (ppm)	Ti (%)	Tm (ppm)	Y (ppm)
Detection Limit	0.3	0.1	0.1	0.2	0.1	3	2.4	0.1	6	0.01	0.1	0.1
Analysis Method	FUS	FUS	FUS	FUS	FUS	FUS	FUS	FUS	FUS	FUS	FUS	FUS
MOM11-457-ROC8	<0.3	<0.1	0.3	<0.2	<0.1	5	<2.4	<0.1	<6	<0.01	<0.1	0.4
MOM14-579-ROC1	<0.3	<0.1	0.3	<0.2	<0.1	6	<2.4	<0.1	<6	<0.01	<0.1	0.3
MOM13-532-ROC1	<0.3	<0.1	0.3	<0.2	0.1	7	<2.4	<0.1	<6	<0.01	<0.1	0.7
MOM13-532-ROC2	<0.3	<0.1	<0.1	<0.2	<0.1	<3	<2.4	<0.1	<6	<0.01	<0.1	0.2
Site 85 m SW of Tour Eiffel												
MOM12-504-ROC1	<0.3	<0.1	1	<0.2	<0.1	<3	<2.4	<0.1	<6	<0.01	<0.1	1.2
Sintra												
MOM11-452-ROC1	0.5	0.4	0.5	<0.2	<0.1	5	<2.4	0.4	<6	<0.01	<0.1	3.3
MOM11-452-ROC2	<0.3	<0.1	<0.1	<0.2	<0.1	<3	<2.4	<0.1	<6	<0.01	<0.1	0.2
MOM11-452-ROC3	<0.3	<0.1	<0.1	<0.2	<0.1	3	<2.4	<0.1	<6	<0.01	<0.1	0.2
MOM12-502-ROC1	<0.3	<0.1	<0.1	<0.2	<0.1	<3	<2.4	<0.1	<6	<0.01	<0.1	0.3
Isabel												
MOM15-PL607_ROC5	<0.3	<0.1	<0.1	<0.2	<0.1	6	<2.4	<0.1	<6	<0.01	<0.1	0.2
Chimiste												
MOM15-PL607_ROC3	<0.3	<0.1	<0.1	<0.2	0.1	11	<2.4	<0.1	<6	<0.01	<0.1	0.1
Cyprès												
MOM14-HN29008-ROCK	<0.3	<0.1	<0.1	<0.2	<0.1	7	<2.4	<0.1	<6	<0.01	<0.1	0.2
Crystal												
HT010-CR12	<0.3	<0.1	<0.1	<0.2	<0.1	10	2.9	<0.1	<6	0.06	<0.1	0.5
Cimendef												
MOM14-HT007-ROCK	<0.3	<0.1	<0.1	<0.2	<0.1	12	<2.4	<0.1	<6	<0.01	<0.1	0.2

FUS = analysis by ICP-OES or ICP-MS, with samples prepared by fusion with a Na_2O_2 flux
INAA = analysis by instrumental neutron activation

Appendix 3 : Compiled geochemistry of hydrothermal deposits in mid-ocean ridges.

SAMPLE	Site	Host rock	Au ppb	Ag ppm	As ppm	Cd ppm	Co ppm	Cr ppm	Mo ppm	Ni ppm	Sb ppm
ALV1445-3A	Endeavour	E-MORB	70	11.7							
ALV1445-3B	Endeavour	E-MORB	100	16.1							
ALV1445-3C	Endeavour	E-MORB	170	28.4							
ALV1445-3D	Endeavour	E-MORB	140	30.2							
Endv-1. vent	Endeavour	E-MORB	1	18	4		13	23	4	28	
ALV1417-1b b2	Endeavour	E-MORB	30	16	458		97	17	101	28	3
ALV1417-2a b5	Endeavour	E-MORB	1	22	418		65	27	146	57	9
ALV1419-1b b3	Endeavour	E-MORB	23	6	105		30	230	266	31	1
ALV1417-1c b22	Endeavour	E-MORB	7	1	267		94	14	28	20	1
ALV1419-2 b10	Endeavour	E-MORB	10	4	164		280	12	177	26	1
ALV1418-8b b6	Endeavour	E-MORB	38	12	1304		8	5	49	35	13
ALV1417-1d b7	Endeavour	E-MORB	55	1	58		130	16	82	27	1
ALV1417-c b9	Endeavour	E-MORB	7	1	152		280	160	183	28	2
ALV1418-1d b2	Endeavour	E-MORB	7	18	290		8	12	438	29	3
ALV1418-1d b5	Endeavour	E-MORB	15	12	418		300	24	259	24	2
ALV1417-1e	Endeavour	E-MORB	7	22	301		8	12	453	28	3
ALV1418-3a	Endeavour	E-MORB	5	12	393		290	16	257	23	3
ALV1417-2b	Endeavour	E-MORB	10	10	105		33	16		33	
ALV1417-5b b12	Endeavour	E-MORB	61	1100	256		41	40	21	55	309
ALV1419-1a b2	Endeavour	E-MORB	174	190			23	17		43	
ALV1417-5c b13	Endeavour	E-MORB	58	1200	370		41	39	21	57	320
ALV1417-5a b11	Endeavour	E-MORB	56	1200	256		41	38	23	49	309
ALV1417-5d b14	Endeavour	E-MORB	58	1100	267		39	36	22	57	320
ALV1418-6b b9	Endeavour	E-MORB	71	170	718		10	20	120	36	92
ALV1417-1b b8	Endeavour	E-MORB	99	160	686		10	25	124	42	84
ALV1417-1c b2	Endeavour	E-MORB	336	58	579		19	27	306	30	20

SAMPLE	Site	Host rock	Au ppb	Ag ppm	As ppm	Cd ppm	Co ppm	Cr ppm	Mo ppm	Ni ppm	Sb ppm
ALV1417-1a b2	Endeavour	E-MORB	872	230	1881		7	26	142	30	105
ALV1419-1d b31	Endeavour	E-MORB	9	100	55		6	17	12	36	19
ALV1419-1h b4	Endeavour	E-MORB	13	14000	140		5	8	16	39	60
ALV1418-1e b2	Endeavour	E-MORB	16	32	94		3	130	16	52	92
ALV1419-1c b2	Endeavour	E-MORB	18	44	95		5	8	18	39	91
ALV1419-1d b3	Endeavour	E-MORB	6	16	301		8	5	32	230	97
G2 mucus	Endeavour	E-MORB	33	<5	8.7		4	22	73	30.5	0.5
TT-170-66D-B23-C	Endeavour	E-MORB		59.1		415	31.9			4.2	
Al-G	Endeavour	E-MORB		165.5		44.4	29.9			6.9	
WF-22D-5	Endeavour	E-MORB		139.3		350	30.4			25.6	
WF-22D-6	Endeavour	E-MORB		219		1470	33.6			32.8	
ALV2448-1	Endeavour	E-MORB	155	11	380	80	13	17	74	5	13
ALV2449-1	Endeavour	E-MORB	162	19	340	104	18	23	53	5	13
ALV2450-2	Endeavour	E-MORB	76	16	120	90	260	12	130	5	11
ALV2450-3b (crust)	Endeavour	E-MORB	134	<5	487	<50	7	32	90	5	13
ALV2452-1	Endeavour	E-MORB	47	<5	150	86	110	26	100	10	4.8
ALV2453-1b	Endeavour	E-MORB	67	30	170	207	81	19	130	10	13
ALV2453-2 (puffer)	Endeavour	E-MORB	30	12	220	<50	190	39	44	5	6.1
ALV2453-3	Endeavour	E-MORB	51	<5	130	123	110	<10	120	5	7
ALV2465-R1-4b	Endeavour	E-MORB	112	54	140	598	23	27	130	5	14
ALV2465-R1-6c	Endeavour	E-MORB	268	120	320	219	2	88	140	5	47
ALV2465-R2-1e	Endeavour	E-MORB	<5	18	3.5	<50	2	20	16	13	0.3
ALV2465-R2-2a2	Endeavour	E-MORB	17	20	21	54	88	51	60	5	1.3
ALV2465-R2-2d2	Endeavour	E-MORB	12	<5	19	<50	<2	<10	17	5	0.6
ALV2465-R2-3b	Endeavour	E-MORB	35	15	110	<50	3	21	37	5	3.1
ALV2465-R2b	Endeavour	E-MORB	151	40	180	358	5	13	130	5	14
ALV2465-R3-2a	Endeavour	E-MORB	8	<5	9	<50	170	54	21	5	0.3

SAMPLE	Site	Host rock	Au ppb	Ag ppm	As ppm	Cd ppm	Co ppm	Cr ppm	Mo ppm	Ni ppm	Sb ppm
ALV2466 A	Endeavour	E-MORB	600	480	1200	36	5		110	5	200
ALV2466 E	Endeavour	E-MORB	280	41	770	155	5		120	10	38
ALV2466-b	Endeavour	E-MORB	222	58	360	508	7	39	170	5	27
ALV2466-c	Endeavour	E-MORB	269	50	640	298	7	45	79	5	33
ALV2466-R1-4b	Endeavour	E-MORB	117	9	400	<50	14	42	190	5	9.8
ALV2466-R3	Endeavour	E-MORB	209	18	610	420	3	49	87	5	16
ALV2466-R3-1b1	Endeavour	E-MORB	132	<5	310	409	3	88	52	16	14
ALV2466-R3-1b2	Endeavour	E-MORB	258.5	55	680	<50	4	33.5	94.5	5	34
ALV2466-R4	Endeavour	E-MORB	66	7	190	234	10	22	78	5	5.8
ALV2466-R5-8/1	Endeavour	E-MORB	138	59	240	382	26	35	84	5	18
ALV2466-R5-8/2	Endeavour	E-MORB	128	26	340	376	26	140	64	47	9.6
ALV2466-R5-8/3	Endeavour	E-MORB	153	23	420	318	6	710	93	23	11
ALV2466-R5-8/4	Endeavour	E-MORB	259	91	330	331	2	84	110	5	30
ALV2467-R1-14d	Endeavour	E-MORB	92	27	120	250	41	28	130	5	18
ALV2467-R1-1b3	Endeavour	E-MORB	82	11	90	235	11	23	68	5	9
ALV2467-R1exc	Endeavour	E-MORB	<2	<5	9.1	<50	26	18	82	5	1.3
ALV2467-R3	Endeavour	E-MORB	634	125	385	<50	<1	42.5	91	5	69
HYS-278-01	Endeavour	E-MORB	990	682.5	520	57.9	5	<5	200	5	99
HYS-278-02a	Endeavour	E-MORB	960	393.7	570	438.2	3	23	89	13	190
HYS-278-02b	Endeavour	E-MORB	1620	625.8	630	192.2	<1	<5	30	10	160
HYS-278-09a	Endeavour	E-MORB	32	4.6	200	<0.5	180	<5	260	3	1.9
HYS-278-09b	Endeavour	E-MORB	72	4	430	8.9	74	<5	180	3	4.3
HYS-278-10	Endeavour	E-MORB	61	19.3	470	0.7	370	<5	470	4	0.5
HYS-278-11	Endeavour	E-MORB	31	6.1	380	1.2	470	15	220	1078	0.1
HYS-278-14a	Endeavour	E-MORB	44	2.7	130	<0.5	370	10	150	8	2.2
HYS-278-14b	Endeavour	E-MORB	63	3.7	220	6.4	480	<5	190	4	1.5
HYS-278-16	Endeavour	E-MORB	132	20.1	290	23.5	6	<5	100	5	3.7

SAMPLE	Site	Host rock	Au ppb	Ag ppm	As ppm	Cd ppm	Co ppm	Cr ppm	Mo ppm	Ni ppm	Sb ppm
HYS-347-01	Endeavour	E-MORB	179	8.4	600	<0.5	<1	19	61	7	18
HYS-347-02	Endeavour	E-MORB	73	23.4	38	155.6	28	<5	70	2	17
HYS-350-01	Endeavour	E-MORB	83	13.3	240	99	4	13	46	2	17
HYS-350-02	Endeavour	E-MORB	30	10.1	60	190.3	1	9	34	3	9.3
HYS-355-01	Endeavour	E-MORB	<2	4.5	26	1420.4	3	<5	19	2	6.6
HYS-355-02	Endeavour	E-MORB	<2	3.2	61	1545.9	3	<5	40	2	11
HYS-355-B	Endeavour	E-MORB	244	238.5	740	44	<1	<5	117	10	120
HYS-363-01A	Endeavour	E-MORB	43	1.8	16	1677.1	3	<5	17	2	1.7
HYS-363-01B	Endeavour	E-MORB	413	225.4	3100	199	3	<5	58	26	200
HYS-363-01C	Endeavour	E-MORB	19	51.4	420	1038.7	4	<5	27	6	46
HYS-356-01A	Endeavour	E-MORB	16	33.3	130	379	88	<5	<1	10	1.2
HYS-356-01B	Endeavour	E-MORB	<2	38.3	47	11.2	130	<5	<1	10	<0.1
HYS-356-02A	Endeavour	E-MORB	<2	2.1	5.3	193.6	2	<5	2	2	0.6
ALV2463-R7-6B	Endeavour	E-MORB	20	95	207	138	1.5		<1	5	42
ALV2463-R7-6C	Endeavour	E-MORB	40	74	178	33	1		7	5	26
ALV2463-R7-6G	Endeavour	E-MORB	160	203	274	10	1		<1	5	50
ALV2467-R4-misc	Endeavour	E-MORB	56	<5	130	<0.5	2	69	140	5	3
HYS-350-02(?)	Endeavour	E-MORB	336	351.1	790	18.2	2	<5	14	12	280
ALV2451-1	Endeavour	E-MORB	230	35	380	435	7	19	210	5	13
ALV2460 B	Endeavour	E-MORB	360	33	639	184	1		41	5	19
ALV2460 E	Endeavour	E-MORB	290	30	230	888	5		370	5	18
ALV2464 B	Endeavour	E-MORB			43	1550	7		<1	5	5.8
ALV2464 F-V	Endeavour	E-MORB	100	24	250	121	83		130	5	3.7
ALV2461 A	Endeavour	E-MORB	820	120	500	85	3		70	13	69
ALV2461 E	Endeavour	E-MORB	1130	190	1900	11	3		100	15	140
ALV2463 A	Endeavour	E-MORB		21	220	37	260		190	5	1.3
ALV2463 F	Endeavour	E-MORB	50	22	90	23	430		47	5	1.4

SAMPLE	Site	Host rock	Au ppb	Ag ppm	As ppm	Cd ppm	Co ppm	Cr ppm	Mo ppm	Ni ppm	Sb ppm
ALV2462 A1	Endeavour	E-MORB	310	140	610	22	57		150	21	45
ALV2460-R2-14a	Endeavour	E-MORB	85	7	76	<50	12	86	28	5	1.6
ALV2460-R2-14b	Endeavour	E-MORB	371	110	340	398	4	130	88	5	25
ALV2460-R2-15	Endeavour	E-MORB	177	<5	140	457	9	90	72	5	9
ALV2460-R3-3	Endeavour	E-MORB	294	69	110	356	83	26	180	5	17
ALV2460-R3-3c	Endeavour	E-MORB	297	61	110	316	83	25	150	5	13
ALV2460-R3-5	Endeavour	E-MORB	192	24	150	265	41	25	120	5	5.8
ALV2460-R4-1c	Endeavour	E-MORB	<5	<5	520	453	10	110	150	17	<0.1
ALV2460-R5	Endeavour	E-MORB	7	<5	5.3	<50	14	17	11	5	0.3
ALV2461-R10b2	Endeavour	E-MORB	76	<5	150	<50	81	75	170	5	1.9
ALV2461-R11-9	Endeavour	E-MORB	276	65	260	642	3	45	140	5	19
ALV2461-R12-2	Endeavour	E-MORB	245	98	370	208	2	18	210	5	27
ALV2461-R13 TIP	Endeavour	E-MORB	287	120	350	84	3	42	100	5	33
ALV2461-R13-4-BOT	Endeavour	E-MORB	171	190	360	580	3	58	110	5	37
ALV2461-R13/1	Endeavour	E-MORB	213	63	400	274	4	62	130	5	24
ALV2461-R13/2	Endeavour	E-MORB	302	63	570	151	3	60	210	5	28
ALV2461-R13/3	Endeavour	E-MORB	438	130	650	192	5	44	140	5	59
ALV2461-R13/4	Endeavour	E-MORB	687	320	710	<50	5	46	150	5	110
ALV2461-R1b2	Endeavour	E-MORB	287	64	380	347	19	65	310	5	28
ALV2461-R3c1	Endeavour	E-MORB	27	<5	510	450	3	36	310	12	6.5
ALV2461-R4d	Endeavour	E-MORB	10	2.5	27	<50	2	65	110	13	0.5
ALV2461-R6-4	Endeavour	E-MORB	380	83	350	483	2	25	170	5	23
ALV2461-R7c2	Endeavour	E-MORB	560	140	580	133	5	41	230	5	51
ALV2461-R8-3	Endeavour	E-MORB	6	<5	<0.5	<50	<2	11	<1	5	0.1
ALV2462-R1a	Endeavour	E-MORB	261	42	170	403	24	20	170	5	11
ALV2462-R1b	Endeavour	E-MORB	5	<5	1.8	<50	<2	10	<1	5	0.2
ALV2462-R1c	Endeavour	E-MORB	259	34	280	300	26	37	160	5	11

SAMPLE	Site	Host rock	Au ppb	Ag ppm	As ppm	Cd ppm	Co ppm	Cr ppm	Mo ppm	Ni ppm	Sb ppm
ALV2462-R6-1d2	Endeavour	E-MORB	33	27	14	165	35	42	1.5	5	0.4
ALV2462-R7-1b	Endeavour	E-MORB	195	45	200	232	53	21	170	5	12
ALV2463-R1-2	Endeavour	E-MORB	894	97	1100	88	5	26	170	5	71
ALV2463-R2-1a	Endeavour	E-MORB	25	<5	37	<50	340	120	200	12	0.7
ALV2463-R3-3	Endeavour	E-MORB	125.5	49.5	265	<50	<5	50.5	130	5	42.5
ALV2463-R3-misc	Endeavour	E-MORB									
ALV2463-R4-pc	Endeavour	E-MORB	117	20	29	<50	3	30	12	5	9.6
ALV2463-R5c2	Endeavour	E-MORB	114	37	450	125	4	92	20	5	11
ALV2463-R5c3	Endeavour	E-MORB	359	50	120	125	5	57	33	5	7.7
ALV2463-R6-misc	Endeavour	E-MORB	53	14	390	<50	440	65	72	18	4.2
ALV2464-R5-3	Endeavour	E-MORB	1010	130	220	759	2	37	19	5	50
ALV2464-R6-2c	Endeavour	E-MORB	195	60	220	1063	2	27	210	5	16
ALV2464-R8-1b	Endeavour	E-MORB	492	98	630	186	13	46	300	5	41
Gabriels Trumpet (chimney)	Broken Spur	N-MORB					135			9	
Saracens Head (subsamples)	Broken Spur	N-MORB					167			13	
Saracens Head (main body of chimney)	Broken Spur	N-MORB					513			19	
Dragon (chimney)	Broken Spur	N-MORB					430			17	
BX16 (main body of chimney)	Broken Spur	N-MORB					97			18	
BX16 (base)	Broken Spur	N-MORB					53			23	
NWBX16 (main body of chimney)	Broken Spur	N-MORB					29			15	
Wasps nest (main body of chimney)	Broken Spur	N-MORB					475			23	
ALV2624-1-1	Broken Spur	N-MORB	8	<0.4	262	5.6	5	11	120	8	4.6
ALV2624-3-2	Broken Spur	N-MORB	46	1.9	4.2	9.1	550	10	30	5	0.2
ALV2624-3-4A	Broken Spur	N-MORB	29	1.3	2.5	8.6	220	6	27	2	0.4

SAMPLE	Site	Host rock	Au ppb	Ag ppm	As ppm	Cd ppm	Co ppm	Cr ppm	Mo ppm	Ni ppm	Sb ppm
ALV2624-3-4B	Broken Spur	N-MORB	3980	103.1	260	331.3	59	<5	81	2	34
ALV2624-3-5A	Broken Spur	N-MORB	1500	23.5	208	93.4	62	5	39	5	11
ALV2624-3-5B	Broken Spur	N-MORB	4340	68.8	410	315.4	7	<5	41	7	32
ALV2625-3-12	Broken Spur	N-MORB	146	8.1	8.1	27.2	71	6	14	4	0.7
ALV2625-4-1	Broken Spur	N-MORB	195	10.2	17.9	18.8	99	<5	18	2	1.1
ALV2625-4-4	Broken Spur	N-MORB	5580	75.8	900	224	2	9	88	7	35
ALV2625-4-5A	Broken Spur	N-MORB	3830	68.3	390	400.6	2	<5	62	4	35
ALV2625-4-5B	Broken Spur	N-MORB	928	25.4	97.7	99.1	35	10	64	6	7.5
ALV2625-4-7	Broken Spur	N-MORB	2190	28.5	350	98.4	220	<5	100	7	15
ALV2625-4-9A	Broken Spur	N-MORB	112	3.3	11.2	10.4	180	<5	10	5	0.7
ALV2625-4-9B	Broken Spur	N-MORB	98	3.5	4.1	19.2	500	<5	19	2	0.1
4334_2	Broken Spur	N-MORB	680	39.8							
3434-50	Broken Spur	N-MORB									
4796 2/2 intern.	Broken Spur	N-MORB		76	123.3	450	384	5.3		1.8	22.5
4796 2/2 extern.	Broken Spur	N-MORB		45	18	210	990	3.7		0.3	0.4
4796-2 basal part	Broken Spur	N-MORB		102	87	520	1	2.7		2.5	22.4
4796-2 upper part	Broken Spur	N-MORB		17	33.7	145	7	0.8		0.5	25.4
4793-1/3 middle part	Broken Spur	N-MORB		150	736	610	--	3.1		5.5	10.1
4796-3 internal Cu pipe	Broken Spur	N-MORB		15	19.9	8	92	3.4		8.5	3.8
4796-3 extern.	Broken Spur	N-MORB		10	3.6	10	180	0.8		14.7	0.5
4797-3 base of the Spire mound	Broken Spur	N-MORB		70	43.4	114	440	4.6		2.9	0.5
4796-5 sulfide pipe	Broken Spur	N-MORB		14	12.6	20	230	1		2.5	1.1
4797-3 central part	Broken Spur	N-MORB		108	2.4	265	360	0.3		0.5	3.8
4797-7 cornice	Broken Spur	N-MORB		55	97.7	180	10	0.3		0.6	5
4797-8 central diffuser	Broken Spur	N-MORB		5.7	20.5	9	16	3.7		2.2	0.6

SAMPLE	Site	Host rock	Au ppb	Ag ppm	As ppm	Cd ppm	Co ppm	Cr ppm	Mo ppm	Ni ppm	Sb ppm
4797-9 Fe–Mn crown	Broken Spur	N-MORB		16	49.4	25	250	0.6		0.7	1.1
SH1-DR3-2-3	Rainbow Field	Ultramafic	4450	2	1.1	2.7	1680	1240	9	309	<0.1
SH1-DR3-2-1	Rainbow Field	Ultramafic	1900	3.4	6.8	4.1	1730	7	53	104	0.5
IR-DR-01-C-01	Rainbow Field	Ultramafic	12100	6.6	<0.5	5	2810	244	19	439	<0.1
IR-DR-01-G-02	Rainbow Field	Ultramafic	1530	9.7	1	2.7	3120	204	18	448	<0.1
SH1-DR3-1-2	Rainbow Field	Ultramafic	6300	5	7.9	2.3	4770	<5	16	0.5	<0.1
IR96-3	Rainbow Field	Ultramafic	5770	46.2	680	76.5	6300	<5	12	0.5	17.7
LOG7-6	Logatchev	Ultramafic	300	88.81	340	70	200			200	
LOG7-2	Logatchev	Ultramafic	36300	57.09	200	20	200			150	
LOG7-12	Logatchev	Ultramafic	6100	83.52	28	10	200			300	
LOG7-101	Logatchev	Ultramafic	7970	16.22	480		450			60	
LOG7-4	Logatchev	Ultramafic	3200	71.63	28	70	600			150	
LOG7-3	Logatchev	Ultramafic	6800	83.52	57	10	300			200	
LOG7-13	Logatchev	Ultramafic	3700	42.55	<5	10	200			300	
LOG7-9	Logatchev	Ultramafic	8200	65.02	1560	40	600			400	
3453-5	Logatchev	Ultramafic			270		240	<10		10	
3453-7	Logatchev	Ultramafic			370		1960	<10		10	
3453-8	Logatchev	Ultramafic			580		1080	<10		10	
3453-9	Logatchev	Ultramafic			460		630	<10		10	
3453-10	Logatchev	Ultramafic			450		1280	<10		10	
3454-1	Logatchev	Ultramafic			170		250	<10		10	
3454-3	Logatchev	Ultramafic			520		430	<10		10	
3454-4	Logatchev	Ultramafic			290		350	15		10	
3453-3	Logatchev	Ultramafic	500	0.42							
3453-5	Logatchev	Ultramafic	800	25							
3453-7	Logatchev	Ultramafic	6200	18.6							
3453-8	Logatchev	Ultramafic	5700	0.68							

SAMPLE	Site	Host rock	Au ppb	Ag ppm	As ppm	Cd ppm	Co ppm	Cr ppm	Mo ppm	Ni ppm	Sb ppm
3453-10	Logatchev	Ultramafic	5000	45.6							
3454-2	Logatchev	Ultramafic	300	0.5							
3453-6	Logatchev	Ultramafic					160	14		58	
3453-7	Logatchev	Ultramafic			370		1960	<10		10	
3453-9	Logatchev	Ultramafic			460		630	<10		10	
3453	Logatchev	Ultramafic			520		430	<10		10	
Logatchev-4-72-m Cu-Zone	Logatchev	Ultramafic	13400	54.13	360		100			5	
Logatchev-4-72-b	Logatchev	Ultramafic	8780	24.15	360		120			70	
Logatchev-5-142-m	Logatchev	Ultramafic	6800	18.84	240		50			100	
Logatchev-5-142-b	Logatchev	Ultramafic	15500	26.7	<100		250			200	
Logatchev-1-6-m	Logatchev	Ultramafic	630	13	<100		66			14	
Logatchev-1-2-c	Logatchev	Ultramafic	2780	9.8			92			3	
Logatchev-1-12-m	Logatchev	Ultramafic	170	11	300		32			170	
Logatchev-1-12-b	Logatchev	Ultramafic	720	3.4	<100		21			27	
Logatchev-1-140-m	Logatchev	Ultramafic	25500	34.5	460		700			200	
Logatchev-1-140-b	Logatchev	Ultramafic	18500	52.6	360		480			600	
Logatchev-1-121-m	Logatchev	Ultramafic	7600	26.27	760		500			400	
Logatchev-1-121-b	Logatchev	Ultramafic	20510	46.07	680		300			250	
Logatchev-1-119-c Zn-Zone	Logatchev	Ultramafic	7220	79.25	760		480			100	
Logatchev-1-101-c	Logatchev	Ultramafic	5730	15.8	600		230			60	
Logatchev-1-101-m	Logatchev	Ultramafic	2010	7.37	100		620			100	
Logatchev-1-101-b	Logatchev	Ultramafic	4820	21.38	360		470			50	
Logatchev-1-4-c(1) Fe-Zn-Zone	Logatchev	Ultramafic	1300	58	500		410			46	
Logatchev-1-4-c(2)	Logatchev	Ultramafic	6300	22	100		1200			11	
Logatchev-1-3-m	Logatchev	Ultramafic	5000	68	520		180			14	
Logatchev-2-13-m(1)	Logatchev	Ultramafic	2050	3.5	300		140			20	

SAMPLE	Site	Host rock	Au ppb	Ag ppm	As ppm	Cd ppm	Co ppm	Cr ppm	Mo ppm	Ni ppm	Sb ppm
Logatchev-2-13-m(2)	Logatchev	Ultramafic		3.7			31			160	
Logatchev-2-13-c	Logatchev	Ultramafic	11400	18	100		92			35	
Logatchev-3-9-c	Logatchev	Ultramafic	6300	34			1600			28	
Logatchev-3-9-m	Logatchev	Ultramafic	4050	2.5			1400			460	
MS18-05	Logatchev	Ultramafic	6600	15	<20		244		16	88	<10
MS18-06	Logatchev	Ultramafic	5900	20	36		448		9	210	<10
MS21-06a	Logatchev	Ultramafic	n.a.	<10	<20		75		80	5	<10
MS19-09	Logatchev	Ultramafic	1500	28	<20		172		8	240	<10
MS18-10A	Logatchev	Ultramafic	300	<10	<20		170		<3	160	<10
MS18-10b	Logatchev	Ultramafic	100	<10	<20		54		<3	5	<10
MS21-08A	Logatchev	Ultramafic	600	<10	<20		390		3	445	<10
MS21-10	Logatchev	Ultramafic	15000	40	70		1010		16	5	<10
MS19-9	Logatchev	Ultramafic	n.a.	40	30		650		35	5	<10
MS20-01	Logatchev	Ultramafic	56000	265	600		280		64	30	337
MS21-03A	Logatchev	Ultramafic	700	10	<20		195		<3	145	<10
MS21-03B	Logatchev	Ultramafic	700	10	<20		182		<3	113	<10
MS21-04	Logatchev	Ultramafic	5400	<10	<20		60		10	5	<10
MS21-07	Logatchev	Ultramafic	17000	40	145		1310		12	5	12
ALV1683-1-1a	Snakepit	N-MORB	296	5	64	13	107		18	34	4
ALV1683-1-1b	Snakepit	N-MORB	347	30	46	22	129		9	36	5.3
ALV1683-1-2	Snakepit	N-MORB	201	11	30	23	127		5	31	2.7
ALV1683-3-1	Snakepit	N-MORB	937	5	473	5	36		52	48	4.6
ALV1683-4-1a	Snakepit	N-MORB	2345	69	307	216	8		23	44	29
ALV1683-4-1b	Snakepit	N-MORB	389	10	122	74	100		14	31	10.1
ALV1683-5-1	Snakepit	N-MORB	3863	57	1346	152	2		20	64	40.1
ALV1683-6-1	Snakepit	N-MORB	882	13	340	15	73		36	44	8.3
ALV1683-8-1	Snakepit	N-MORB	10739	1147	881	515	7		25	109	162.5

SAMPLE	Site	Host rock	Au ppb	Ag ppm	As ppm	Cd ppm	Co ppm	Cr ppm	Mo ppm	Ni ppm	Sb ppm
ALV1683-8-1a	Snakepit	N-MORB	2610	138	197	419	7		24		58
ALV1683-8-1a	Snakepit	N-MORB	2566	124	188	423	6		26		53.3
ALV1683-8-1a	Snakepit	N-MORB	2680	120	205	513	6		29		61
ALV1683-9-1	Snakepit	N-MORB	844	15	327	50	74		41	46	5
CY87-5-1	Snakepit	N-MORB	898	2.5	174	5	3		31		1.3
CY87-5-2	Snakepit	N-MORB	5376	122	489	285	9		36		52.5
CY87-5-6	Snakepit	N-MORB	495	30	53	79	67		13		8.5
CY87-11-8	Snakepit	N-MORB	58	9	0.05	5	960		17		0.25
CY87-6-6	Snakepit	N-MORB									
HS5-4	Snakepit	N-MORB	400	27	58	61	155		21	10	0.7
HS11-1	Snakepit	N-MORB	1750	91	282	210	248		25	10	1.9
HS10-1	Snakepit	N-MORB	2530	81	256	478	21		38	10	4.6
HS5-2	Snakepit	N-MORB	4200	148	551	893	<5		36	30	8.1
HS8-1	Snakepit	N-MORB	570	17	127	295	<5		32	10	2.2
HS11-2	Snakepit	N-MORB	130	<10	25	<10	400		32	10	0.2
HS3-1	Snakepit	N-MORB	3580	112	640	337	13		43	10	4.1
HS3-3	Snakepit	N-MORB	1740	66	215	232	<5		39	10	2.6
HS3-4	Snakepit	N-MORB	1220	55	208	406	<5		52	10	3.8
HS3-4b	Snakepit	N-MORB	1390	44	237	520	<5		48	10	3.7
HS5-6	Snakepit	N-MORB	1910	100	216	269	122		24	10	2.6
HS8-2	Snakepit	N-MORB	2480	102	443	417	22		33	10	4.6
HS10-2	Snakepit	N-MORB	2050	85	257	349	30		32	10	3.4
HS10-3	Snakepit	N-MORB	2360	132	125	391	46		36	10	4.1
HS10-5a	Snakepit	N-MORB	1770	83	298	413	17		48	10	3.4
HS10-5b	Snakepit	N-MORB	520	29	75	60	283		34	10	<10
HS10-6	Snakepit	N-MORB	5670	268	870	657	13		41	10	6.9
HS11-5	Snakepit	N-MORB	3040	113	87	520	<5		39	10	4

SAMPLE	Site	Host rock	Au ppb	Ag ppm	As ppm	Cd ppm	Co ppm	Cr ppm	Mo ppm	Ni ppm	Sb ppm
HS5-3	Snakepit	N-MORB	960	52	296	<10	155		118	10	0.4
HS5-5	Snakepit	N-MORB	1090	19	554	<10	<5		103	10	0.5
HS6-5	Snakepit	N-MORB	950	39	752	55	<5		34	10	0.8
HS5-1	Snakepit	N-MORB	20	<10	127	<10	7		123	10	0.3
HS11-3a	Snakepit	N-MORB	1560	40	500	<10	30		129	10	1.1
HS11-3b	Snakepit	N-MORB	1210	61	280	16	28		187	10	1.2
HS11-6	Snakepit	N-MORB	360	39	255	22	945		43	10	0.3
HS11-8	Snakepit	N-MORB	60	13	10	<10	1250		43	10	<10
HS6-6b-4	Snakepit	N-MORB	1500	107	370	16	<5		296	10	3.7
HS6-6b	Snakepit	N-MORB	3640	296	630	139	<5		56	10	5.5
HS6-6b-5	Snakepit	N-MORB	3600	375	760	228	<5		12	10	6.5
HS6-6a	Snakepit	N-MORB	3020	115	355	22	<5		199	10	3.3
HS6-6c	Snakepit	N-MORB	<20	<10	280	<10	50		70	58	<10
MIR 70	Snakepit	N-MORB	300	90	<30	30	2.5		<5		<30
MIR 71-1	Snakepit	N-MORB	1260	35.5	<30	<5	360		78		<30
MIR 160	Snakepit	N-MORB	7100	79.53	200	39	1400		<5		<30
MIR158-1	Snakepit	N-MORB	240	5.1							
MIR 158-2	Snakepit	N-MORB	740	22.16	300	25	1100		12		<30
MIR 159-3	Snakepit	N-MORB	1100	173.6	540	740	50		<5		190
MIR 98	Snakepit	N-MORB	980	32.3	360	240	130		70		<30
MIR 83	Snakepit	N-MORB	160	12	350	<5	330		72		<30
MIR 153	Snakepit	N-MORB	240	4.11	380	5	70		37		<30
MIR 159	Snakepit	N-MORB	1900	23.4	380	32	250		14		<30
MIR 161	Snakepit	N-MORB	470	3.27	490	7	52		5		<30
MIR 166	Snakepit	N-MORB	810	12.24	450	16	520		<5		<30
MIR 154	Snakepit	N-MORB	180	59	350	140	720		15		<30
MIR 150	Snakepit	N-MORB	540	66.6	600	120	43		30		70

SAMPLE	Site	Host rock	Au ppb	Ag ppm	As ppm	Cd ppm	Co ppm	Cr ppm	Mo ppm	Ni ppm	Sb ppm
MIR 152	Snakepit	N-MORB	810	46.3	300	270	270		13		80
MIR 156	Snakepit	N-MORB	9100	38.8	320	800	82		30		100
MIR 172	Snakepit	N-MORB	770	43.9	330	130	23		30		<30
MIR 149	Snakepit	N-MORB	1800	9.75	440	18	25		30		<30
MIR 172-2	Snakepit	N-MORB	760	13	480	28	42		62		<30
MIR 173	Snakepit	N-MORB	1100	39	490	72	18		62		<30
MIR 95	Snakepit	N-MORB	2400	18	340	<5	18		37		<30
MIR 155	Snakepit	N-MORB	1300	1.91	340	<5	24		26		<30
MIR 162-1	Snakepit	N-MORB	430	4.83	360	7	20		15		<30
MIR 163	Snakepit	N-MORB	170	2.28	440	<5	5		13		<30
MIR 165	Snakepit	N-MORB	2000	93	600	280	170		10		30
MIR 169	Snakepit	N-MORB	4500	233.6	1000	540	13		35		60
MIR 151-3	Snakepit	N-MORB	2100	161.3	690	250	70		40		130
MIR 168	Snakepit	N-MORB	2500	80.7	570	330	620		49		30
MIR 90	Snakepit	N-MORB	2280	57	260	1000	27		27		100
MIR 157-7	Snakepit	N-MORB	120	10.93							
MIR 157-8	Snakepit	N-MORB	1000	59	300	260	54		16		50
MIR 164	Snakepit	N-MORB	1100	9.9	600	10	100		3		<30
ALV2192-1A	Snakepit	N-MORB	190	9	38	10	51	<10	6	5	1.8
ALV2192-3	Snakepit	N-MORB	1640	67	242	240	<2	<10	28	5	28
ALV2192-3A	Snakepit	N-MORB	6340	76	182	280	<2	<10	29	5	29
ALV2193-1-1E	Snakepit	N-MORB	140	26	18	40	220	<10	16	5	2.6
ALV2193-1-1F	Snakepit	N-MORB	490	61	91	100	238	<10	21	5	9.4
ALV2193-4-1A	Snakepit	N-MORB	1910	14	393	<10	5	31	58	5	6.3
ALV2193-5-1A	Snakepit	N-MORB	170	4	70	<10	447	24	70	5	1.8
ALV2193-6-1A	Snakepit	N-MORB	440	11	191	97	33	100	85	16	7.8
ALV2194-1A	Snakepit	N-MORB	90	12	13	<10	145	11	5	20	0.9

SAMPLE	Site	Host rock	Au ppb	Ag ppm	As ppm	Cd ppm	Co ppm	Cr ppm	Mo ppm	Ni ppm	Sb ppm
ALV2194-2-1A	Snakepit	N-MORB	40	5	3	<10	109	<10	7	5	0.2
ALV2194-2-2A	Snakepit	N-MORB	60	4	12	<10	78	<10	15	5	0.7
ALV2194-2-2B	Snakepit	N-MORB	120	12	47	15	114	<10	18	5	1.9
ODP 106-649B-1-1	Snakepit	N-MORB	699		129		635			155	19
ODP 106-649B-1-2	Snakepit	N-MORB	639		170		621			155	20
ODP 106-649B-1-3	Snakepit	N-MORB	622		157		602			155	18
ODP 106-649B-1-4	Snakepit	N-MORB	715		175		787			160	20
ODP 106-649B-1-5	Snakepit	N-MORB	624		151		600			158	19
ODP 106-649B-1-6	Snakepit	N-MORB	551		27		787			153	19
ODP 106-649B-1-7	Snakepit	N-MORB	290		44		634			160	25
ODP 106-649B-1-8	Snakepit	N-MORB	694		51		533			158	22
ODP 106-649B-1D-5 (80-86)	Snakepit	N-MORB		20		240	560			5	
ODP 106-649B-1D-7 (84-90)	Snakepit	N-MORB		20		310	780			5	
ODP 106-649B-1D-8 (50-56)	Snakepit	N-MORB		20		195	600			5	
ODP 106-649B-1D-8 (134-140)	Snakepit	N-MORB		10		300	510			5	
ODP 106-649G-1D-1 (14-16_#4)	Snakepit	N-MORB		<10		50	730			5	
17A-TVG7-1A1	Kairei	Mafic and ultramafic	96	18.1	<0.5	9	120		14	3	<0.1
17A-TVG7-1A2	Kairei	Mafic and ultramafic	850	14.8	10	13	92		44	23	34
17A-TVG7-1B1	Kairei	Mafic and ultramafic	155	20	8	3	1320		22	12	<0.1
17A-TVG7-1B2	Kairei	Mafic and ultramafic	2600	27.3	45	9	617		14	28	5.5
17A-TVG7-1C	Kairei	Mafic and ultramafic	412	14.4	2	15	165		19	4	<0.1
17A-TVG7-1D	Kairei	Mafic and ultramafic	230	6	10	7	354		9	20	3.7

SAMPLE	Site	Host rock	Au ppb	Ag ppm	As ppm	Cd ppm	Co ppm	Cr ppm	Mo ppm	Ni ppm	Sb ppm
19III-TVG6-1	Kairei	Mafic and ultramafic	133	5.3	4	2	79		21	2	<0.1
19III-TVG6-2	Kairei	Mafic and ultramafic	1623	10.7	4	3	37		3	1	<0.1
19III-TVG6-3-2	Kairei	Mafic and ultramafic	988	13.3	8	3	7		7	1	<0.1
19III-TVG7-1	Kairei	Mafic and ultramafic	1856	16.3	3	<1	32		11	1	<0.1
19III-TVG7-2	Kairei	Mafic and ultramafic	1702	33.9	23	<1	34		22	11	0.6
17A-TVG9-1A	Kairei	Mafic and ultramafic	20100	249	300	574	590		<1	3	26.6
17A-TVG9-1B	Kairei	Mafic and ultramafic	21300	199	143	128	1070		14	2	7.5
17A-TVG9-1C	Kairei	Mafic and ultramafic	10400	68.3	108	85	201		<1	2	5.1
17A-TVG9-1D	Kairei	Mafic and ultramafic	10700	231	408	694	902		<1	3	34.5
17A-TVG9-1E	Kairei	Mafic and ultramafic	770	9	47	2	151		50	5	1.7
17A-TVG9	Kairei	Mafic and ultramafic	15800	208	691	623	1046		25	29	36.6
17A-TVG7-2	Kairei	Mafic and ultramafic	28	0.6	1	10	44		72	3	0.3
17A-TVG7-3A	Kairei	Mafic and ultramafic	757	0.5	9	<1	14		33	4	0.4
17A-TVG7-3B	Kairei	Mafic and ultramafic	397	0.5	9	2	17		39	8	0.7
17A-TVG7-3C2	Kairei	Mafic and ultramafic	1550	45.6	7	<1	34		56	5	0.7
19III-TVG7-3	Kairei	Mafic and ultramafic	109	6.2	5	10	99		44	5	0.4
19III-TVG7-4	Kairei	Mafic and ultramafic	<5	0.7	106	2	59		19	15	5.6
34II-TVG22-1–2	Yuhuang-1	Mafic and ultramafic	90	13.8	25.4	21.5	76.1	2	49.6	8.5	2
34II-TVG22-7	Yuhuang-1	Mafic and ultramafic	340	2.7	3.4	5.5	4.4	3	5.6	6.2	0.3

SAMPLE	Site	Host rock	Au ppb	Ag ppm	As ppm	Cd ppm	Co ppm	Cr ppm	Mo ppm	Ni ppm	Sb ppm
34II-TVG22-5	Yuhuang-1	Mafic and ultramafic	1970	32	23.3	23.4	26.3	2	7.1	7.6	2.6
34II-TVG22-2	Yuhuang-1	Mafic and ultramafic	9090	95.2	47	547	126	10	13.1	3	16.1
34II-TVG22-1	Yuhuang-1	Mafic and ultramafic	850	29.4	26.6	16.4	18.3	4	9.8	8.9	2.5
34II-TVG22-3	Yuhuang-1	Mafic and ultramafic	1030	17.35	14.1	15.3	16.6	2	2.6	16.3	2
34II-TVG22-4	Yuhuang-1	Mafic and ultramafic	2630	16.55	39.5	22	30	3	7.2	10.4	2.5
34II-TVG22-6	Yuhuang-1	Mafic and ultramafic	710	29.9	17	56.3	42.2	4	14	12.7	1.7
39II-TVG04-2	Yuhuang-1	Mafic and ultramafic		5.84	17.9	0.4	13.6	2	35.5	6.6	1.8
34II-TVG23-1H	Yuhuang-1	Mafic and ultramafic	240	97.3	15.7	15.8	64.4	1	17.4	6.5	1.5
21VII-TVG22-1	Yuhuang-1	Mafic and ultramafic	2970	56.3	2.3	104	1290	1	6.1	1.3	1.6
21VII-TVG22-2	Yuhuang-1	Mafic and ultramafic	4730	115.5	30	482	370	1	16.7	4	11.5
21VII-TVG22-A-3	Yuhuang-1	Mafic and ultramafic		36	275	609	994	<1	13.8	1.4	14.7
34II-TVG23-1	Yuhuang-1	Mafic and ultramafic	20	54.9	14.4	5.5	21.6	1	11.5	5.8	0.4
34II-TVG23-3	Yuhuang-1	Mafic and ultramafic	280	98.2	42	98.8	72	1	17.7	4	7
34II-TVG23-4	Yuhuang-1	Mafic and ultramafic	<20	43.8	13.3	10.2	26.3	2	14.2	5.3	0.4
21VII-TVG22-A	Yuhuang-1	Mafic and ultramafic		2.76	4.6	26.5	187	5	9.6	6.3	0.5
21VII-TVG22-7	Yuhuang-1	Mafic and ultramafic		46.74	45.9	109	299.4	3	13.4	3.9	8.2
64	Beebe	Mafic and ultramafic	458	3.76		0.684	162	0.233	2.69	0.724	0.064
67	Beebe	Mafic and ultramafic	920	15.1		1.19	300	0.19	2.03	5.01	0.133
69	Beebe	Mafic and ultramafic	1730	58.1		0.433	3.83	4.1	93.3	18.2	3.35

SAMPLE	Site	Host rock	Au ppb	Ag ppm	As ppm	Cd ppm	Co ppm	Cr ppm	Mo ppm	Ni ppm	Sb ppm
80	Beebe	Mafic and ultramafic	2140	22.6		0.625	555	0.427	1.86	46	
93	Beebe	Mafic and ultramafic	7850	57.5		1.24	403	0.285	4.05	50	0.578
56	Beebe	Mafic and ultramafic	1370	39.9		3.84	759	31.1	27.7	16.8	1.27
60	Beebe	Mafic and ultramafic	3510	42.3		0.91	165	1.85	101	3.27	6
66	Beebe	Mafic and ultramafic	5470	12.9		1.09	139	1.26	72.3	0.819	1.94
68	Beebe	Mafic and ultramafic	5550	15		2.03	7.39	0.448	57.2	0.849	0.949
73	Beebe	Mafic and ultramafic	6880	49		12	107	1.34	89.2	1.86	
74	Beebe	Mafic and ultramafic	7790	113		10.1	182	0.59	35.2	0.893	8.22
75	Beebe	Mafic and ultramafic	4590	35.7		58.1	100	0.751	74.4	1.19	6.58
77	Beebe	Mafic and ultramafic	9070	71.8		5.24	881	0.307	7.98	0.153	1.92
78	Beebe	Mafic and ultramafic	1150	5.88		1.38	221	1.06	80.8	1.41	0.804
79	Beebe	Mafic and ultramafic	7140	55.3		1.81	84.8	0.467	13.2	0.421	1.29
81	Beebe	Mafic and ultramafic	5840	12.8		8.93	1.82	2.8	64.7	2.88	1.88
82	Beebe	Mafic and ultramafic	7150	9.78		8.84	113	1.76	62.8	7.92	2.12
88	Beebe	Mafic and ultramafic	15000	124		207	106	4.57	76.3	2.45	28.1
89	Beebe	Mafic and ultramafic	502	11.8		1.72	73.6	0.34	50.9	0.324	0.201
92	Beebe	Mafic and ultramafic	6090	29.8		1.55	943	2.9	83.7	6.04	5.15
94	Beebe	Mafic and ultramafic	4780	49.5		2.74	63.2	1.49	90.5	16.8	3.87
58	Beebe	Mafic and ultramafic	93600	347		323	239	0.525	44.6	1.31	75.1

SAMPLE	Site	Host rock	Au ppb	Ag ppm	As ppm	Cd ppm	Co ppm	Cr ppm	Mo ppm	Ni ppm	Sb ppm
61	Beebe	Mafic and ultramafic	80600	141		152	33.2	0.385	29	0.825	27.2
62	Beebe	Mafic and ultramafic	49700	443		285	202	0.64	30.5	1.01	49.5
63	Beebe	Mafic and ultramafic	51800	296		266	42.3	0.485	29	0.939	
71	Beebe	Mafic and ultramafic	18700	509		562	9.34	0.403	25.5	2.13	94
72	Beebe	Mafic and ultramafic	34100	268		226	418	0.599	27.6	0.866	40.5
87	Beebe	Mafic and ultramafic	23500	77.7		89.8	557	0.406	23.5	6.32	19.7
90	Beebe	Mafic and ultramafic	38800	389		331	27.5	16.9	14.2	9.16	40.6
ALV1675-1	TAG surface	N-MORB	0.297	12	10	5	247		180	40	1
ALV1675-1	TAG surface	N-MORB	0.208	14	5	5	142		129		0.6
ALV1675-11	TAG surface	N-MORB	0.309	9	12	5	290		102		1.2
ALV1675-3	TAG surface	N-MORB	0.167	7	7	5	206		104	78	0.7
ALV1675-4	TAG surface	N-MORB	0.134	3	4	5	145		51	32	0.5
ALV1676-1-3	TAG surface	N-MORB		206	66	1604	55		0.5		56
ALV1676-2-5	TAG surface	N-MORB	1.081	20	86	30	1373		267	42	3.6
ALV1676-2-7	TAG surface	N-MORB	1.662	36	135	94	1843		104		8.3
ALV1676-5-12	TAG surface	N-MORB	3.437	59	150	74	48		126		9.1
ALV1676-5-13	TAG surface	N-MORB	5.529	221	51	2100	100		18		101.3
ALV1676-6-15B avg3	TAG surface	N-MORB	5.102667	178	34.66667	1662.667	102.3333		13.66667	249	48.43333
ALV1676-6-15T	TAG surface	N-MORB	3.261	138	25	1234	63		21	143	69.8
ALV1677-1-1	TAG surface	N-MORB	2.03	61	106	59	117		90		7.4
ALV1677-2-1	TAG surface	N-MORB	0.018	2.5	0.4	5	7		5		0.25
ALV2183-9-1A	TAG surface	N-MORB	1.63	79	151	18	20	18	62	29	37
ALV2179-4	TAG surface	N-MORB	0.05	6	1	5	106	14	140	5	0.1
ALV2190-14-1C	TAG surface	N-MORB	0.11	1570	153	1810	1	5	64	23	282

SAMPLE	Site	Host rock	Au ppb	Ag ppm	As ppm	Cd ppm	Co ppm	Cr ppm	Mo ppm	Ni ppm	Sb ppm
ALV2190-14-1D avg2	TAG surface	N-MORB	6.015	1250	88	1820	1	5	45	18	321.5
ALV2190-14-1E	TAG surface	N-MORB	0.07	1690	137	930	1	5	16	5	126
ALV2190-14-1F	TAG surface	N-MORB	3.18	1300	89	1680	1	5	42	16	266
ALV2190-7-1A	TAG surface	N-MORB	0.7	28	48	20	154	100	100	20	11
ALV2189-4-1 pc1	TAG surface	N-MORB	0.19	2.5	35		10	26	100	5	1.8
ALV2584-9	TAG surface	N-MORB	0.688	2.5	30		8	2.5	73	5	1.4
ALV2587-1	TAG surface	N-MORB	0.62	2.5	68		430	2.5	120	5	1.9
ALV2179-1-1A	TAG surface	N-MORB	0.88	2.5	120	20	1190	5	150	5	3.6
ALV2179-1-1B	TAG surface	N-MORB	0.97	6	51	5	189	5	150	10	5.9
ALV2179-2-2A	TAG surface	N-MORB	0.38	6	43	5	910	5	160	5	1.6
ALV2179-4-1-1	TAG surface	N-MORB	0.13	6	8	5	205	12	68	5	0.7
ALV2179-4-1-4	TAG surface	N-MORB	0.03	1	1	5	56	11	9	5	0.1
ALV2179-4-1A1	TAG surface	N-MORB	0.1	3	4	5	131	11	51	5	0.3
ALV2179-4-1T1	TAG surface	N-MORB	0.05	2.5	1	5	47	17	15	5	0.1
ALV2181-1-1A2	TAG surface	N-MORB	0.25	7	19	5	330	10	110	5	0.5
ALV2183-4-1A avg2	TAG surface	N-MORB	13.18	1385	62.5	1875	1	5	44	13	98.5
ALV2183-4-1B	TAG surface	N-MORB	20.75	1060	42	2000	1	5	48	16	90
ALV2183-4-1C	TAG surface	N-MORB	13.36	1920	79	1780	1	5	56	14	93
ALV2183-6-2A	TAG surface	N-MORB	1.87	170	120	78	41	170	120	14	15
ALV2183-7-OA	TAG surface	N-MORB	0.0025	2.5	1	5	13	5	6	5	0.05
ALV2187-1-1A1 avg3	TAG surface	N-MORB	6.596667	176.6667	47.33333	1723.333	1	5	74.66667	10	201
ALV2187-1-1A2	TAG surface	N-MORB	0.986	150	32	1680	1	11	108	18	199
ALV2187-1-1B avg2	TAG surface	N-MORB	2.62	180	51	1080	1	7.5	68	11	145
ALV2187-1-1C avg3	TAG surface	N-MORB	42.96	185.6667	19	2043.333	1	5	244	18	308
ALV2187-1-4A	TAG surface	N-MORB	0.34	580	91	2260	1	18	0.5	26	370
ALV2187-1-6A	TAG surface	N-MORB	0.18	560	117	950	1	5	0.5	19	63

SAMPLE	Site	Host rock	Au ppb	Ag ppm	As ppm	Cd ppm	Co ppm	Cr ppm	Mo ppm	Ni ppm	Sb ppm
ALV2189-5-2A	TAG surface	N-MORB	0.66	44	44	5	89	210	125	5	2.9
ALV2190-11-1A avg2	TAG surface	N-MORB	13.22	225	47.5	2205	1	5	44	11	224
ALV2190-11-1B	TAG surface	N-MORB	4.69	70	64	1380	1	13	42	15	127
ALV2190-13-1A	TAG surface	N-MORB	1.01	240	63	250	2	56	37	5	77
ALV2190-14-1A avg2	TAG surface	N-MORB	15.085	1125	87	1610	1	5	56.5	27	252
ALV2190-14-1B avg2	TAG surface	N-MORB	0.295	1190	103.5	1230	1	5	40	17	180.5
ALV2190-8-1A	TAG surface	N-MORB	0.1	2.5	35	5	337	20	78	5	0.7
MIR 1902-11/1	TAG surface	N-MORB	0.3	11		10	220	5		29	
MIR 1902-11/2	TAG surface	N-MORB	0.3	14		50	27	15		20	
MIR 1902-11/3	TAG surface	N-MORB	1.4	10		25	460	15		22	
MIR 1902-2/2	TAG surface	N-MORB	1.5	9		15	380	15		22	
MIR 1902-2/6	TAG surface	N-MORB	0.6	20		5	38	85		66	
MIR 1902-3/2	TAG surface	N-MORB	1.3	60		92	1000	15		24	
MIR 1902-5/1	TAG surface	N-MORB	1.2	165		430	300	10		40	
MIR 1902-5/2	TAG surface	N-MORB	1.4	135		380	200	10		40	
MIR 1902-6/1	TAG surface	N-MORB	0.7	8		6	130	6		25	
MIR 1902-6/2	TAG surface	N-MORB	0.6	10		20	500	10		20	
MIR 1902-6/3	TAG surface	N-MORB	0.7	5		8	130	20		23	
MIR 1902-7	TAG surface	N-MORB	0.4	8		15	140	20		22	
MIR 1902-8/1	TAG surface	N-MORB	0.7	12		25	770	15		30	
MIR 1902-8/2	TAG surface	N-MORB	0.7	30		40	1300	15		13	
MIR 1902-8/3	TAG surface	N-MORB	0.6	18		22	1100	5		25	
MIR 1902-8/4	TAG surface	N-MORB	0.8	15		28	900	30		25	
MIR 1902-9/1	TAG surface	N-MORB	1.3	16		33	400	8		24	
MIR 2-75 /1	TAG surface	N-MORB	1.15	2.5	62		81	2.5	62	5	2.6
MIR sample - 1	TAG surface	N-MORB	0.57	4.2	170		34		47		0.99

SAMPLE	Site	Host rock	Au ppb	Ag ppm	As ppm	Cd ppm	Co ppm	Cr ppm	Mo ppm	Ni ppm	Sb ppm
MIR sample - 2	TAG surface	N-MORB	2.75	120	66		2.5		43		11.4
MIR sample - 3	TAG surface	N-MORB	0.15	1.2	21.5		350		87		0.5
MIR sample - 4	TAG surface	N-MORB	0.22	11			740		230		3.2
TG1-2	TAG surface	N-MORB	0.544	19	41	256	3		15		3.9
TG1-4A	TAG surface	N-MORB		30							
TG1-7B(1)	TAG surface	N-MORB		2.5							
TG1-7B(2)	TAG surface	N-MORB		285							
TG1-7C(2)	TAG surface	N-MORB		2.5							
TG1-8(2)	TAG surface	N-MORB		95							
TG1-8A(1)	TAG surface	N-MORB		185							
TG1-10	TAG surface	N-MORB		50							
TG1-11(3)	TAG surface	N-MORB		10							
TG1-12A	TAG surface	N-MORB		150							
TG1-13A(1)	TAG surface	N-MORB		225							
TG1-14(2)	TAG surface	N-MORB		75							
TG1-16	TAG surface	N-MORB		165							
TG1-26A(1)	TAG surface	N-MORB		50							
TG1-43(1)	TAG surface	N-MORB		40							
TG1-43(4)	TAG surface	N-MORB		265							
TG1-43(5)	TAG surface	N-MORB		115							
TG1-44	TAG surface	N-MORB		2.5							
TG1-36	TAG surface	N-MORB		160							
TG1-46(1)	TAG surface	N-MORB		155							
TG1-8	TAG surface	N-MORB	3.545	95	243		2		71		28.4
TG1-8	TAG surface	N-MORB	3.694	96	272	491	2		63		31
TG1-10	TAG surface	N-MORB	1.6	20	50	48	0.5		72		4
TG1-10	TAG surface	N-MORB	1.634	10	50	50	1		78		4.1

SAMPLE	Site	Host rock	Au ppb	Ag ppm	As ppm	Cd ppm	Co ppm	Cr ppm	Mo ppm	Ni ppm	Sb ppm
TG1-10	TAG surface	N-MORB	0.829	12	45	46	3		71	42	2.5
TG1-11	TAG surface	N-MORB	0.667	40	49	101	3		24		3.4
TG1-11	TAG surface	N-MORB	0.717	36	67	103	4		33		3.4
TG1-12a	TAG surface	N-MORB	0.281	30	122	45	4		55		16
TG1-15a	TAG surface	N-MORB	2.901	335	74	580	5		42	83	29.7
TG1-16	TAG surface	N-MORB	4.001	23	120		3		51		10.1
TG1-16	TAG surface	N-MORB	4.003	41	121	86	4		51		9.8
TG1-21	TAG surface	N-MORB	3.881	175	165	258	5		57	71	19.4
TG1-23	TAG surface	N-MORB	4.325	112	92	337	4		7	67	21.7
TG1-24	TAG surface	N-MORB	3.666	302	119	633	4		44		35.9
TG1-24	TAG surface	N-MORB	3.562	237	113	561	5		31		31.4
TG1-25b	TAG surface	N-MORB	1.897	28	48	235	3		53	82	24.6
TG1-32c	TAG surface	N-MORB	0.492	32	173	89	4		86		17
TG1-32c	TAG surface	N-MORB	0.485	25	167	80	4		72		15.3
TG1-45	TAG surface	N-MORB	3.034	39	48	189	3	2.5	49		14.5
TG1-45	TAG surface	N-MORB	2.963	38	50		2				13
TG1-45	TAG surface	N-MORB	2.963	33	50	209	5		41		14.1
TG1-45(2)	TAG surface	N-MORB		85							
ALV2178-1	TAG surface	N-MORB	0.005	1	85	5	2.5	5	30	5	0.8
ALV2178-6-2A	TAG surface	N-MORB	0.005	1	32	5	6	14	24	5	0.7
ALV2183-10-2A	TAG surface	N-MORB	0.005	1	140	5	17		28	5	4.8
ALV2183-5-1A	TAG surface	N-MORB	0.01	1	14	5	6		14	5	2.4
ALV2183-5-1B	TAG surface	N-MORB	0.005	1	15	5	1		12	5	2.2
ALV2183-5-2(1)	TAG surface	N-MORB	0.03	2.5	24		10	2.5	7	5	2.7
ALV2183-5-2A	TAG surface	N-MORB	0.03	4	18	5	8		17	5	2.7
ALV2189-2-1A	TAG surface	N-MORB					17	5		5	
ALV2190-12-1(A)	TAG surface	N-MORB	0.009	2.5	22		8	24	34	12	4.6

SAMPLE	Site	Host rock	Au ppb	Ag ppm	As ppm	Cd ppm	Co ppm	Cr ppm	Mo ppm	Ni ppm	Sb ppm
ALV2190-12-2A	TAG surface	N-MORB	0.005	1	12	5	9		20	5	4.6
ALV2583-3	TAG surface	N-MORB	0.0025	2.5	110		4	2.5	36	5	11
ALV2588-1	TAG surface	N-MORB	0.038	2.5	65		10	18	31	5	2.6
MIR 1-77 /1	TAG surface	N-MORB	0.0025	2.5	0.3		6	2.5	1	5	0.4
TG1-18	TAG surface	N-MORB		2.5							
TG1-3(1)	TAG surface	N-MORB		15							
TG1-3(2)	TAG surface	N-MORB		2.5							
TG1-3(3)	TAG surface	N-MORB		2.5							
TG1-39(2)	TAG surface	N-MORB		150							
TG1-43(2)	TAG surface	N-MORB		2.5							
1242 (S1)	TAG surface	N-MORB	0.011	1.00E-04	29	1.00E-04	10		818	440	30.4
1242-3	TAG surface	N-MORB	0.009	1.00E-04	38	1.00E-04	13		892	400	35.5
1243-1	TAG surface	N-MORB	0.005	1.00E-04	22	1.00E-04	15		535	65	4.3
1244-1-B	TAG surface	N-MORB	0.013	1.00E-04	6	1.00E-04	95		490	89	2.9
1247-1-1B	TAG surface	N-MORB	0.015	1.00E-04	84	1.00E-04	31		573	369	23.2
ALV2188-3-1B	TAG surface	N-MORB					1100	170		36	
ALV2188-6-1	TAG surface	N-MORB					5	5		5	
ALV2195-1A	TAG surface	N-MORB					230	59		20	
ALV2195-1B	TAG surface	N-MORB					440	17		23	
MIR-3-76-3A	TAG surface	N-MORB	6.4	40	20	2.5	12	23	140	5	7
MIR-3-76-3B	TAG surface	N-MORB	6.4	10	75	2.5	15	65	230	13	5
MIR-3-76-3BF	TAG surface	N-MORB	8.3	40	90	2.5	12	33	140	5	5
MIR-3-76-5Aavg2	TAG surface	N-MORB	12.9	240	180	840	6.5	8.5	70	13	40
MIR-3-76-5B	TAG surface	N-MORB	7.7	150	210	450	12	43	130	22	25
MIR-3-76-6A	TAG surface	N-MORB	2.5	30	100	10	10	19	80	5	10
MIR-3-76-6B	TAG surface	N-MORB	14.5	110	190	1050	12	93	40	14	60
MIR-3-76-8-1	TAG surface	N-MORB	9.1	100	100	90	11	26	140	11	20

SAMPLE	Site	Host rock	Au ppb	Ag ppm	As ppm	Cd ppm	Co ppm	Cr ppm	Mo ppm	Ni ppm	Sb ppm
MIR-3-76-8-2	TAG surface	N-MORB	15.5	140	150	230	12	55	110	28	30
MIR-3-76-8-3	TAG surface	N-MORB	9	170	170	270	9	26	70	25	30
MIR-3-76-9A	TAG surface	N-MORB	3.3	30	170	10	10	27	210	5	5
MIR-3-76-9B	TAG surface	N-MORB	2.4	20	130	10	14	58	230	11	4
MIR-3-76-10	TAG surface	N-MORB	0.8	40	10	5	13	24	130	12	4
sample 13	TAG surface	N-MORB	0.67	9.9	70	12	12		62		25
sample 19	TAG surface	N-MORB	0.91	24	70	30	2.5		62		25
sample 7	TAG surface	N-MORB	0.96	28.9	90	12	160		130		25
sample 5	TAG surface	N-MORB	1.4	178.35	100	50	9		64		110
sample 4	TAG surface	N-MORB	1.14	41.2	90	20	20		46		25
sample 20-1	TAG surface	N-MORB	5.05	225.15	150	270	2.5		36		120
sample 20-2	TAG surface	N-MORB	2.7	69.65	170	95	2.5		54		100
sample 6	TAG surface	N-MORB	7.5	239.35	260	550	29		120		150
sample 3	TAG surface	N-MORB	1.05	34.35	60	12	10		51		25
sample 16	TAG surface	N-MORB	3.37	440	25	12	2.5		25		140
sample 14	TAG surface	N-MORB	0.31	4.45	55	5	280		78		25
sample 11-2	TAG surface	N-MORB	0.08	2.68	90	1	2.5		90		25
ALV2188-4-1A	TAG surface	N-MORB					18	5		44	
sample 15	TAG surface	N-MORB	0.21	2.5	25	5	3000		940		25
sample 18	TAG surface	N-MORB	0.2	1.17	50	1	98		650		25
sample 10	TAG surface	N-MORB	0.12	0.95	70	12	50		1100		400
sample 11-1	TAG surface	N-MORB	0.21	1.8	25	11	73		1080		25
ALV2599-9	TAG surface	N-MORB	1.02	31	46		10	8	73	5	2
ALV2599-10-7/1	TAG surface	N-MORB	0.95	11	86		23	79	107	5	5.3
ALV2599-10-7/2	TAG surface	N-MORB	0.68	30	84		20	75	95	5	2.6
ALV2599-11-2/1	TAG surface	N-MORB	0.849	2.5	117		22	64	45	5	3.6
JL126-G04-1	Daxi	Mafic and ultramafic	0.006	2.5	36	0.3	38.9		3.5	1.4	0.81

SAMPLE	Site	Host rock	Au ppb	Ag ppm	As ppm	Cd ppm	Co ppm	Cr ppm	Mo ppm	Ni ppm	Sb ppm
JL126-G04-2	Daxi	Mafic and ultramafic	<0.01	8.54	36	0.35	63		2	2	3.84
JL126-G05-1	Daxi	Mafic and ultramafic	0.382	62.1	80.6	277	1620		8.67	0.5	19.45
JL126-G05-2	Daxi	Mafic and ultramafic	0.203	381	51.7	1520	382		13.35	0.5	66.6
JL126-G09	Daxi	Mafic and ultramafic	0.013	393	17.8	1430	321		9.48	2.2	49.4
JL128-G03-1	Daxi	Mafic and ultramafic	0.907	359	108.5	1530	349		13.85	2.5	73.5
JL128-G03-2	Daxi	Mafic and ultramafic	1.45	281	180	1240	698		6.52	4.1	70.7
JL128-G03-3	Daxi	Mafic and ultramafic	6.11	56.9	303	170.5	4670		6.88	1.4	16.95
JL128-G06-1	Daxi	Mafic and ultramafic	0.063	385	38.2	1420	250		11.1	3.2	76.2
JL128-G06-2	Daxi	Mafic and ultramafic	0.706	365	60.8	1530	374		8.6	1.9	84
JL128-G06-3	Daxi	Mafic and ultramafic	0.275	284	46.6	663	548		20.3	1.2	35.9
33I-TVG18C-1	Daxi	Mafic and ultramafic	0.382378	276	34	1270	821		12	6	52
33I-TVG18C-3-1	Daxi	Mafic and ultramafic	0.584722	344	42	1490	747		12.6	21	59.4
33I-TVG18C-3-2	Daxi	Mafic and ultramafic	0.424548	319	27	1360	557		12.7	17	46.2
33I-TVG18C-5-1	Daxi	Mafic and ultramafic	0.537631	291	38	1335	797		9.7	13	50.7
33I-TVG18C-5-2	Daxi	Mafic and ultramafic	0.40643	342	30	1455	649		13.7	16	53.7
33I-TVG18C-7-1	Daxi	Mafic and ultramafic	0.66	268	32	1310	1190		8.9	14	53.4
33I-TVG18C-7-2	Daxi	Mafic and ultramafic	0.402698	347	30	1440	706		13.1	15	55.9
33I-TVG18C-9-1	Daxi	Mafic and ultramafic	0.557943	186	28	931	1500		7.1	11	39.6
33I-TVG18C-9-2	Daxi	Mafic and ultramafic	0.651504	279	30	1135	1050		10.2	21	45.8

SAMPLE	Site	Host rock	Au ppb	Ag ppm	As ppm	Cd ppm	Co ppm	Cr ppm	Mo ppm	Ni ppm	Sb ppm
33I-TVG18C-11-1	Daxi	Mafic and ultramafic	0.384083	159.5	27	777	1820		7.2	17	35.3
33I-TVG18C-11-2	Daxi	Mafic and ultramafic	0.651379	316	40	1300	924		9.6	23	54
33I-TVG18C-12-1	Daxi	Mafic and ultramafic	0.414905	141.5	31	770	1930		8.5	10	36.4
33I-TVG18C-12-2	Daxi	Mafic and ultramafic	0.460879	329	31	1265	698		10.3	13	48.4
33I-TVG18C-13-1	Daxi	Mafic and ultramafic	0.368321	328	35	1335	704		9.9	7	51.1
33I-TVG18C-14-2	Daxi	Mafic and ultramafic	0.334476	390	30	1195	869		12.1	10	45.7
33I-TVG18C-e	Daxi	Mafic and ultramafic	0.393143	361	26	1295	648		11.8	5	48.4
33I-TVG18C-m	Daxi	Mafic and ultramafic	0.59	328	43	1360	843		5.9	4	58.1
33I-TVG18C-i	Daxi	Mafic and ultramafic	1.06	132.5	76	984	1900		8.3	4	42.3
JL126-G08-1	Daxi	Mafic and ultramafic	0.831	44.2	41.8	60.4	3770		11.4	64.1	5.01
JL126-G08-2	Daxi	Mafic and ultramafic	1.44	47.6	49.7	50.5	3540		12.05	40.6	4.84
JL128-G04	Daxi	Mafic and ultramafic	4.19	19.4	210	48	3910		2.9	2.9	4.66
JL128-G05	Daxi	Mafic and ultramafic	3.15	12.35	48.5	12.35	2430		33.2	14.1	3.79
JL126-G01	Daxi	Mafic and ultramafic	2.27	2.23	35.8	5.09	3580		3.69	1.1	1.08
JL126-G03	Daxi	Mafic and ultramafic	3.45	3.18	94.1	1.74	3980		3.42	0.6	1.15
JL126-G07	Daxi	Mafic and ultramafic	0.279	30.6	42.5	41.5	551		47.2	35.7	10.35
33I-TVG18-1-1	Daxi	Mafic and ultramafic	2.18	13.05	72.9	38.2	3290		6.55	4.9	4.78
33I-TVG18-1-2	Daxi	Mafic and ultramafic	2.53	8.47	164.5	22.6	4930		6.95	7.6	4.06
33I-TVG18-1-3	Daxi	Mafic and ultramafic	4.02	84.6	206	340	2550		32.1	11	22.3

SAMPLE	Site	Host rock	Au ppb	Ag ppm	As ppm	Cd ppm	Co ppm	Cr ppm	Mo ppm	Ni ppm	Sb ppm
33I-TVG18-2-1	Daxi	Mafic and ultramafic	5.51	74	215	267	5280		22.6	0.5	18
33I-TVG18-2-2	Daxi	Mafic and ultramafic	1.35	79.9	90	304	3610		6.3	13	19.6
M11-ROC1	Lucky Strike	E-MORB	1340	49	635	9	467	4.6	67	20	39
M11-ROC2	Lucky Strike	E-MORB	1010	94	223	25	225	0.25	100	10	19
M11-ROC3	Lucky Strike	E-MORB	677	59	242	59	47.5	0.25	59	10	28
M11-ROC7	Lucky Strike	E-MORB	625	88	307	288	337	0.25	318	10	23.7
M11-ROC8	Lucky Strike	E-MORB	2030	278	346	1700	33	0.25	59	10	166
PL1-1	Lucky Strike	E-MORB	369	89	168	98	8.5	0.25	11	5	29.5
MOM2012-ROCK-PL3-1	Lucky Strike	E-MORB	1750	165	642	291	50.6	0.25	66	20	82.8
MOM14-PL579-ROC1	Lucky Strike	E-MORB	724	76	387	288	107	0.25	167	40	36.9
MOM14-PL583-ROC1-S	Lucky Strike	E-MORB	258	22	128	43	277	0.25	33	5	11.4
MOM14-PL583-ROCK4A	Lucky Strike	E-MORB	256	21	291	55	158	3.2	37	10	15
MOM14-PL583-ROCK4B	Lucky Strike	E-MORB	237	22	229	30	258	0.25	40	10	11.4
MOM14-HN29008-ROCK	Lucky Strike	E-MORB	37	6	85	1	559	0.25	6	60	0.5
MOM14-HT007-ROCK	Lucky Strike	E-MORB	47	1	96	3	86.8	6.1	11	20	1.1
M15-603-7-Rock#5	Lucky Strike	E-MORB	748	152	277	1250	64.6	0.25	121	5	50
MOM15-PL-603-7-R6	Lucky Strike	E-MORB	205	9	142	17	604	0.25	351	30	5
M15-PL607-11-Rock#3-S	Lucky Strike	E-MORB	496	59	477	27	89.2	0.25	69	20	9.6
PL-607-11-R5	Lucky Strike	E-MORB	539	44	268	6	409	0.25	267	10	6.3
HT010-CR12	Lucky Strike	E-MORB	189	28	97	122	101	1780	444	1450	12.4
MOM13-PL7-Rock#1	Lucky Strike	E-MORB	309	1	449	4	48.5	0.25	25	20	2.3
LS-BS-WHOI	Lucky Strike	E-MORB	228	52	120	92	198	0.25	212	30	8.3

SAMPLE	Site	Host rock	Au ppb	Ag ppm	As ppm	Cd ppm	Co ppm	Cr ppm	Mo ppm	Ni ppm	Sb ppm
MOM13-PL12-Rock#1-S	Lucky Strike	E-MORB	323	39	236	213	14.1	11.3	69	10	49.9
PL7-R2-S	Lucky Strike	E-MORB	73	1	99	1	167	0.25	22	10	1.6
M15-PL605-9-ROCK#2	Lucky Strike	E-MORB	8	1	14	1	7.4	0.25	7	10	0.8
Ledge	Lucky Strike	E-MORB		148	310						
Chimney 1	Lucky Strike	E-MORB		117	790						
Chimney 2	Lucky Strike	E-MORB		42	620						
4377_6	Lucky Strike	E-MORB				35	236	32		140	
4377_4	Lucky Strike	E-MORB				3	265	20		120	
4377_5	Lucky Strike	E-MORB				6	308	40		140	
4384_1	Lucky Strike	E-MORB				33	100	34		210	
4383_1	Lucky Strike	E-MORB				502	112	16		100	
4376_1a	Lucky Strike	E-MORB				10	352	40		100	
4376_1b	Lucky Strike	E-MORB				3	210	22		100	
4377_10-2	Lucky Strike	E-MORB				26	134	28		140	
4377_10-4	Lucky Strike	E-MORB				43	102	23		200	
4379_2	Lucky Strike	E-MORB				20	265	32		160	
4383_3	Lucky Strike	E-MORB				29	396	14		140	
4383_4	Lucky Strike	E-MORB				27	188	22		240	
4383_6	Lucky Strike	E-MORB				20	188	40		220	
4383_7	Lucky Strike	E-MORB				22	200	8		140	
4383_2	Lucky Strike	E-MORB				650	81	20		130	
4377_8	Lucky Strike	E-MORB				64	481	38		170	
4377_9	Lucky Strike	E-MORB				20	140	29		60	
4376_2-2	Lucky Strike	E-MORB				44	190	25		110	
4376_2-3	Lucky Strike	E-MORB				27	14	34		110	
4376_3	Lucky Strike	E-MORB				63	440	28		110	

SAMPLE	Site	Host rock	Au ppb	Ag ppm	As ppm	Cd ppm	Co ppm	Cr ppm	Mo ppm	Ni ppm	Sb ppm
4376_4	Lucky Strike	E-MORB				566	57	20		80	
4379_1	Lucky Strike	E-MORB				3	4	26		130	
4377_7-1	Lucky Strike	E-MORB				28	298	29		100	
4377_7-2	Lucky Strike	E-MORB				30	265	26		120	
4582-2	Menez Gwen	E-MORB				1	4	10	25	50	
4578-01-01	Menez Gwen	E-MORB				9.71	41	80	25	5	
4578-01-02	Menez Gwen	E-MORB				16.8	41	60	25	5	
4578-01-06	Menez Gwen	E-MORB				1	41	80	25	5	
4574-03-02	Menez Gwen	E-MORB				9.71	1.8	300	25	5	
4574-04-02	Menez Gwen	E-MORB				26.3	4	80	25	5	
4592-03-04	Menez Gwen	E-MORB				57	4	90	25	40	
4592-04-01	Menez Gwen	E-MORB				75.6	4	40	110	5	
4594-1	Menez Gwen	E-MORB				4.98	4	60	110	5	
4582-06-01	Menez Gwen	E-MORB				759	106	210	880	5	
4582-06-02	Menez Gwen	E-MORB				365	73	280	610	5	
4582-06-03	Menez Gwen	E-MORB				467	41	170	720	5	

Appendix 3: *continued* Compiled geochemistry of hydrothermal deposits in mid-ocean ridges.

SAMPLE	Se ppm	Sn ppm	Sr ppm	Cu wt.%	Zn wt.%	Pb wt.%	Ba ppm	Cu/Zn	Ba/Co	Depth (mbsl)	Reference
ALV1445-3A				31.6	0.07	0.007	0	451.4286		2200	Tivey and Delaney, 1986
ALV1445-3B				1.11	0.36	0.032	0	3.083333		2200	Tivey and Delaney, 1986
ALV1445-3C				1.64	0.53	0.047	0	3.09434		2200	Tivey and Delaney, 1986
ALV1445-3D				1.02	0.24	0.052	0	4.25		2200	Tivey and Delaney, 1986
Endv-1. vent	117			30.2	0.4	0.0017	70	75.5	5.384615	2200	Geological Survey of Canada, unpublished

SAMPLE	Se ppm	Sn ppm	Sr ppm	Cu wt.%	Zn wt.%	Pb wt.%	Ba ppm	Cu/Zn	Ba/Co	Depth (mbsl)	Reference
ALV1417-1b b2	95		11	4.4	0.26	0.013	290	16.92308	2.989691	2200	Samson, 1986; Geological Survey of Canada unpublished data
ALV1417-2a b5	191		540	9.7	6.7	0.01	21000	1.447761	323.0769	2200	Samson, 1986; Geological Survey of Canada unpublished data
ALV1419-1b b3	41		11	0.73	0.076	0.0037	210	9.605263	7	2200	Geological Survey of Canada, unpublished data; Hannington et al., 2004; Toffolo et al. 2020
ALV1417-1c b22	147		91	3.9	0.16	0.0019	4700	24.375	50	2200	Geological Survey of Canada, unpublished data; Hannington et al., 2004;Toffolo et al. 2020
ALV1419-2 b10	66			0.033	0.078	0.0063	80	0.423077	0.285714	2200	Samson, 1986; Geological Survey of Canada unpublished data
ALV1418-8b b6	16		1	1.5	0.58	0.021	120	2.586207	15	2200	Samson, 1986; Geological Survey of Canada unpublished data
ALV1417-1d b7	55		11	0.036	0.024	0.0041	28	1.5	0.215385	2200	Geological Survey of Canada, unpublished data; Hannington et al., 2004; Toffolo et al. 2020
ALV1417-c b9	67			0.035	0.1	0.011	110	0.35	0.392857	2200	Geological Survey of Canada, unpublished data; Hannington et al., 2004; Toffolo et al. 2020
ALV1418-1d b2	64			1.5	0.34	0.0023	70	4.411765	8.75	2200	Geological Survey of Canada, unpublished data; Hannington et al., 2004; Toffolo et al. 2020
ALV1418-1d b5	47		210	0.51	0.034	0.0018	14000	15	46.66667	2200	Geological Survey of Canada, unpublished

SAMPLE	Se ppm	Sn ppm	Sr ppm	Cu wt.%	Zn wt.%	Pb wt.%	Ba ppm	Cu/Zn	Ba/Co	Depth (mbsl)	Reference
ALV1417-1e	65			1.6	0.34	0.0019	20	4.705882	2.5	2200	Geological Survey of Canada, unpublished data; Hannington et al., 2004; Toffolo et al. 2020
ALV1418-3a	40		210	0.49	0.031	0.0018	14000	15.80645	48.27586	2200	Samson, 1986; Geological Survey of Canada unpublished data
ALV1417-2b			14	0.71	0.078	0.0068	160	9.102564	4.848485	2200	Geological Survey of Canada, unpublished data; Hannington et al., 2004; Toffolo et al. 2020
ALV1417-5b b12	4			0.12	2	7.1	40	0.06	0.97561	2200	Geological Survey of Canada, unpublished data; Hannington et al., 2004; Toffolo et al. 2020
ALV1419-1a b2			470	0.33	5.8	0.13	13000	0.056897	565.2174	2200	Samson, 1986; Geological Survey of Canada unpublished data
ALV1417-5c b13	4		24	0.12	19.8	6.6	30	0.006061	0.731707	2200	Geological Survey of Canada, unpublished data; Hannington et al., 2004; Toffolo et al. 2020
ALV1417-5a b11	4			0.12	20.3	7	20	0.005911	0.487805	2200	Geological Survey of Canada, unpublished data; Hannington et al., 2004; Toffolo et al. 2020
ALV1417-5d b14	4		24	0.12	20.4	6.3	80	0.005882	2.051282	2200	Geological Survey of Canada, unpublished data; Hannington et al., 2004; Toffolo et al. 2020
ALV1418-6b b9	2		370	0.69	25.1	0.28	13000	0.02749	1300	2200	Samson, 1986; Geological Survey of Canada unpublished data
ALV1417-1b b8	2		410	0.73	25.2	0.23	12000	0.028968	1200	2200	Geological Survey of Canada, unpublished

SAMPLE	Se ppm	Sn ppm	Sr ppm	Cu wt.%	Zn wt.%	Pb wt.%	Ba ppm	Cu/Zn	Ba/Co	Depth (mbsl)	Reference
ALV1417-1c b2	33		2200	1.6	2.4	0.03	89000	0.666667	4684.211	2200	Samson, 1986; Geological Survey of Canada unpublished data
ALV1417-1a b2	<3		2000	0.17	1.5	0.089	88000	0.113333	12571.43	2200	Samson, 1986; Geological Survey of Canada unpublished data
ALV1419-1d b31	5		4300	0.097	2.1	0.11	220000	0.04619	36666.67	2200	Samson, 1986; Geological Survey of Canada unpublished data
ALV1419-1h b4	9		6900	0.03	0.62	0.13	320000	0.048387	64000	2200	Samson, 1986; Geological Survey of Canada unpublished data
ALV1418-1e b2	14		6900	0.031	0.65	0.16	370000	0.047692	123333.3	2200	Geological Survey of Canada, unpublished data; Hannington et al., 2004; Toffolo et al. 2020
ALV1419-1c b2	14		6900	0.03	0.62	0.13	370000	0.048387	74000	2200	Samson, 1986; Geological Survey of Canada unpublished data
ALV1419-1d b3	16		7400	0.048	0.72	0.068	390000	0.066667	48750	2200	Samson, 1986; Geological Survey of Canada unpublished data
G2 mucus	<3	<100	<50		0.017					2200	Geological Survey of Canada, unpublished data
TT-170-66D-B23-C				0.83	13.2	0.154	0	0.062879		2200	Morgan and Selk (1984)
Al-G				0.02	1.6	0.353	0	0.0125		2200	Morgan and Selk (1984)
WF-22D-5				0.26	32.3	0.464	0	0.00805		2200	Morgan and Selk (1984)
WF-22D-6				0.14	54.4	0.111	0	0.002574		2200	Morgan and Selk (1984)
ALV2448-1	15	<100	450	0.11	3.6	0.0352	29000	0.030556	2230.769	2200	Geological Survey of Canada, unpublished data; Hannington et al., 2004; Toffolo et al. 2020

SAMPLE	Se ppm	Sn ppm	Sr ppm	Cu wt.%	Zn wt.%	Pb wt.%	Ba ppm	Cu/Zn	Ba/Co	Depth (mbsl)	Reference
ALV2449-1	22	<100	290	0.21	4.5	0.0456	16000	0.046667	888.8889	2200	Geological Survey of Canada, unpublished data; Hannington et al., 2004; Toffolo et al. 2020
ALV2450-2	230	<100	65	1.6	5.4	0.0208	2400	0.296296	9.230769	2200	Geological Survey of Canada, unpublished data; Hannington et al., 2004; Toffolo et al. 2020
ALV2450-3b (crust)	15	<100	210	0.1	0.68	0.0803	8000	0.147059	1142.857	2200	Geological Survey of Canada, unpublished data; Hannington et al., 2004; Toffolo et al. 2020
ALV2452-1	160	<100	97	2.2	2.5	0.0198	150	0.88	1.363636	2200	Geological Survey of Canada, unpublished data; Hannington et al., 2004; Toffolo et al. 2020
ALV2453-1b	170	<100	<20	2.9	7.6	0.0176	80	0.381579	0.987654	2200	Geological Survey of Canada, unpublished data; Hannington et al., 2004; Toffolo et al. 2020
ALV2453-2 (puffer)	690	<100	76	3.2	1.9	0.0131	600	1.684211	3.157895	2200	Geological Survey of Canada, unpublished data; Hannington et al., 2004; Toffolo et al. 2020
ALV2453-3	210	<100	<20	4	4.2	0.0155	100	0.952381	0.909091	2200	Geological Survey of Canada, unpublished data; Hannington et al., 2004; Toffolo et al. 2020
ALV2465-R1-4b	100	<100	650	1.8	12.7	0.0786	5600	0.141732	243.4783	2200	Tivey et al., 1999; Geological Survey of Canada, unpublished data
ALV2465-R1-6c	68	<100	210	1.6	8.3	0.2393	7600	0.192771	3800	2200	Tivey et al., 1999; Geological Survey of Canada, unpublished data

SAMPLE	Se ppm	Sn ppm	Sr ppm	Cu wt.%	Zn wt.%	Pb wt.%	Ba ppm	Cu/Zn	Ba/Co	Depth (mbsl)	Reference
ALV2465-R2-1e	430	<100	460	11.7	0.27	<0.005	80	43.33333	40	2200	Tivey et al., 1999; Geological Survey of Canada, unpublished data
ALV2465-R2-2a2	150	<100	1600	2.2	0.94	0.0066	350	2.340426	3.977273	2200	Tivey et al., 1999; Geological Survey of Canada, unpublished data
ALV2465-R2-2d2	15	<100	2000	0.21	0.09	<0.005	940	2.333333		2200	Tivey et al., 1999; Geological Survey of Canada, unpublished data
ALV2465-R2-3b	220	<100	1100	7.1	0.85	0.0138	600	8.352941	200	2200	Tivey et al., 1999; Geological Survey of Canada, unpublished data
ALV2465-R2b	91	<100	100	0.85	9.2	0.0717	390	0.092391	78	2200	Tivey et al., 1999; Geological Survey of Canada, unpublished data
ALV2465-R3-2a	220	<100	2000	2.8	0.11	<0.005	290	25.45455	1.705882	2200	Tivey et al., 1999; Geological Survey of Canada, unpublished data
ALV2466 A	7		311	0.17	9.84	2.49	8900	0.017276	1780	2200	Tivey et al., 1999; Geological Survey of Canada, unpublished data
ALV2466 E	16		282	0.27	12.2	0.27	11300	0.022131	2260	2200	Geological Survey of Canada, unpublished data; Hannington et al., 2004; Toffolo et al. 2020
ALV2466-b	29	<100	220	0.54	14.8	0.1454	1700	0.036486	242.8571	2200	

SAMPLE	Se ppm	Sn ppm	Sr ppm	Cu wt.%	Zn wt.%	Pb wt.%	Ba ppm	Cu/Zn	Ba/Co	Depth (mbsl)	Reference
ALV2466-c	30	<100	80	0.43	10	0.1344	2000	0.043	285.7143	2200	Geological Survey of Canada, unpublished data; Hannington et al., 2004; Toffolo et al. 2020
ALV2466-R1-4b	150	<100	28	0.42	0.47	0.0483	70	0.893617	5	2200	Tivey et al., 1999; Geological Survey of Canada, unpublished data
ALV2466-R3	48	<100	81	0.56	9.6	0.063	3300	0.058333	1100	2200	Geological Survey of Canada, unpublished data; Hannington et al., 2004; Toffolo et al. 2020
ALV2466-R3-1b1	19	<100	120	0.39	9.2	0.0645	4500	0.042391	1500	2200	Tivey et al., 1999; Geological Survey of Canada, unpublished data
ALV2466-R3-1b2	6.75	<100	115	0.15	8	<0.005	3700	0.01875	925	2200	Tivey et al., 1999; Geological Survey of Canada, unpublished data
ALV2466-R4	57	<100	650	0.7	4.7	0.0302	190	0.148936	19	2200	Geological Survey of Canada, unpublished data; Hannington et al., 2004; Toffolo et al. 2020
ALV2466-R5-8/1	120	<100	190	2.5	9.8	0.1233	4300	0.255102	165.3846	2200	Tivey et al., 1999; Geological Survey of Canada, unpublished data
ALV2466-R5-8/2	91	<100	120	0.67	9.6	0.0622	150	0.069792	5.769231	2200	Tivey et al., 1999; Geological Survey of Canada, unpublished data
ALV2466-R5-8/3	60	<100	<20	0.44	9.7	0.0643	200	0.045361	33.33333	2200	Tivey et al., 1999; Geological Survey of Canada, unpublished data

SAMPLE	Se ppm	Sn ppm	Sr ppm	Cu wt.%	Zn wt.%	Pb wt.%	Ba ppm	Cu/Zn	Ba/Co	Depth (mbsl)	Reference
ALV2466-R5-8/4	21	<100	190	0.3	12.7	0.2501	6100	0.023622	3050	2200	Tivey et al., 1999; Geological Survey of Canada, unpublished data
ALV2467-R1-14d	150	<100	230	3.7	9.4	0.0449	690	0.393617	16.82927	2200	Tivey et al., 1999; Geological Survey of Canada, unpublished data
ALV2467-R1-1b3	52	<100	65	0.7	6.5	0.0282	540	0.107692	49.09091	2200	Tivey et al., 1999; Geological Survey of Canada, unpublished data
ALV2467-R1exc	110	<100	1900	2.2	0.77	<0.005	400	2.857143	15.38462	2200	Tivey et al., 1999; Geological Survey of Canada, unpublished data
ALV2467-R3	<3	<100	2000	0.024	1.6	0.3584	265000	0.015		2200	TU Freiberg and Geological Survey of Canada, unpublished data; Hannington et al., 2004; Toffolo et al. 2020
HYS-278-01	16	<400	227	0.29	8.6094	3.9274	9800	0.033684	1960	2200	TU Freiberg and Geological Survey of Canada, unpublished data; Hannington et al., 2004; Toffolo et al. 2020
HYS-278-02a	<3	<400	350	0.59	26	0.9234	12000	0.022692	4000	2200	TU Freiberg and Geological Survey of Canada, unpublished data; Hannington et al., 2004; Toffolo et al. 2020
HYS-278-02b	<3	<300	406	0.42	19	2.7878	8500	0.022105		2200	TU Freiberg and Geological Survey of
HYS-278-09a	62	<200	6	4.88	0.0537	0.0048		90.87523		2200	

SAMPLE	Se ppm	Sn ppm	Sr ppm	Cu wt.%	Zn wt.%	Pb wt.%	Ba ppm	Cu/Zn	Ba/Co	Depth (mbsl)	Reference
HYS-278-09b	29	<300	3	2.96	0.3118	0.0216		9.493265		2200	TU Freiberg and Geological Survey of Canada, unpublished data; Hannington et al., 2004; Toffolo et al. 2020
HYS-278-10	210	<300	16	15.065	0.0539	0.0073	570	279.4991	1.540541	2200	TU Freiberg and Geological Survey of Canada, unpublished data; Hannington et al., 2004; Toffolo et al. 2020
HYS-278-11	150	<300	4	8.009	0.0782	0.0094		102.4169		2200	TU Freiberg and Geological Survey of Canada, unpublished data; Hannington et al., 2004; Toffolo et al. 2020
HYS-278-14a	140	<200	2	6.511	0.0223	0.0065		291.9731		2200	TU Freiberg and Geological Survey of Canada, unpublished data; Hannington et al., 2004; Toffolo et al. 2020
HYS-278-14b	65	<200	2	3.92	0.1476	0.0126		26.55827		2200	TU Freiberg and Geological Survey of Canada, unpublished data; Hannington et al., 2004; Toffolo et al. 2020
HYS-278-16	49	<200	238	0.94	0.6089	0.0074	28000	1.543767	4666.667	2200	TU Freiberg and Geological Survey of Canada, unpublished data; Hannington et al., 2004; Toffolo et al. 2020
HYS-347-01	3	2	167	0.0061	0.9719	0.0424	18000	0.006276		2200	TU Freiberg and Geological Survey of Canada, unpublished

SAMPLE	Se ppm	Sn ppm	Sr ppm	Cu wt.%	Zn wt.%	Pb wt.%	Ba ppm	Cu/Zn	Ba/Co	Depth (mbsl)	Reference
HYS-347-02	60	2	105	1.4956	7.1806	0.0182	100	0.208283	3.571429	2200	TU Freiberg and Geological Survey of Canada, unpublished data; Hannington et al., 2004; Toffolo et al. 2020
HYS-350-01	36	1	162	0.6525	4.2949	0.0284	2400	0.151924	600	2200	TU Freiberg and Geological Survey of Canada, unpublished data; Hannington et al., 2004; Toffolo et al. 2020
HYS-350-02	23	3	161	0.84	6.4135	0.0182	170	0.130974	170	2200	TU Freiberg and Geological Survey of Canada, unpublished data; Hannington et al., 2004; Toffolo et al. 2020
HYS-355-01	160	11	6	13.7	33	0.0098	470	0.415152	156.6667	2200	TU Freiberg and Geological Survey of Canada, unpublished data; Hannington et al., 2004; Toffolo et al. 2020
HYS-355-02	130	3	2	5.72	33	0.0147	50	0.173333	16.66667	2200	TU Freiberg and Geological Survey of Canada, unpublished data; Hannington et al., 2004; Toffolo et al. 2020
HYS-355-B	100	3	761	0.2822	5.7641	1.9364	48000	0.048958		2200	TU Freiberg and Geological Survey of Canada, unpublished data; Hannington et al., 2004; Toffolo et al. 2020
HYS-363-01A	300	22	141	2.7211	48	0.0043	150	0.05669	50	2200	TU Freiberg and Geological Survey of Canada, unpublished data; Hannington et al., 2004; Toffolo et al. 2020

SAMPLE	Se ppm	Sn ppm	Sr ppm	Cu wt.%	Zn wt.%	Pb wt.%	Ba ppm	Cu/Zn	Ba/Co	Depth (mbsl)	Reference
HYS-363-01B	160	6	226	1.3429	9.7927	0.3307	110000	0.137133	36666.67	2200	TU Freiberg and Geological Survey of Canada, unpublished data; Hannington et al., 2004; Toffolo et al. 2020
HYS-363-01C	320	13	33	3.5487	36	0.6259	65	0.098575	16.25	2200	TU Freiberg and Geological Survey of Canada, unpublished data; Hannington et al., 2004; Toffolo et al. 2020
HYS-356-01A	300	4	226	19.5	4.8817	0.01	480	3.99451	5.454545	2200	TU Freiberg and Geological Survey of Canada, unpublished data; Hannington et al., 2004; Toffolo et al. 2020
HYS-356-01B	420	4	74	25	0.16	2.50E-04	50	156.25	0.384615	2200	TU Freiberg and Geological Survey of Canada, unpublished data; Hannington et al., 2004; Toffolo et al. 2020
HYS-356-02A	8	2	1648	0.1091	2.7525	0.0084	450	0.039637	225	2200	TU Freiberg and Geological Survey of Canada, unpublished data; Hannington et al., 2004; Toffolo et al. 2020
ALV2463-R7-6B	47			0.84	8.03	3.02	2200	0.104608	1466.667	2200	Tivey et al., 1999; Geological Survey of Canada, unpublished data
ALV2463-R7-6C	9		3610	0.27	2.49	1.39	107000	0.108434	107000	2200	Tivey et al., 1999; Geological Survey of Canada, unpublished data
ALV2463-R7-6G	6		8900	0.1	1.05	0.35	305000	0.095238	305000	2200	Tivey et al., 1999; Geological Survey of Canada, unpublished data

SAMPLE	Se ppm	Sn ppm	Sr ppm	Cu wt.%	Zn wt.%	Pb wt.%	Ba ppm	Cu/Zn	Ba/Co	Depth (mbsl)	Reference
ALV2467-R4-misc	16	<100	<20	0.19	0.44	0.0189	130	0.431818	65	2200	Tivey et al., 1999; Geological Survey of Canada, unpublished data
HYS-350-02(?)	33	3	990	0.2115	2.1111	0.543	250000	0.100185	125000	2200	TU Freiberg and Geological Survey of Canada, unpublished data; Hannington et al., 2004; Toffolo et al. 2020
ALV2451-1	32	<100	300	0.57	16	0.04	730	0.035625	104.2857	2200	Geological Survey of Canada, unpublished data; Hannington et al., 2004; Toffolo et al. 2020
ALV2460 B	8		<20	0.35		0.1	4400		4400	2200	Tivey et al., 1999; Geological Survey of Canada, unpublished data
ALV2460 E	32		<20	1.17	30	0.09	800	0.039	160	2200	Tivey et al., 1999; Geological Survey of Canada, unpublished data
ALV2464 B			<20	0.79	53.2	0.01		0.01485		2200	Tivey et al., 1999; Geological Survey of Canada, unpublished data
ALV2464 F-V	310		<20	5.4	3.91	0.01	100	1.381074	1.204819	2200	Tivey et al., 1999; Geological Survey of Canada, unpublished data
ALV2461 A	26		2800	0.28	2.68	0.13	88700	0.104478	29566.67	2200	Tivey et al., 1999; Geological Survey of Canada, unpublished data
ALV2461 E	23		215	0.24	1.34	0.54	6300	0.179104	2100	2200	Tivey et al., 1999; Geological Survey of Canada, unpublished data

SAMPLE	Se ppm	Sn ppm	Sr ppm	Cu wt.%	Zn wt.%	Pb wt.%	Ba ppm	Cu/Zn	Ba/Co	Depth (mbsl)	Reference
ALV2463 A	160		<20	10	0.86	0.01	100	11.62791	0.384615	2200	Tivey et al., 1999; Geological Survey of Canada, unpublished data
ALV2463 F	190		<20	10	0.58	0.01		17.24138		2200	Tivey et al., 1999; Geological Survey of Canada, unpublished data
ALV2462 A1	220		1480	5.5	1.22	0.34	40700	4.508197	714.0351	2200	Tivey et al., 1999; Geological Survey of Canada, unpublished data
ALV2460-R2-14a	27	<100	440	0.71	0.86	0.0069	26000	0.825581	2166.667	2200	Tivey et al., 1999; Geological Survey of Canada, unpublished data
ALV2460-R2-14b	19	<100	65	0.83	15.6	0.2232	5800	0.053205	1450	2200	Tivey et al., 1999; Geological Survey of Canada, unpublished data
ALV2460-R2-15	45	<100	250	1.2	14	0.0267	8600	0.085714	955.5556	2200	Tivey et al., 1999; Geological Survey of Canada, unpublished data
ALV2460-R3-3	88	<100	400	2.6	11.7	0.085	12000	0.222222	144.5783	2200	Tivey et al., 1999; Geological Survey of Canada, unpublished data
ALV2460-R3-3c	82	<100	350	2.5	11.1	0.0807	9800	0.225225	118.0723	2200	Tivey et al., 1999; Geological Survey of Canada, unpublished data
ALV2460-R3-5	61	<100	730	1.1	8.3	0.0228	7500	0.13253	182.9268	2200	Tivey et al., 1999; Geological Survey of Canada, unpublished data

SAMPLE	Se ppm	Sn ppm	Sr ppm	Cu wt.%	Zn wt.%	Pb wt.%	Ba ppm	Cu/Zn	Ba/Co	Depth (mbsl)	Reference
ALV2460-R4-1c	59	<100	<20	0.89	12.4	<0.005	190	0.071774	19	2200	Tivey et al., 1999; Geological Survey of Canada, unpublished data
ALV2460-R5	15	<100	2100	0.56	0.5	<0.005	410	1.12	29.28571	2200	Tivey et al., 1999; Geological Survey of Canada, unpublished data
ALV2461-R10b2	200	<100	<20	4.4	0.34	0.0094	150	12.94118	1.851852	2200	Tivey et al., 1999; Geological Survey of Canada, unpublished data
ALV2461-R11-9	44	<100	380	0.85	18.2	0.1031	12000	0.046703	4000	2200	Tivey et al., 1999; Geological Survey of Canada, unpublished data
ALV2461-R12-2	39	<100	200	0.63	10.9	0.2218	2800	0.057798	1400	2200	Tivey et al., 1999; Geological Survey of Canada, unpublished data
ALV2461-R13 TIP	<3	<100	1000	0.26	6.3	0.3486	46000	0.04127	15333.33	2200	Tivey et al., 1999; Geological Survey of Canada, unpublished data
ALV2461-R13-4-BOT	29	<100	350	1.1	20.9	0.6519	9700	0.052632	3233.333	2200	Tivey et al., 1999; Geological Survey of Canada, unpublished data
ALV2461-R13/1	16	<100	120	0.82	13.6	0.2616	2800	0.060294	700	2200	Tivey et al., 1999; Geological Survey of Canada, unpublished data
ALV2461-R13/2	17	<100	110	0.59	9.2	0.1631	3200	0.06413	1066.667	2200	Tivey et al., 1999; Geological Survey of Canada, unpublished data

SAMPLE	Se ppm	Sn ppm	Sr ppm	Cu wt.%	Zn wt.%	Pb wt.%	Ba ppm	Cu/Zn	Ba/Co	Depth (mbsl)	Reference
ALV2461-R13/3	12	<100	280	0.58	11.3	0.528	11000	0.051327	2200	2200	Tivey et al., 1999; Geological Survey of Canada, unpublished data
ALV2461-R13/4	<3	<100	950	0.076	4.3	1.6082	56000	0.017674	11200	2200	Tivey et al., 1999; Geological Survey of Canada, unpublished data
ALV2461-R1b2	34	<100	290	1	13.4	0.149	7300	0.074627	384.2105	2200	Tivey et al., 1999; Geological Survey of Canada, unpublished data
ALV2461-R3c1	55	<100	160	1	16.9	0.0109	80	0.059172	26.66667	2200	Tivey et al., 1999; Geological Survey of Canada, unpublished data
ALV2461-R4d	200	<100	<20	3.3	0.1	<0.005	70	33	35	2200	Tivey et al., 1999; Geological Survey of Canada, unpublished data
ALV2461-R6-4	45	<100	370	1.2	19.1	0.1363	15000	0.062827	7500	2200	Tivey et al., 1999; Geological Survey of Canada, unpublished data
ALV2461-R7c2	18	<100	440	0.31	10.4	0.3735	17000	0.029808	3400	2200	Tivey et al., 1999; Geological Survey of Canada, unpublished data
ALV2461-R8-3	<3	<100	2200	0.0081	0.0077	<0.005	250	1.051948		2200	Tivey et al., 1999; Geological Survey of Canada, unpublished data
ALV2462-R1a	64	<100	240	1.1	12.4	0.0584	7600	0.08871	316.6667	2200	Tivey et al., 1999; Geological Survey of Canada, unpublished data

SAMPLE	Se ppm	Sn ppm	Sr ppm	Cu wt.%	Zn wt.%	Pb wt.%	Ba ppm	Cu/Zn	Ba/Co	Depth (mbsl)	Reference
ALV2462-R1b	<3	<100	2500	0.082	0.31	<0.005	410	0.264516		2200	Tivey et al., 1999; Geological Survey of Canada, unpublished data
ALV2462-R1c	69	<100	210	1.3	10.4	0.0592	6200	0.125	238.4615	2200	Tivey et al., 1999; Geological Survey of Canada, unpublished data
ALV2462-R6-1d2	520	<100	28	10.1	0.47	0.1157	700	21.48936	20	2200	Tivey et al., 1999; Geological Survey of Canada, unpublished data
ALV2462-R7-1b	86	<100	420	2	7.9	0.0635	6000	0.253165	113.2075	2200	Tivey et al., 1999; Geological Survey of Canada, unpublished data
ALV2463-R1-2	<3	<100	<20	0.8	6	0.1298	100	0.133333	20	2200	Tivey et al., 1999; Geological Survey of Canada, unpublished data
ALV2463-R2-1a	140	<100	<20	5.1	0.16	<0.005	70	31.875	0.205882	2200	Tivey et al., 1999; Geological Survey of Canada, unpublished data
ALV2463-R3-3	32.5	<100	3650	0.26	0.895	0.4113	220000	0.290503		2200	Tivey et al., 1999; Geological Survey of Canada, unpublished data
ALV2463-R3-misc							0			2200	Tivey et al., 1999; Geological Survey of Canada, unpublished data
ALV2463-R4-pc	12	<100	5700	0.0089	0.036	0.018	260000	0.247222	86666.67	2200	Tivey et al., 1999; Geological Survey of Canada, unpublished data

SAMPLE	Se ppm	Sn ppm	Sr ppm	Cu wt.%	Zn wt.%	Pb wt.%	Ba ppm	Cu/Zn	Ba/Co	Depth (mbsl)	Reference
ALV2463-R5c2	<3	<100	290	0.46	4	0.0102	18000	0.115	4500	2200	Tivey et al., 1999; Geological Survey of Canada, unpublished data
ALV2463-R5c3	17	<100	320	0.12	2.6	0.0514	42000	0.046154	8400	2200	Tivey et al., 1999; Geological Survey of Canada, unpublished data
ALV2463-R6-misc	140	<100	<20	5.4	0.78	0.0062	50	6.923077	0.113636	2200	Tivey et al., 1999; Geological Survey of Canada, unpublished data
ALV2464-R5-3	<3	<100	380	0.48	28.9	0.1334	17000	0.016609	8500	2200	Tivey et al., 1999; Geological Survey of Canada, unpublished data
ALV2464-R6-2c	54	<100	250	1	28.4	0.0826	6200	0.035211	3100	2200	Tivey et al., 1999; Geological Survey of Canada, unpublished data
ALV2464-R8-1b	45	<100	370	0.51	10.2	0.2268	11000	0.05	846.1538	2200	Tivey et al., 1999; Geological Survey of Canada, unpublished data
Gabriels Trumpet (chimney)				4.83	0.265	0.0092	71	18.22642	0.525926	3100	Bogdanov et al., 1995
Saracens Head (subsamples)				8.43	4.65	0.007	306	1.812903	1.832335	3100	Bogdanov et al., 1995
Saracens Head (main body of chimney)				17.3	0.155	0.0145	113	111.6129	0.220273	3100	Bogdanov et al., 1995
Dragon (chimney)				1.64	0.0022	0.0017	200	745.4545	0.465116	3100	Bogdanov et al., 1995
BX16 (main body of chimney)				0.12	5.22	0.174	286	0.022989	2.948454	3100	Bogdanov et al., 1995
BX16 (base)				1.26	8	0.0528	290	0.1575	5.471698	3100	Bogdanov et al., 1995
NWBX16 (main body of chimney)				0.75	8.5	0.043	213	0.088235	7.344828	3100	Bogdanov et al., 1995
Wasps nest (main body of chimney)				5.55	8.41	0.0602	410	0.659929	0.863158	3100	Bogdanov et al., 1995

SAMPLE	Se ppm	Sn ppm	Sr ppm	Cu wt.%	Zn wt.%	Pb wt.%	Ba ppm	Cu/Zn	Ba/Co	Depth (mbsl)	Reference
ALV2624-1-1	<3	<100	174	0.0785	0.1373	9.00E-04		0.571741		3100	TU Freiberg, unpublished data; Hannington et al., 2004; Toffolo et al. 2020
ALV2624-3-2	240	<100	226	4.8041	0.0332	9.00E-04		144.7018		3100	TU Freiberg, unpublished data; Toffolo et al. 2020
ALV2624-3-4A	280	<100	367	5.0644	0.0337	<0.0005		150.2789		3100	TU Freiberg, unpublished data; Toffolo et al. 2020
ALV2624-3-4B	200	<100	47	2.3019	8.6283	0.0478		0.266785		3100	TU Freiberg, unpublished data; Toffolo et al. 2020
ALV2624-3-5A	31	<100	76	0.4482	2.4035	0.042		0.186478		3100	TU Freiberg, unpublished data; Toffolo et al. 2020
ALV2624-3-5B	21	<100	33	0.533	9.3002	0.0759		0.057311		3100	TU Freiberg, unpublished data; Toffolo et al. 2020
ALV2625-3-12	1250	<100	230	15	0.1957	<0.0005		76.64793		3100	TU Freiberg, unpublished data; Toffolo et al. 2020
ALV2625-4-1	350	<100	1990	6.0785	0.4112	0.003	80	14.78234	0.808081	3100	TU Freiberg, unpublished data; Toffolo et al. 2020
ALV2625-4-4	130	<200	27	1.2596	5.5929	0.072		0.225214		3100	TU Freiberg, unpublished data; Toffolo et al. 2020
ALV2625-4-5A	76	<200	5	0.7884	15	0.053		0.05256		3100	TU Freiberg, unpublished data; Toffolo et al. 2020
ALV2625-4-5B	140	<100	140	2.2944	2.3115	0.0184		0.992602		3100	TU Freiberg, unpublished data; Toffolo et al. 2020
ALV2625-4-7	350	<100	22	8.9673	1.9559	0.0387	200	4.584744	0.909091	3100	TU Freiberg, unpublished data; Toffolo et al. 2020
ALV2625-4-9A	250	<100	2124	4.8134	0.2046	0.0012		23.5259		3100	TU Freiberg, unpublished data; Toffolo et al. 2020
ALV2625-4-9B	580	<100	494	15	0.1656	<0.0005		90.57971		3100	TU Freiberg, unpublished data; Toffolo et al. 2020
4334_2							0			3100	Lisitsyn et al., 1999
3434-50				5.3	6	0.0315	227	0.883333		3100	Peresypkin et al., 1999
4796 2/2 intern.	136.2			3.71	12.2	0.0363	0	0.304098		3100	Bogdanov et al. (2008)
4796 2/2 extern.	187.6			12.3	4.7	0.0047	0	2.617021		3100	Bogdanov et al. (2008)
4796-2 basal part	22.2			0.73	14.1	0.0416	0	0.051773		3100	Bogdanov et al. (2008)
4796-2 upper part	35			0.65	5.88	0.0065	0	0.110544		3100	Bogdanov et al. (2008)

SAMPLE	Se ppm	Sn ppm	Sr ppm	Cu wt.%	Zn wt.%	Pb wt.%	Ba ppm	Cu/Zn	Ba/Co	Depth (mbsl)	Reference
4793-1/3 middle part	13.7			0.76	13.1	0.166	0	0.058015		3100	Bogdanov et al. (2008)
4796-3 internal Cu pipe	178			27.7	0.33	9.70E-04	0	83.93939		3100	Bogdanov et al. (2008)
4796-3 extern.	427.7			30	0.25	-	0	120		3100	Bogdanov et al. (2008)
4797-3 base of the Spire mound	134.9			12.6	3.48	0.0043	0	3.62069		3100	Bogdanov et al. (2008)
4796-5 sulfide pipe	127.4			22.7	0.65	0.0025	0	34.92308		3100	Bogdanov et al. (2008)
4797-3 central part	159.9			6.05	4.45	0.0065	0	1.359551		3100	Bogdanov et al. (2008)
4797-7 cornice	44.5			1.49	5.78	0.02	0	0.257785		3100	Bogdanov et al. (2008)
4797-8 central diffuser	57.7			2.03	0.52	0.0026	0	3.903846		3100	Bogdanov et al. (2008)
4797-9 Fe–Mn crown	80.9			4.9	1.2	0.013	0	4.083333		3100	Bogdanov et al. (2008)
SH1-DR3-2-3	<3	2	1	0.25	0.0124	<0.0003	8	20.16129	0.004762	2320	Marques et al 2007
SH1-DR3-2-1	<3	2	7	2.98	0.1152	<0.0003	72	25.86806	0.041618	2320	Marques et al 2007
IR-DR-01-C-01	134	<1	1	19.78	0.1757	6.00E-04	4	112.5783	0.001423	2320	Marques et al 2007
IR-DR-01-G-02	139	6	<1	22.18	0.0394	0.0109	3	562.9442	9.62E-04	2320	Marques et al 2007
SH1-DR3-1-2	42	6	2	27.98	0.0672	0.004	15	416.369	0.003145	2320	Marques et al 2007
IR96-3	<3	31	<1	8.35	5.122	0.0065	9	1.630223	0.001429	2320	Marques et al 2007
LOG7-6				33.17	0.2	0.015	360	165.85	1.8	3050	Krasnov et al., 1995; Mozgova et al., 1999
LOG7-2				48.36	0.24	0.04	590	201.5	2.95	3050	Krasnov et al., 1995; Mozgova et al., 1999
LOG7-12				22.22	0.11	0.04	5300	202	26.5	3050	Krasnov et al., 1995; Mozgova et al., 1999
LOG7-101				32.49	0.32	0.022	0	101.5313		3050	Mozgova et al., 1999
LOG7-4				5.16	5.75	0.06	7100	0.897391	11.83333	3050	Krasnov et al., 1995; Mozgova et al., 1999
LOG7-3				8.62	1.15	0.05	6930	7.495652	23.1	3050	Krasnov et al., 1995; Mozgova et al., 1999

SAMPLE	Se ppm	Sn ppm	Sr ppm	Cu wt.%	Zn wt.%	Pb wt.%	Ba ppm	Cu/Zn	Ba/Co	Depth (mbsl)	Reference
LOG7-13				6.66	1.05	0.015	360	6.342857	1.8	3050	Krasnov et al., 1995; Mozgova et al., 1999
LOG7-9				8.35	2.1	0.05	5400	3.97619	9	3050	Krasnov et al., 1995; Mozgova et al., 1999
3453-5				29.9	0.48	<0.010	820	62.29167	3.416667	3050	Bogdanov et al., 1997
3453-7				13.6	2.47	0.012	270	5.506073	0.137755	3050	Bogdanov et al., 1997
3453-8				27.5	6.52	0.049	350	4.217791	0.324074	3050	Bogdanov et al., 1997
3453-9				34	16	0.018	1570	2.125	2.492063	3050	Bogdanov et al., 1997
3453-10				8.3	18.7	0.034	8750	0.44385	6.835938	3050	Bogdanov et al., 1997
3454-1				35.5	<0.01	<0.010	300		1.2	3050	Bogdanov et al., 1997
3454-3				23.2	5.12	<0.010		4.53125		3050	Bogdanov et al., 1997
3454-4				12.9	13.5	0.05	1080	0.955556	3.085714	3050	Bogdanov et al., 1997
3453-3							0			3050	Lisitsyn et al., 1999
3453-5							0			3050	Lisitsyn et al., 1999
3453-7							0			3050	Lisitsyn et al., 1999
3453-8							0			3050	Lisitsyn et al., 1999
3453-10							0			3050	Lisitsyn et al., 1999
3454-2							0			3050	Lisitsyn et al., 1999
3453-6			400	0.18	0.028	0.0063		6.428571		3050	Peresypkin et al., 1999
3453-7				13.6	2.47	0.012	270	5.506073	0.137755	3050	Peresypkin et al., 1999
3453-9				34	16	0.019	1570	2.125	2.492063	3050	Peresypkin et al., 1999
3453				23.2	5.12	<0.010		4.53125		3050	Peresypkin et al., 1999
Logatchev-4-72-m Cu-Zone				45.5	0.39	0.02	400	116.6667	4	3050	Mozgova et al., 1999
Logatchev-4-72-b				21.68	0.22	0.02	400	98.54546	3.333333	3050	Mozgova et al., 1999
Logatchev-5-142-m				38.89	0.08	0.05	200	486.125	4	3050	Mozgova et al., 1999
Logatchev-5-142-b				16.7	0.18	0.02		92.77778		3050	Mozgova et al., 1999
Logatchev-1-6-m				43.25	0.05	0.02		865		3050	Mozgova et al., 1999
Logatchev-1-2-c				42.25	0.08	0.02		528.125		3050	Mozgova et al., 1999

SAMPLE	Se ppm	Sn ppm	Sr ppm	Cu wt.%	Zn wt.%	Pb wt.%	Ba ppm	Cu/Zn	Ba/Co	Depth (mbsl)	Reference
Logatchev-1-12-m				0.08	0.04	0.04	30000	2	937.5	3050	Mozgova et al., 1999
Logatchev-1-12-b				11.55	0.05	0.03	4400	231	209.5238	3050	Mozgova et al., 1999
Logatchev-1-140-m				59.36	0.58	0.02		102.3448		3050	Mozgova et al., 1999
Logatchev-1-140-b				18.48	0.59	0.02	100	31.32203	0.208333	3050	Mozgova et al., 1999
Logatchev-1-121-m				47.63	0.06	<0.010	0	793.8333		3050	Mozgova et al., 1999
Logatchev-1-121-b				39.1	0.04	<0.010	100	977.5	0.333333	3050	Mozgova et al., 1999
Logatchev-1-119-c Zn-Zone				0.36	27.5	0.21	1500	0.013091	3.125	3050	Mozgova et al., 1999
Logatchev-1-101-c				50.91	0.46	<0.010		110.6739		3050	Mozgova et al., 1999
Logatchev-1-101-m				5.86	0.23	0.028	1600	25.47826	2.580645	3050	Mozgova et al., 1999
Logatchev-1-101-b				27.02	0.97	0.013	0	27.85567		3050	Mozgova et al., 1999
Logatchev-1-4-c(1) Fe-Zn-Zone				2.75	11.78	0.06	1100	0.233447	2.682927	3050	Mozgova et al., 1999
Logatchev-1-4-c(2)				39	1.97	0.02		19.79695		3050	Mozgova et al., 1999
Logatchev-1-3-m				10.55	7.75	0.05	5200	1.36129	28.88889	3050	Mozgova et al., 1999
Logatchev-2-13-m(1)				10.85	0.02	0.03	700	542.5	5	3050	Mozgova et al., 1999
Logatchev-2-13-m(2)				1.6	0.03	0.03		53.33333		3050	Mozgova et al., 1999
Logatchev-2-13-c				28.1	0.18	0.03	4400	156.1111	47.82609	3050	Mozgova et al., 1999
Logatchev-3-9-c				27.75	8.55	0.04		3.245614		3050	Mozgova et al., 1999
Logatchev-3-9-m				10.26	0.11	0.04	300	93.27273	0.214286	3050	Mozgova et al., 1999
MS18-05	540	100	1085	29.9	<0.10	<0.005	0			3050	Murphy and Meyer, 1998
MS18-06	908	125		34.3	0.36	<0.005	0	95.27778		3050	Murphy and Meyer, 1998
MS21-06a	1108			56.2	<0.10	0.006	0			3050	Murphy and Meyer, 1998
MS19-09	1255	75	30	40.56	0.25	<0.005	0	162.24		3050	Murphy and Meyer, 1998
MS18-10A	915	55	635	29.2	<0.10	<0.005	0			3050	Murphy and Meyer, 1998
MS18-10b	3			0.36	<0.10	<0.005	0			3050	Murphy and Meyer, 1998
MS21-08A	1505	48		35.95	<0.10	<0.005	0			3050	Murphy and Meyer, 1998
MS21-10	567	320	32	30.1	1.81	0.015	0	16.62983		3050	Murphy and Meyer, 1998

SAMPLE	Se ppm	Sn ppm	Sr ppm	Cu wt.%	Zn wt.%	Pb wt.%	Ba ppm	Cu/Zn	Ba/Co	Depth (mbsl)	Reference
MS19-9	310	180		35.9	0.12	<0.005	0	299.1667		3050	Murphy and Meyer, 1998
MS20-01	105	920	290	4.93	24.1	0.384	0	0.204564		3050	Murphy and Meyer, 1998
MS21-03A	915	410	170	32.05	<0.10	<0.005	0			3050	Murphy and Meyer, 1998
MS21-03B	625	1675	465	23.2	<0.10	<0.005	0			3050	Murphy and Meyer, 1998
MS21-04	15		1250	6.9	2.35	0.0055	0	2.93617		3050	Murphy and Meyer, 1998
MS21-07	575	245		33.03	<0.10	0.014	0			3050	Murphy and Meyer, 1998
ALV1683-1-1a	114	6	5	1.78	0.63	0.01	50	2.825397	0.46729	3500	Hannington, 1989; Hannington et al., 1991b
ALV1683-1-1b	363	9	439	5.8	0.69	0.005	50	8.405797	0.387597	3500	Hannington, 1989; Hannington et al., 1991b
ALV1683-1-2	227		1001	3.54	0.86	0.006	50	4.116279	0.393701	3500	Hannington, 1989; Hannington et al., 1991b
ALV1683-3-1	120	1	7	0.81	0.12	0.015	20	6.75	0.555556	3500	Hannington, 1989; Hannington et al., 1991b
ALV1683-4-1a	115	13	2	1.71	6.3	0.049	50	0.271429	6.25	3500	Hannington, 1989; Hannington et al., 1991b
ALV1683-4-1b	136	7	7	2	2	0.016	50	1	0.5	3500	Hannington, 1989; Hannington et al., 1991b
ALV1683-5-1	0.1	39	10	2.1	4.44	0.113	66	0.472973	33	3500	Hannington, 1989; Hannington et al., 1991b
ALV1683-6-1	12	6	2	0.08	0.49	0.02	19	0.163265	0.260274	3500	Hannington, 1989; Hannington et al., 1991b
ALV1683-8-1	1	35		0.76	23.84	0.68	13	0.031879	1.857143	3500	Hannington, 1989; Hannington et al., 1991b
ALV1683-8-1a	26			0.76	13.15		50	0.057795	7.142857	3500	Hannington, 1989; Hannington et al., 1991b
ALV1683-8-1a	23				13.1		50		8.333333	3500	Hannington, 1989; Hannington et al., 1991b
ALV1683-8-1a	22				13.52		50		8.333333	3500	Hannington, 1989; Hannington et al., 1991b
ALV1683-9-1	50	6	15	1.07	2.29	0.02	16	0.467249	0.216216	3500	Hannington, 1989; Hannington et al., 1991b
CY87-5-1	4				0.02		50		16.66667	3500	Hannington et al., 1991b

SAMPLE	Se ppm	Sn ppm	Sr ppm	Cu wt.%	Zn wt.%	Pb wt.%	Ba ppm	Cu/Zn	Ba/Co	Depth (mbsl)	Reference
CY87-5-2	0.1				17.69		50		5.555556	3500	Hannington, 1989; Hannington et al., 1991b
CY87-5-6	193				2.23		50		0.746269	3500	Hannington, 1989; Hannington et al., 1991b
CY87-11-8	262				0.06		50		0.052083	3500	Hannington, 1989; Hannington et al., 1991b
CY87-6-6							0			3500	Hannington, 1989
HS5-4	150	<10	822	2.64	1.54	0.0144	0	1.714286		3500	Fouquet et al., 1993
HS11-1	366	<10	195	8.05	5.18	0.0596	0	1.554054		3500	Fouquet et al., 1993
HS10-1	159	32	<10	2.46	11.33	0.0705	0	0.217123		3500	Fouquet et al., 1993
HS5-2	1	12	23	0.15	22.43	0.268	0	0.006687		3500	Fouquet et al., 1993
HS8-1	72	21	<10	1.08	5.2	0.0189	0	0.207692		3500	Fouquet et al., 1993
HS11-2	149	<10	<10	2.31	0.08	0.0053	0	28.875		3500	Fouquet et al., 1993
HS3-1	44	13	<10	1.46	9.73	0.134	0	0.150051		3500	Fouquet et al., 1993
HS3-3	145	13	<10	1.92	5.93	0.0368	0	0.323777		3500	Fouquet et al., 1993
HS3-4	48	16	<10	1.21	11.44	0.0388	0	0.105769		3500	Fouquet et al., 1993
HS3-4b	64	25	<10	1.33	9.94	0.0423	0	0.133803		3500	Fouquet et al., 1993
HS5-6	273	16	23	4.11	7.41	0.0806	0	0.554656		3500	Fouquet et al., 1993
HS8-2	125	21	<10	2.1	11.06	0.0891	0	0.189873		3500	Fouquet et al., 1993
HS10-2	162	19	<10	2.04	8.75	0.0532	0	0.233143		3500	Fouquet et al., 1993
HS10-3	292	25	<10	5.64	12.61	0.0883	0	0.447264		3500	Fouquet et al., 1993
HS10-5a	106	31	<10	1.56	9.1	0.0726	0	0.171429		3500	Fouquet et al., 1993
HS10-5b	234	<10	<10	3.28	1.82	0.0212	0	1.802198		3500	Fouquet et al., 1993
HS10-6	6	53	<10	0.27	18.5	0.1395	0	0.014595		3500	Fouquet et al., 1993
HS11-5	48	47	40	1.13	12.71	0.0316	0	0.088906		3500	Fouquet et al., 1993
HS5-3	222	28	<10	5.52	0.25	0.0169	0	22.08		3500	Fouquet et al., 1993
HS5-5	2	<10	<10	0.03	0.21	0.0173	0	0.142857		3500	Fouquet et al., 1993
HS6-5	5	25	<10	0.07	1.15	0.0323	0	0.06087		3500	Fouquet et al., 1993
HS5-1	21	<10	<10	0.08	0.13	0.0127	0	0.615385		3500	Fouquet et al., 1993

SAMPLE	Se ppm	Sn ppm	Sr ppm	Cu wt.%	Zn wt.%	Pb wt.%	Ba ppm	Cu/Zn	Ba/Co	Depth (mbsl)	Reference
HS11-3a	5	84	<10	22.42	0.11	0.0226	0	203.8182		3500	Fouquet et al., 1993
HS11-3b	140	92	<10	24.89	0.23	0.014	0	108.2174		3500	Fouquet et al., 1993
HS11-6	410	18	<10	27.33	0.38	0.0034	0	71.92105		3500	Fouquet et al., 1993
HS11-8	527	<10	<10	28.37	0.08	<0.002	0	354.625		3500	Fouquet et al., 1993
HS6-6b-4	5	43	90	37.07	0.63	0.026	0	58.84127		3500	Fouquet et al., 1993
HS6-6b	6	63	<10	52.54	2.57	0.0448	0	20.44358		3500	Fouquet et al., 1993
HS6-6b-5	6	72	<10	54.43	4.04	0.048	0	13.47277		3500	Fouquet et al., 1993
HS6-6a	8	48	1860	27.32	0.96	0.0403	0	28.45833		3500	Fouquet et al., 1993
HS6-6c	4	<10	395	0.26	0.79	0.0156	0	0.329114		3500	Fouquet et al., 1993
MIR 70		31		45.04	0.53	0.0055	0	84.98113		3500	Krasnov et al., 1995
MIR 71-1		29		30.8	0.13	3.00E-04	0	236.9231		3500	Krasnov et al., 1995
MIR 160		11		25	2.33	0.0032	0	10.72961		3500	Krasnov et al., 1995
MIR158-1				6.63	0.43		0	15.41861		3500	Krasnov et al., 1995
MIR 158-2		6		11	1.49	0.0064	0	7.38255		3500	Krasnov et al., 1995
MIR 159-3		71		0.88	22.13	0.17	0	0.039765		3500	Krasnov et al., 1995
MIR 98		17		1.46	4.2	0.026	0	0.347619		3500	Krasnov et al., 1995
MIR 83		3		0.17	0.08	0.009	0	2.125		3500	Krasnov et al., 1995
MIR 153		5		0.2	0.15	0.0061	0	1.333333		3500	Krasnov et al., 1995
MIR 159		10		0.84	2.33	0.0076	0	0.360515		3500	Krasnov et al., 1995
MIR 161		11		3.45	0.15	0.0022	0	23		3500	Krasnov et al., 1995
MIR 166		6		2.22	1.03	0.008	0	2.15534		3500	Krasnov et al., 1995
MIR 154		22		11.38	8	0.018	0	1.4225		3500	Krasnov et al., 1995
MIR 150		20		2.91	3.75	0.024	0	0.776		3500	Krasnov et al., 1995
MIR 152		15		5.07	6.44	0.024	0	0.787267		3500	Krasnov et al., 1995
MIR 156		25		2.36	4.82	0.027	0	0.489627		3500	Krasnov et al., 1995
MIR 172		16		1.9	4.2	0.028	0	0.452381		3500	Krasnov et al., 1995
MIR 149		17		1.73	1.21	0.01	0	1.429752		3500	Krasnov et al., 1995

SAMPLE	Se ppm	Sn ppm	Sr ppm	Cu wt.%	Zn wt.%	Pb wt.%	Ba ppm	Cu/Zn	Ba/Co	Depth (mbsl)	Reference
MIR 172-2		7		1	1.5	0.0083	0	0.666667		3500	Krasnov et al., 1995
MIR 173		9		1.01	2.53	0.014	0	0.399209		3500	Krasnov et al., 1995
MIR 95		7		0.13	0.24	0.013	0	0.541667		3500	Krasnov et al., 1995
MIR 155		4		0.19	0.22	0.0064	0	0.863636		3500	Krasnov et al., 1995
MIR 162-1		4		0.9	0.25	0.0054	0	3.6		3500	Krasnov et al., 1995
MIR 163		7		0.89	0.54	0.006	0	1.648148		3500	Krasnov et al., 1995
MIR 165		35		6.25	11.66	0.02	0	0.536021		3500	Krasnov et al., 1995
MIR 169		110		0.44	17.19	0.065	0	0.025596		3500	Krasnov et al., 1995
MIR 151-3		13		1.55	5.62	0.093	0	0.275801		3500	Krasnov et al., 1995
MIR 168		37		2.15	6.6	0.055	0	0.325758		3500	Krasnov et al., 1995
MIR 90		28		0.77	10.4	0.052	0	0.074038		3500	Krasnov et al., 1995
MIR 157-7				0.9	1.11		0	0.810811		3500	Krasnov et al., 1995
MIR 157-8		19		2.93	8.94	0.029	0	0.32774		3500	Krasnov et al., 1995
MIR 164		8		0.89	0.54	0.0055	0	1.648148		3500	Krasnov et al., 1995
ALV2192-1A	93		2100	1.4	0.34	0.0058	410	4.117647	8.039216	3500	Geological Survey of Canada, unpublished data; Hannington et al., 2004; Toffolo et al. 2020
ALV2192-3	190		10	2.6	6	0.037	170	0.433333		3500	Geological Survey of Canada, unpublished data; Hannington et al., 2004; Toffolo et al. 2020
ALV2192-3A	220		10	2.7	6.4	0.033	530	0.421875		3500	Geological Survey of Canada, unpublished data; Hannington et al., 2004; Toffolo et al. 2020
ALV2193-1-1E	420		700	8.5	0.62	0.0028	40	13.70968	0.181818	3500	Geological Survey of Canada, unpublished data; Hannington et al., 2004; Toffolo et al. 2020
ALV2193-1-1F	510		110	11	2.3	2.1	190	4.782609	0.798319	3500	Geological Survey of Canada, unpublished

SAMPLE	Se ppm	Sn ppm	Sr ppm	Cu wt.%	Zn wt.%	Pb wt.%	Ba ppm	Cu/Zn	Ba/Co	Depth (mbsl)	Reference
ALV2193-4-1A	<2		10	0.028	0.049	0.024	240	0.571429	48	3500	data; Hannington et al., 2004; Toffolo et al. 2020 Geological Survey of Canada, unpublished data; Hannington et al., 2004; Toffolo et al. 2020
ALV2193-5-1A	30		10	0.074	0.09	0.031	80	0.822222	0.178971	3500	Geological Survey of Canada, unpublished data; Hannington et al., 2004; Toffolo et al. 2020
ALV2193-6-1A	15		10	0.59	2.7	0.002	40	0.218519	1.212121	3500	Geological Survey of Canada, unpublished data; Hannington et al., 2004; Toffolo et al. 2020
ALV2194-1A	300		1600	6	0.21	0.0058	40	28.57143	0.275862	3500	Geological Survey of Canada, unpublished data; Hannington et al., 2004; Toffolo et al. 2020
ALV2194-2-1A	140		1200	2.6	0.081	0.0089	40	32.09877	0.366972	3500	Geological Survey of Canada, unpublished data; Hannington et al., 2004; Toffolo et al. 2020
ALV2194-2-2A	99		2200	1.6	0.1	0.042		16		3500	Geological Survey of Canada, unpublished data; Hannington et al., 2004; Toffolo et al. 2020
ALV2194-2-2B	220		1600	4	0.31	0.034		12.90323		3500	Geological Survey of Canada, unpublished data; Hannington et al., 2004; Toffolo et al. 2020
ODP 106-649B-1-1	176		5	12.64	6.75		127	1.872593	0.2	3500	Honnorez et al., 1990
ODP 106-649B-1-2	184		5	12.31	6.14		204	2.004886	0.328502	3500	Honnorez et al., 1990
ODP 106-649B-1-3	188		30	12.61	6.25		21	2.0176	0.034884	3500	Honnorez et al., 1990

SAMPLE	Se ppm	Sn ppm	Sr ppm	Cu wt.%	Zn wt.%	Pb wt.%	Ba ppm	Cu/Zn	Ba/Co	Depth (mbsl)	Reference
ODP 106-649B-1-4	186		12	11.97	6.37		13	1.879121	0.016518	3500	Honnorez et al., 1990
ODP 106-649B-1-5	185		13	12.79	5.98		277	2.138796	0.461667	3500	Honnorez et al., 1990
ODP 106-649B-1-6	181		40	12.59	6.04		362	2.084437	0.459975	3500	Honnorez et al., 1990
ODP 106-649B-1-7	172		73	10.51	6.98		326	1.505731	0.514196	3500	Honnorez et al., 1990
ODP 106-649B-1-8	149		23	10.87	8.95		81	1.214525	0.15197	3500	Honnorez et al., 1990
ODP 106-649B-1D-5 (80-86)	263			5.5	2.22	0.035	0	2.477477		3500	Kase et al., 1990
ODP 106-649B-1D-7 (84-90)	266			6.07	2.81	0.033	0	2.160142		3500	Kase et al., 1990
ODP 106-649B-1D-8 (50-56)	351			7.15	1.92	0.035	0	3.723958		3500	Kase et al., 1990
ODP 106-649B-1D-8 (134-140)	249			5.68	2.55	0.034	0	2.227451		3500	Kase et al., 1990
ODP 106-649G-1D-1 (14-16_#4)				16.08	0.12	0.003	0	134		3500	Kase et al., 1990
17A-TVG7-1A1	263	<1	<2	35.2	0.3	<0.0005	13	117.3333	0.108333	2460	Wang et al. 2014
17A-TVG7-1A2	332	15	14	32.2	0.41	0.0016	24	78.53659	0.26087	2460	Wang et al. 2014
17A-TVG7-1B1	244	<1	2	36.4	0.04	<0.0005	9	910	0.006818	2460	Wang et al. 2014
17A-TVG7-1B2	200	31	7	31.7	0.16	0.0032	15	198.125	0.024311	2460	Wang et al. 2014
17A-TVG7-1C	278	<1	<2	38.3	0.5	<0.0005	10	76.6	0.060606	2460	Wang et al. 2014
17A-TVG7-1D	753	13	4	34	0.31	0.0012	12	109.6774	0.033898	2460	Wang et al. 2014
19III-TVG6-1	26	8	17	24.2	0.08	<0.0005	4	302.5	0.050633	2460	Wang et al. 2014
19III-TVG6-2	28	9	<2	25.9	0.08	<0.0005		323.75		2460	Wang et al. 2014
19III-TVG6-3-2	17	15	3	27.6	0.1	0.0021	14	276	2	2460	Wang et al. 2014
19III-TVG7-1	16	14	<2	23.1	0.02	<0.0005		1155		2460	Wang et al. 2014
19III-TVG7-2	8	10	3	22.9	0.02	8.00E-04	21	1145	0.617647	2460	Wang et al. 2014
17A-TVG9-1A	3	81	3	5.07	31.8	0.128	12	0.159434	0.020339	2460	Wang et al. 2014
17A-TVG9-1B	104	3	2	20.4	9.1	0.0346	18	2.241758	0.016822	2460	Wang et al. 2014

SAMPLE	Se ppm	Sn ppm	Sr ppm	Cu wt.%	Zn wt.%	Pb wt.%	Ba ppm	Cu/Zn	Ba/Co	Depth (mbsl)	Reference
17A-TVG9-1C	111	44	3	26.4	5.02	0.0194	15	5.258964	0.074627	2460	Wang et al. 2014
17A-TVG9-1D	35	245	5	1.02	35.2	0.184	9	0.028977	0.009978	2460	Wang et al. 2014
17A-TVG9-1E	3	4	11	0.52	0.1	0.0086	8	5.2	0.05298	2460	Wang et al. 2014
17A-TVG9	129	183	6	3.02	26.9	0.1733	21	0.112268	0.020076	2460	Wang et al. 2014
17A-TVG7-2	<3	<1	2	2.57	0.09	0.0017	22	28.55556	0.5	2460	Wang et al. 2014
17A-TVG7-3A	<3	<1	4	0.07	0.05	0.0118	17	1.4	1.214286	2460	Wang et al. 2014
17A-TVG7-3B	<3	1	3	0.37	0.05	0.0191		7.4		2460	Wang et al. 2014
17A-TVG7-3C2	<3	<1	3	1.37	0.04	0.0128		34.25		2460	Wang et al. 2014
19III-TVG7-3	4	7	8	5.4	0.48	<0.0005	24	11.25	0.242424	2460	Wang et al. 2014
19III-TVG7-4	<3	20	171	1.18	0.32	0.0372	561	3.6875	9.508475	2460	Wang et al. 2014
34II-TVG22-1–2	2	1.2		0.14	1.49	0.0084	0.7	0.09396	0.009198	1500	Liao et al. 2018
34II-TVG22-7	0.6	0.4		0.04	0.09	0.00189	0.6	0.444444	0.136364	1500	Liao et al. 2018
34II-TVG22-5	1.9	0.2		0.1	5.07	0.0141	1.8	0.019724	0.068441	1500	Liao et al. 2018
34II-TVG22-2	13.4	137		0.77	39.77	0.009	0.5	0.019361	0.003968	1500	Liao et al. 2018
34II-TVG22-1	0.9	3.4		0.1	0.7	0.0043	0.9	0.142857	0.04918	1500	Liao et al. 2018
34II-TVG22-3	2	1.8		0.11	4.43	0.0054	1.4	0.024831	0.084337	1500	Liao et al. 2018
34II-TVG22-4	1.9	1.2		0.14	4.72	0.0057	1	0.029661	0.033333	1500	Liao et al. 2018
34II-TVG22-6	1.9	8.8		0.22	1.26	0.0055	1.1	0.174603	0.026066	1500	Liao et al. 2018
39II-TVG04-2	12	1		0.49	0	4.90E-04	20		1.470588	1500	Liao et al. 2018
34II-TVG23-1H	3.4	1.1		0.09	1.94	0.0076	2	0.046392	0.031056	1500	Liao et al. 2018
21VII-TVG22-1	8.5	66.2		2.65	5.73	0.0043	2.2	0.462478	0.001705	1500	Liao et al. 2018
21VII-TVG22-2	7.6	205		2.96	29.89	0.0071	1.7	0.09903	0.004595	1500	Liao et al. 2018
21VII-TVG22-A-3	25	148		2.49	45.44	0.0029	8.7	0.054798	0.008753	1500	Liao et al. 2018
34II-TVG23-1	0.3	0.2		0.05	0.85	0.0067	1	0.058824	0.046296	1500	Liao et al. 2018
34II-TVG23-3	2.6	20		0.08	10	0.0144	0.5	0.008	0.006944	1500	Liao et al. 2018
34II-TVG23-4	0.4	0.2		0.02	0.63	0.0064	1.1	0.031746	0.041825	1500	Liao et al. 2018
21VII-TVG22-A	1	0.4		0.08	0.11	0.0049	6.4	0.727273	0.034225	1500	Liao et al. 2018

SAMPLE	Se ppm	Sn ppm	Sr ppm	Cu wt.%	Zn wt.%	Pb wt.%	Ba ppm	Cu/Zn	Ba/Co	Depth (mbsl)	Reference
21VII-TVG22-7	5.7	27.6		0.21	11.64	0.0127	9.7	0.018041	0.032398	1500	Liao et al. 2018
64	36	1.78	1560	3.36	0.031	4.02E-04	5.4	108.3871	0.033333	4957	Webber et al. 2015
67	348	9.23	1360	15.9	0.124	6.34E-04	9.79	128.2258	0.032633	4957	Webber et al. 2015
69	7.05	9.27	17.5	0.316	0.067	0.0206	19.8	4.716418	5.169713	4957	Webber et al. 2015
80	822	13	42.8	39.7	0.246	2.13E-04	51.8	161.3821	0.093333	4957	Webber et al. 2015
93	673	19.5	43.5	47.1	0.317	8.57E-04	0.269	148.5804	6.67E-04	4957	Webber et al. 2015
56	181	11.2	3.19	16.8	0.213	0.00276	4.76	78.87324	0.006271	4957	Webber et al. 2015
60	32.2	24.8	3.52	1.88	0.108	0.00815	0.73	17.40741	0.004424	4957	Webber et al. 2015
66	14.2	11.7	2.85	1.06	0.06	0.0054	1.02	17.66667	0.007338	4957	Webber et al. 2015
68	118	12.9	7.5	6.44	0.094	0.00142	0.178	68.51064	0.024087	4957	Webber et al. 2015
73		17	7.18	0.106	0.631	0.0562	0.781	0.167987	0.007299	4957	Webber et al. 2015
74	1.64	14.7	3.01	0.212	0.398	0.0276	0.654	0.532663	0.003593	4957	Webber et al. 2015
75	2.35	49.7	147	0.25	2.46	0.0123	3.03	0.101626	0.0303	4957	Webber et al. 2015
77	399	61.6	3.22	34.4	0.321	6.60E-04	0.273	107.1651	3.10E-04	4957	Webber et al. 2015
78	5.76	10.3	11	0.297	0.044	0.00842	0.908	6.75	0.004109	4957	Webber et al. 2015
79	6.02	39.6	1.54	0.086	0.059	0.00903	0.283	1.457627	0.003337	4957	Webber et al. 2015
81	1.97	9.62	30.8	0.325	0.261	0.0114	2.55	1.245211	1.401099	4957	Webber et al. 2015
82	2	4.23	3.05	0.239	0.255	0.00856	0.368	0.937255	0.003257	4957	Webber et al. 2015
88	16.4	193	40.7	1.3	7.35	0.0156	1.22	0.176871	0.011509	4957	Webber et al. 2015
89	93.6	1.28	2.02	12.7	0.109	3.07E-04	0.286	116.5138	0.003886	4957	Webber et al. 2015
92	16.6	6.35	2.78	0.761	0.063	0.0127	3.67	12.07937	0.003892	4957	Webber et al. 2015
94	4.13	14.3	15.9	0.162	0.186	0.0174	1.37	0.870968	0.021677	4957	Webber et al. 2015
58	64.2	321	2.06	4.15	9.12	0.0744	0.182	0.455044	7.62E-04	4957	Webber et al. 2015
61	43.5	77.4	4.19	2.72	3.75	0.0166	0.086	0.725333	0.00259	4957	Webber et al. 2015
62	24.4	29.4	3.45	1.52	9.08	0.144	0.238	0.167401	0.001178	4957	Webber et al. 2015
63		127	2.01	1.24	7.19	0.0516	0.223	0.172462	0.005272	4957	Webber et al. 2015
71	2.54	747	5.62	0.603	14.6	0.0839	16.4	0.041301	1.755889	4957	Webber et al. 2015

SAMPLE	Se ppm	Sn ppm	Sr ppm	Cu wt.%	Zn wt.%	Pb wt.%	Ba ppm	Cu/Zn	Ba/Co	Depth (mbsl)	Reference
72	41.4	145	2.92	2.09	6.57	0.0733	0.227	0.318113	5.43E-04	4957	Webber et al. 2015
87	39.6	68.7	3.05	2.73	0.782	0.0347	0.092	3.491049	1.65E-04	4957	Webber et al. 2015
90	9.1	195	4690	0.59	12.9	0.116	8.74	0.045736	0.317818	4957	Webber et al. 2015
ALV1675-1	474		761	31.77	0.11		50	288.8182	0.202429	3670	Hannington et al. 1991
ALV1675-1	396		6		0.06		50		0.352113	3670	Hannington et al. 1991
ALV1675-11	297				0.19		50		0.172414	3670	Hannington et al. 1991
ALV1675-3	146			9.66	0.08	0.005	50	120.75	0.242718	3670	Hannington et al. 1991
ALV1675-4	153			6.84	0.03	0.005	50	228	0.344828	3670	Hannington et al. 1991
ALV1676-1-3	1				60.51		0			3670	Hannington et al. 1991
ALV1676-2-5	122		14	16.42	1.21	0.015	11	13.57025	0.008012	3670	Hannington et al. 1991
ALV1676-2-7	15			2.19	3.29	0.02	50	0.665653	0.02713	3670	Hannington et al. 1991
ALV1676-5-12	1			8.07	3.27	0.01	50	2.46789	1.041667	3670	Hannington et al. 1991
ALV1676-5-13	1			5.83	51.54	0.06	50	0.113116	0.5	3670	Hannington et al. 1991
ALV1676-6-15B avg3	1			8.6	51.71	0.03	8	0.166312	0.078176	3670	Hannington et al. 1991
ALV1676-6-15T	6		18		26.31	0.016	16		0.253968	3670	Hannington et al. 1991
ALV1677-1-1	2			0.68	2.27	0.03	50	0.299559	0.42735	3670	Hannington et al. 1991
ALV1677-2-1	4				0.01		50		7.142857	3670	Hannington et al. 1991
ALV2183-9-1A	10		130	17.6	0.38	0.015	350	46.31579	17.5	3670	Hannington et al., 1993; GSC unpubl. data
ALV2179-4	630		160	23.5	0.041	0.001	70	573.1707	0.660377	3670	Hannington et al., 1993; GSC unpubl. data
ALV2190-14-1C	1		10	0.46	57.9	0.11	15	0.007945	15	3670	Hannington et al., 1993; GSC unpubl. data
ALV2190-14-1D avg2	4		10	0.7	54.5	0.076	15	0.012844	15	3670	Hannington et al., 1993; GSC unpubl. data
ALV2190-14-1E	1		10	0.34	57.1	0.11	500	0.005954	500	3670	Hannington et al., 1993; GSC unpubl. data
ALV2190-14-1F	1		10	0.63	57.7	0.055	140	0.010919	140	3670	Hannington et al., 1993; GSC unpubl. data

SAMPLE	Se ppm	Sn ppm	Sr ppm	Cu wt.%	Zn wt.%	Pb wt.%	Ba ppm	Cu/Zn	Ba/Co	Depth (mbsl)	Reference
ALV2190-7-1A	5		10	15.9	1.1	0.015	15	14.45455	0.097403	3670	Hannington et al., 1993; GSC unpubl. data
ALV2189-4-1 pc1	2.5		10	0.01	0.01		90	1	9	3670	Petersen unpubl. Data
ALV2584-9	7		10	0.11	8.4	0.08	90	0.013095	11.25	3670	Petersen unpubl. Data
ALV2587-1	52		75	10.6	0.064		110	165.625	0.255814	3670	Petersen unpubl. Data
ALV2179-1-1A	34		10	2.5	0.81	0.014	160	3.08642	0.134454	3670	Hannington et al., 1993; Tivey et al., 1994
ALV2179-1-1B	52		10	23	0.37	0.0034	50	62.16216	0.26455	3670	Hannington et al., 1993; Tivey et al., 1994
ALV2179-2-2A	230		900	9.5	0.14	0.0034	30	67.85714	0.032967	3670	Hannington et al., 1993; Tivey et al., 1994
ALV2179-4-1-1	315		1600	10.8	0.083	0.001	230	130.1205	1.121951	3670	Hannington et al., 1993; Tivey et al., 1994
ALV2179-4-1-4	120		1900	3.96	0.023	0.001	15	172.1739	0.267857	3670	Hannington et al., 1993; Tivey et al., 1994
ALV2179-4-1A1	370		980	11.6	0.045	0.001	210	257.7778	1.603053	3670	Hannington et al., 1993; Tivey et al., 1994
ALV2179-4-1T1	390		1400	12.1	0.028	0.001	110	432.1429	2.340426	3670	Hannington et al., 1993; Tivey et al., 1994
ALV2181-1-1A2	160		1000	8.5	0.24	0.0031	40	35.41667	0.121212	3670	Hannington et al., 1993; Tivey et al., 1994
ALV2183-4-1A avg2	1		10	0.41	53.4	0.035	330	0.007678	330	3670	Hannington et al., 1993; Tivey et al., 1994
ALV2183-4-1B	1		10	0.51	51.9	0.03	120	0.009827	120	3670	Hannington et al., 1993; Tivey et al., 1994
ALV2183-4-1C	1		10	0.41	54.2	0.048	220	0.007565	220	3670	Hannington et al., 1993; Tivey et al., 1994
ALV2183-6-2A	8		10	1.7	6.6	0.031	30	0.257576	0.731707	3670	Hannington et al., 1993; Tivey et al., 1994
ALV2183-7-OA	10		1500	0.23	0.016	0.0022	15	14.375	1.153846	3670	Hannington et al., 1993; Tivey et al., 1994
ALV2187-1-1A1 avg3	1		10	0.63	51.6	0.0405	480	0.012209	480	3670	Hannington et al., 1993; Tivey et al., 1994
ALV2187-1-1A2	1		10	0.65	51.4	0.037	140	0.012646	140	3670	Hannington et al., 1993; Tivey et al., 1994

SAMPLE	Se ppm	Sn ppm	Sr ppm	Cu wt.%	Zn wt.%	Pb wt.%	Ba ppm	Cu/Zn	Ba/Co	Depth (mbsl)	Reference
ALV2187-1-1B avg2	1		10	0.43	41.2	0.06	145	0.010437	145	3670	Hannington et al., 1993; Tivey et al., 1994
ALV2187-1-1C avg3	1		10	1.4	56.3	0.016	110	0.024867	110	3670	Hannington et al., 1993; Tivey et al., 1994
ALV2187-1-4A	1		10	0.61	55.4	0.082	50	0.011011	50	3670	Hannington et al., 1993; Tivey et al., 1994
ALV2187-1-6A	1		10	0.54	54.8	0.1	15	0.009854	15	3670	Hannington et al., 1993; Tivey et al., 1994
ALV2189-5-2A	5		10	1.02	0.44	0.013	40	2.318182	0.449438	3670	Hannington et al., 1993; Tivey et al., 1994
ALV2190-11-1A avg2	1		10	0.61	55.1	0.037	450	0.011071	450	3670	Hannington et al., 1993; Tivey et al., 1994
ALV2190-11-1B	1		10	0.68	40.8	0.04	60	0.016667	60	3670	Hannington et al., 1993; Tivey et al., 1994
ALV2190-13-1A	1		10	0.35	17.9	0.038	60	0.019553	30	3670	Hannington et al., 1993; Tivey et al., 1994
ALV2190-14-1A avg2	1		10	0.61	57.4	0.08	15	0.010627	15	3670	Hannington et al., 1993; Tivey et al., 1994
ALV2190-14-1B avg2	1		10	0.38	49.9	0.08	15	0.007615	15	3670	Hannington et al., 1993; Tivey et al., 1994
ALV2190-8-1A	58		760	4.1	0.047	0.0022	60	87.23404	0.178042	3670	Hannington et al., 1993; Tivey et al., 1994
MIR 1902-11/1				1.8	0.048	0.001	0	37.5		3670	Lisitsyn et al., 1990
MIR 1902-11/2				0.26	0.0046	0.001	0	56.52174		3670	Lisitsyn et al., 1990
MIR 1902-11/3				8.8	0.09	0.027	0	97.77778		3670	Lisitsyn et al., 1990
MIR 1902-2/2				9.9	0.06	0.023	1000	165	2.631579	3670	Lisitsyn et al., 1990
MIR 1902-2/6						0.009	0			3670	Lisitsyn et al., 1990
MIR 1902-3/2				6.3	4	0.035	1200	1.575	1.2	3670	Lisitsyn et al., 1990
MIR 1902-5/1				0.4	29	0.045	1000	0.013793	3.333333	3670	Lisitsyn et al., 1990
MIR 1902-5/2				0.4	26.4	0.05	1000	0.015152	5	3670	Lisitsyn et al., 1990
MIR 1902-6/1				1.12	0.024	0.001	0	46.66667		3670	Lisitsyn et al., 1990
MIR 1902-6/2				8.6	0.05	0.023	0	172		3670	Lisitsyn et al., 1990
MIR 1902-6/3				1	0.0115	0.001	0	86.95652		3670	Lisitsyn et al., 1990

SAMPLE	Se ppm	Sn ppm	Sr ppm	Cu wt.%	Zn wt.%	Pb wt.%	Ba ppm	Cu/Zn	Ba/Co	Depth (mbsl)	Reference
MIR 1902-7				0.2	0.023	0.001	0	8.695652		3670	Lisitsyn et al., 1990
MIR 1902-8/1				15.3	0.04	0.018	0	382.5		3670	Lisitsyn et al., 1990
MIR 1902-8/2				2.6	0.24	0.026	0	10.83333		3670	Lisitsyn et al., 1990
MIR 1902-8/3				4.2	0.2	0.022	0	21		3670	Lisitsyn et al., 1990
MIR 1902-8/4				8.2	0.3	0.022	0	27.33333		3670	Lisitsyn et al., 1990
MIR 1902-9/1				8.8	0.5	0.031	1300	17.6	3.25	3670	Lisitsyn et al., 1990
MIR 2-75 /1	2.5		10	0.011	0.11	0.023	100	0.1	1.234568	3670	Petersen unpubl. Data
MIR sample - 1				35.33	0.4	0.015	0	88.325		3670	Krasnov et al., 1995
MIR sample - 2				0.43	5.32	0.022	0	0.080827		3670	Krasnov et al., 1995
MIR sample - 3				3.1	0.05	0.0055	0	62		3670	Krasnov et al., 1995
MIR sample - 4				4.74	0.32	0.0062	0	14.8125		3670	Krasnov et al., 1995
TG1-2	1				7.25		50		16.66667	3670	Hannington, 1989; Hannington et al. 1991
TG1-4A			1800	0.77	0.01	0.005	10	77		3670	Thompson et al. 1988
TG1-7B(1)			10	43.8	0.1	0.005	5	438		3670	Thompson et al. 1988
TG1-7B(2)				39.8	0.04	0.005	50	995		3670	Thompson et al. 1988
TG1-7C(2)			5	68.3	0.06	0.005	5	1138.333		3670	Thompson et al. 1988
TG1-8(2)			4300	0.1	6.65	0.01	700	0.015038		3670	Thompson et al. 1988
TG1-8A(1)			81	0.17	21.6	0.13	50	0.00787		3670	Thompson et al. 1988
TG1-10			2.5	0.09	2.78	0.1	50	0.032374		3670	Thompson et al. 1988
TG1-11(3)			3100	0.02	6.28	0.04	50	0.003185		3670	Thompson et al. 1988
TG1-12A			12	1.76	4.25	0.11	50	0.414118		3670	Thompson et al. 1988
TG1-13A(1)			2520	0.13	17.25	0.04	50	0.007536		3670	Thompson et al. 1988
TG1-14(2)			630	1.78	2.4	0.08	50	0.741667		3670	Thompson et al. 1988
TG1-16			4550	2.74	4.45	0.05	50	0.61573		3670	Thompson et al. 1988
TG1-26A(1)				32.5	1.5	0.02	50	21.66667		3670	Thompson et al. 1988
TG1-43(1)			800	0.29	0.47	0.02	10	0.617021		3670	Thompson et al. 1988

SAMPLE	Se ppm	Sn ppm	Sr ppm	Cu wt.%	Zn wt.%	Pb wt.%	Ba ppm	Cu/Zn	Ba/Co	Depth (mbsl)	Reference
TG1-43(4)				42.6	6.25	0.04	50	6.816		3670	Thompson et al. 1988
TG1-43(5)			17	2.35	1.09	0.1	50	2.155963		3670	Thompson et al. 1988
TG1-44				25	0.53	0.005	50	47.16981		3670	Thompson et al. 1988
TG1-36			20	0.08	1.55	0.005	5	0.051613		3670	Thompson et al. 1988
TG1-46(1)				39	0.64	0.02	50	60.9375		3670	Thompson et al. 1988
TG1-8	3.5	0.5		0.17	15.85	0.13	50	0.010726	25	3670	Hannington, 1989; Hannington et al. 1991
TG1-8	1				17.91		50		25	3670	Hannington, 1989; Hannington et al. 1991
TG1-10					2.13		50		100	3670	Hannington, 1989; Hannington et al. 1991
TG1-10	2	1	2.5		2.09		0			3670	Hannington, 1989; Hannington et al. 1991
TG1-10	1		3	0.07	2.01	0.1	24	0.034826	8	3670	Hannington, 1989; Hannington et al. 1991
TG1-11	1				15.14		0			3670	Hannington, 1989; Hannington et al. 1991
TG1-11	1				14.09		50		12.5	3670	Hannington, 1989; Hannington et al. 1991
TG1-12a	2				3.69		50		12.5	3670	Hannington, 1989; Hannington et al. 1991
TG1-15a	1		2976	0.22	13.91	0.05	500	0.015816	100	3670	Hannington, 1989; Hannington et al. 1991
TG1-16	2	0.5			3.17		0			3670	Hannington, 1989; Hannington et al. 1991
TG1-16					3.23		50		12.5	3670	Hannington, 1989; Hannington et al. 1991
TG1-21	1		1981	2.72	9.05	0.049	50	0.300552	10	3670	Hannington, 1989; Hannington et al. 1991
TG1-23	1		3639	2.52	11.71	0.025	50	0.215201	12.5	3670	Hannington, 1989; Hannington et al. 1991
TG1-24	1				16.67		50		12.5	3670	Hannington, 1989; Hannington et al. 1991
TG1-24	1				16.3		50		10	3670	Hannington, 1989; Hannington et al. 1991

SAMPLE	Se ppm	Sn ppm	Sr ppm	Cu wt.%	Zn wt.%	Pb wt.%	Ba ppm	Cu/Zn	Ba/Co	Depth (mbsl)	Reference
TG1-25b	1		28	0.36	11.09	0.034	50	0.032462	16.66667	3670	Hannington, 1989; Hannington et al. 1991
TG1-32c	1				5.6		50		12.5	3670	Hannington, 1989; Hannington et al. 1991
TG1-32c	1				6.15		50		12.5	3670	Hannington, 1989; Hannington et al. 1991
TG1-45	1	1	2.5	0.16	7.24	0.06	0	0.022099		3670	Hannington et al. 1991
TG1-45	1				7.14		50		25	3670	Hannington et al. 1991
TG1-45					7.29		50		10	3670	Hannington et al. 1991
TG1-45(2)			2.5	0.16	10.9	0.06	50	0.014679		3670	Thompson et al. 1988
ALV2178-1	1		26	0.002	0.042	0.001	390	0.047619	156	3670	Tivey et al., 1994; GSC unpubl. data
ALV2178-6-2A	4		59	0.018	0.02	0.001	610	0.9	101.6667	3670	Tivey et al., 1994; GSC unpubl. data
ALV2183-10-2A	6			0.099	0.085	0.0035	290	1.164706	17.05882	3670	Tivey et al., 1994
ALV2183-5-1A	1			0.0094	0.047	0.016	15	0.2	2.5	3670	Tivey et al., 1994
ALV2183-5-1B	1			0.001	0.022	0.022	15	0.045455	15	3670	Tivey et al., 1994
ALV2183-5-2(1)	2.5		10	0.017	0.019		10	0.894737	1	3670	Petersen unpubl. Data
ALV2183-5-2A	3			0.045	0.026	0.017	15	1.730769	1.875	3670	Tivey et al., 1994
ALV2189-2-1A			190	0.075	0.031	0.0022	90	2.419355	5.294118	3670	Tivey et al., 1994; GSC unpubl. data
ALV2190-12-1(A)	2.5		10	0.026	0.041		8	0.634146	1	3670	Petersen unpubl. Data
ALV2190-12-2A	1			0.009	0.071	0.044	110	0.126761	12.22222	3670	Tivey et al., 1994
ALV2583-3	2.5		10	0.0041	0.024		50	0.170833	12.5	3670	Petersen unpubl. Data
ALV2588-1	2.5		170	0.099	0.026		130	3.807692	13	3670	Petersen unpubl. Data
MIR 1-77 /1	2.5		10	0.012	0.0079		130	1.518987	21.66667	3670	Petersen unpubl. Data
TG1-18			65	0.1	0.32	0.05	50	0.3125		3670	Thompson et al. 1988
TG1-3(1)			58	0.16	0.62	0.02	0	0.258065		3670	Thompson et al. 1988
TG1-3(2)			45	0.21	0.49	0.09	0	0.428571		3670	Thompson et al. 1988
TG1-3(3)			38	0.57	0.96	0.09	0	0.59375		3670	Thompson et al. 1988

SAMPLE	Se ppm	Sn ppm	Sr ppm	Cu wt.%	Zn wt.%	Pb wt.%	Ba ppm	Cu/Zn	Ba/Co	Depth (mbsl)	Reference
TG1-39(2)			50	0.1	0.06	0.03	15	1.666667		3670	Thompson et al. 1988
TG1-43(2)			73	0.12	1.87	0.04	0	0.064171		3670	Thompson et al. 1988
1242 (S1)	1.00E-04		381	0.017	0.04	0.001	200	0.425	20	3670	Hannington 1989
1242-3	1.00E-04		408	0.012	0.04	0.001	500	0.3	38.46154	3670	Hannington 1989
1243-1	1.00E-04		277	0.004	0.01	0.001	100	0.4	6.666667	3670	Hannington 1989
1244-1-B	1.00E-04		300	0.016	0.01	0.001	0	1.6		3670	Hannington 1989
1247-1-1B	1.00E-04		425	0.01	0.01		200	1	6.451613	3670	Hannington 1989
ALV2188-3-1B			10	9.1	0.032	0.0031	15	284.375	0.013636	3670	GSC unpubl. Data
ALV2188-6-1			10	0.0068	0.022	0.0035	260	0.309091	52	3670	GSC unpubl. Data
ALV2195-1A			10	21.7	0.052	0.001	15	417.3077	0.065217	3670	GSC unpubl. Data
ALV2195-1B			10	20.1	0.035	0.001	15	574.2857	0.034091	3670	GSC unpubl. Data
MIR-3-76-3A	1		10	22.4	0.038	0.0027	15	589.4737	1.25	3670	Rona et al. 1993; GSC unpubl. data
MIR-3-76-3B	1		10	20.8	0.1	0.0029	15	208	1	3670	Rona et al. 1993; GSC unpubl. data
MIR-3-76-3BF	10		10	16	0.054	0.002	15	296.2963	1.25	3670	Rona et al. 1993; GSC unpubl. data
MIR-3-76-5Aavg2	1		10	0.53	21.85	0.0505	125	0.024256	19.23077	3670	Rona et al. 1993; GSC unpubl. data
MIR-3-76-5B	1		27	5.1	10.7	0.0026	90	0.476636	7.5	3670	Rona et al. 1993; GSC unpubl. data
MIR-3-76-6A	1		10	17.7	0.8	0.0026	30	22.125	3	3670	Rona et al. 1993; GSC unpubl. data
MIR-3-76-6B	1		10	11	22	0.001	15	0.5	1.25	3670	Rona et al. 1993; GSC unpubl. data
MIR-3-76-8-1	1		10	20.7	3.6	0.001	30	5.75	2.727273	3670	Rona et al. 1993; GSC unpubl. data
MIR-3-76-8-2	2		28	13.9	7.1	0.0044	40	1.957746	3.333333	3670	Rona et al. 1993; GSC unpubl. data

SAMPLE	Se ppm	Sn ppm	Sr ppm	Cu wt.%	Zn wt.%	Pb wt.%	Ba ppm	Cu/Zn	Ba/Co	Depth (mbsl)	Reference
MIR-3-76-8-3	1		25	8.5	7.6	0.004	100	1.118421	11.11111	3670	Rona et al. 1993; GSC unpubl. data
MIR-3-76-9A	2		10	15.5	0.35	0.0031	40	44.28571	4	3670	Rona et al. 1993; GSC unpubl. data
MIR-3-76-9B	1		10	17.8	0.19	0.0024	50	93.68421	3.571429	3670	Rona et al. 1993; GSC unpubl. data
MIR-3-76-10	1		10	26.8	0.08	0.014	30	335	2.307692	3670	Rona et al. 1993; GSC unpubl. data
sample 13		35		18.1	0.2	0.01	0	90.5		3670	Krasnov et al., 1995
sample 19		9		15.2	0.79	0.02	0	19.24051		3670	Krasnov et al., 1995
sample 7		23		12.75	0.34	0.015	0	37.5		3670	Krasnov et al., 1995
sample 5		47		9.28	1.54	0.017	0	6.025974		3670	Krasnov et al., 1995
sample 4		16		11.75	1.53	0.012	0	7.679739		3670	Krasnov et al., 1995
sample 20-1		4		2.4	7.55	0.06	0	0.317881		3670	Krasnov et al., 1995
sample 20-2		6		4.75	3.22	0.02	0	1.475155		3670	Krasnov et al., 1995
sample 6		30		1.21	15.05	0.025	0	0.080399		3670	Krasnov et al., 1995
sample 3		5		0.81	1.9	0.01	0	0.426316		3670	Krasnov et al., 1995
sample 16		3		0.12	0.96	0.06	0	0.125		3670	Krasnov et al., 1995
sample 14		13		0.45	0.14	0.005	0	3.214286		3670	Krasnov et al., 1995
sample 11-2		1		0.07	0.17	0.02	0	0.411765		3670	Krasnov et al., 1995
ALV2188-4-1A			410	6.4	0.51	0.001	430	12.54902	23.88889	3670	GSC unpubl. Data
sample 15		1		4.6	0.09	0.04	0	51.11111		3670	Krasnov et al., 1995
sample 18		1		8.3	0.66	0.005	0	12.57576		3670	Krasnov et al., 1995
sample 10		1		1.3	0.67	0.005	0	1.940299		3670	Krasnov et al., 1995
sample 11-1		1		3.1	0.63	0.005	0	4.920635		3670	Krasnov et al., 1995
ALV2599-9	1.5		10	5.7	0.14	0.0092	90	40.71429	9	3670	Petersen PhD thesis
ALV2599-10-7/1	2.5		10	0.57	0.46	0.0094	110	1.23913	4.782609	3670	Petersen PhD thesis
ALV2599-10-7/2	2.5		10	1.65	0.165	0.0081	100	10	5	3670	Petersen PhD thesis
ALV2599-11-2/1	2.5		10	0.12	0.31	0.0092	110	0.387097	5	3670	Petersen PhD thesis

SAMPLE	Se ppm	Sn ppm	Sr ppm	Cu wt.%	Zn wt.%	Pb wt.%	Ba ppm	Cu/Zn	Ba/Co	Depth (mbsl)	Reference
JL126-G04-1	<1	0.2		0.00842	0.679	0.107	212	0.012401	5.449871	3480	Wang et al. 2021
JL126-G04-2	<1	0.3		0.01	1.18	0.463	72	0.008475	1.142857	3480	Wang et al. 2021
JL126-G05-1	3	364		1.254216	11.04697	0.0753	2.6	0.113535	0.001605	3480	Wang et al. 2021
JL126-G05-2	16	1710		0.827	57.28354	0.189	1.3	0.014437	0.003403	3480	Wang et al. 2021
JL126-G09	16	1430		0.492	58.569	0.1785	1.2	0.0084	0.003738	3480	Wang et al. 2021
JL128-G03-1	16	1690		0.774	55.19466	0.21	4.3	0.014023	0.012321	3480	Wang et al. 2021
JL128-G03-2	15	1430		3.586897	48.60665	0.149	2	0.073794	0.002865	3480	Wang et al. 2021
JL128-G03-3	5	288		8.787499	7.38339	0.01875	0.01	1.190171	2.14E-06	3480	Wang et al. 2021
JL128-G06-1	16	1690		0.642	53.26646	0.0969	0.5	0.012053	0.002	3480	Wang et al. 2021
JL128-G06-2	17	2000		0.994	56.39978	0.1535	2	0.017624	0.005348	3480	Wang et al. 2021
JL128-G06-3	12	752		0.817	38.96566	0.1475	3.5	0.020967	0.006387	3480	Wang et al. 2021
33I-TVG18C-1	20	1400		1.27819	45.6332	0.159	0.03	0.02801	3.65E-05	3480	Wang et al. 2021
33I-TVG18C-3-1	20	1710		1.310144	50.53395	0.175	0.02	0.025926	2.68E-05	3480	Wang et al. 2021
33I-TVG18C-3-2	20	1420		0.695016	53.18517	0.224	0.03	0.013068	5.39E-05	3480	Wang et al. 2021
33I-TVG18C-5-1	20	1500		1.27819	48.76646	0.166	0.02	0.02621	2.51E-05	3480	Wang et al. 2021
33I-TVG18C-5-2	20	1610		0.766914	52.38177	0.199	0.02	0.014641	3.08E-05	3480	Wang et al. 2021
33I-TVG18C-7-1	20	1520		1.150371	44.0264	0.168	0.02	0.026129	1.68E-05	3480	Wang et al. 2021
33I-TVG18C-7-2	20	1600		0.758925	52.94415	0.174	0.02	0.014334	2.83E-05	3480	Wang et al. 2021
33I-TVG18C-9-1	10	1100		1.022552	33.50184	0.0991	0.02	0.030522	1.33E-05	3480	Wang et al. 2021
33I-TVG18C-9-2	20	1220		1.070484	48.76646	0.201	0.03	0.021951	2.86E-05	3480	Wang et al. 2021
33I-TVG18C-11-1	10	948		0.958642	30.04721	0.121	0.03	0.031905	1.65E-05	3480	Wang et al. 2021
33I-TVG18C-11-2	20	1450		1.118416	51.73905	0.214	0.03	0.021616	3.25E-05	3480	Wang et al. 2021
33I-TVG18C-12-1	10	880		0.91071	31.73435	0.152	0.02	0.028698	1.04E-05	3480	Wang et al. 2021
33I-TVG18C-12-2	20	1370		0.718982	55.03299	0.214	0.02	0.013065	2.87E-05	3480	Wang et al. 2021
33I-TVG18C-13-1	20	1470		0.846801	54.06891	0.208	0.02	0.015662	2.84E-05	3480	Wang et al. 2021
33I-TVG18C-14-2	20	1260		0.679038	54.47061	0.293	0.02	0.012466	2.30E-05	3480	Wang et al. 2021
33I-TVG18C-e	20	1430		0.742948	53.50653	0.264	0.01	0.013885	1.54E-05	3480	Wang et al. 2021

SAMPLE	Se ppm	Sn ppm	Sr ppm	Cu wt.%	Zn wt.%	Pb wt.%	Ba ppm	Cu/Zn	Ba/Co	Depth (mbsl)	Reference
33I-TVG18C-m	20	1600		1.294167	53.74755	0.172	0.01	0.024079	1.19E-05	3480	Wang et al. 2021
33I-TVG18C-i	20	1110		2.356662	36.07272	0.0966	0.03	0.065331	1.58E-05	3480	Wang et al. 2021
JL126-G08-1	2	183		4.561511	2.506657	0.025	2.6	1.819759	6.90E-04	3480	Wang et al. 2021
JL126-G08-2	2	213		4.729272	1.960334	0.03	1.3	2.412483	3.67E-04	3480	Wang et al. 2021
JL128-G04	3	87.8		6.798329	1.486319	0.00777	4.1	4.573937	0.001049	3480	Wang et al. 2021
JL128-G05	6	14.6		6.303034	1.189055	0.0284	36	5.300876	0.014815	3480	Wang et al. 2021
JL126-G01	3	8.9		3.666784	0.208	4.30E-04	1.1	17.62877	3.07E-04	3480	Wang et al. 2021
JL126-G03	5	5		6.870227	0.0511	2.10E-04	1.2	134.4467	3.02E-04	3480	Wang et al. 2021
JL126-G07	4	44.6		0.526	5.511431	0.213	11.8	0.095438	0.021416	3480	Wang et al. 2021
33I-TVG18-1-1	1	52		3.602897	1.430054	0.00499	0.03	2.519413	9.12E-06	3480	Wang et al. 2021
33I-TVG18-1-2	1	28		4.321879	0.931946	0.00307	0.03	4.63748	6.09E-06	3480	Wang et al. 2021
33I-TVG18-1-3	10	403		6.167265	13.57748	0.0658	0.02	0.454227	7.84E-06	3480	Wang et al. 2021
33I-TVG18-2-1	10	317		7.485398	13.8185	0.056	0.03	0.541694	5.68E-06	3480	Wang et al. 2021
33I-TVG18-2-2	10	392		2.995757	13.21595	0.0414	0.03	0.226677	8.31E-06	3480	Wang et al. 2021
M11-ROC1	69.9	1.1	407	2.45	0.554	0.0993	14200	4.422383	30.40685	1740	This study
M11-ROC2	346	4.2	24	25.6	0.593	0.0379	310	43.17032	1.377778	1740	This study
M11-ROC3	106	1.6	41	26.4	1.57	0.0306	2870	16.81529	60.42105	1740	This study
M11-ROC7	127	2.5	850	4.02	7.57	0.0489	19300	0.531044	57.27003	1740	This study
M11-ROC8	0.25	1.1	1040	1.52	37.4	0.0823	34500	0.040642	1045.455	1740	This study
PL1-1	0.25	0.9	5110	0.036	5.08	0.0541	381000	0.007087	44823.53	1740	This study
MOM2012-ROCK-PL3-1	0.25	0.6	1420	1.02	10.8	0.0502	112000	0.094444	2213.439	1740	This study
MOM14-PL579-ROC1	179	2.3	667	7.36	7.62	0.0454	23800	0.965879	222.4299	1740	This study
MOM14-PL583-ROC1-S	0.25	3.7	1150	5.4	1.01	0.0113	45200	5.346535	163.1769	1740	This study
MOM14-PL583-ROCK4A	131	5.3	97	5.09	2.49	0.0193	1760	2.044177	11.13924	1740	This study
MOM14-PL583-ROCK4B	150	3.3	20	11.4	1.53	0.0137	330	7.45098	1.27907	1740	This study

SAMPLE	Se ppm	Sn ppm	Sr ppm	Cu wt.%	Zn wt.%	Pb wt.%	Ba ppm	Cu/Zn	Ba/Co	Depth (mbsl)	Reference
MOM14-HN29008-ROCK	227	17.7	36	8.5	0.049	8.10E-04	10	173.4694	0.017889	1740	This study
MOM14-HT007-ROCK	385	2.2	132	5.25	0.098	0.00182	560	53.57143	6.451613	1740	This study
M15-603-7-Rock#5	42.6	3.5	239	1.41	27.6	0.0887	4960	0.051087	76.78019	1740	This study
MOM15-PL-603-7-R6	237	2.3	1700	10.1	0.614	0.0209	38300	16.44951	63.4106	1740	This study
M15-PL607-11-Rock#3-S	28.9	1	20	1.27	0.562	0.0354	270	2.259786	3.026906	1740	This study
PL-607-11-R5	907	5.9	23	13.5	0.22	0.0177	380	61.36364	0.929095	1740	This study
HT010-CR12	70.6	3	2100	2.41	2.12	0.023	7420	1.136792	73.46535	1740	This study
MOM13-PL7-Rock#1	0.25	1	2080	0.012	0.128	0.0746	99400	0.09375	2049.485	1740	This study
LS-BS-WHOI	490	2.3	1360	15.2	2.13	0.0201	32300	7.13615	163.1313	1740	This study
MOM13-PL12-Rock#1-S	0.25	1	737	0.0459	6.64	0.0716	12900	0.006913	914.8936	1740	This study
PL7-R2-S	2570	6.3	48	19.4	0.037	0.00199	950	524.3243	5.688623	1740	This study
M15-PL605-9-ROCK#2	0.25	1.7	5940	0.035	0.048	0.00313	444000	0.729167	60000	1740	This study
Ledge			8600	0.31	5.63	0.17	397000	0.055062		1740	Bogdanov et al. 2006
Chimney 1			1900	1.14	12.95	0.0505	149000	0.088031		1740	Bogdanov et al. 2006
Chimney 2			2593	1.95	1.71	0.029	91000	1.140351		1740	Bogdanov et al. 2006
4377_6			100	2.82	0.534	0.051		5.280899		1740	Bogdanov et al. 2006
4377_4			780	29.44	0.101	0.022		291.4851		1740	Bogdanov et al. 2006
4377_5			100	5.05	0.19	0.038		26.57895		1740	Bogdanov et al. 2006
4384_1			920	14.09	0.183	0.005		76.99454		1740	Bogdanov et al. 2006
4383_1			160	7.76	8.6	0.051		0.902326		1740	Bogdanov et al. 2006
4376_1a			120	6.78	0.093	0.057		72.90323		1740	Bogdanov et al. 2006
4376_1b			276	2.11	0.097	0.04		21.75258		1740	Bogdanov et al. 2006
4377_10-2			170	4.52	0.414	0.072		10.91787		1740	Bogdanov et al. 2006

SAMPLE	Se ppm	Sn ppm	Sr ppm	Cu wt.%	Zn wt.%	Pb wt.%	Ba ppm	Cu/Zn	Ba/Co	Depth (mbsl)	Reference
4377_10-4			160	8.79	0.292	0.048		30.10274		1740	Bogdanov et al. 2006
4379_2			122	3.38	0.094	0.048		35.95745		1740	Bogdanov et al. 2006
4383_3			130	6.93	0.234	0.036		29.61539		1740	Bogdanov et al. 2006
4383_4			40	6.03	0.02	0.024		301.5		1740	Bogdanov et al. 2006
4383_6			40	15.29	0.023	0.005		664.7826		1740	Bogdanov et al. 2006
4383_7			60	4.07	0.037	0.005		110		1740	Bogdanov et al. 2006
4383_2			2200	0.566	7.5	0.066		0.075467		1740	Bogdanov et al. 2006
4377_8			70	2.82	0.092	0.042		30.65217		1740	Bogdanov et al. 2006
4377_9			40	16.48	0.052	0.045		316.9231		1740	Bogdanov et al. 2006
4376_2-2			1800	1.66	1.46	0.04		1.136986		1740	Bogdanov et al. 2006
4376_2-3			1060	0.122	0.712	0.061		0.171348		1740	Bogdanov et al. 2006
4376_3			900	7.53	1.76	0.051		4.278409		1740	Bogdanov et al. 2006
4376_4			1600	0.1	9.2	0.068		0.01087		1740	Bogdanov et al. 2006
4379_1			2200	1.89	0.059	0.01		32.0339		1740	Bogdanov et al. 2006
4377_7-1			60	5.1	0.346	0.041		14.73988		1740	Bogdanov et al. 2006
4377_7-2			156	1.89	0.223	0.04		8.475336		1740	Bogdanov et al. 2006
4582-2			2130	0.0701	0.0969	0.0025	1800	0.723426	450	865	Bogdanov et al. 2005
4578-01-01			2130	0.0262	0.315	0.021	194000	0.083175	4731.707	865	Bogdanov et al. 2005
4578-01-02			2470	0.0168	0.293	0.0181	279000	0.057338	6804.878	865	Bogdanov et al. 2005
4578-01-06			1890	0.0199	0.119	0.0025	260000	0.167227	6341.463	865	Bogdanov et al. 2005
4574-03-02			630	2.33	0.0618	0.0121	135000	37.70227	75000	865	Bogdanov et al. 2005
4574-04-02			3190	1.09	0.29	0.0359	310000	3.758621	77500	865	Bogdanov et al. 2005
4592-03-04			2680	0.48	0.94	0.0303	376000	0.510638	94000	865	Bogdanov et al. 2005
4592-04-01			2220	0.06	1.34	0.0121	348000	0.044776	87000	865	Bogdanov et al. 2005
4594-1			630	0.0597	0.107	0.0715	301000	0.557944	75250	865	Bogdanov et al. 2005
4582-06-01			70	12.6	18.4	0.0448	250	0.684783	2.358491	865	Bogdanov et al. 2005
4582-06-02			60	15.7	8.07	0.024	250	1.945477	3.424658	865	Bogdanov et al. 2005

SAMPLE	Se ppm	Sn ppm	Sr ppm	Cu wt.%	Zn wt.%	Pb wt.%	Ba ppm	Cu/Zn	Ba/Co	Depth (mbsl)	Reference
4582-06-03			530	6.73	17.4	0.0092	30000	0.386782	731.7073	865	Bogdanov et al. 2005

Appendix 4 : Photomicrographs of hydrothermally cemented breccias (slabs) from Lucky Strike.

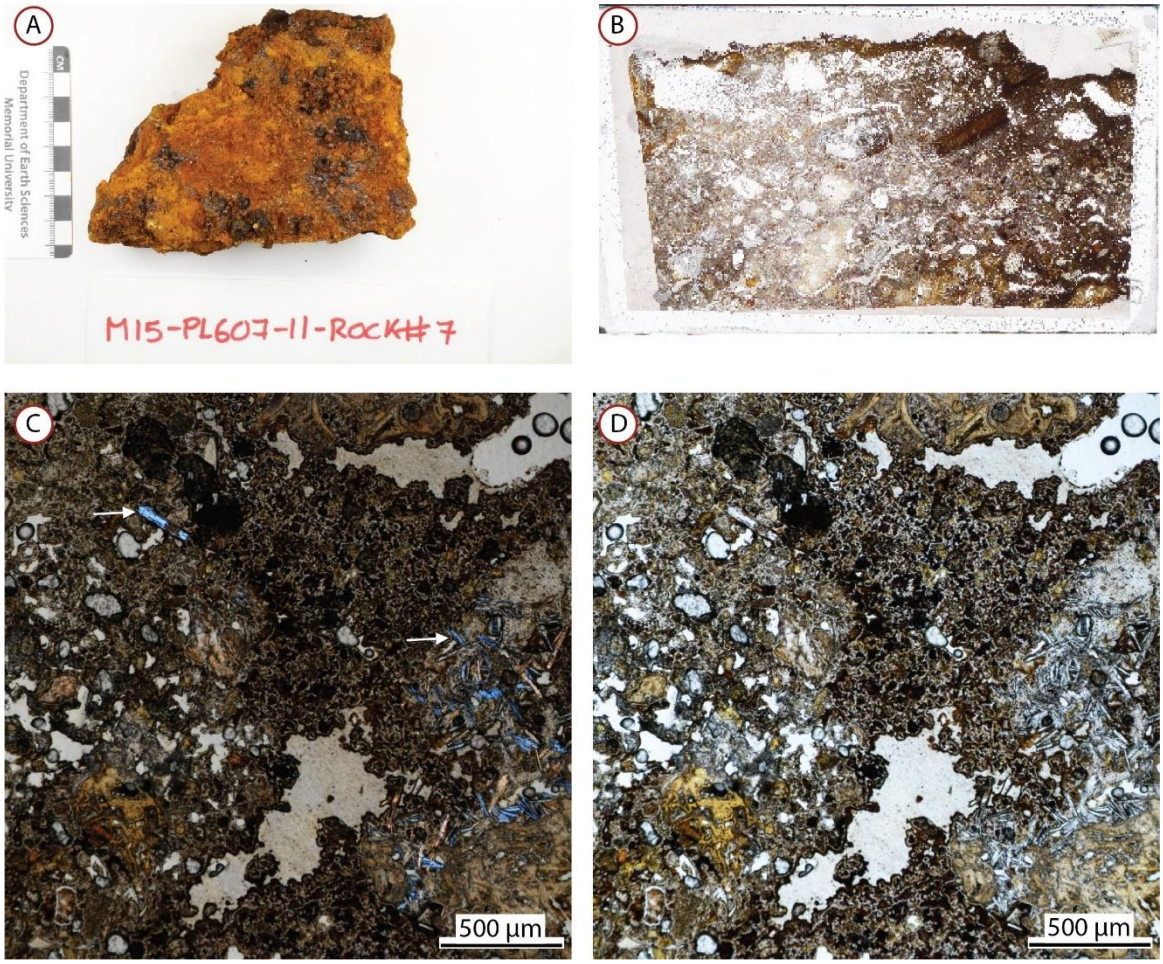

Figure A4.1. Sample MOM15-607-R7. 20 m SE from the Isabel site. Age: 6347 years. Volcaniclastic rock with barite infilling clasts on a hematitic groundmass. A) Hand sample. B) Whole thin section scan. C) Photomicrograph of sample on transmitted light (XPL), white arrows point to acicular barite. D) Photomicrograph of sample on transmitted light (PPL).

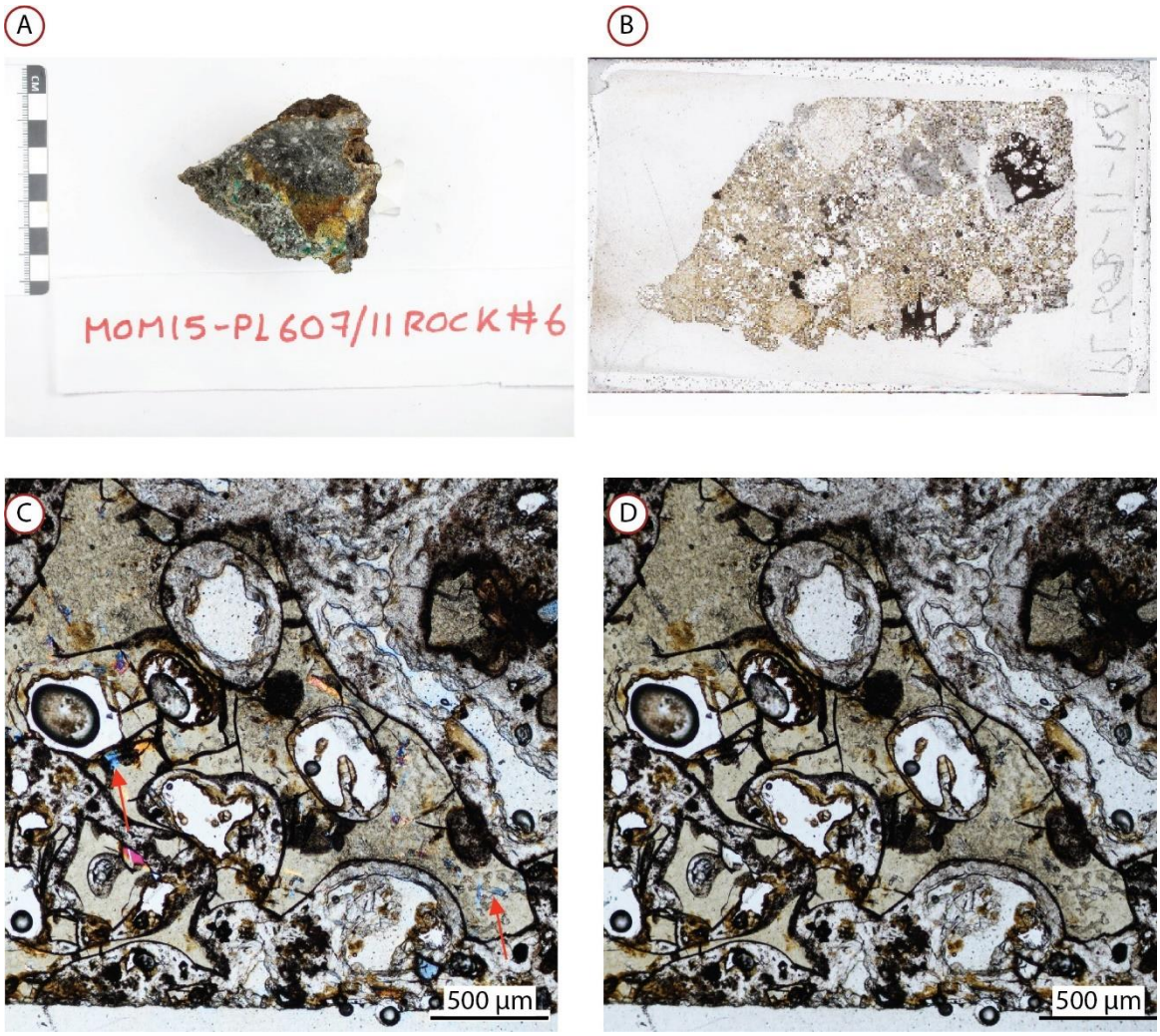

Figure A4.2. Sample MOM15-607-R6. Isabel site. Age: 2662 years. Volcaniclastic rock with pyrite framboids and barite within glass shards and surrounding shards. A) Hand sample. B) Whole thin section scan. C) Photomicrograph of sample on transmitted light (XPL), red arrows point to acicular barite. D) Photomicrograph of sample on transmitted light (PPL).

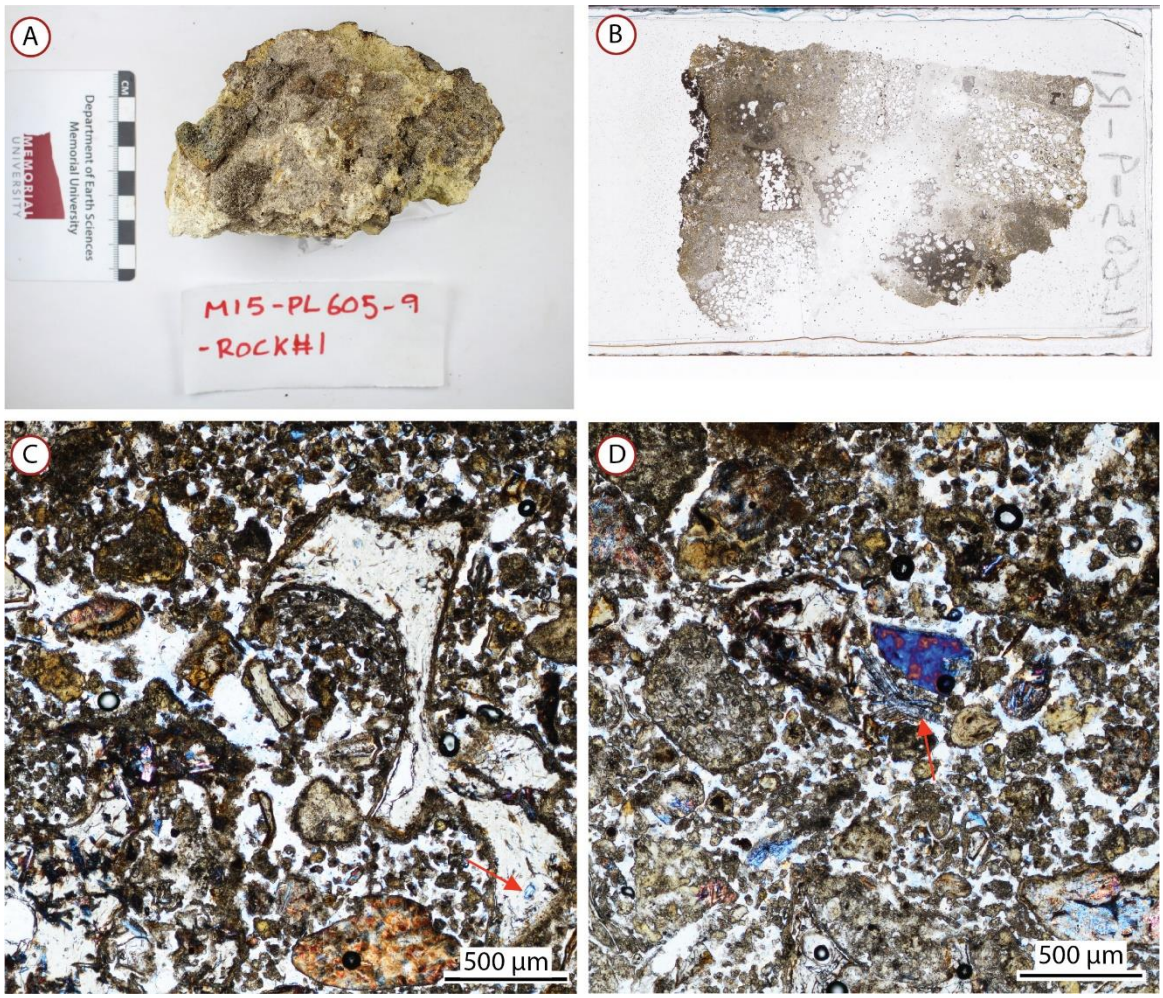

Figure A4.3. Sample MOM15-605-ROC1. Bairro Alto site. Age: 6403 years. Volcaniclastic rock with barite within glass shards and infilling voids. A) Hand sample. B) Whole thin section scan. C) Photomicrograph of sample on transmitted light (XPL), red arrows point to acicular barite within a glass shard. D) Photomicrograph of sample on transmitted light (XPL), red arrow shows barite infilling voids.

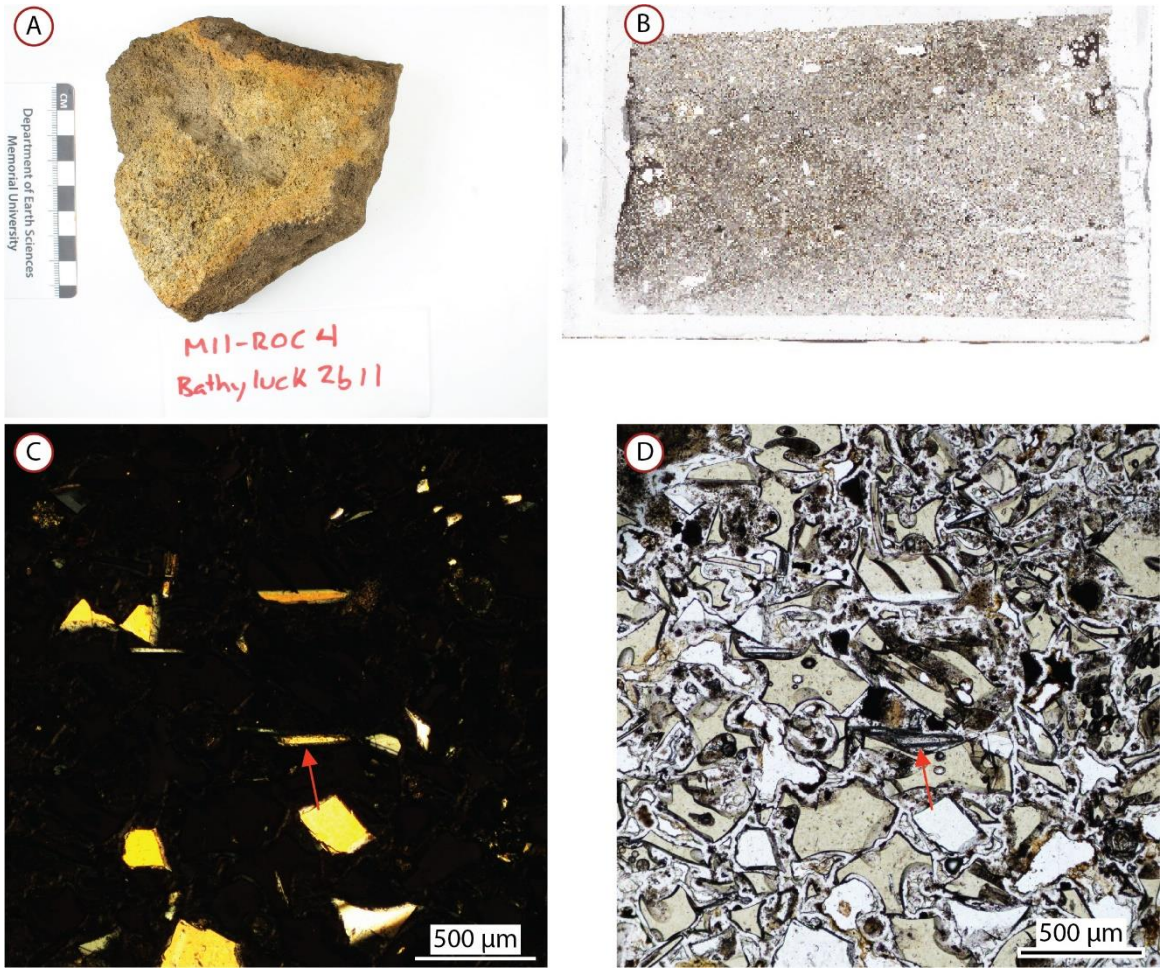

Figure A4.4. Sample MOM11-452-ROC4. Base of the Tour Eiffel site. Age: 3840 years. Volcaniclastic rock with minor pyrite and barite infilling voids. A) Hand sample. B) Whole thin section scan. C) Photomicrograph of sample on transmitted light (XPL), red arrows point to acicular barite within a glass shard. D) Photomicrograph of sample on transmitted light (PPL), red arrow shows barite infilling voids.

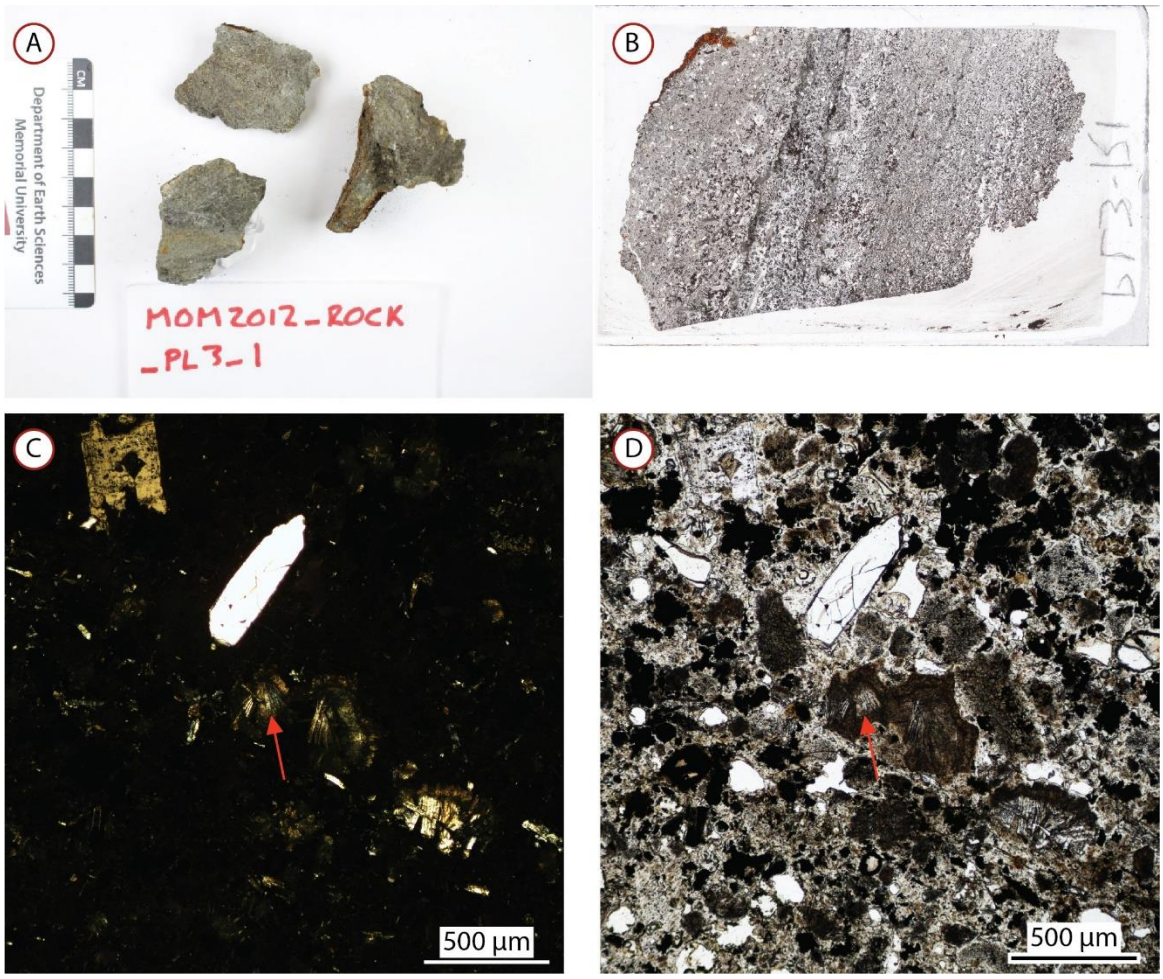

Figure A4.5. Sample MOM12-504-ROC1. 85 m SW of the Tour Eiffel site. Age: 2115 years. Volcaniclastic rock with disseminated marcasite, barite, chalcopyrite, covellite, hematite/goethite, and sphalerite. A) Hand sample. B) Whole thin section scan. C) Photomicrograph of sample on transmitted light (XPL), red arrows point to barite within the groundmass. D) Photomicrograph of sample on transmitted light (PPL), red arrow shows barite infilling voids within the groundmass.

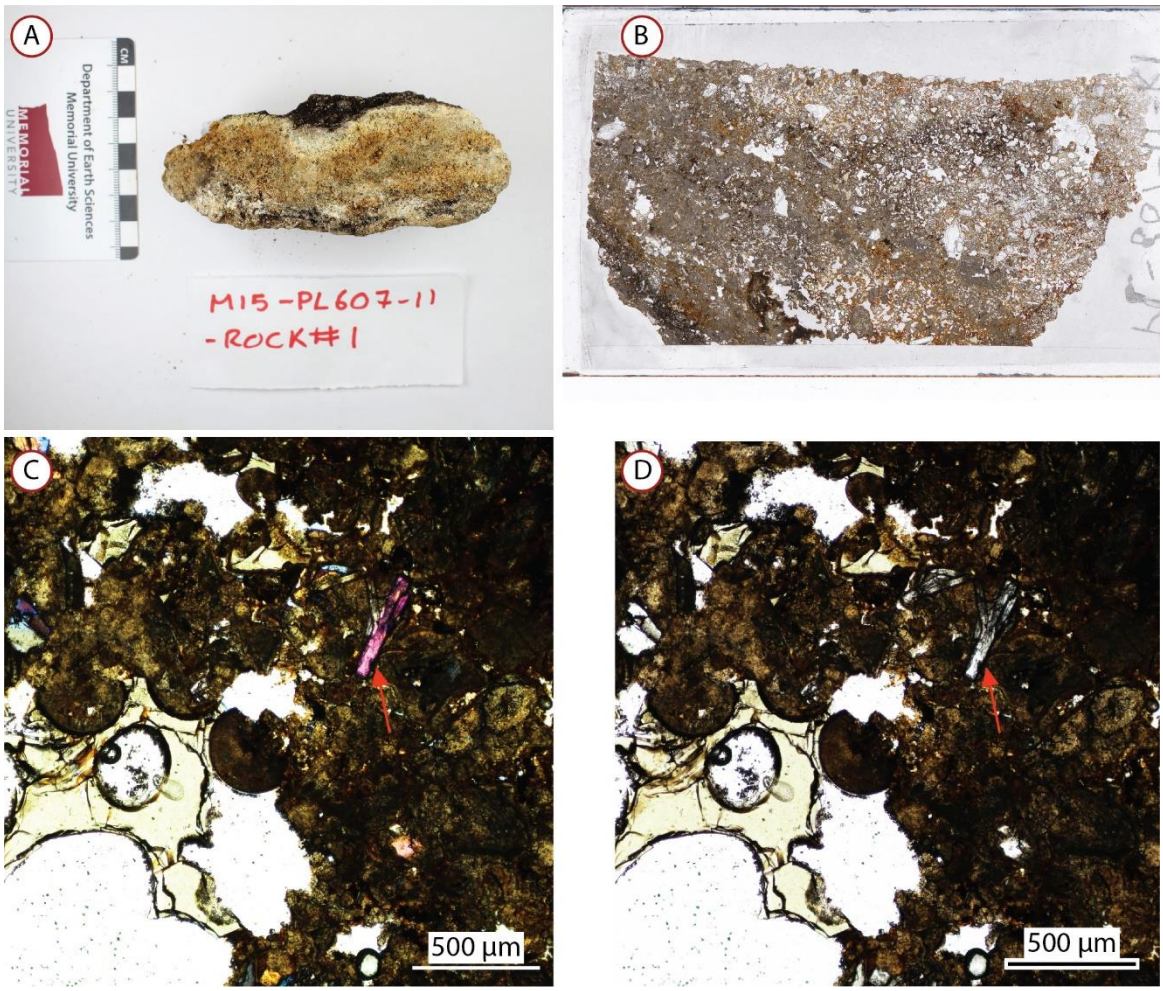

Figure A4.6. Sample MOM15-607-ROC1. 70 m W of the Tour Eiffel site. Age: 4060 years. Volcaniclastic rock with barite and minor pyrite. A) Hand sample. B) Whole thin section scan. C) Photomicrograph of sample on transmitted light (XPL), red arrows point to acicular barite within the groundmass. D) Photomicrograph of sample on transmitted light (PPL), red arrow shows acicular barite infilling voids within the groundmass.

Appendix 5 : Photomicrographs of SIMS sulfur isotope spots.

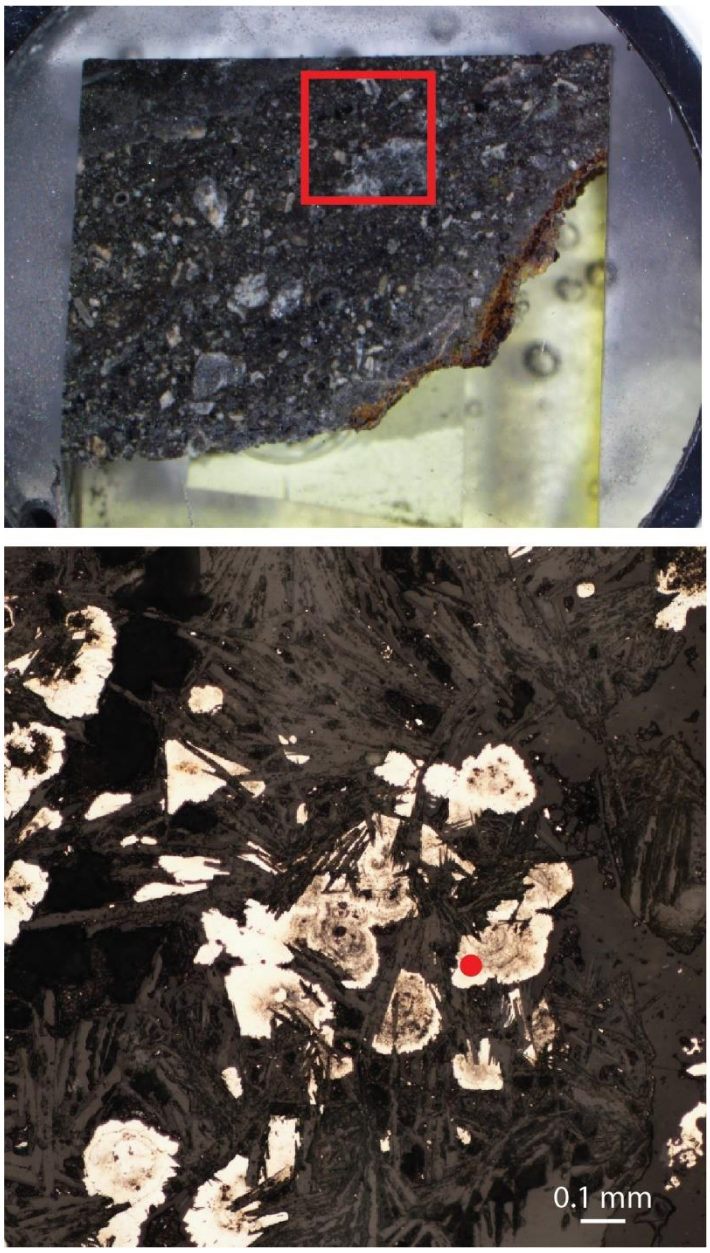

Figure A5.1. Sample MOM12-504-ROC1 (PL3-R1). Top photo is a puck with a red square showing the location in the image below. Photomicrograph in reflected light below of colloform marcasite and barite, red dot is the SIMS spot analysis for sulfur isotopes.

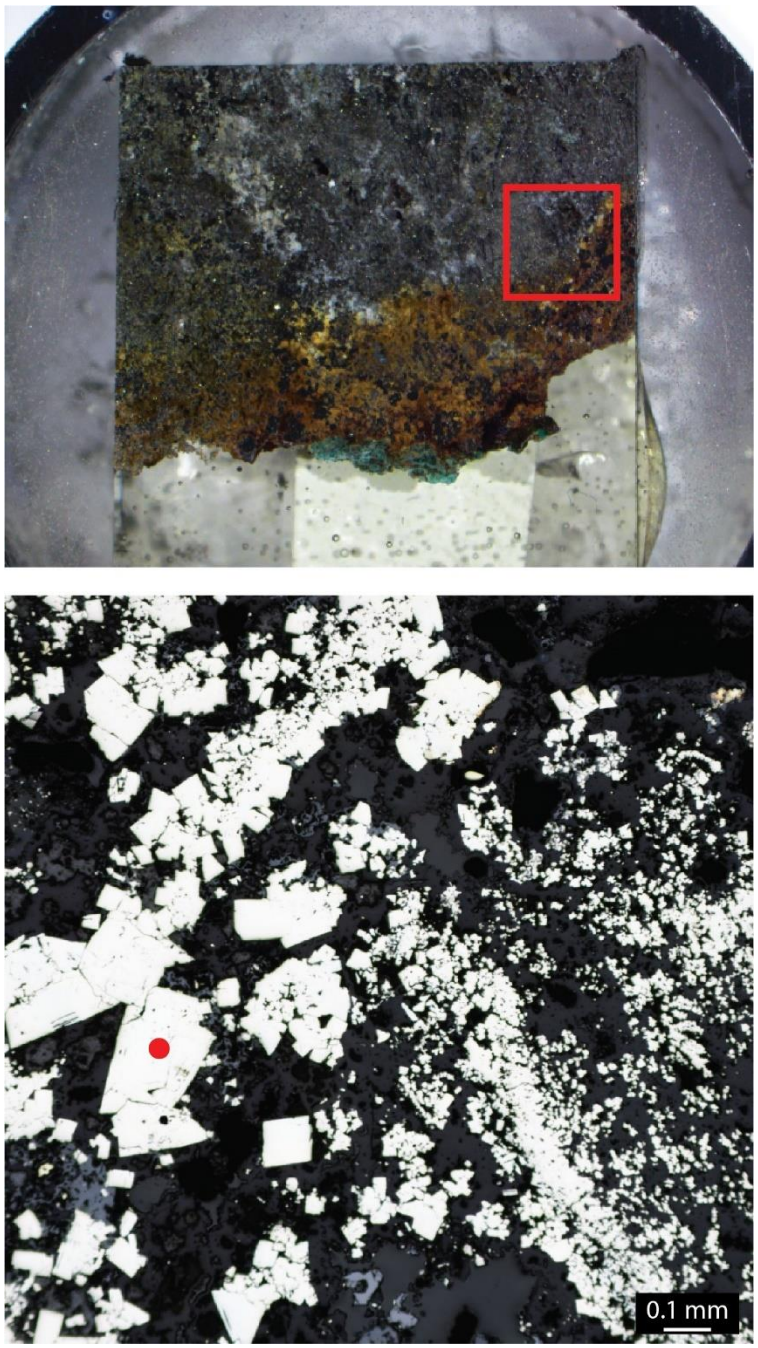

Figure A5.2. Sample MOM15-PL607-ROC3. Top photo is a puck with a red square showing the location in the image below. Photomicrograph of reflected light below of euhedral marcasite, red dot is the SIMS spot analysis for sulfur isotopes.

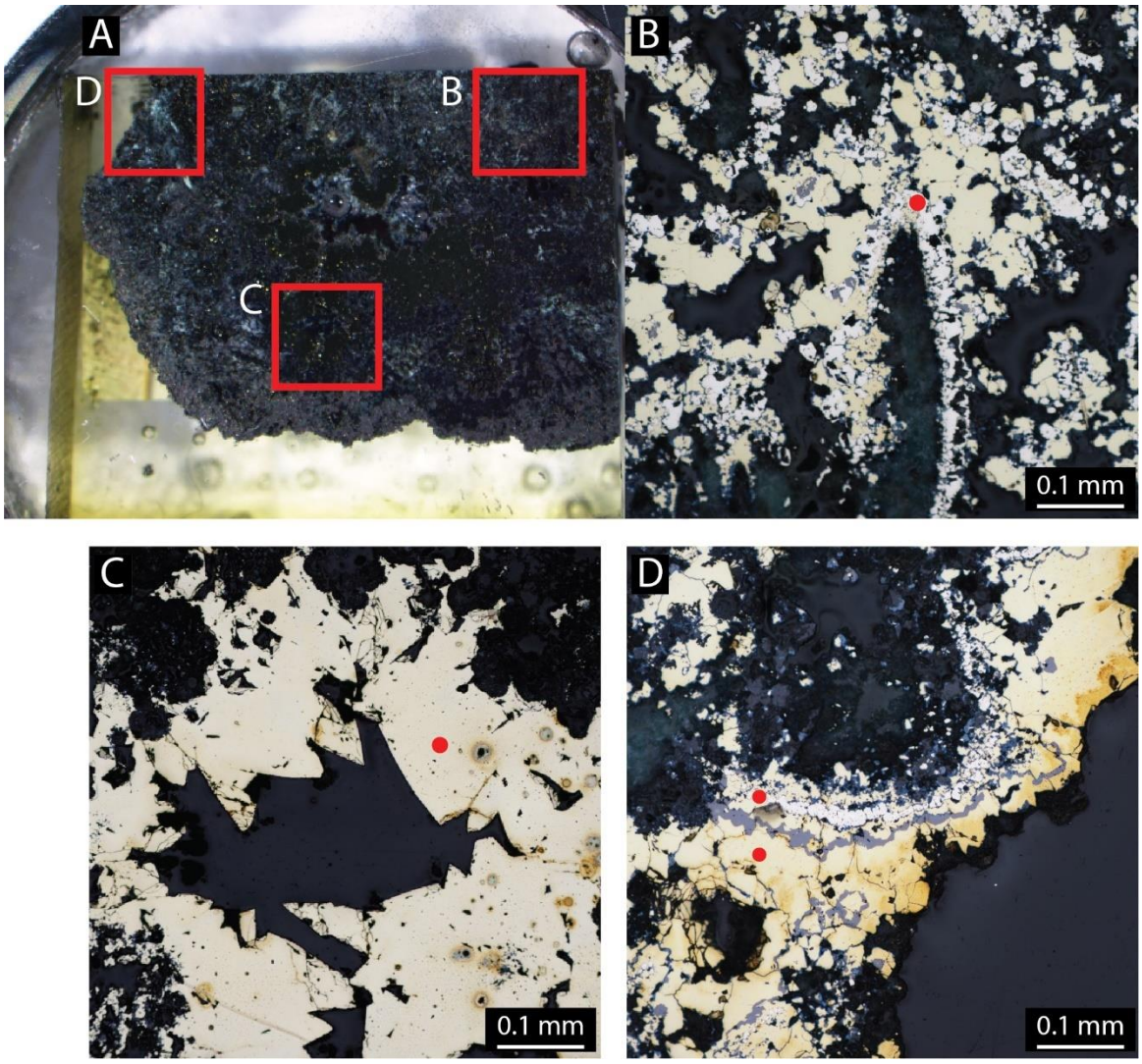

Figure A5.3. Sample MOM11-452-ROC3 (M11-R3). A) Photo is a puck with red squares showing the location of photomicrographs. B) Photomicrograph in reflected light of ring marcasite, red dot is the SIMS spot analysis for sulfur isotopes. C) Photomicrograph in reflected light of euhedral chalcopyrite, red dot is the SIMS spot analysis for sulfur isotopes. D) Photomicrograph in reflected light of massive chalcopyrite, red dots are the SIMS spots analysis for sulfur isotopes.

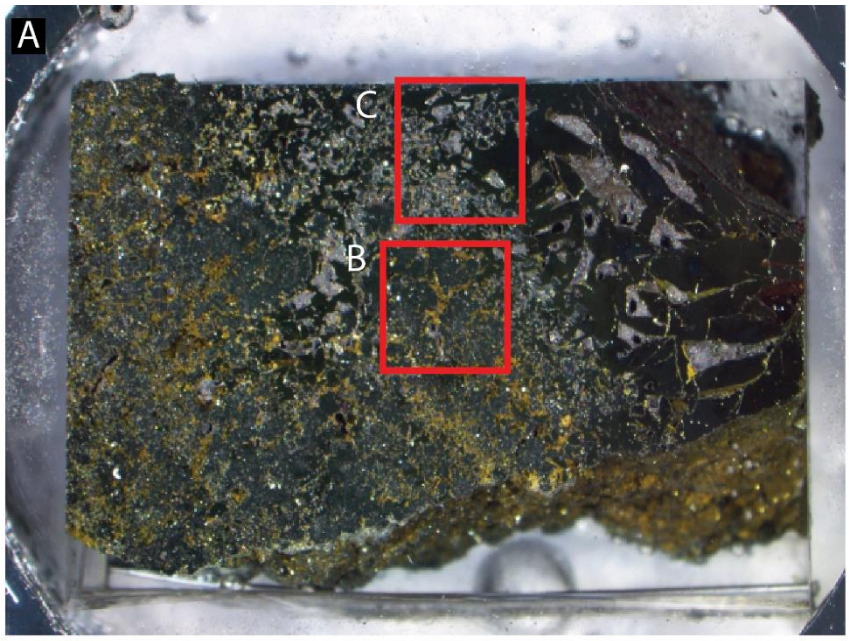

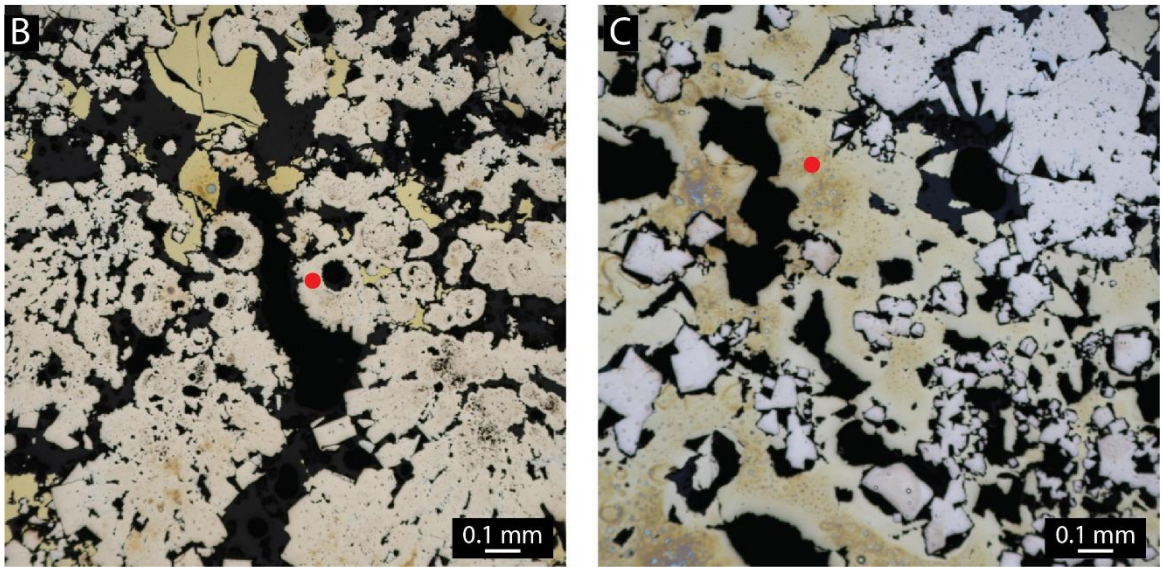

Figure A5.4. Sample MOM13-532-ROC2 (PL7-R2). A) Photo is a puck with red squares showing the location of photomicrographs. B) Photomicrograph in reflected light of euhedral/massive marcasite, red dot is the SIMS spot analysis for sulfur isotopes. C) Photomicrograph in reflected light of massive chalcopyrite, red dot is the SIMS spot analysis for sulfur isotopes.

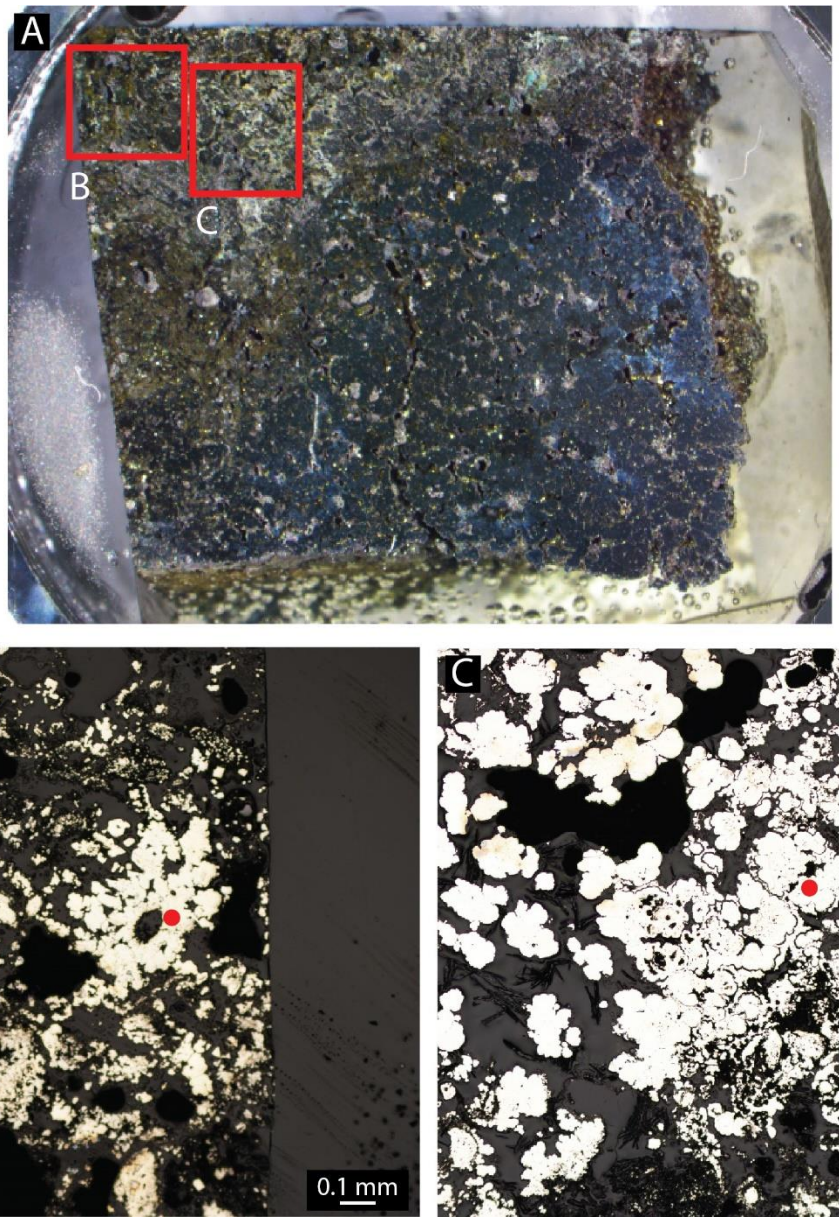

Figure A5.5. Sample MOM11-452-ROC1 (M11-R1). A) Photo is a puck with red squares showing the location of photomicrographs. B) Photomicrograph in reflected light of colloform marcasite, red dot is the SIMS spot analysis for sulfur isotopes. C) Photomicrograph in reflected light of colloform marcasite, red dot is the SIMS spot analysis for sulfur isotopes.

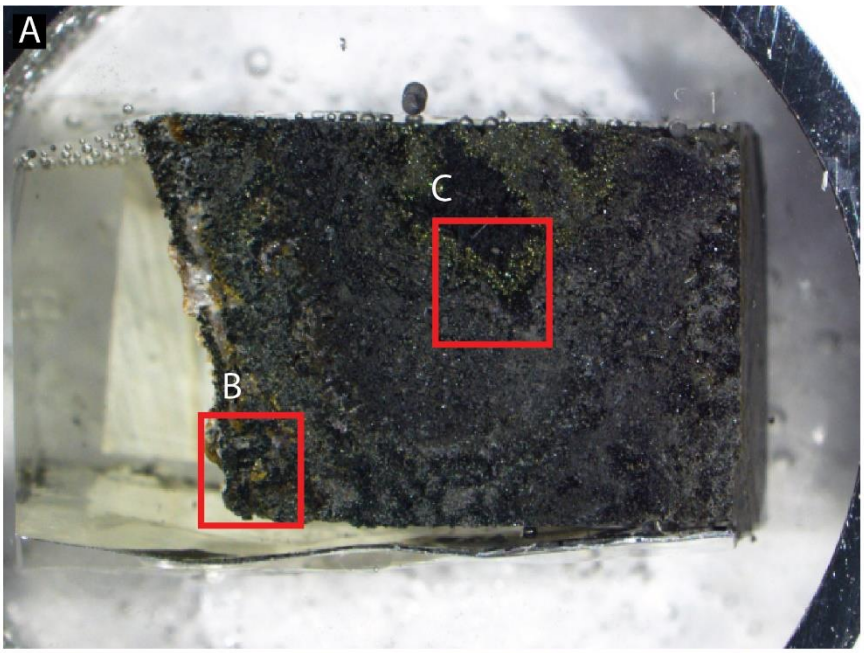

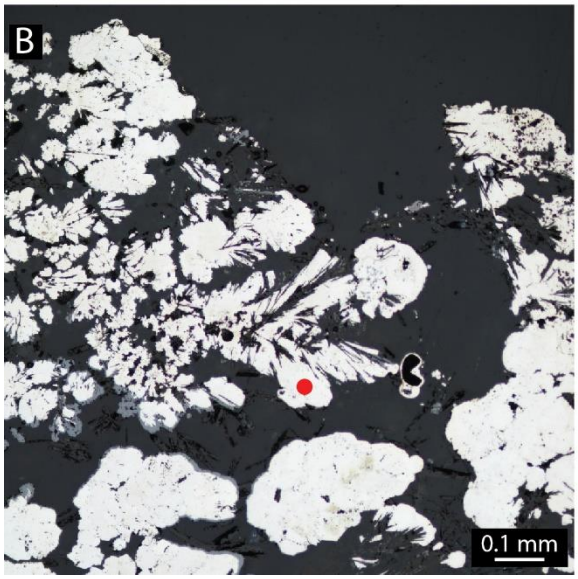

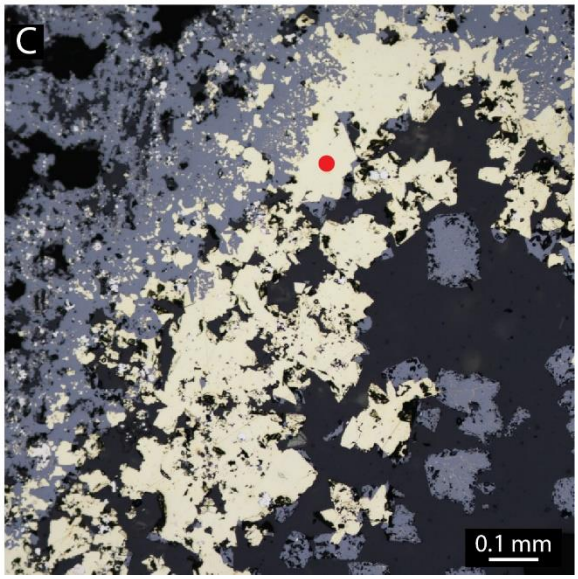

Figure A5.6. Sample MOM11-457-ROC8 (M11-R8). A) Photo is a puck with red squares showing the location of photomicrographs. B) Photomicrograph in reflected light of plumose marcasite, red dot is the SIMS spot analysis for sulfur isotopes. C) Photomicrograph in reflected light of massive chalcopyrite, red dot is the SIMS spot analysis for sulfur isotopes.

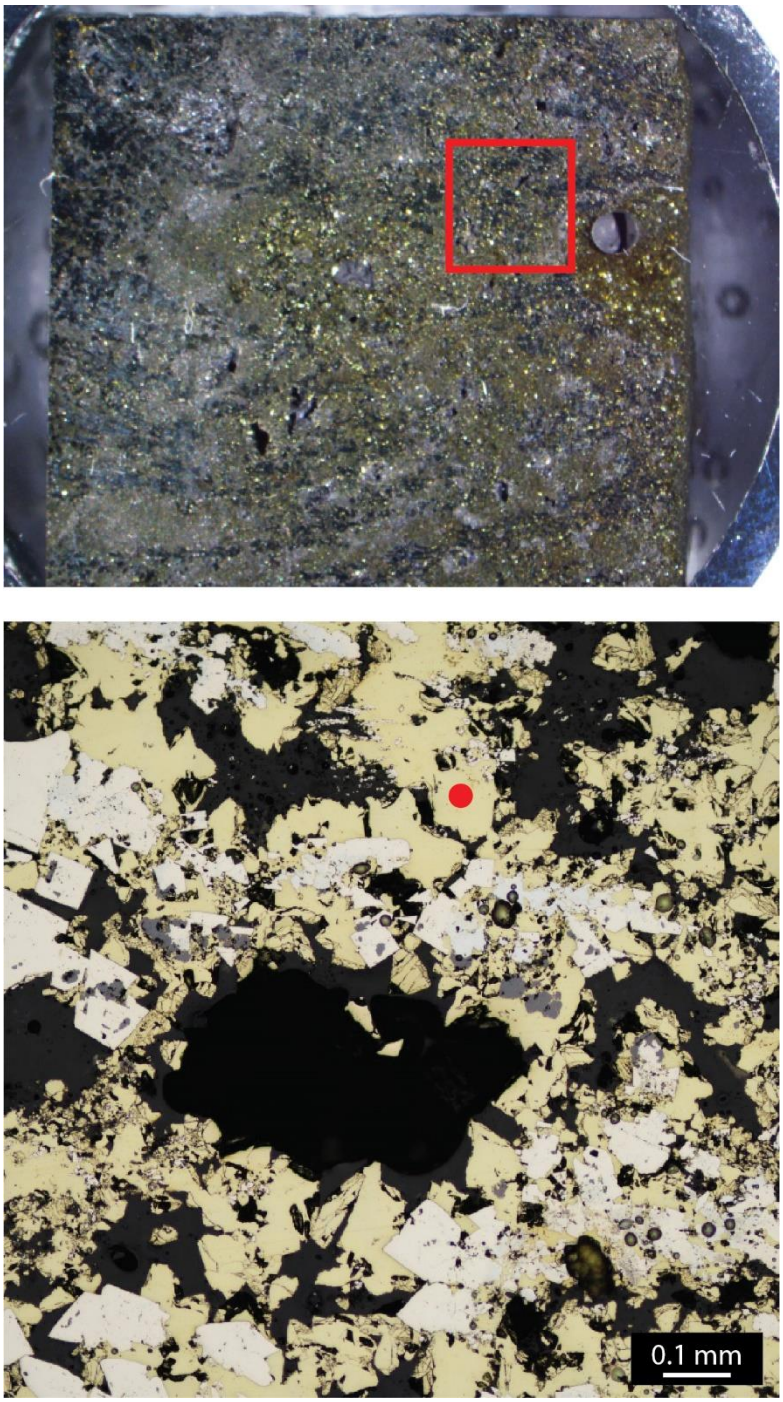

Figure A5.7. Sample MOM14-PL583-ROC4 (583-R4B). Photo on the top is a puck with a red square showing the location of photomicrographs. Photomicrograph (on the bottom) in reflected light of euhedral/massive chalcopyrite, red dot is the SIMS spot analysis for sulfur isotopes.

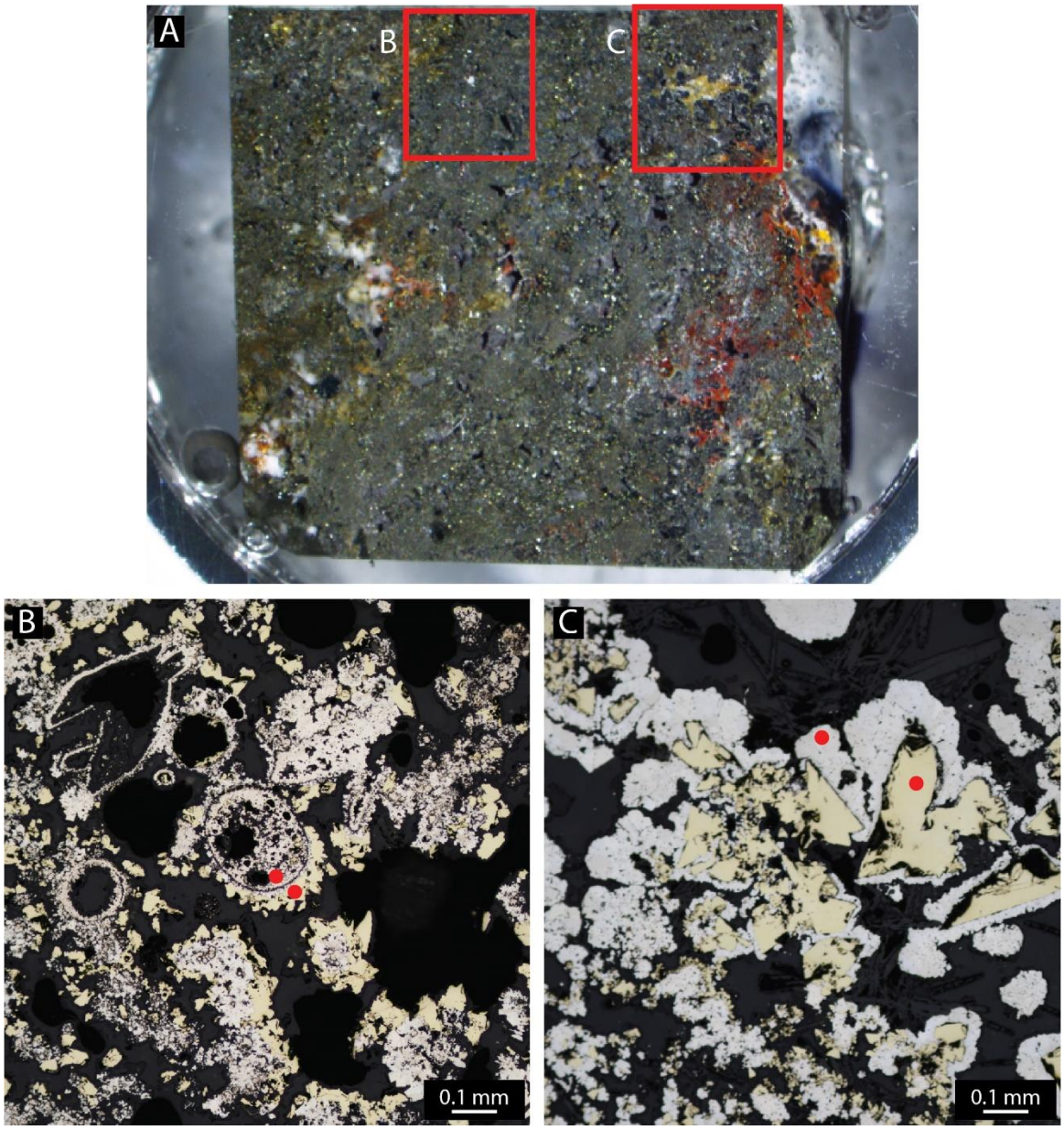

Figure A5.8. Sample MOM14-PL583-ROC1-S (583-R1). A) Photo is a puck with red squares showing the location of photomicrographs. B) Photomicrograph in reflected light of ooidal/ring marcasite and overgrowing euhedral chalcopyrite, the red dots are the SIMS spot analysis for sulfur isotopes. C) Photomicrograph in reflected light of massive/subhedral marcasite and infilling euhedral/massive chalcopyrite, the red dots are the SIMS spot analysis for sulfur isotopes.

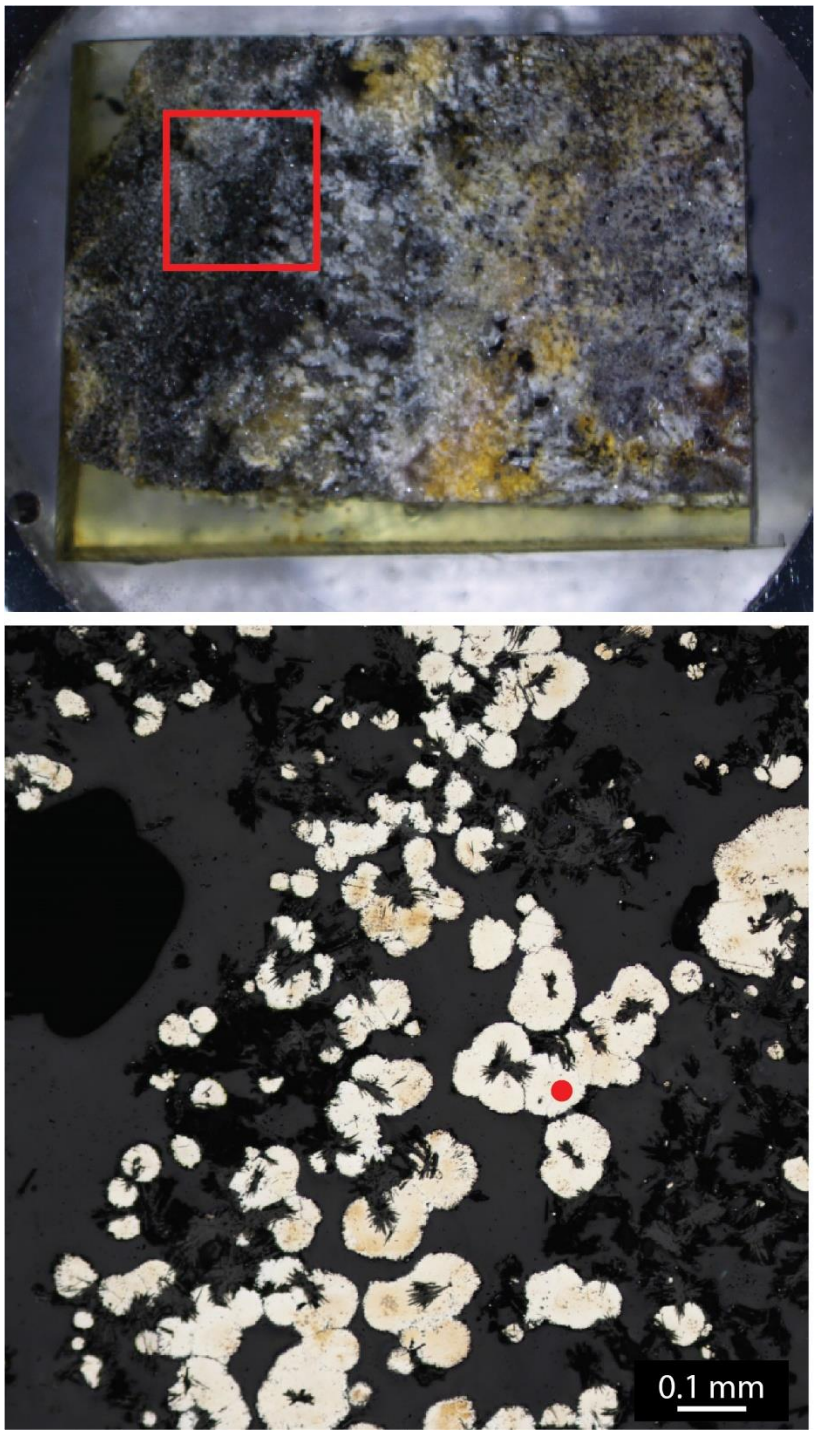

Figure A5.9. Sample MOM14-PL583-ROC4 (583-R4B). Photo on the top is a puck with a red square showing the location of photomicrographs. Photomicrograph (on the bottom) in reflected light of euhedral/massive chalcopyrite, red dot is the SIMS spot analysis for sulfur isotopes.

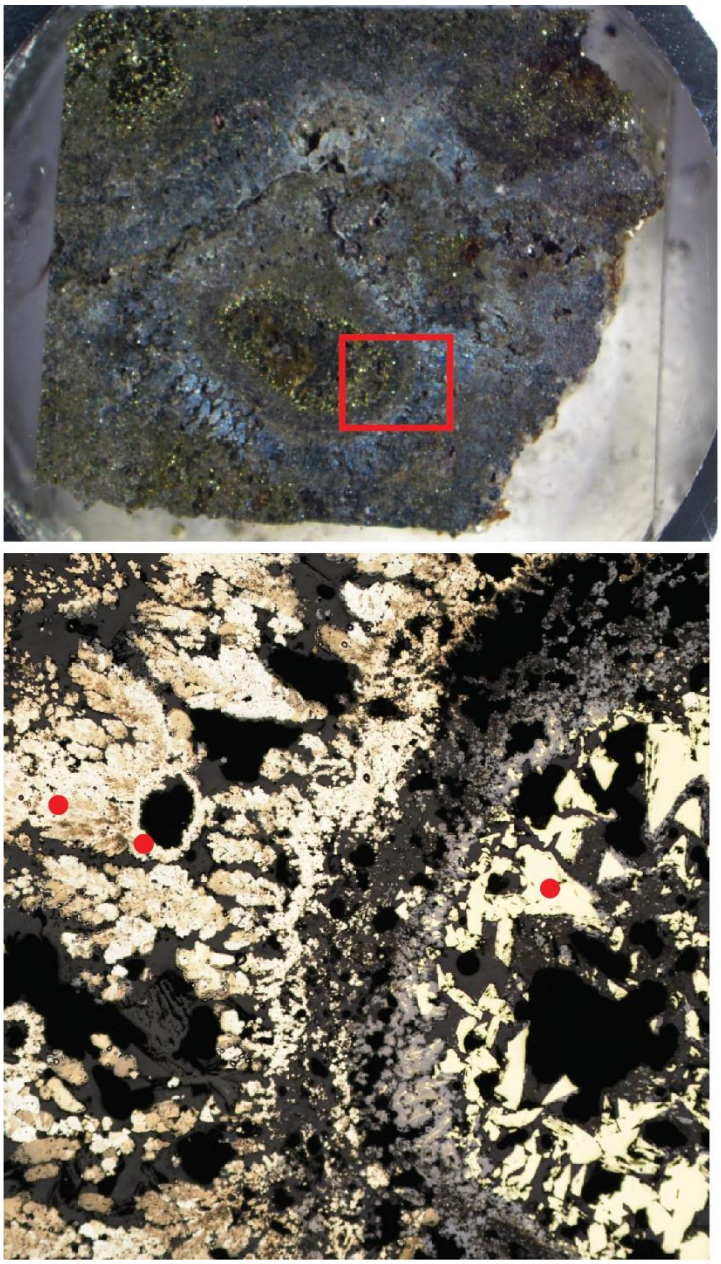

Figure A5.10. Sample MOM14-PL579-ROC1 (579-R1). Photo on the top is a puck with a red square showing the location of the photomicrograph. Photomicrograph (on the bottom) in reflected light of plumose marcasite, ooidal/ring marcasite, and euhedral chalcopyrite (from left to right), the red dots are the SIMS spot analysis for sulfur isotopes.

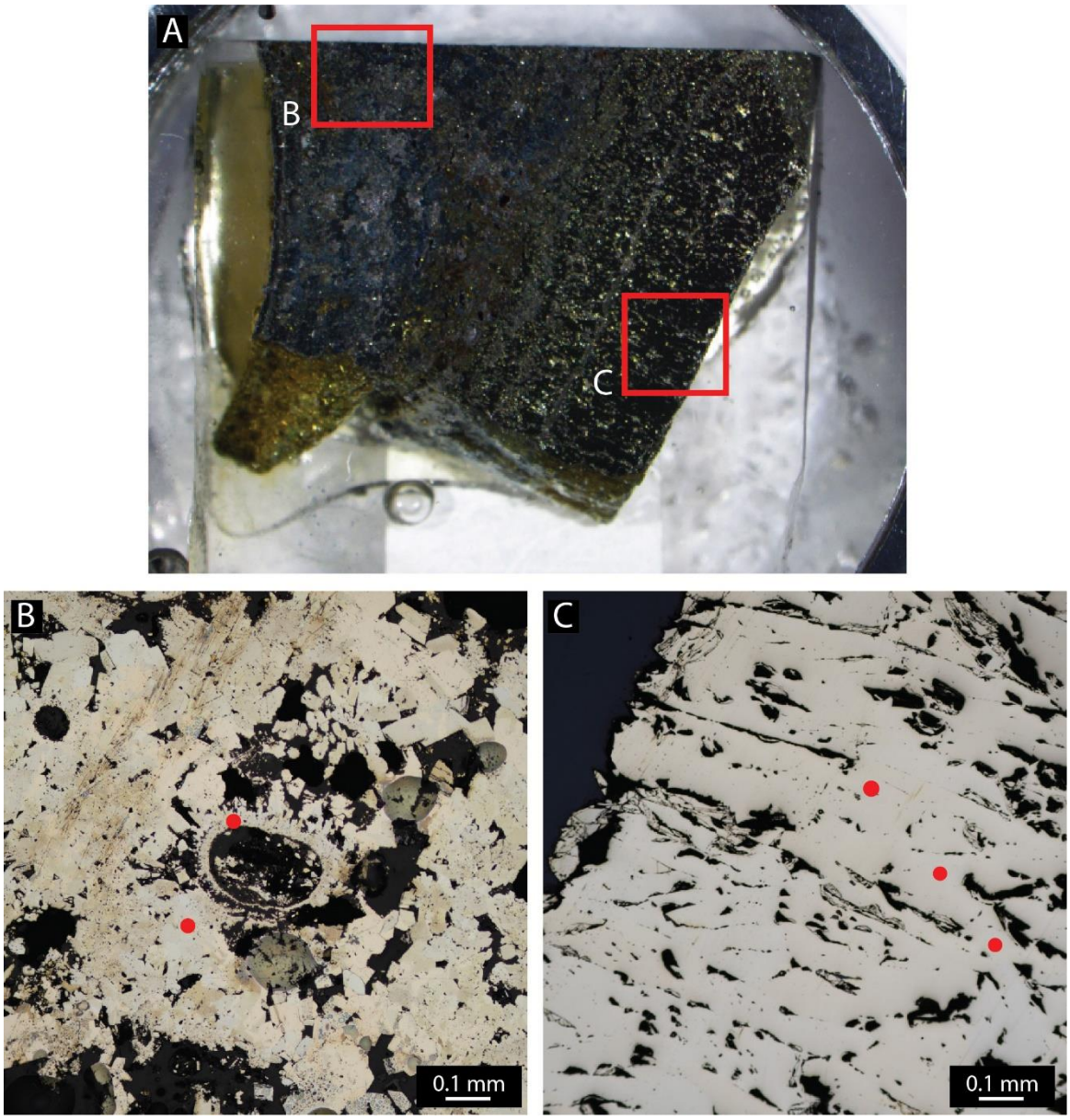

Figure A5.11. Sample MOM14-PL579-ROC1 (583-R4A). A) Photo is a puck with red squares showing the location of photomicrographs. B) Photomicrograph in reflected light of ooidal/ring and euhedral/massive marcasite, the red dots are the SIMS spot analysis for sulfur isotopes. C) Photomicrograph in reflected light of massive chalcopyrite, the red dots are the SIMS spot analysis for sulfur isotopes.

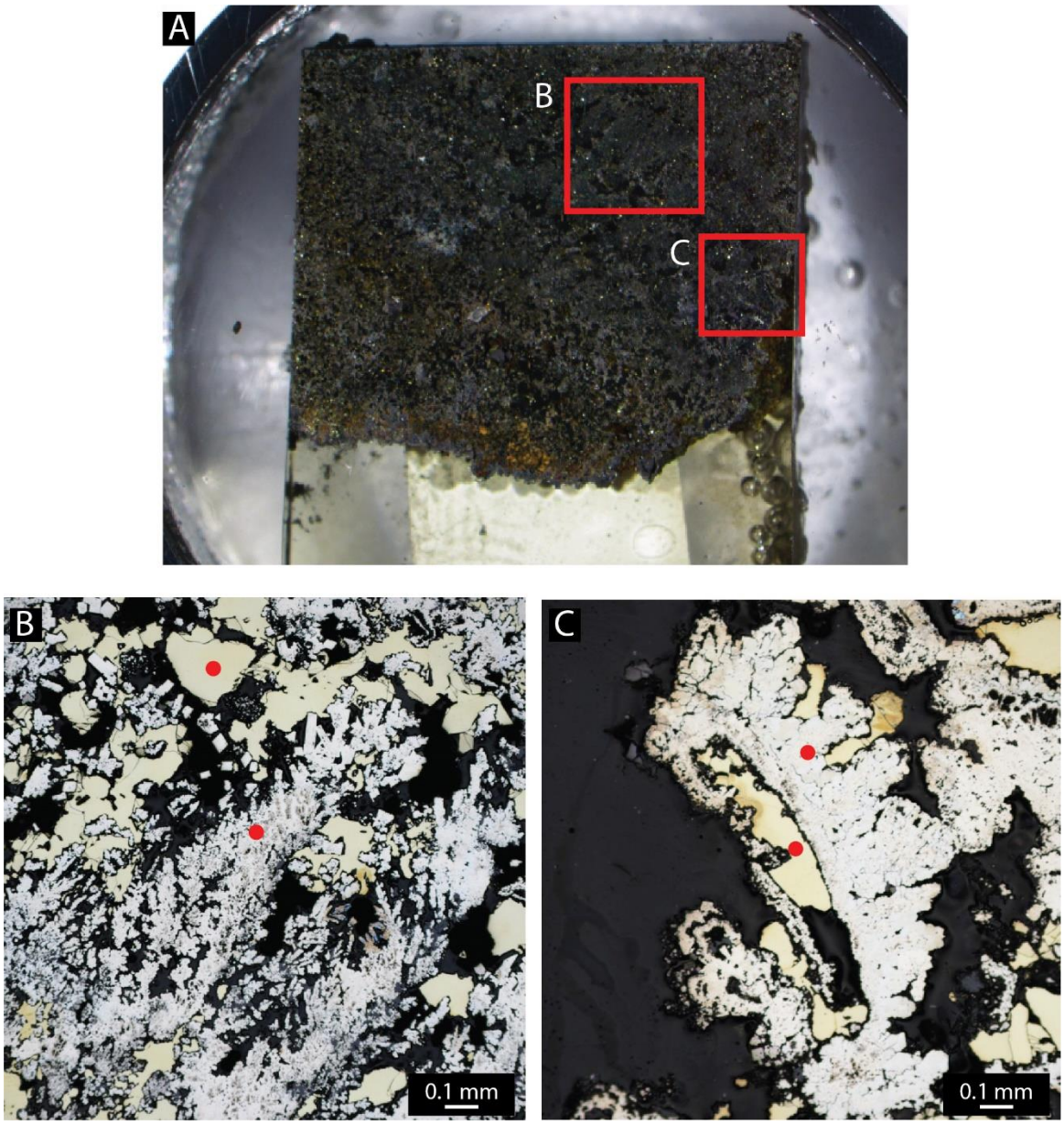

Figure A5.12. Sample MOM15-PL607-11-ROC5 (607-11-R5). A) Photo is a puck with red squares showing the location of photomicrographs. B) Photomicrograph in reflected light of plumose marcasite and overgrowing euhedral chalcopyrite, the red dots are the SIMS spot analysis for sulfur isotopes. C) Photomicrograph in reflected light of colloform marcasite with infilling massive chalcopyrite, the red dots are the SIMS spot analysis for sulfur isotopes.

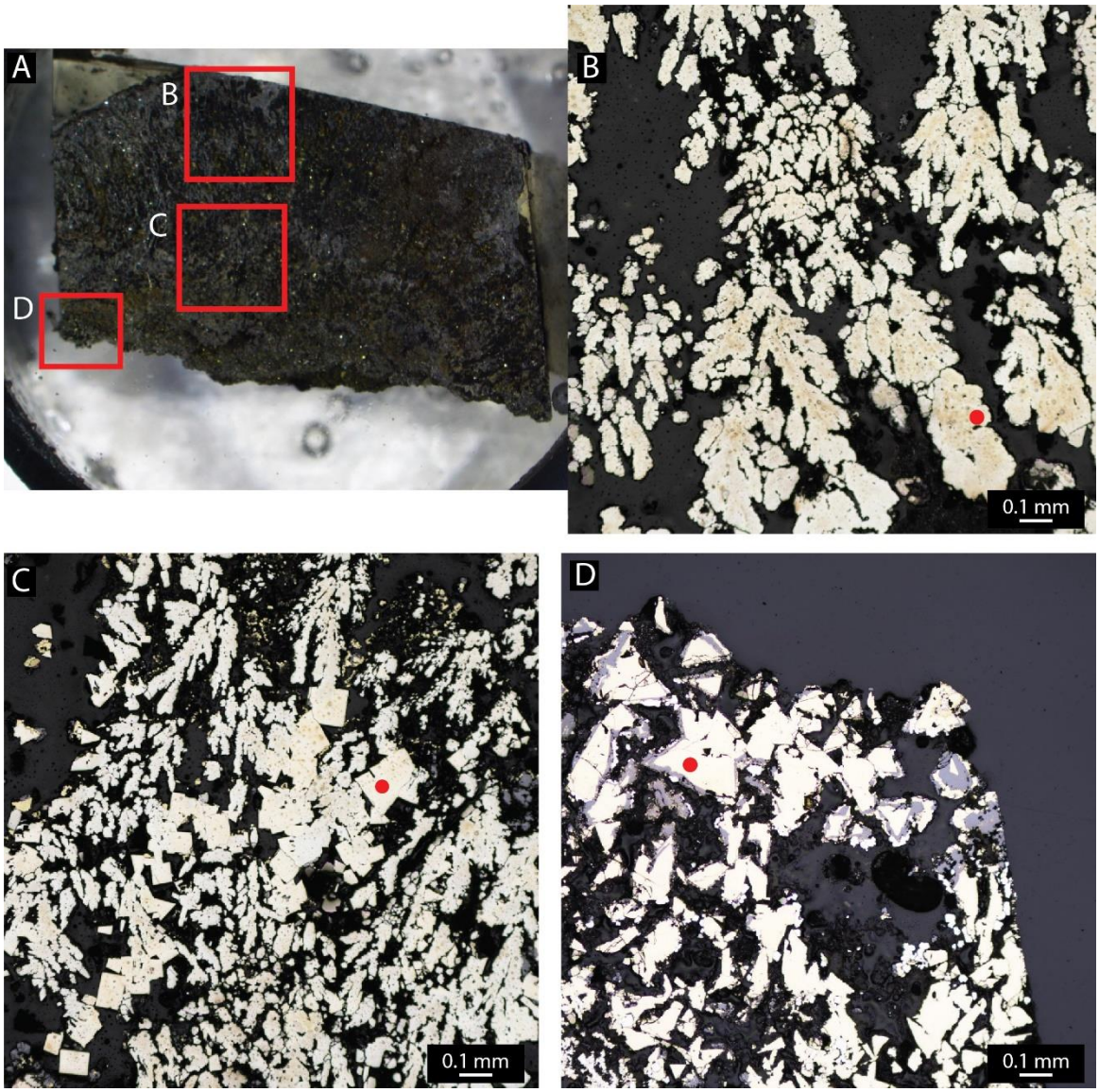

Figure A5.13. Sample MOM11-454-ROC7 (M11-R7). A) Photo is a puck with red squares showing the location of photomicrographs. B) Photomicrograph in reflected light of plumose marcasite, the red dot is the SIMS spot analysis for sulfur isotopes. C) Photomicrograph in reflected light of plumose/euhedral marcasite, the red dot is the SIMS spot analysis for sulfur isotopes. D) Photomicrograph in reflected light of euhedral chalcopyrite, the red dot is the SIMS spot analysis for sulfur isotopes.

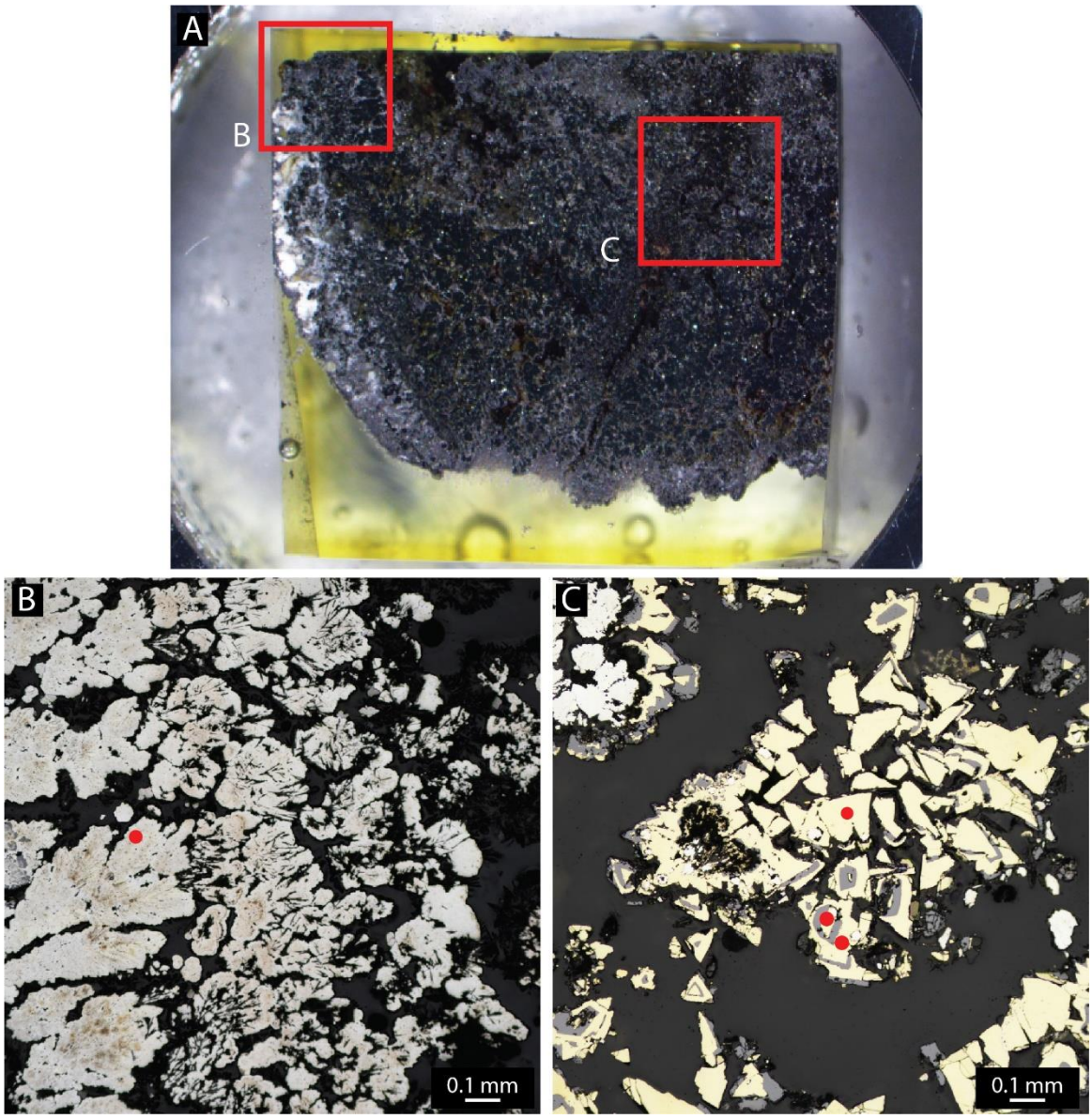

Figure A5.14. Sample LS-BS-WHOI. A) Photo is a puck with red squares showing the location of photomicrographs. B) Photomicrograph in reflected light of plumose marcasite, the red dot is the SIMS spot analysis for sulfur isotopes. C) Photomicrograph in reflected light of euhedral chalcopyrite, the red dots are the SIMS spot analysis for sulfur isotopes.

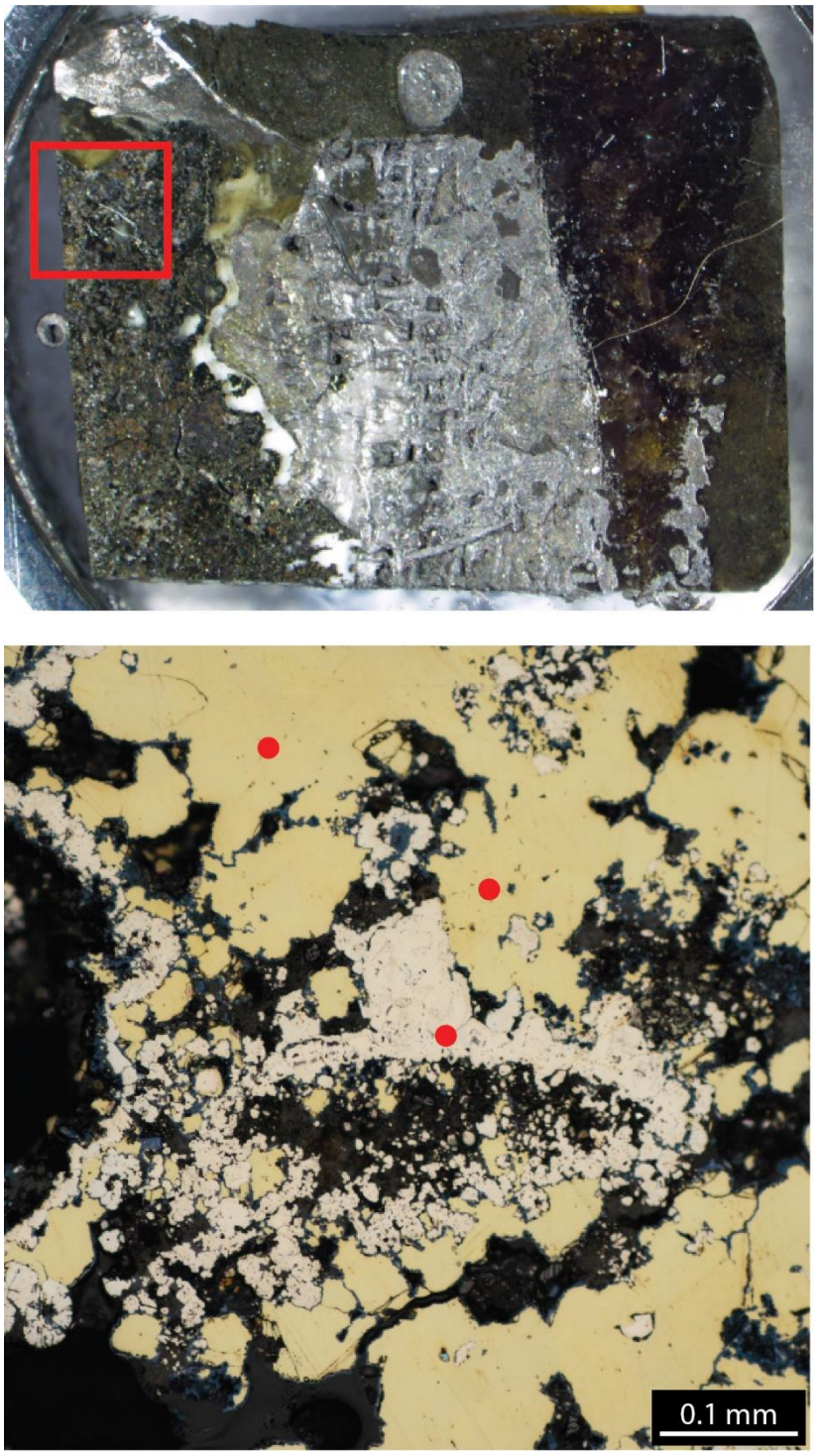

Figure A5.15. Sample MOM11-452-ROC2 (M11-R2). Photo on the top is a puck with a red square showing the location of the photomicrograph. Photomicrograph (on the bottom) in reflected light of euhedral marcasite and infilling massive chalcopyrite, the red dots are the SIMS spot analysis for sulfur isotopes.

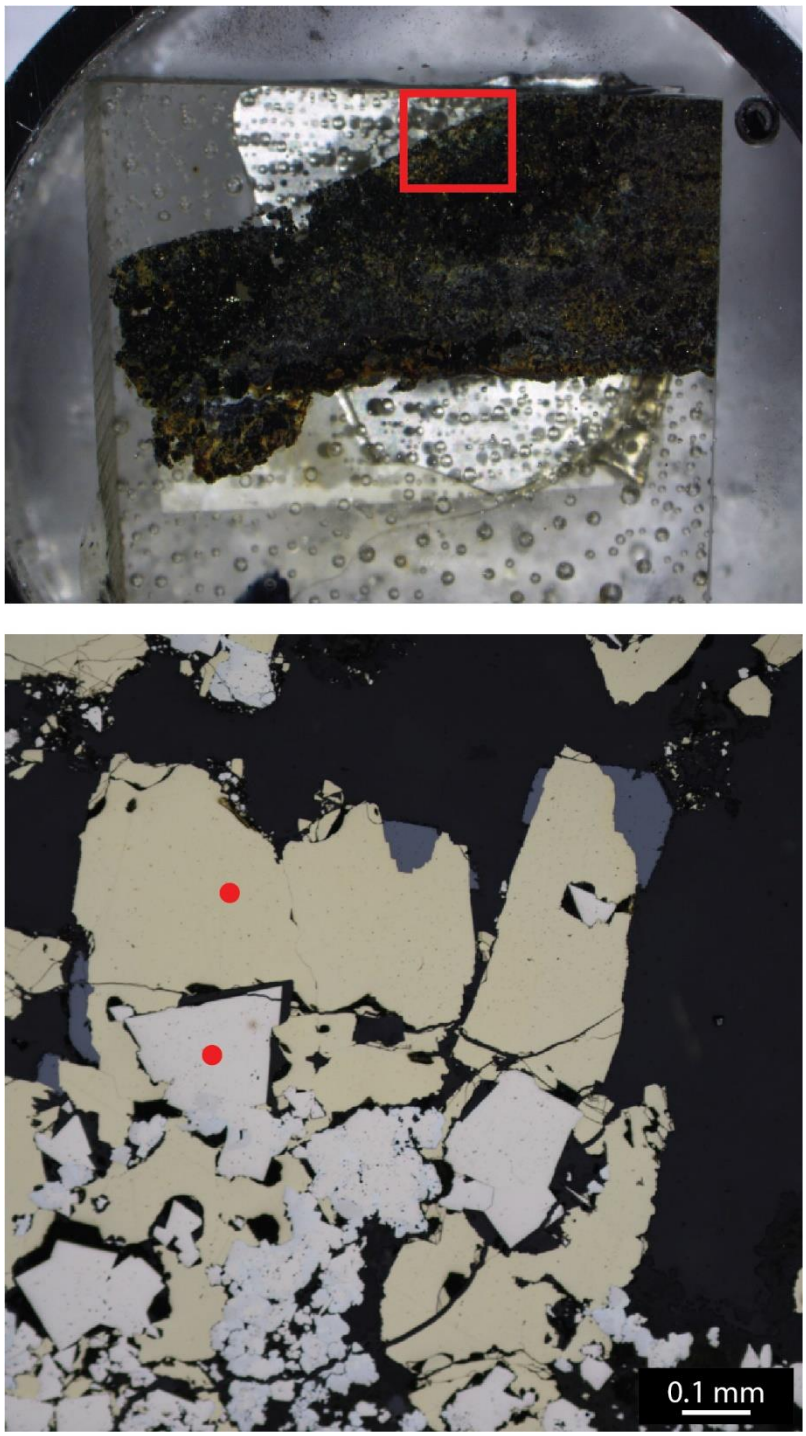

Figure A5.16. Sample MOM15-603-ROC6 (603-7-R6). Photo on the top is a puck with a red square showing the location of the photomicrograph. Photomicrograph (on the bottom) in reflected light of euhedral marcasite and overgrowing euhedral chalcopyrite, the red dots are the SIMS spot analysis for sulfur isotopes.

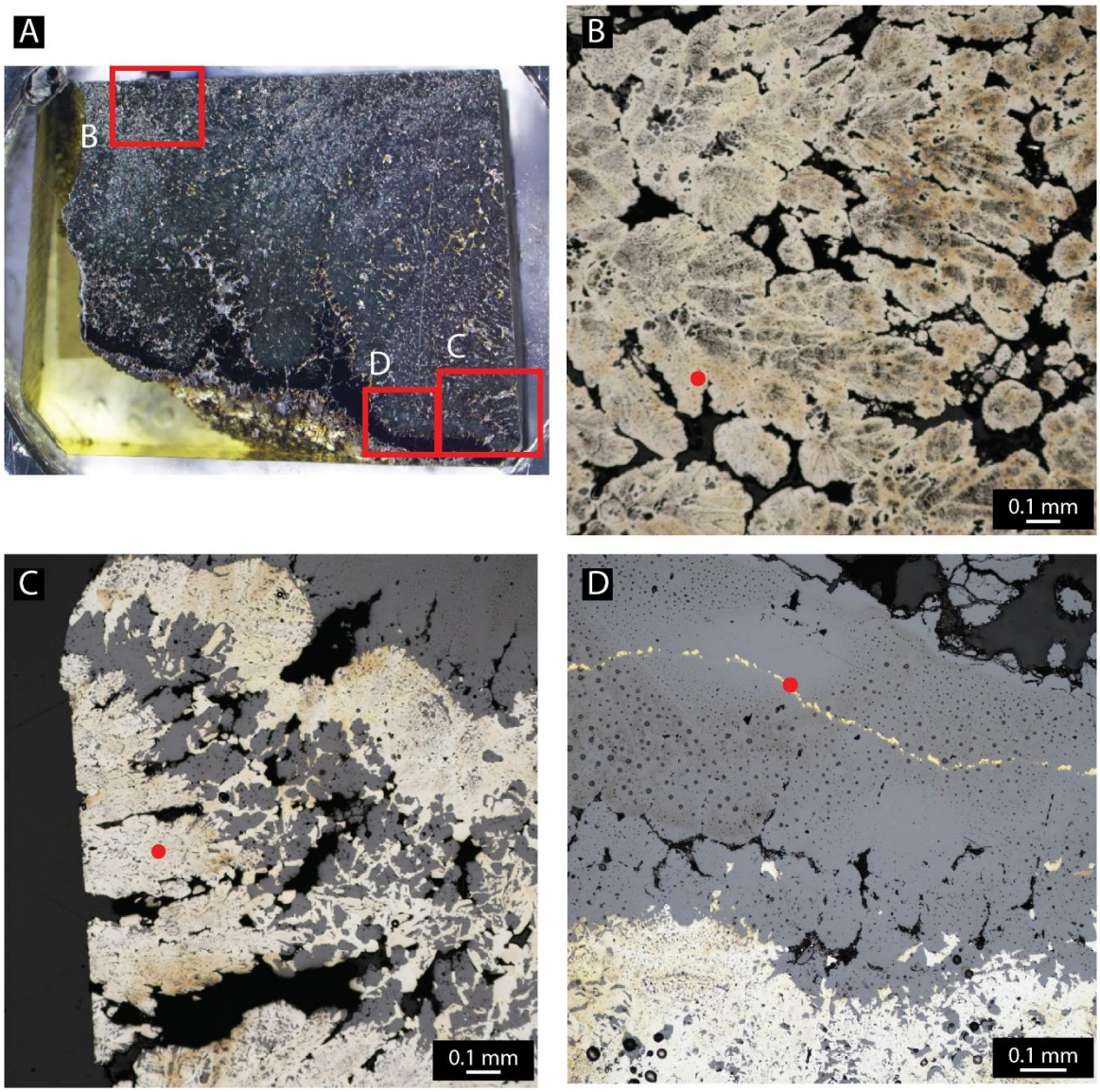

Figure A5.17. Sample MOM13-528-ROC1-S (PL12-R1-CA). A) Photo is a puck with red squares showing the location of photomicrographs. B) Photomicrograph in reflected light of plumose marcasite, the red dot is the SIMS spot analysis for sulfur isotopes. C) Photomicrograph in reflected light of plumose marcasite, the red dot is the SIMS spot analysis for sulfur isotopes. D) Photomicrograph in reflected light of chalcopyrite (chalcopyrite disease) within sphalerite, the red dot is the SIMS spot analysis for sulfur isotopes.

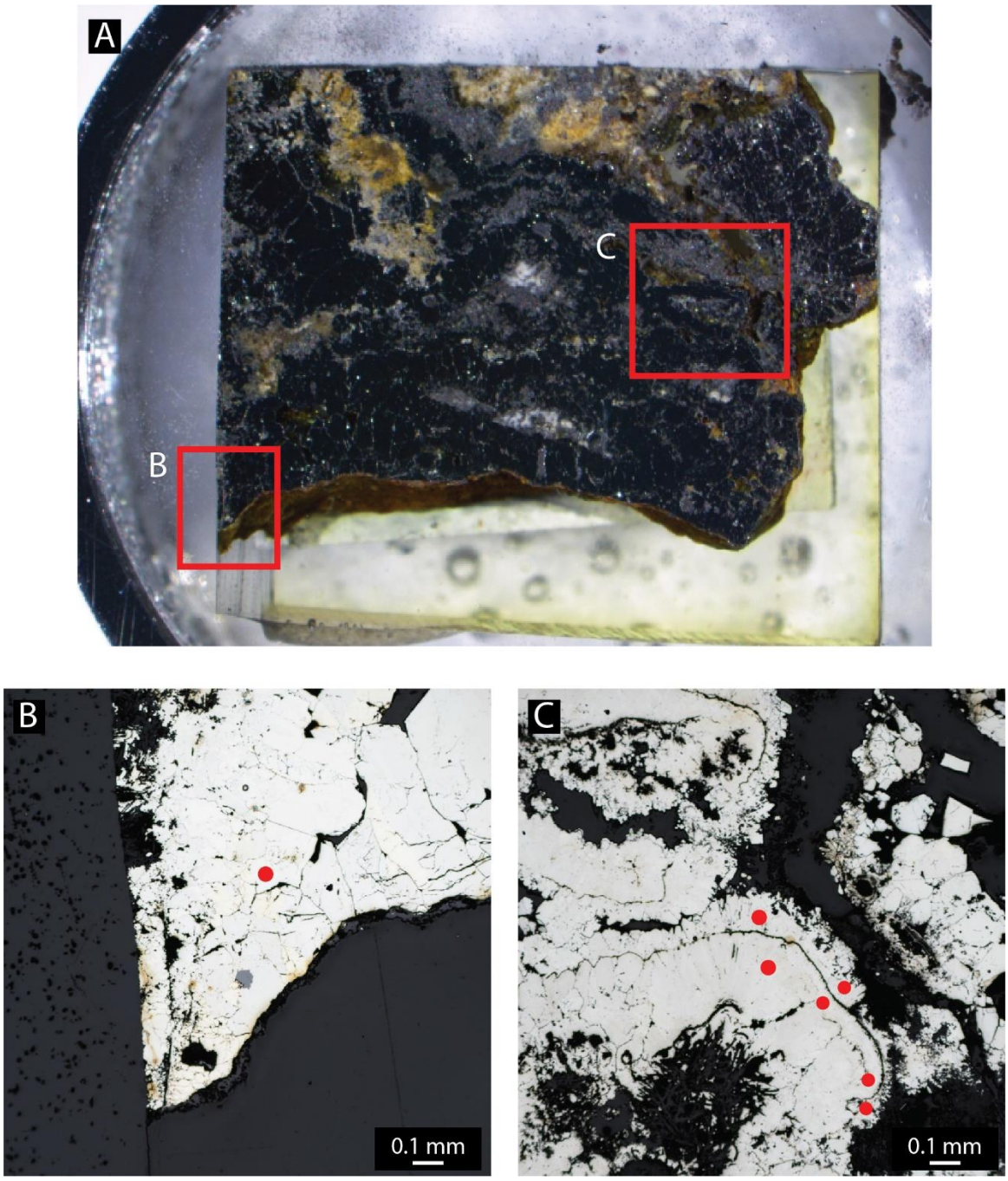

Figure A5.18. Sample MOM13-532-ROC1 (PL7-R1). A) Photo is a puck with red squares showing the location of photomicrographs. B) Photomicrograph in reflected light of massive marcasite, the red dot is the SIMS spot analysis for sulfur isotopes. C) Photomicrograph in reflected light of colloform chalcopyrite, the red dots are the SIMS spot analysis for sulfur isotopes.